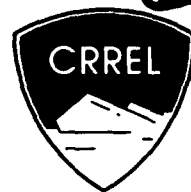
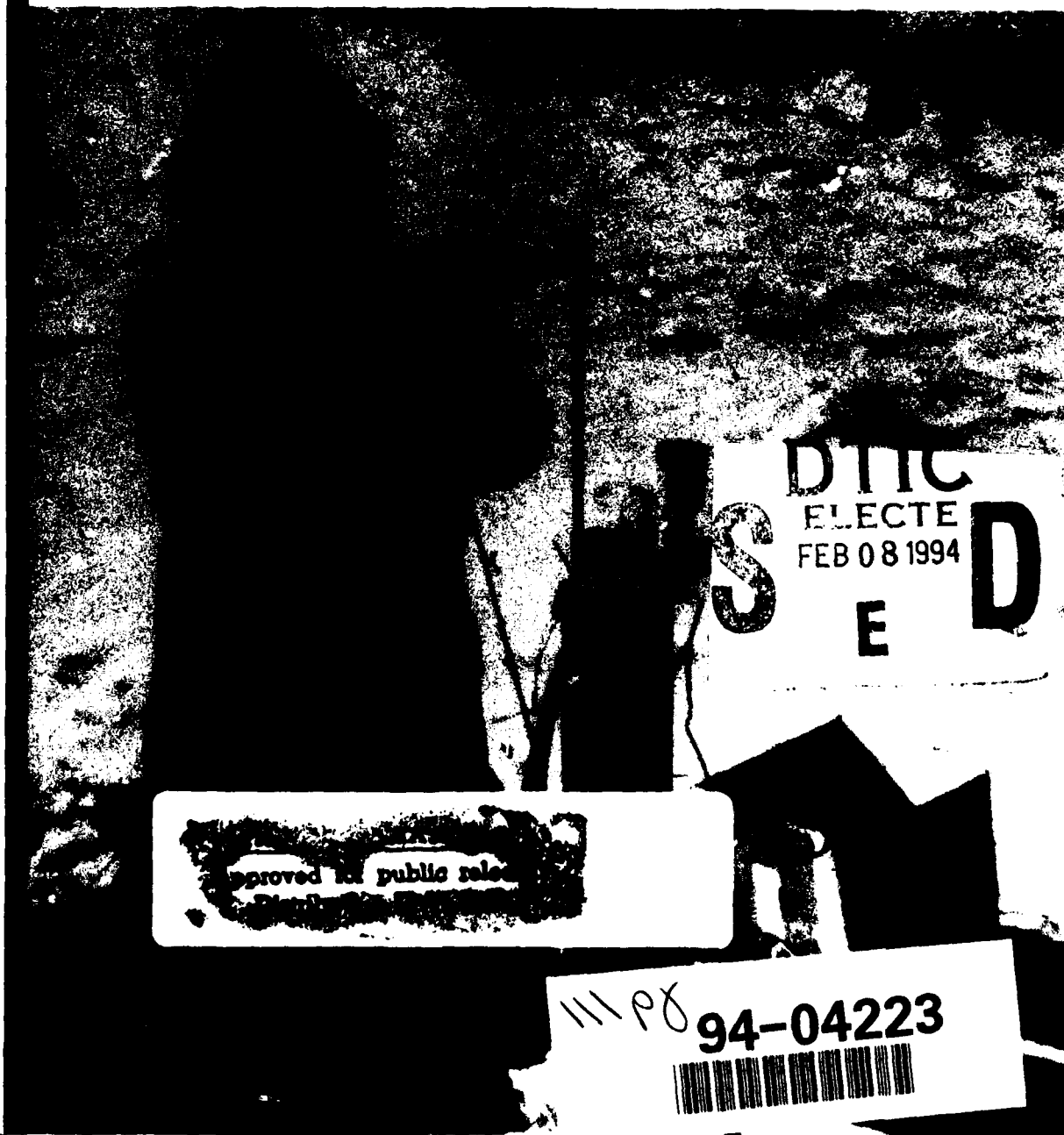


94 2 07 057



Donald G. Albert

November 1993



### **Abstract**

The absorption of sound energy by the ground has been studied extensively because of its importance in understanding noise propagation through the atmosphere. This report investigates the attenuative effect of snow on sound propagation, and provides quantitative measurements and an accurate model for predicting these effects. Summer and winter experiments were conducted at a site in northern Vermont to investigate the effect of a snow cover on low energy sound propagation in the 5- to 500-Hz frequency band for propagation distances between 1 and 274 m. Pistol shots were used as the source of the acoustic waves, with geophones and microphones serving as the receivers. A comparison of the summer and winter recordings revealed a number of effects caused by the introduction of a 0.25-m-thick snow cover. The peak amplitude of the air wave was more strongly attenuated in the winter, with a decay rate proportional to  $r^{-1.6}$  versus  $r^{-1.2}$  in the summer, corresponding to an order of magnitude difference in the signal levels after 100 m of propagation. The waveforms were also markedly changed, with broadened pulses and greatly enhanced low frequencies appearing in the winter recordings. The pulse broadening and peak amplitude decay rates of the acoustic waveforms were successfully predicted theoretically using a layered, rigid, porous model of the snow, with an assumed surface effective flow resistivity of  $20 \text{ kN s m}^{-4}$ . Calculations of ground motion induced by the atmospheric sound waves were made using a viscoelastic model of the ground and the wavenumber integration technique. Although soil ground motions were successfully modeled, induced motions in the snow were not, and the model always underpredicted the observed decay rates. An investigation of plane wave transmission from a fluid into a porous solid using Biot's theory shows that the presence of pores in the solid is the most important factor in the acoustic energy loss, not attenuation by transmission to the solid frame, and an explicitly porous model will be necessary to compute correctly the motion induced in the snow.

*Cover: .45-caliber blank pistol shots were used as an acoustic source to measure differences in atmospheric acoustic waves traveling above snow-covered or bare ground. The pistol was pointed toward the sensor array and fixed at a height of 1 m. A box containing a microphone and a pulse detection circuit was used to start the data recording.*

For conversion of SI metric units to U.S./British customary units of measurement consult ASTM Standard E380-89a, *Standard Practice for Use of the International System of Units*, published by the American Society for Testing and Materials, 1916 Race St., Philadelphia, Pa. 19103.



**US Army Corps  
of Engineers**

Cold Regions Research &  
Engineering Laboratory

# Attenuation of Outdoor Sound Propagation Levels by a Snow Cover

Donald G. Albert

November 1993

Accession For	
NTIS	CRA&I <input checked="" type="checkbox"/>
DTIC	TAB <input type="checkbox"/>
Unannounced <input type="checkbox"/>	
Justification .....	
By .....	
Distribution /	
Availability Codes	
Dist	Avail and / or Special
A-1	

Prepared for  
OFFICE OF THE CHIEF OF ENGINEERS

Approved for public release; distribution is unlimited.

DTIC QUALITY INSPECTED 8

## PREFACE

This report was prepared by Dr. Donald G. Albert, Geophysicist, Geophysical Sciences Branch, Research Division, U.S. Army Cold Regions Research and Engineering Laboratory. Funding was provided by the Office of the Chief of Engineers, Directorate of Research and Development, under DA Projects 4A762730AT24 and 4A762730AT42, and by the U.S. Army Civilian Long-Term Training Program.

Originally, this report was prepared as a Ph.D. dissertation in Earth Sciences at Scripps Institute of Oceanography, University of California, San Diego. The dissertation committee consisted of Dr. John A. Orcutt, Chair, Dr. Alistair J. Harding, Dr. William S. Hodgkiss, Dr. Robert L. Parker, Dr. David T. Sandwell and Dr. Frieder Seible.

Many people contributed to the success of this project. The author thanks Captain D. Briggs and the Vermont National Guard for the use of the field site. G. Aitken, M. Hardenberg, D. Harp, J. Lancaster, M. Pacillo, E. Perkins, S. Smith, R. Stover, R. Weil and E. Wright provided editorial or administrative assistance. Useful comments and reviews were provided by Dr. S. Arcone, Dr. K. Attenborough, Dr. H. Bass, Dr. S. Colbeck, Dr. K. Jezek, Dr. T. Landers, Dr. M. Mellor, P. Sellmann, Dr. L. Sutherland and Dr. S. Tooms. Assistance with the field experiment was given by R. Meyer, Dr. L. Peck and R. Stoops.

Special thanks are given to Dr. T. Sereno, for educating the author in the wavenumber technique, and to S. Decato, who provided invaluable field assistance, hundreds of pistol shots and hammer blows, and who suggested improvements to the field procedures.

Finally, the author thanks Mary, Marion and Michael Albert for their support and encouragement during the long process of completing this research.

Some of the text and figures of this report have appeared previously in the *Journal of the Acoustical Society of America* (Albert and Orcutt 1989, 1990). Permission has been granted by the American Institute of Physics to include this copyrighted material.

The contents of this report are not to be used for advertising or promotional purposes. Citation of brand names does not constitute an official endorsement or approval of the use of such commercial products.

## CONTENTS

	Page
Preface .....	ii
Introduction .....	1
Experimental methods .....	2
Experimental objectives .....	2
Overview of the experimental design and equipment .....	2
Experimental procedures .....	5
Calibration .....	8
Site characterization .....	12
Seismic velocity structure .....	12
Soil and snow properties .....	17
Meteorological data .....	23
Elevations .....	23
Observed data .....	23
Data set .....	25
Air wave coupling .....	25
Coupling to body waves .....	32
Summary .....	35
Data analysis .....	35
Observations .....	35
Comparison of theoretical and experimental acoustic waveforms .....	39
Modeling of acoustically induced ground motion .....	48
Computation of induced ground motion .....	48
Synthetic seismograms for simple Earth models .....	50
Comparison with experimental measurements .....	60
Summary .....	69
Reflection and transmission of plane waves across a fluid/porous-solid interface .....	69
Summary of Biot's theory .....	70
Application to air-filled materials .....	73
Summary .....	87
Conclusions .....	89
Literature cited .....	90
Appendix A: Conversion of data from SEG Y IBM floating point format .....	95
Appendix B: Seismic refraction data .....	97
Appendix C: Meteorological data recorded at the Camp Ethan Allen test site, 6 January 1986 .....	99
Appendix D: Viscosity correction term $F(\lambda)$ .....	103
Abstract .....	105

## ILLUSTRATIONS

### Figure

1. Comparison of the acoustic source strength of a single blank shot from a .45 caliber pistol and a .22 caliber pistol .....	3
2. Digital recording system .....	4
3. Location map. ....	4
4. Schematic cross-sectional view of the sensor arrays used in the experiments .....	5
5. Receiver array .....	6
6. Emplacement of microphones and geophones .....	7

	Page
7. Typical microphone calibration time series and spectrum .....	8
8. Procedure used for the BB drop calibrations of the vertical component geophones .....	9
9. Typical vertical component geophone responses to a BB impact and following bounces .....	9
10. BB impact velocity vs. the ratio of the geophone velocities .....	10
11. Examples of initial impacts and following bounces for each of the geophone channels .....	10
12. Bandwidth of the vertical geophone channels estimated from recorded BB drops .....	11
13. Source used for the <i>P</i> -wave refraction experiments was a vertical sledge hammer blow upon a metal plate placed on the ground .....	12
14. Location of the <i>P</i> -wave refraction lines .....	13
15. Source used for the <i>S</i> -wave refraction experiments .....	13
16. Example <i>SH</i> -wave refraction seismograms .....	14
17. Example <i>SH</i> -wave refraction seismograms with and without noise removal ....	15
18. Spectra of <i>SH</i> -wave traces before and after application of a low-pass digital filter .....	16
19. Example of a <i>P</i> -wave refraction record with the preamplifier gain setting too low .....	17
20. Distance vs. travel time plots for both source directions for <i>P</i> -wave refraction array 1 .....	17
21. Results of <i>P</i> -wave refraction measurements .....	18
22. Location of the snow pit, frost tubes and soil samples .....	19
23. Grain size distribution of the soil samples. ....	20
24. Vertical component geophone recordings of .45 caliber blank pistol shots in the summer .....	24
25. Vertical component geophone recordings of .45 caliber blank pistol shots in the winter .....	26
26. Vertical component geophone recordings of vertical sledge hammer blows in the summer .....	27
27. Vertical component geophone recordings of vertical sledge hammer blows in the winter .....	29
28. Comparison of recordings of a pistol shot from a microphone 0.5 m above the surface in summer and winter .....	28
29. Comparison of recordings of a pistol shot from vertical component geophones at the surface in summer and winter .....	31
30. Comparison of recordings for vertical component geophones at the surface in summer and winter, using 10 vertical sledge hammer blows .....	31
31. Comparison of recordings for microphones at the surface in summer and winter, using 10 vertical sledge hammer blows .....	32
32. Effect of low-pass filtering on recordings of .45 caliber pistol shots in summer and winter .....	33
33. Vertical component seismograms obtained from .45 caliber blank pistol shots in the winter, with a 0.25-m-thick snow cover present at the site .....	34
34. True amplitude comparison of vertical component geophone recordings in summer and winter .....	35
35. Particle motion diagrams from summer and winter surface geophones .....	36
36. Plot of first arrival amplitude vs. distance from the source for vertical component geophones .....	38
37. Geometry of the calculations and observations .....	40

	Page
38. Excess attenuation as a function of frequency calculated using the Delaney and Bazley model with $\sigma = 32,000 \text{ kN s m}^{-4}$ .....	43
39. Waveforms calculated using the Delaney and Bazley model with $\sigma = 32,000 \text{ kN s m}^{-4}$ for ranges of 0.1, 1 and 3 km .....	43
40. Excess attenuation as a function of frequency calculated using the Delaney and Bazley model with $\sigma = 10 \text{ kN s m}^{-4}$ .....	44
41. Waveforms calculated using the Delaney and Bazley model with $\sigma = 10 \text{ kN s m}^{-4}$ for ranges of 0.1, 1 and 3 km .....	44
42. Comparison of normalized waveforms for pulse propagation over grassland .....	45
43. Comparison of normalized waveforms for pulse propagation over snow .....	45
44. Power spectral density as a function of frequency for a surface microphone and a surface vertical component geophone in the summer .....	46
45. Plot of first arrival amplitude vs. distance from the source for pulse propagation .....	47
46. Model of the Earth used for the synthetic seismogram calculations .....	46
47. Synthetic seismograms for air over a solid half space with $V_p > V_p > c$ .....	51
48. Same seismograms as in 47, plotted at a constant gain .....	52
49. Displacements for half space model 2, consisting of air over a solid half space with $V_p > c > V_s$ .....	53
50. Displacements calculated for half space model 3, consisting of air over a solid half space with $c > V_p > V_s$ .....	54
51. Comparison of the effect of increasing attenuation in the solid .....	55
52. Calculated response of models with a single soil layer over a half space to an explosion in the air .....	56
53. Calculated effect of ground attenuation for a single layer over a half space, with $c > V_p > V_a$ and a layer thickness of 1 m .....	57
54. Calculated effect of layer thickness on ground motion .....	58
55. Observed waveforms of surface particle velocity in the summer .....	60
56. Observed waveforms of surface vertical particle velocity for the entire sensor array in the summer .....	61
57. Observed waveforms of surface displacement in the summer .....	62
58. Comparison of observed and calculated waveforms for summer conditions ....	63
59. Comparison of observed and calculated waveforms for summer conditions ....	64
60. Peak amplitude decay as a function of range measured in the summer and calculated for the models in Table 11 .....	65
61. Observed surface particle velocity waveforms in the winter recorded by surface geophones from a .45 caliber blank pistol shot .....	65
62. Observed snow surface and ground surface vertical particle velocity waveforms for the entire sensor array in the winter .....	67
63. Comparison of observed and calculated waveforms for winter conditions .....	67
64. Comparison of observed winter condition waveforms with waveforms calculated using various nonlinear attenuation mechanisms .....	68
65. Acoustic properties predicted by the Biot theory for soils 1, 2 and 3 .....	75
66. Predicted acoustic properties for soil 2 .....	79
67. Effect of tortuosity $q^2$ on the plane wave reflection and transmission coefficients for soil 2 .....	81
68. Effect of loss decrement $\delta$ on the $P_1$ - and S-plane wave transmission coefficients .....	82
69. Acoustic properties predicted by the Biot theory for snow 1 .....	84

	Page
70. $P_2$ -wave velocity as a function of frequency for snow with permeability values of 0.1, 10 and $10^3 \times 10^{-10} \text{ m}^2$ .....	85
71. Plane wave potential amplitude reflection coefficient $ A_r $ for a wave incident on an air/snow interface as a function of incident angle. ....	85
72. Plane wave potential amplitude transmission coefficient $ B_2 $ for a wave incident on an air/snow interface as a function of incident angle. ....	85
73. Plane wave potential amplitude transmission coefficients $ A_1 $ and $ A_3 $ for a wave incident on an air/snow interface as a function of incident angle .....	86
74. Acoustic properties predicted by the Biot theory .....	87
75. Power spectral densities for surface microphones in the summer and winter ...	89
76. Plane wave reflected and transmitted displacement potential amplitude coefficients for a wave incident on an air/air-filled porous solid interface as a function of incident angle .....	89

## TABLES

### Table

1. Microphone calibration RMS sound pressure levels .....	8
2. Geophone sensitivity determined from BB drops .....	10
3. Results of intercept time analysis .....	18
4. Soil properties .....	19
5. Snow layer profile of 26 January 1986, 1530 hours .....	22
6. Snow depths and ground surface elevations .....	23
7. Attenuation measurements .....	36
8. Range decay for air waves .....	37
9. Physical properties of the half space models .....	50
10. Physical properties of the single layered models .....	51
11. Input parameters used to calculate traces for comparison with the summer observations .....	62
12. Input parameters used to calculate traces for comparison with the winter observations .....	66
13. Input parameters and nonlinear attenuation mechanisms used to calculate traces for comparison with the winter observations .....	68
14. Estimated and derived parameters .....	74



# Attenuation of Outdoor Sound Propagation Levels by a Snow Cover

DONALD G. ALBERT

## INTRODUCTION

The absorption of sound energy by the ground has been studied extensively (Attenborough 1985, Chessell 1977, Embleton et al. 1976, 1983, Embleton and Daigle 1987) because of its importance in understanding noise propagation through the atmosphere. Predictions of outdoor sound levels produced by various sources can be usefully applied to practical problems, such as the reduction of traffic or industrial noise, and the estimation of community nuisance or damage levels from artillery firing ranges, construction blasting and other explosions. These predictions are also of interest in estimating acoustic-to-seismic coupling phenomena, which can have large effects on the performance of sensor systems that utilize ground motion to detect intruders or to locate military targets. In all of these applications, ground absorption is a major contributor to the overall sound level. Most studies have reported ground absorption effects as a function of frequency in terms of excess attenuation, the ratio of the sound level with the ground present to the sound level in free space at the same propagation range, expressed in decibels. Only a few studies (Don and Cramond 1987, Raspet et al. 1983, 1985) have dealt with the effect of the ground on acoustic pulse propagation, which requires integration over the frequency bandwidth of interest.

Early investigations of acoustic-to-seismic coupling, which date back to the 1930s, focused on air-coupled Rayleigh waves or flexural waves that can be observed at very large ranges (Albert 1987a, Embleton and Daigle 1987). Recently, work has been done on coupling at shorter ranges. Researchers (Attenborough et al. 1986, Bass et al. 1980, Sabatier et al. 1986a,b,c) developed probe microphones that can be inserted into the soil and, using continuous sound

sources, they showed that the coupling was mainly a local phenomenon, with the seismic waves being induced by the passage of the air wave directly over the sensors, in agreement with the earlier work. Body waves as well as surface waves have been detected from impulsive sources in the air (Gudesen 1985, van Hoof 1985, Knapp 1986).

A 0.70-m-thick snow cover can strongly attenuate the coupling (Albert 1987b), while enhanced coupling has been observed when a thin snow layer was present (Gudesen 1985). Increases and decreases in the coupling through various snow layers have been measured that could not be explained by a simple dependence on layer thickness (Peck 1986).

In this report, measurements and calculations of the absorption effects of snow-covered ground on acoustic pulse propagation are presented. Experiments were conducted at a site in northern Vermont, under both summer and winter conditions, to allow the effect of a 0.25-m-thick snow cover to be assessed by direct comparison. The experiments used simple point sources (blank pistol shots and sledge hammer blows) and were designed to allow the various wave types to be identified and examined individually, so that their importance could be assessed and the changes that result from the presence of snow could be measured. Acoustic propagation above snow has been studied in the past, although infrequently (Embleton et al. 1983, Nicolas et al. 1985), and primarily using continuous rather than impulsive sources. Gubler (1977) did make some impulse measurements over snow, but reported only the amplitude decay rates observed and did not make waveform comparisons. This study differs from previous studies of pulse propagation in two ways: first, I calculate absorption effects using a physically based theoretical model of finite ground impedance, the four-param-

eter model of Attenborough (1985), and compare these calculations to those using the semi-empirical, single-parameter model of Delaney and Bazley (1970) that has been used in past work; and second, I compare the model predictions with measurements over snow-covered ground. Apparently, this is the first report of extensive impulse measurements over such a highly absorptive geological boundary.

The following section presents a detailed discussion of the experimental methods, and includes the design, equipment selection and calibration, and field techniques used. This is followed by a section describing the site characterization techniques and results. All relevant site properties were measured, including seismic velocity, soil and snow properties, meteorological conditions and topography. An overview and discussion of the measured data are given in the *Observed Data* section, while the section following that summarizes the observations, with emphasis on comparing the acoustically induced ground motion in summer and winter.

The acoustic waveforms were modeled using a physically based theoretical model of finite ground impedance, the four-parameter model of Attenborough (1985). Forward modeling of the waveforms was performed, based on a steepest descent (i.e., high frequency) approximation. Exact agreement with both the summer and winter data was obtained with reasonable model parameters, although the winter data could not be modeled without introducing a layer to represent the snow cover. The development and verification of the Attenborough model is reported here. This model is a useful tool for predicting sound levels under a variety of ground conditions, and is the only one available that has been verified to incorporate a snow cover correctly.

Additional efforts were made to predict the acoustically induced ground motion using the wave-number integration technique. These computations treated the ground as a viscoelastic solid. Good qualitative agreement was obtained with the summer measurements, but not with the winter ones. The computations failed to predict enough attenuation of overall signal level and enough decay of the high frequencies in the pulse waveforms to match the observed data, even with unrealistic input parameters.

The reasons for the failure of these computations for snow are discussed, where Biot's classical theory is used to model snow as a viscoporous rather than a viscoelastic material. When the transmission of acoustic waves from air into snow is examined, the theoretical results show that the largest transmission is to compressional waves traveling mostly in the pores, a mode of transmission that is completely absent from

the viscoelastic material model used in the wave-number integration effort. This transmission mode accounts for the much higher energy loss observed by sound propagating over snow compared to grassland.

Finally, the results of these studies are summarized and additional work outlined in the *Conclusions*. Future efforts will be directed toward obtaining measurements on additional snow covers and toward incorporating porous materials into the full wave-number integration code, a formidable programming task.

## EXPERIMENTAL METHODS

### Experimental objectives

The main objective of these experiments was to determine the effect of introducing a snow cover on acoustic waves propagating through the atmosphere. Thus, the experiments were designed to provide accurate measurements of the velocity, amplitude and attenuation rate of the waves. Another objective of these experiments was to identify and characterize the waves that take part in acoustic-to-seismic coupling. Finally, accurate waveform recordings were desired to check theoretical modeling results and to allow modern data reduction and analysis methods to be used.

### Overview of the experimental design and equipment

The arrangement of sources and receivers is perhaps the most important experimental design factor in studies of this type. Previous studies (e.g., Bass et al. 1980) used only a few receivers, with spacings of 30 m or more, which are too large for accurate velocity measurements and for following individual waves with confidence. In this study, the receivers were arranged in a line along the air/ground interface, with a maximum spacing of 3 m, which corresponds to a 10-ms travel time between sensors for acoustic waves. Because the receiver array required a few hours to install, it remained in a fixed location for each particular experiment while the position of the source was varied. Recordings were made with the source close to the receiver array; then the source was moved away at intervals slightly less than the array length (to provide some overlap) and the measurements were repeated. This procedure allowed propagation distances from 1 to 274 m to be recorded with distance intervals of 3 m between different ranges. The fine spatial sampling and the recording procedure used allowed the entire wavefield to be determined

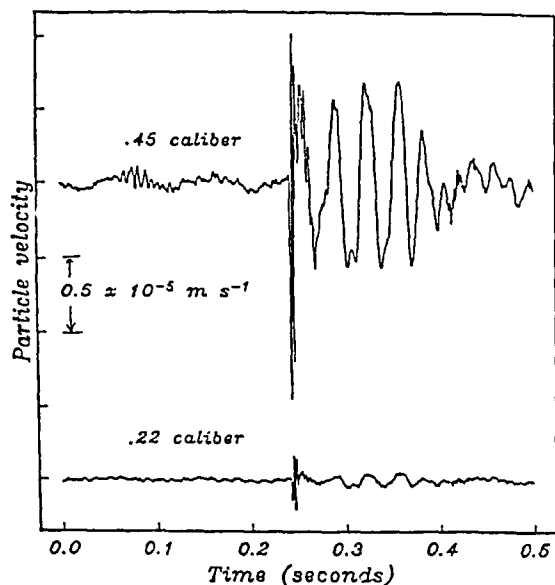


Figure 1. Comparison of the acoustic source strength of a single blank shot from a .45 caliber pistol (top) and a .22 caliber pistol (bottom). Both shots were recorded by a vertical component geophone at the surface of the snow layer 79 m away. For each shot, the pistol was held 1 m above the snow surface and pointed in a horizontal direction toward the geophone. The shots were recorded less than 2 minutes apart. Although there happened to be a higher level of low-frequency background noise during the .45 caliber shot (probably from a vehicle on the road near the test site), it produced a high-frequency air wave that was about six times greater in amplitude than the .22 caliber shot. The low-frequency surface wave following the air wave was about a factor of 10 larger for the .45 caliber shot.

accurately. Since different waves travel at different velocities, they can be observed separating from one another as the propagation distance increases. The recording geometry allows travel time vs distance and amplitude vs distance curves to be constructed, from which the velocity and the amplitude decay of the waves can be determined.

Another factor important in the experimental design is the selection of a source of the acoustic waves. It must be repeatable, easily controlled and have a large enough signal output to provide a good signal-to-noise ratio. The use of an impulsive source rather than a continuously emitting one was desired because it allows the individual wave arrivals to be detected and identified. Impulsive sources are more difficult to use than continuous sources, however, because greater timing accuracy and control are needed. It is also easier to measure spectral properties using continuous sources, which can be tuned to any desired frequency. For the acoustic source, a .45 caliber pistol firing hand-loaded blanks was selected for safety, output consistency and portability. This pistol had a much greater signal output than a .22 caliber blank pistol that was occasionally used (Fig. 1). Other sources that were considered included a "four-deuce" (4.2-in. mortar) and explosive charges, but they were eliminated by logistical complications: storage, shipping, safety and permits were all a problem with these sources. Sledge hammer blows upon a metal plate resting on the ground were used as the source for determining the seismic properties of the test site.

Because low-frequency waves can be detected at greater distances than high-frequency waves, most

sensor systems concentrate on the low-frequency band for the detection and identification of vehicles. In practice, this band is usually from 10 or 20 Hz to a few hundred hertz, the band selected for these measurements.

The signals were recorded digitally using a Geosource DSS-10A seismic recording system (Fig. 2), providing the advantages of great accuracy and wide dynamic range. Twenty-four signal channels were recorded, each sampled at a rate of 2 kHz, with a 500-Hz anti-alias filter applied. Occasionally, a 60-Hz notch filter was necessary, but other filtering was avoided during the measurements so that the recorded bandwidth was as wide as possible. Each sampled data point was written on a nine-track tape in SEG B format as a 16-bit mantissa with 4 gain bits (Northwood et al. 1967). Although single shots were always recorded, the best records were obtained by summing 5 or 10 individual shots in the recording system's memory before writing to tape, as this procedure reduced the effects of uncorrelated noise, especially at the longer propagation ranges.

Vertical component geophones, which measure the particle velocity of the ground, were used for most of the receiver channels. They have the advantage of being sensitive, rugged and inexpensive, and are unaffected by temperature changes. I used Mark Products L-15B geophones with a natural frequency of 4.5 Hz and a sensitivity of  $32 \text{ V}/(\text{m s}^{-1})$ . Horizontal component geophones of the same type were also used to assist in identifying the wave types and to allow the particle motion to be determined. To measure the air pressure variations, Globe 100C low-frequency capacitor microphones with a sensitivity of  $2 \text{ V}/\text{Pa}$



Figure 2. Digital recording system. On the left are the electronics used to filter, amplify, sample and format the incoming data. In the center is a 24-channel analog oscilloscope used to monitor data quality during acquisition. The nine-track tape drive is on the right.

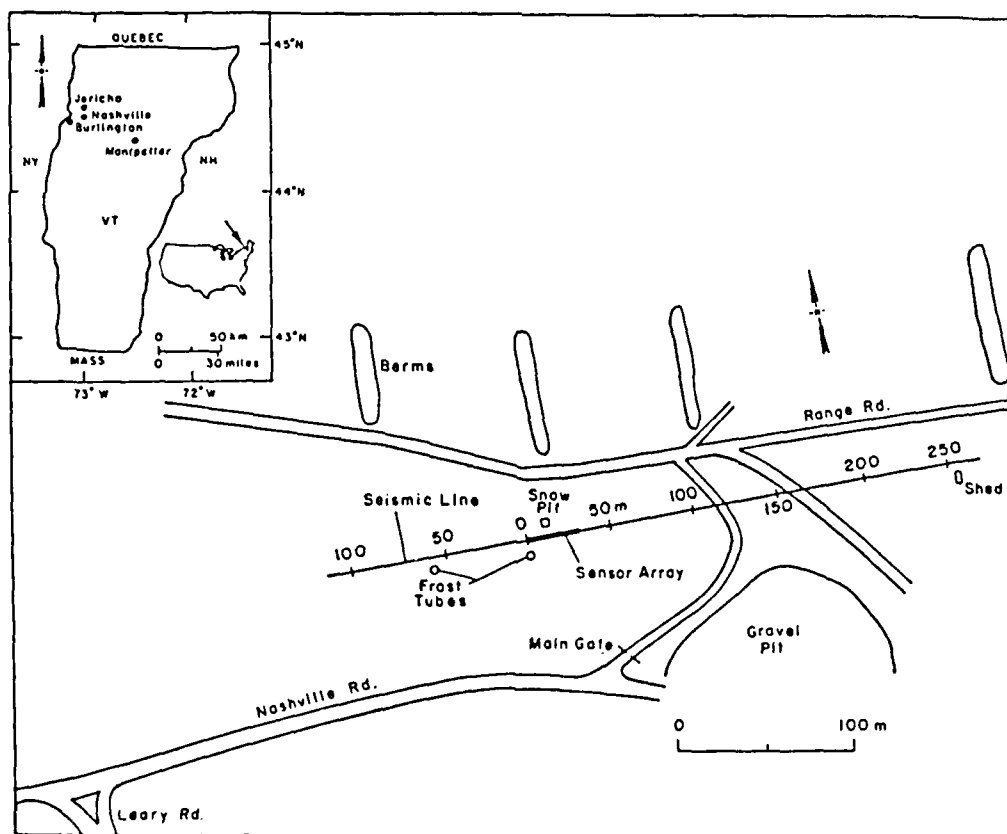


Figure 3. Location map. The site of the experiments was Camp Ethan Allen, located between the villages of Jericho and Nashville, Vermont. The coordinate system adopted for these experiments is shown on the map of the site. The origin was selected as one end of the sensor array, and distances in meters along this line are given to the east or west.

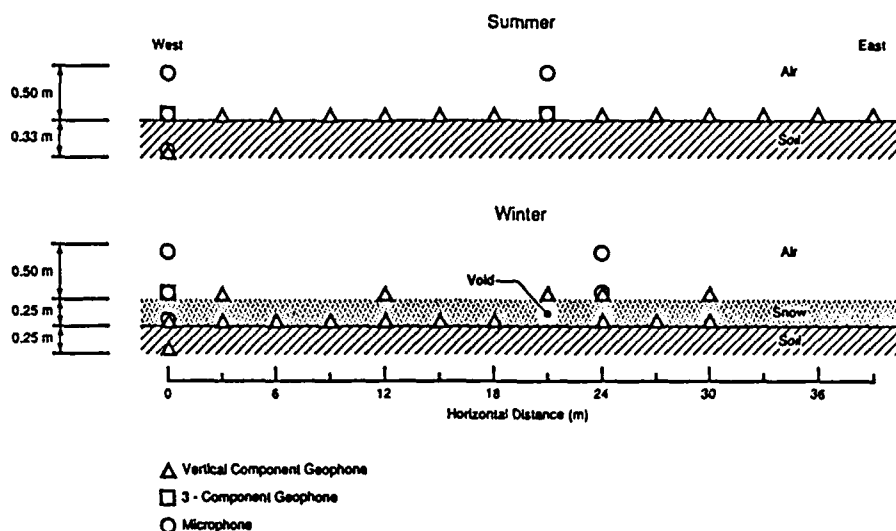


Figure 4. Schematic cross-sectional view of the sensor arrays used in the summer (top) and winter (bottom) experiments.

were used. The number of these microphones was limited because of their expense. They are also less rugged than geophones, require their own separate power supply, and are susceptible to noise problems.

Since the effect of a snow layer was of interest, measurements were conducted under both summer and winter conditions. The experiments took place at the Known Distance Firing Range of the Vermont National Guard's Camp Ethan Allen Training Center in Jericho, Vermont (Fig. 3). This site was accessible during the winter, yet remote enough and protected by a fence so that the snow cover remained undisturbed. The test site is located approximately 17 km east of Burlington, Vermont, at 44°27.5'N, 72°55'W, and is about 240 m above sea level. The relatively flat topography allowed propagation ranges of up to a few hundred meters to be used.

#### Experimental procedures

Figure 4 shows schematic diagrams of the actual receiver arrays used in the summer and winter. Except for the buried geophone used in the winter, which was installed before the snow fell in late November 1984, the sensors were installed just prior to the measurements and connected to the recording system using standard 12-channel geophone cables. The geophones were held in place in the soil or snow by a 7.5-cm-long (3 in.) spike attached to the case. In the winter, a small hole was dug in the snow cover to install the ground geophones. Since there was very little frost present, it was not hard to push the spike into the ground; then the hole was backfilled with

the snow that had been removed. The microphones were placed on the surface or on small wooden platforms, 0.5 m high, and were covered with 0.6-m-diameter hemispherical fiber screens to reduce wind noise. The microphones were connected to the geophone cables through an attenuating resistance bridge that reduced the signal amplitude by a nominal factor of 1000 (the exact measured values were 1260 and 1360), bringing the microphone signal levels close to those of the geophones. The installed receiver arrays are shown in Figure 5, and a view of the microphones and geophones is given in Figure 6.

To record signals from acoustic sources, the pistol was pointed toward the sensor array and fired from a height of 1 m (see cover photo). A small box with a microphone mounted on it and with a pulse circuit inside was placed on the ground directly beneath the pistol. When this surface microphone detected the acoustic wave from a fired shot, a pulse from the circuit was transmitted along a wire to start the recording. The time delay between the actual firing of the shot and the arrival of the acoustic wave at the box to start the recording was 3 ms. The delay from the electronic circuit within the box varied between 0.1 and 0.3 ms depending on the source waveform, but it did not seem to vary with temperature. A number of single and summed shots were recorded at a particular source location. Because seismic waves were also of interest, single and summed vertical hammer blows were also recorded at the same spot before moving to the next source location. A motion-sensitive switch attached to the sledge hammer's



*a. Summer.*



*b. Winter.*

*Figure 5. Receiver array.*

handle was used to start the recording in this case, with a negligible time delay. The source locations were moved in line with the array, with maximum propagation ranges of 157 m from the west and 274 m from the east.

As mentioned above, filters were avoided during recording whenever possible. In some cases, strong

60-Hz noise was present, so a notch filter was necessary to eliminate this hum. Although low-frequency ( $\sim 1$  Hz) background noise was occasionally present, this noise was eliminated later by a zero-phase digital low-pass filter (Albert 1986) during computer processing rather than during the recording.

Between the winter and summer experiments,



Figure 6. Emplacement of microphones (without the windscreens) and geophones. The boxes contain a battery power supply and attenuation resistance bridge for the microphones.

the test site was used for a number of National Guard training exercises, including tank training, so the area had to be left completely cleared between experiments. A few wooden stakes were driven in flush with the ground surface and used upon return to relocate the source points and the receiver array.

After the experiments, the SEG B tapes were sent to a contractor for demultiplexing. The returned tapes, written in SEG Y format (Barry et al. 1975), were then read into a Prime 9750 minicomputer for processing and analysis. The first step was to convert the data from the SEG Y IBM floating point format to a Fortran-readable real array; Appendix A contains a Fortran listing showing how this conversion was accomplished. The next step was to correct the gain and to convert the data values from millivolts to physical units. The geophone channels were converted using the expression

$$u(\text{ms}^{-1}) = d(\text{mV}) / \left[ 10^{\text{gain}(\text{db})/20} \times 1000 \times 32.3 \right]$$

where  $u$  is the particle velocity in  $\text{m s}^{-1}$ ,  $d$  (mV) is the recorded data value in millivolts, gain (dB) is the fixed gain of the preamplifiers in decibels (the four possible values were 12, 24, 36 or 48 dB), the factor 1000 converts millivolts to volts, and the factor 32.3 is the

geophone sensitivity in volts per meter second<sup>-1</sup>. The microphone channels were converted using

$$p(\text{Pa}) = d(\text{mV}) \times \text{atten} / \left[ 10^{\text{gain}(\text{db})/20} \times 1000 \times 2.0 \right]$$

where  $p$  (Pa) is the pressure in pascals, the factor 2.0 is the microphone sensitivity in volts per pascal, and  $\text{atten}$  is the resistance bridge attenuation factor (either 1260 or 1360).

If the shots were summed, an additional correction might have been needed. To prevent overflow, the recording system shifts the data one bit to the right when summing starts and applies an additional bit shift each time the number of summed shots reaches a power of two. For example, three bit shifts will be applied when five shots are summed (a bit shift at one, two and four sums). Since a binary bit shift to the right is equivalent to a division by two, the data values are reduced by a factor of  $2^3 = 8$ . Adding five shots together presumably results in an amplitude five times greater than that for a single shot. Thus, to correct the data to the amplitude level of a single shot, the data values must be multiplied by 8/5. These corrections were carried out on all summed shots.

At this point, the data are ready for analysis. For-

tran programs were written for data display, filtering, spectral analysis and data reduction. Examples will be given below and in the following sections.

### Calibration

Two methods were used to calibrate the equipment in the field. The first method used a microphone "beeper" with a known output level that was recorded at two frequencies for each microphone channel. The second method recorded the signal produced when a small steel sphere was dropped on each implanted geophone from a known height. Recordings of these impacts were used to determine the sensitivity of the geophones and the recording system's bandwidth. Both calibration methods were used during the summer experiments only.

A GenRad Model 1562A pistonphone was used to calibrate the microphones. This calibrator has an output Sound Pressure Level (SPL) of 114 dB (re 20  $\mu$ Pa)  $\pm$  0.7 dB (or  $10.0 \pm 0.8$  Pa) at frequencies of 125 and 250 Hz. Because the Globe microphones are a non-standard size, the calibrator was attached to the microphone using a rubber grommet, and a correction for the volume between the pistonphone and the microphone diaphragm was necessary. This correction, the ratio of the volume for standard microphones to the volume for the low-frequency microphones, amounted to a factor of 0.30, reducing the expected input to the microphone to  $3.0 \pm 0.3$  Pa. The calibrator was applied to each of the microphones and 1 second of the signal was recorded. Then the measured RMS sound pressure level,  $SPL_{rms}$ , from these recordings is calculated and compared to the known calibrator output.

$$SPL_{rms} = \left[ (1/N) \sum_{i=0}^N x_i^2 \right]^{0.5}$$

where  $x_i$  is the individual sound pressure samples and  $N$  is the total number of samples recorded. The ratios of measured to expected sound pressure levels ranged from 0.5 to 1.4; the values for all of the measurements are given in Table 1. An example of the pistonphone signal and its power spectrum recorded by one of the microphones is shown in Figure 7. The power spectrum was calculated by windowing 1000 time series data points, appending 1048 zeros, Fourier transforming using the FFT algorithm, and applying a five-point band average in the frequency domain. The signal at 125 Hz is about a factor of 100 (40 dB) larger than the strongest harmonic

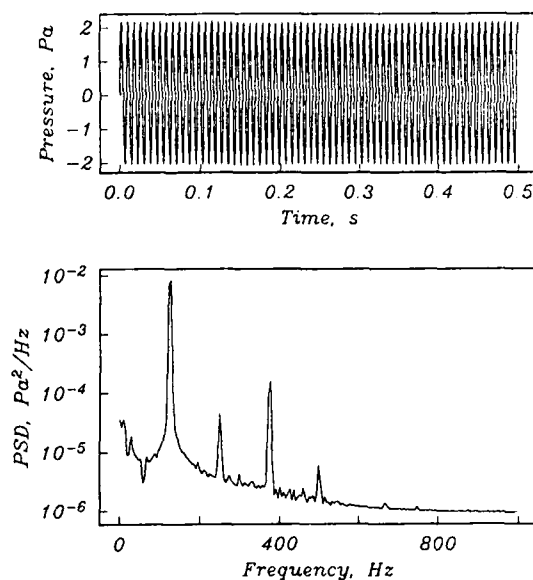


Figure 7. Typical microphone calibration time series (top) and spectrum (bottom). The pistonphone was set to a frequency of 125 Hz and applied to channel 18. The power spectrum display (PSD) shows that harmonic oscillations are present at 250, 375 and 500 Hz, but they are all 40 dB down from the signal level.

at 375 Hz. Weaker harmonics are present at 250 and 500 Hz. The power spectrum confirms that this channel has a dynamic range of at least 80 dB.

In-situ calibration of geophones is rarely attempted, especially in small scale studies of this type, because of the difficulty in applying a known input signal and in isolating the geophone from other sources of ground motion. I had three objectives in calibrating the geophones: to check that the rather complicated tape decoding and gain correction sequence was properly implemented, to measure the variation in sensitivity among individual geophones, and to determine the impulse response and bandwidth of the entire recording system. Without calibration, the accuracy of absolute amplitude measure-

Table 1. Microphone calibration RMS sound pressure levels.

Channel	$SPL_{rms}$ at 125 Hz	$SPL_{rms}$ at 250 Hz	Ratio <sup>†</sup>	Sensitivity (V/Pa)
7	4.7	3.4	1.4	2.7
11	—	2.9	1.0	1.9
18	1.9	2.2	0.7	1.4
22	2.2	2.3	0.8	1.5
24	1.4	1.8	0.5	1.1

<sup>†</sup>Measured RMS SPL divided by expected value of 3.0 Pa.



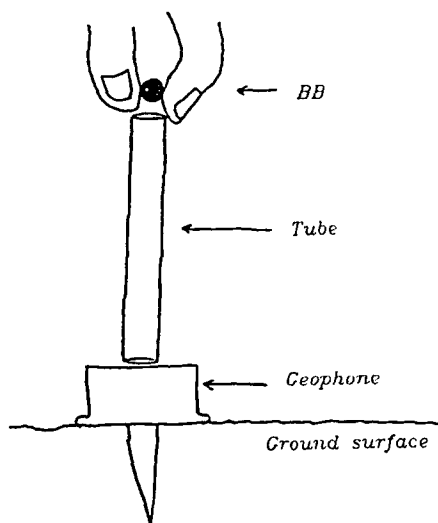


Figure 8. Procedure used for the BB drop calibrations of the vertical component geophones.

ments are assumed to be good to an order of magnitude. Initial amplitude determinations from the winter data indicated much larger ground motions than expected, so the following BB drop method of calibration was devised and led to the discovery of a missing factor of  $2^{-24}$  ( $= 5.96 \times 10^{-8}$ ) in the tape decoding sequence.

BB drops have been used in the past (e.g., Hoover and O'Brien 1980, Krohn 1984), but only to determine the coupling of the geophone to the soil, not to estimate the sensitivity of the geophone or its bandwidth. These researchers used BB impacts to estimate the resonant frequency and damping factor of the geophone-ground system, which they modeled as a damped harmonic oscillator. They were concerned mainly with the frequency response and filtering effect of the coupled system on the actual ground motion.

The experimental procedure was to drop a BB (a small steel sphere manufactured by Daisy) onto a planted vertical-component geophone while recording the geophone's output. A plastic pipe (trade name Goofy Straw), 0.195 m long, was held slightly above the geophone and the BB was dropped through it (Fig. 8), allowing it to bounce a number of times. Since the BB was held and dropped by hand, the exact time of its release and the initial height are not accurately known. However, the output voltage of the

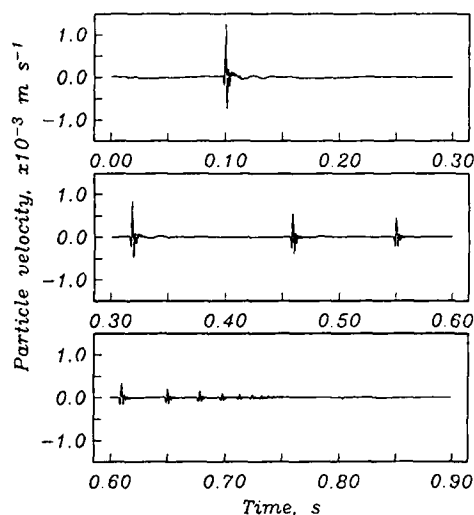


Figure 9. Typical vertical component geophone responses to a BB impact and following bounces (geophone channel 10). The initial impact occurs at 0.1 seconds, and bounces at 0.32, 0.46, 0.55, 0.61, ... seconds, with measured peak particle velocities of  $12.5, 8.3, 5.6, 4.5, 3.2, \dots \times 10^{-4} \text{ m s}^{-1}$  respectively.

geophone and the time interval  $\Delta t$  between bounces can be accurately measured (Fig. 9), allowing the impact velocity  $v$  of the BB to be determined from

$$v = g\Delta t/2$$

where  $g = 9.8 \text{ m s}^{-2}$ . The law of conservation of momentum for the collision between the BB (of mass  $m^{bb}$  and velocity  $v^{bb}$ ) and the geophone (with mass  $M^{geo}$  and velocity  $V^{geo}$ ) is

$$m^{bb}v_1^{bb} = M^{geo}V_2^{geo} - m^{bb}v_2^{bb}$$

where the subscripts 1 and 2 refer to before and after the impact; the geophone is initially at rest ( $V_1^{geo} = 0$ ). Rearranging gives

$$V_2^{geo} = (v_1^{bb} + v_2^{bb})m^{bb}/M^{geo}$$

The masses  $M^{geo}$  (0.280 kg) and  $m^{bb}$  (0.000313 kg) were determined by weighing. These values were used to determine  $v_2^{bb}$  from the above equation, and compared to the velocity found from the output voltage of the geophone itself and the manufacturer's stated sensitivity of  $32.3 \text{ V/m s}^{-1}$ . Results are given in Table 2. The geophone sensitivities determined from the BB drops are all greater than the sensitivity given by the manufacturer, by a factor ranging from

**Table 2. Geophone sensitivity determined from BB drops.**

Channel	N*	Ratio†	Standard deviation	Sensitivity (V/m s <sup>-1</sup> )	K*
1	17	1.35	0.155	43.6	9
2	14	1.93	0.215	62.3	10
3	19	2.13	0.306	68.8	11
4	18	1.71	0.219	55.2	10
5	19	1.43	0.237	46.2	8
6	17	1.89	0.309	61.0	11
10	18	1.91	0.253	61.7	10
12	19	1.85	0.199	59.8	10
13	18	2.09	0.272	67.5	11
14	16	2.08	0.295	67.2	12
15	17	3.05	0.698	98.5	11
16	23	1.75	0.223	56.5	11
17	15	1.67	0.170	53.9	10
21	12	1.01	0.100	32.6	11

\*N= Number of BB bounces used to determine the average ratio.

K= Number of BB bounces used to determine the bandwidth of the channel.

† Ratio of the geophone velocity after impact determined from conservation of momentum to the velocity determined from geophone output voltage times the manufacturer's stated sensitivity.

1.01 to 3.05. Most of the geophones appear to be about twice as sensitive as stated by the manufacturer.

However, the above calculations rely on the assumption that only the geophone is accelerated by the BB. Actually, some portion of surrounding soil will also be accelerated, so the effective mass (denoted by  $m^{\text{eff}}$ ) is  $m^{\text{eff}} = M^{\text{geo}} + m^{\text{soil}}$ , and the calculated geophone sensitivities should be decreased. The value of  $m^{\text{eff}}$  depends on how firmly the geophone is planted in the soil and on the soil properties, and the data indicate that it also depends on the impact velocity of the BB (Fig. 10). For these reasons, it is difficult to determine the correct value of  $m^{\text{eff}}$  and the manufacturer's sensitivity was used in the amplitude measurements presented later on in this report. The results presented in Table 2 serve mainly as an indication of the variability between geophones and their coupling to the soil, and as confirmation that the amplitude measurements are accurate to within a factor of three or better.

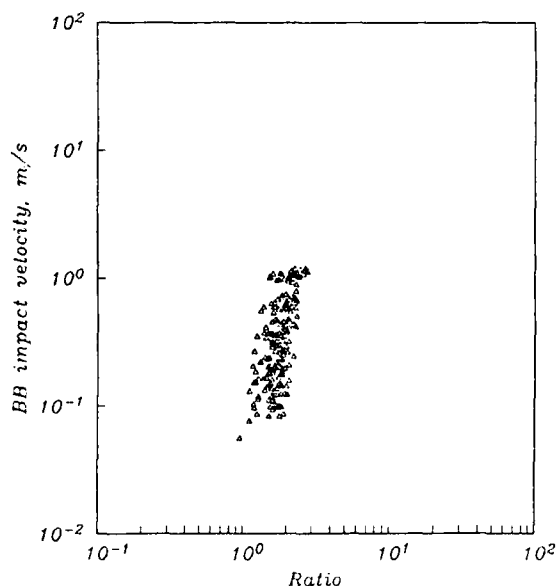


Figure 10. BB impact velocity vs the ratio of the geophone velocity calculated from conservation of momentum to the velocity found from the geophone output voltage.

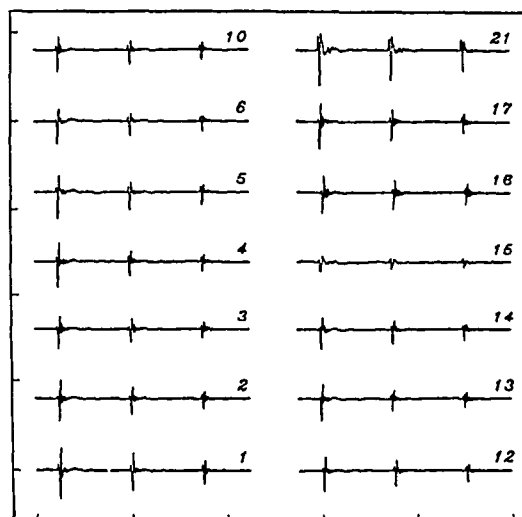


Figure 11. Examples of initial impacts and following bounces for each of the geophone channels (numbers on the plot), shown at true amplitude before normalization. The distance between tick marks corresponds to  $5 \times 10^{-3} \text{ m s}^{-1}$  on the vertical axis, and 0.1 seconds on the horizontal. The signals have been aligned in time on this plot. Note the different appearance of the waveforms for channels 15 and 21.

The recordings of the BB impacts were also used to determine the bandwidth of the entire recording system, from the sensor, through the amplifiers and filters, to the storage on magnetic tape. A number of individual BB impacts were recorded for each channel (Fig. 11). These time series were normalized, windowed and used to estimate the bandwidth of each channel using the block averaging computational scheme detailed below.

Impacts that were at least 100 sample points (0.075 s) away from other impacts or noise were selected for analysis. Each time series was then normalized with respect to energy so that all bounces would be weighted equally, and multiplied by a third-order Kaiser-Bessel window to reduce leakage in a near-optimal manner (see Harris [1978] for details of this window). Zeroes were appended to the windowed impulse to increase the frequency resolution and the amplitude spectrum was calculated using the fast Fourier transform algorithm. All of the spectra for each channel were then block-averaged in the frequency domain to increase the number of degrees of freedom and narrow the confidence interval of the estimate.

If we let  $k$ ,  $m$  and  $n$  be indices referring to the impact number, time and frequency sample, respectively, then the block averaged Fourier transform of  $N$  samples from  $K$  impacts is

$$X_n = \sum_{k=1}^K \sum_{m=0}^{N-1} x_m^{(k)} e^{i2\pi m n/N},$$

$$n = \dots, 0, 1, \dots, N-$$

with

$$\begin{aligned} x_m^{(k)} &= w_m y_m^{(k)}, \quad m = 0, 1, \dots, NY-1 \\ &= 0, \quad m = NY, NY+1, \dots, N-1 \end{aligned}$$

where  $y_m^{(k)}$  represents the  $m^{\text{th}}$  sample of the time series of the  $k^{\text{th}}$  impact. The power spectrum estimate at a frequency  $f_n = n/(N \Delta t)$  is the magnitude squared of  $X_n$ . With  $NY = 150$ ,  $N = 1024$ , and  $\Delta t = 0.0005$  s, the interval between frequencies is  $\Delta f = 1/(N \Delta t) = 1.95$  Hz. Table 2 lists the number of spectra averaged for each estimate. Typically, 10 bounces were averaged (i.e.,  $K = 10$  for 20 degrees of freedom), giving an approximate 95% confidence interval of

$$0.64 P'_n \leq P_n \leq 1.8 P'_n$$

where  $P_n$  is the true power spectrum value at the  $n^{\text{th}}$  frequency and  $P'_n$  is its estimate. The confidence interval is equivalent to a range of 2.6 to -1.9 dB.

The bandwidth estimates are shown in Figure 12. The use of a 60-Hz notch filter during the recording of the impacts appears as a -30-dB dip at this frequency. The frequency response of all but two of the channels is relatively flat from about 200 to 500 Hz, when the anti-aliasing filter causes the response to drop off sharply, reaching -80 dB at 800 Hz. Below 100 Hz, the frequency response is lower because the BB drop did not excite these frequencies.

Figure 12 shows that two of the channels had poorer frequency response characteristics than the rest. Either the anti-aliasing filter for channel 21 was defective or there was some loss of dynamic range for this channel, as the response leveled off at -30 dB at 600 Hz and remained at this level out to 1000 Hz. The waveforms in Figure 11 also indicate that the signal may have been clipped. Channel 15 shows a drop in the response between 300 and 600 Hz that is also visible in the waveforms displayed in Figure 11. With these two exceptions, the BB drop tests confirm the wide bandwidth of the sensing and recording system.

The two channels with narrower frequency response characteristics are also the ones with the highest and lowest measured geophone sensitivities. Without these two channels, the measured geophone sen-

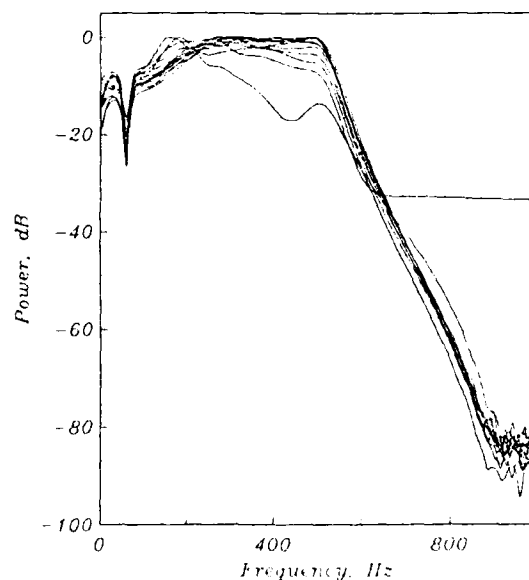


Figure 12. Bandwidth of the vertical geophone channels estimated from recorded BB drops. A 60-Hz notch filter was used during the recording of the impacts.

sitivity ranges from 1.35 to 2.13 times the manufacturer's sensitivity.

## SITE CHARACTERIZATION

Determining the properties of the site of the experiments was an important part of this work. Documentation of the site conditions was needed for estimation of the environmental effects on the wave propagation, for comparison with other experiments and for use in the modeling efforts. The most important characterization effort was the measurement of the compressional ( $P$ ) and shear ( $S$ ) wave seismic velocities as a function of depth. These measurements were obtained using the seismic refraction technique and are discussed in detail below. Other site characteristics that were determined include topography, soil type, snow properties, frost depth and meteorological conditions. Each of these determinations will be discussed in this section.

### Seismic velocity structure

#### *Field procedure*

Standard seismic refraction techniques (Sheriff and Geldart 1984) were used to determine both the  $P$ - and  $S$ -wave velocities of the experimental site. To measure the  $P$ -wave velocity, an array of evenly

spaced vertical component geophones was emplaced on the ground surface, and waves resulting from a vertical sledge hammer blow (Fig. 13) on a metal plate placed on the ground were recorded. The source was moved to a number of different locations off each end of the array and within the array itself. At the longer ranges, 10 or 20 hammer blows were summed to improve the signal-to-noise ratio. In both the summer and the winter, vertical hammer blows were recorded with the same array that was used in the propagation and acoustic-to-seismic coupling experiments (see the previous section and Fig. 3 through 5). This array had a 3-m spacing between geophones, and the longest source-receiver offset was 157 m to the west and 274 m to the east. In the summer, six additional  $P$ -wave arrays were used to provide a detailed picture of the velocity structure of the site. The locations of these arrays are shown in Figure 14.

A single  $SH$  (horizontally polarized shear) wave refraction experiment was also recorded at the site. A linear array of horizontal geophones, spaced 3 m apart, measured the  $SH$  waves as shown in Figure 15. A 0.2- $\times$ 0.2-m wooden beam with metal end caps was positioned at the desired source point and clamped to the ground by the front tires of a pickup truck. Polarized  $SH$  waves were produced by striking one end of the beam, again taking advantage of the summing capabilities of the recording equipment to improve the signal quality. Then the other end of



Figure 13. Source used for the  $P$ -wave refraction experiments was a vertical sledge hammer blow upon a metal plate placed on the ground. A motion-sensitive switch is taped to the hammer, and starts the recording system via the cable.

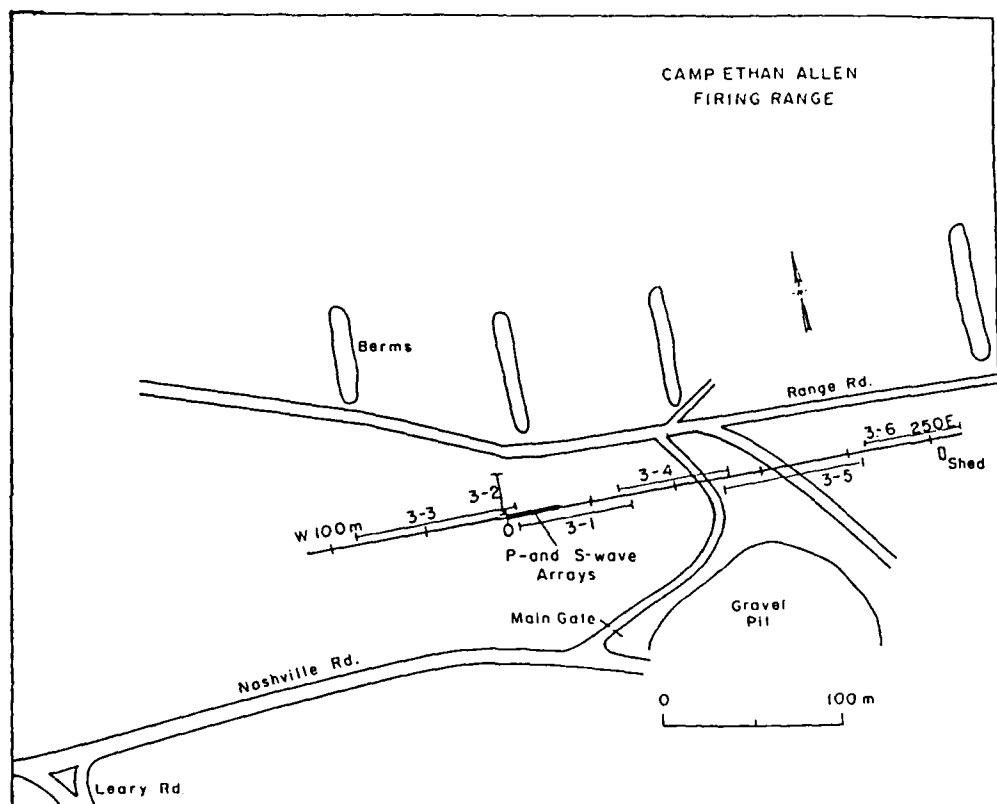


Figure 14. Location of the P-wave refraction lines.

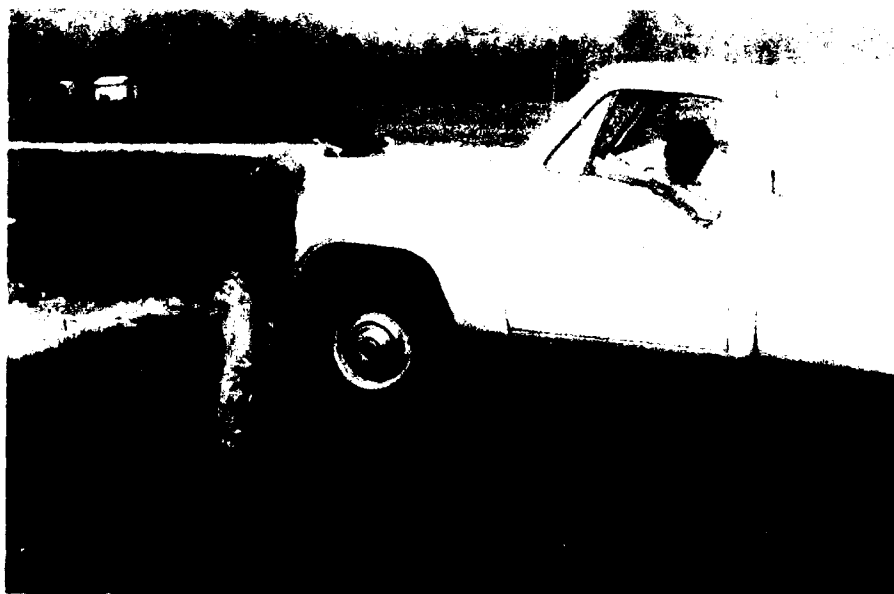


Figure 15. Source used for the S-wave refraction experiments. By recording hammer blows on each end of the beam separately, the reversed polarity of the SH waves that are generated can be used as an aid in their identification on the seismograms.

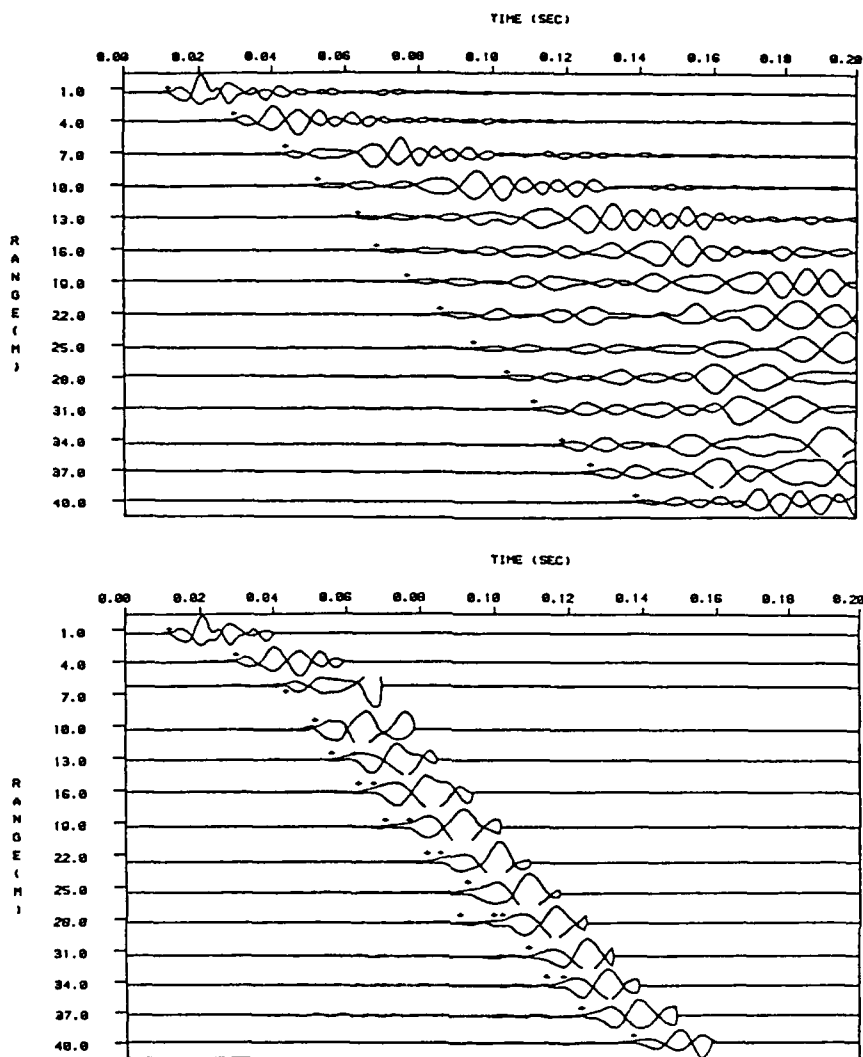


Figure 16. Example SH-wave refraction seismograms. Traces are normalized. Bottom shows the effect of increasing the gain while muting the higher amplitudes later in the traces.

the beam was struck with the hammer and a separate recording was made. A comparison of the two recordings allowed the *SH* waves to be identified, since the ground motion for these waves reversed when the source polarity was changed, while the earlier arrivals from the faster traveling *P* waves remained unchanged.

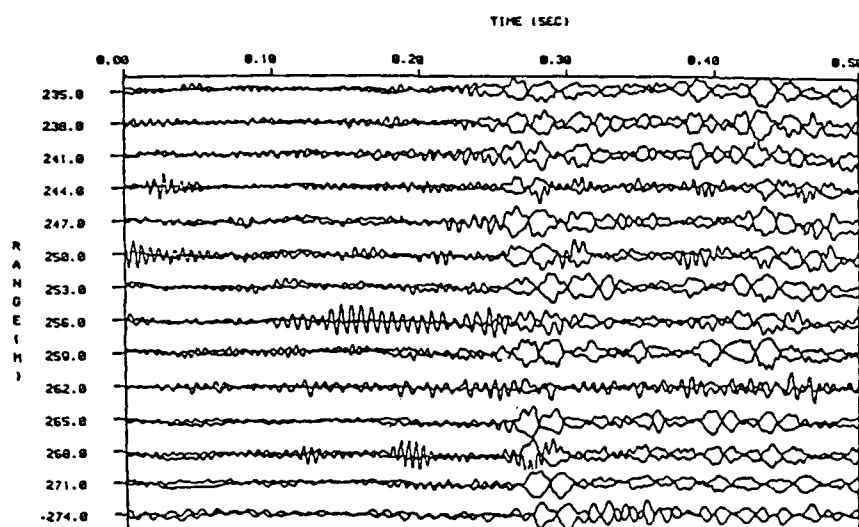
#### Data reduction

Travel times for the first arrivals were determined by displaying the refraction waveforms on a Tektronix 4114 terminal and then picking the arrivals with a cursor. I implemented the method of automatically picking arrival times presented by Hatherly (1982), but I was unable to get consistent results, so all of the travel times were picked by hand.

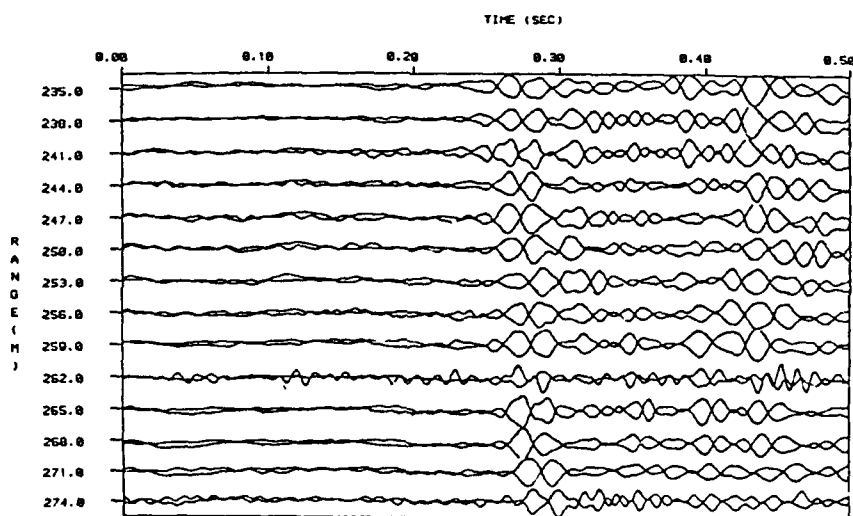
Occasionally, because of poor signal-to-noise ratios, the first peak rather than the first arrival was picked for some of the traces on the seismogram. The exact location of the peak was found from interpolation for all of the traces, including those where the first arrival could be determined. The average difference between the first arrival and the peak times on the good traces was then determined and subtracted from the peak times of the noisy traces to estimate their first arrival times.

In some cases, the data quality was improved by applying a digital filter to remove narrow-band ambient noise. Zero-phase filters (Albert 1986) were used to ensure that the travel times were not affected.

The procedure to reduce the shear wave refraction data was similar to the one used for the *P* waves,



a. Before noise removal.



b. After noise removal by low-pass filtering ( $f_c = 100$  Hz).

Figure 17. Example SH-wave refraction seismograms with and without noise removal.

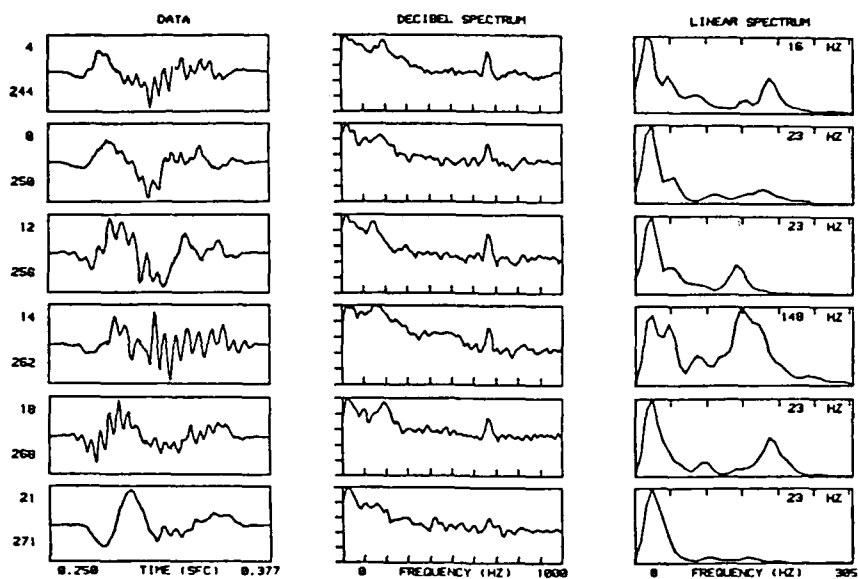
except that two records with opposite source polarity were plotted on the graphics terminal screen for picking. The arrivals were picked mainly by determining when the two traces at a particular range diverged. An example is shown in Figure 16. Digital filtering was also useful in determining the SH-wave arrival times, and examples are shown in Figures 17 and 18.

The data quality was generally high, and the first arrival times could be readily determined with an accuracy of 1 ms. One exception, however, was the P-wave data for sources within the sensor array. While recording these data, I selected a low pream-

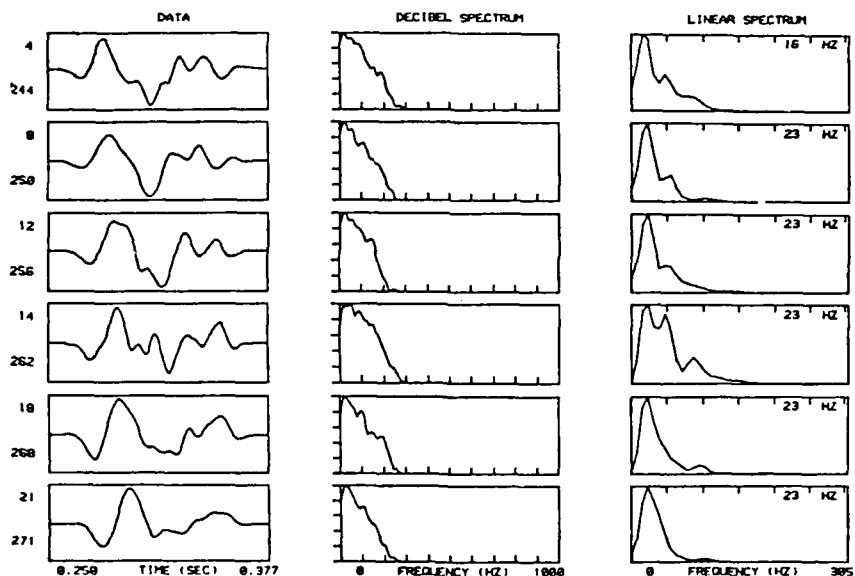
plifier setting to avoid clipping the traces close to the source. Unfortunately, the gain setting was too low to allow the signal from the far traces to be recorded. An example is shown in Figure 19. The poor quality of these data did not affect the overall interpretation, since these recordings were intended to measure the near-surface velocity, which could still be determined from the close traces.

#### *Intercept time inversion*

The intercept time method, used to invert the first arrival travel times, is based on the assumption that the subsurface consists of flat (possibly inclined), con-



a. Before.



b. After.

Figure 18. Spectra of SH-wave traces before and after application of a low-pass digital filter,  $f_c = 100$  Hz.

stant velocity layers with the velocity increasing with depth. Using Snell's law, the refraction data can determine the velocity and thickness of the layers.

Once the travel times were determined for an array, a plot of distance vs travel time was made for all of the source points extending in one direction from the array. Next, the crossover distances (the distance where the first arrival from a slower, shallower inter-

face is replaced by an arrival from a deeper, faster interface) were determined from this plot, and a straight line was fit to the data segment from each refracting interface using least-squares (Fig. 20). The procedure was repeated for all of the source points in the opposite direction from the array. With the assumptions listed above, the apparent velocities of each layer are given by the inverse of the slope of the



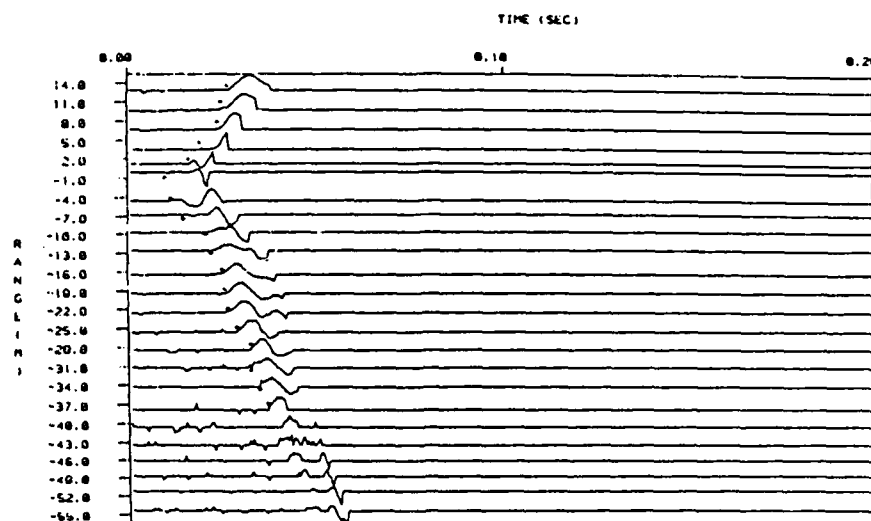
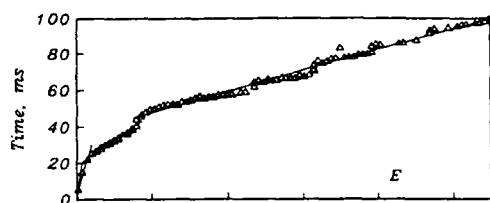
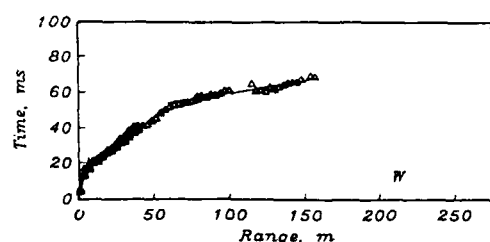


Figure 19. Example of a P-wave refraction record with the preamplifier gain setting too low. The first arrival cannot be picked beyond 37-m range.



a. For these data, the source was moved along a line to the east of the array.



b. The source was moved along a line to the west of the array.

Figure 20. Distance vs travel time plots for both source directions for P-wave refraction array 1. Triangles are the first arrival times picked from the seismograms. The three line segments are least-squares fits to the travel times.

line segments. These apparent velocities can be used to determine the "true" velocity of the layer, and the intercept of the line segments can be used to determine the depth at each end of the array. A computer program provided by Mooney (1973) was used for these determinations.

The results of the intercept time analysis for all of the refraction arrays are given in Table 3, with the travel time plots and fitted lines shown in Appendix B. The results for the detailed P-wave refraction measurements are shown in Figure 21 (where the thicknesses have been plotted, corrected for the surface elevations). Additional measurements using closely spaced geophones revealed typically low P- and S-wave surface soil velocities of 200 and 60  $\text{m s}^{-1}$  respectively. The intercept time analysis shows that the shear wave velocity increased to 160  $\text{m s}^{-1}$  at a depth of 0.2 m, to 360  $\text{m s}^{-1}$  at 1.5 m and to 2900  $\text{m s}^{-1}$  at 24 m depth beneath the 39-m-long receiver array. The P-wave measurements indicate a nearly horizontal layer with a velocity of 1725  $\text{m s}^{-1}$  at 4 m depth, identified as the water table. The velocities range from 3900 to 5700  $\text{m s}^{-1}$  (mean 4630, standard deviation 710  $\text{m s}^{-1}$  for six determinations) beginning at a depth of 15 m at the eastern end of the site, and at 25 m depth at the western end (Fig. 21). These velocities indicate that the upper 15 to 25 m consists of unconsolidated soils, becoming saturated at 4 m depth, with the basement rock below. Note that the shear wave velocity is unaffected by the saturation of the soil, as expected.

### Soil and snow properties

#### Soil

The physical characteristics of the soil at the experimental site were measured as carefully as possible, since this information was useful in documenting the actual experimental conditions, providing in-

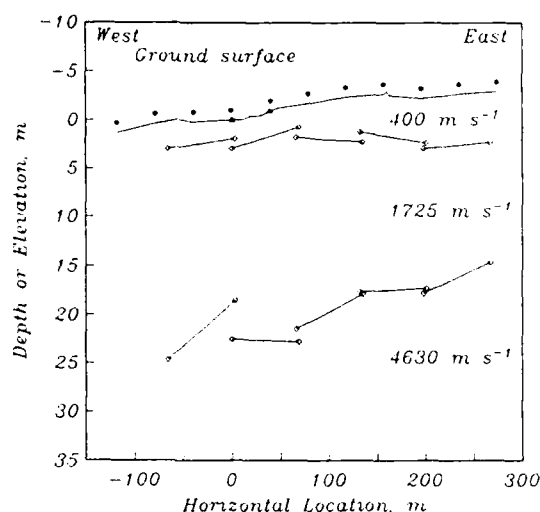


Figure 21. Results of P-wave refraction measurements. Five separate receiver arrays were used; the resulting depths from intercept time analysis are denoted with diamonds. Triangles mark the receiver locations and asterisks the source locations for the propagation and acoustic-to-seismic coupling experiments. The vertical to horizontal exaggeration is 10:1.

put parameters to the modeling efforts and comparing acoustic data from other locations. Soil samples were collected in August 1986 at five representative locations at the test site (Fig. 22) and returned to the laboratory for analysis. In the laboratory, the density, moisture content, grain size distribution and soil type were determined for each sample (Table 4). The grain size distributions are plotted in Figure 23.

Laboratory analysis showed the soils to consist of gravel-sand-silt mixtures or of silty sands with densities around  $1700 \text{ kg m}^{-3}$ . These analyses are consistent with those of Stewart and McClintock (1970), who mapped surface soils in this area as outwash deposits, i.e., glaciofluvial gravels, with a possible thin covering of postglacial alluvium. According to Doll et al. (1961), the bedrock geology of the site belongs to the Pinnacle formation, a lower Cambrian formation of the Camel's Hump group, composed of metamorphosed (albite to chlorite) shistose graywacke.

Two frost tubes were installed in early November 1985 at the locations shown in Figure 22. During the winter experiments in January 1986, these frost tubes indicated frozen soil depths of 0.03 and 0.08 m. The growth of the frozen soil layer is greatly impeded by the presence of a snow cover, which insulates the ground from the low air temperatures, and this frost depth was shallow compared to most winters in Vermont because of the early onset of a snow cover that

Table 3. Results of intercept time analysis.

Array	Velocity ( $\text{m s}^{-1}$ )	Location (m)	Depth (m)	Location (m)	Depth (m)
1	205	0		39	
	360		0.2		0.3
	1130		1.6		2.8
	1640		4.9		3.7
	5150		32.0		18.4
2 (SH)	60	0		39	
	160		0.2		0.2
	350		1.7		1.2
	2880		23.0		24.4
3-2	370	-66		3	
	1710		2.7		2.0
	3870		24.4		18.5
3-1	380	0		69	
	1760		2.9		2.3
	5700		22.5		24.3
3-4	440	66		135	
	1710		3.3		4.8
	4850		23.0		20.4
3-5	400	132		201	
	1660		3.7		4.6
	4570		20.2		19.5
3-6	410	198		267	
	1780		5.2		5.2
	4140		20.0		17.6
3-3	400	0		23N	
	1710		2.8		2.1
	3940		14.1		23.9

year coupled with a November that was warmer than usual.

#### Snow

Snow is a substance with highly variable physical and mechanical properties. In addition, it is driven to metamorphose rapidly by changing environmental conditions. Thus, it is of prime importance to characterize the snow cover simultaneously with the experimental measurements, as vast changes may occur literally overnight.

The winter experiments took place on 16 January 1986, with a snow cover of about 0.25 m and a thin (0.03-m) layer of frozen soil present at the site. To characterize the snow cover, a snow pit was dug during the experiments and the temperature, density, crystal type, grain size and hardness of each layer were determined. Five distinct layers were observed in the snowpack, with measured densities from 190 to  $290 \text{ kg m}^{-3}$  and crystal sizes ranging from 0.1 to 2 mm (Table 5). This snow cover can be considered

Table 4. Soil properties.

Sample no.	Location	Depth (m)	Density ( $\text{kg m}^{-3}$ )	Moisture content (%)	Gravel (%)	Sand (%)	Silt or clay (%)	Soil type
1	1E	0.06	1820	16.9	27.4	39.9	32.7	Gravel-sand-silt
2	40E	0.08	1910	15.7	0.1	68.4	31.5	Silty sand
3	80E	0.05	1810	21.2	7.3	43.2	49.5	Silty sand
4	120E	0.5	1660	10.0	0.0	75.4	24.6	Silty sand
5	200E	2.25	1400	5.1	4.5	94.2	1.3	Gravelly sand

Notes:

1. Samples 1-3 were located along the source-receiver line used for the propagation experiments. Samples 4 and 5 were located 50 m south of this line, and were taken from the side of a gravel pit.
2. The specific gravity of all soils was 2.7.

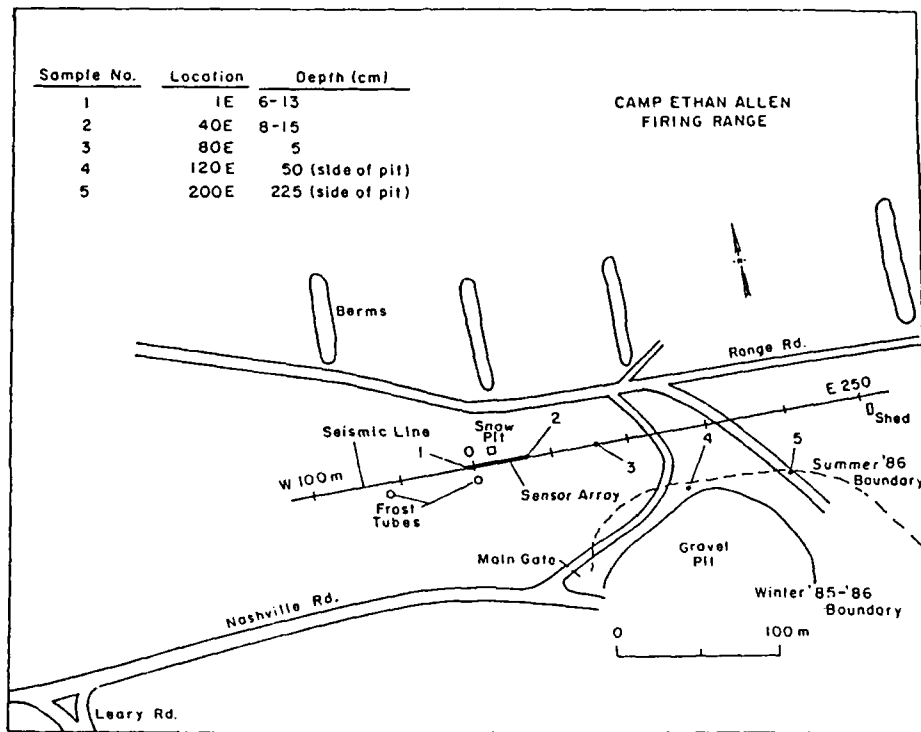


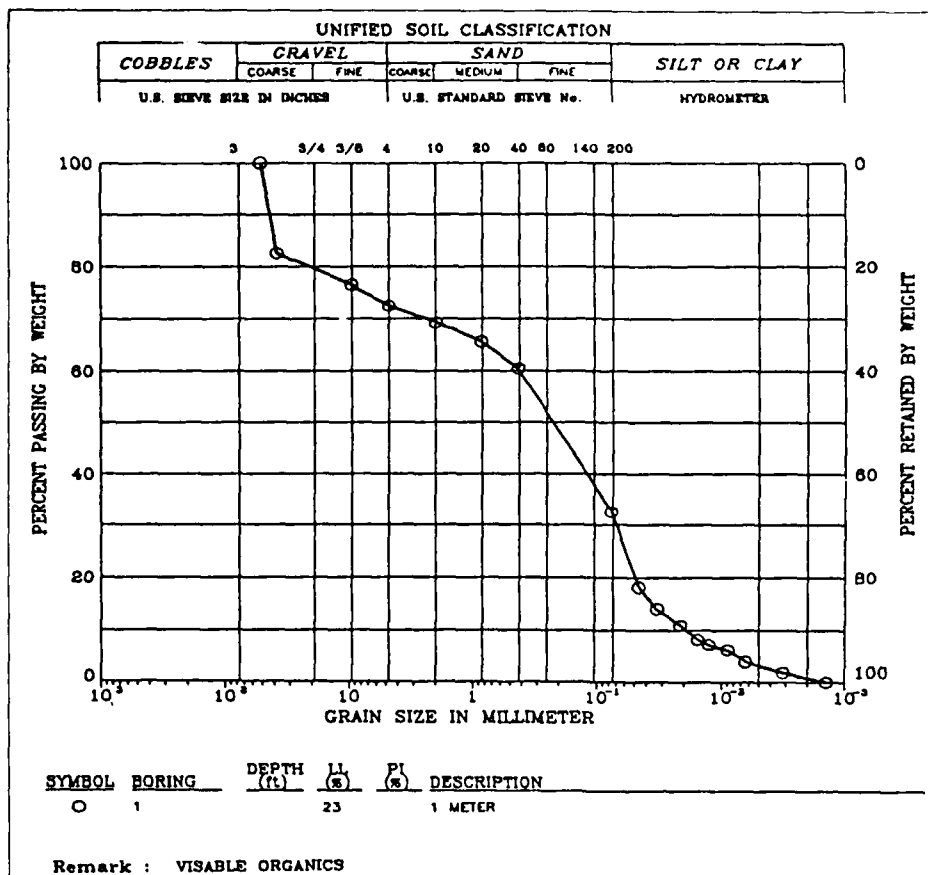
Figure 22. Location of the snow pit, frost tubes and soil samples.

typical of those found during most New England winters. The snow is always layered because of sequential snow storms rather than steady precipitation in the area. Once the snow is on the ground, it tends to change into crystals of lower surface area. These changes are driven primarily by the temperature gradient within the snow. An interpretation of the measurements given in Table 5 follows.

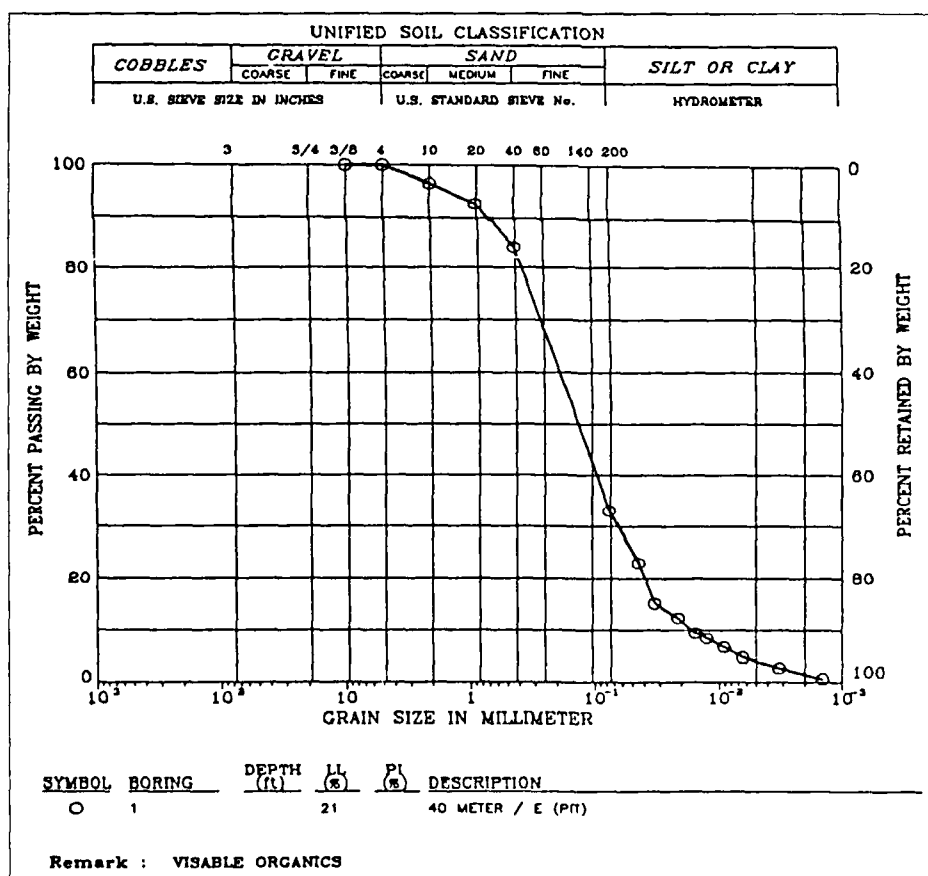
The 0.04-m-thick upper layer consisted of crystals that had fallen two nights before (0.01 to 0.02 m of snowfall occurred at the site on the night of 14 January) and had been broken into shards by wind ac-

tion. The strength of this layer was very low. The second layer, 0.03 m thick, was a hard wind crust. This layer is a further development of a windblown surface layer, and the small, closely packed particles increased in strength by sintering. The density of these upper layers was about  $200 \text{ kg m}^{-3}$ .

The next two layers, composing most of the snow cover (0.16 m thick), was made up of hexagonal and columnar crystals that are formed from high-temperature-gradient metamorphism. This recrystallization produces the crystal shapes noted (a temperature gradient of more than  $10^\circ\text{C/m}$  is usually needed

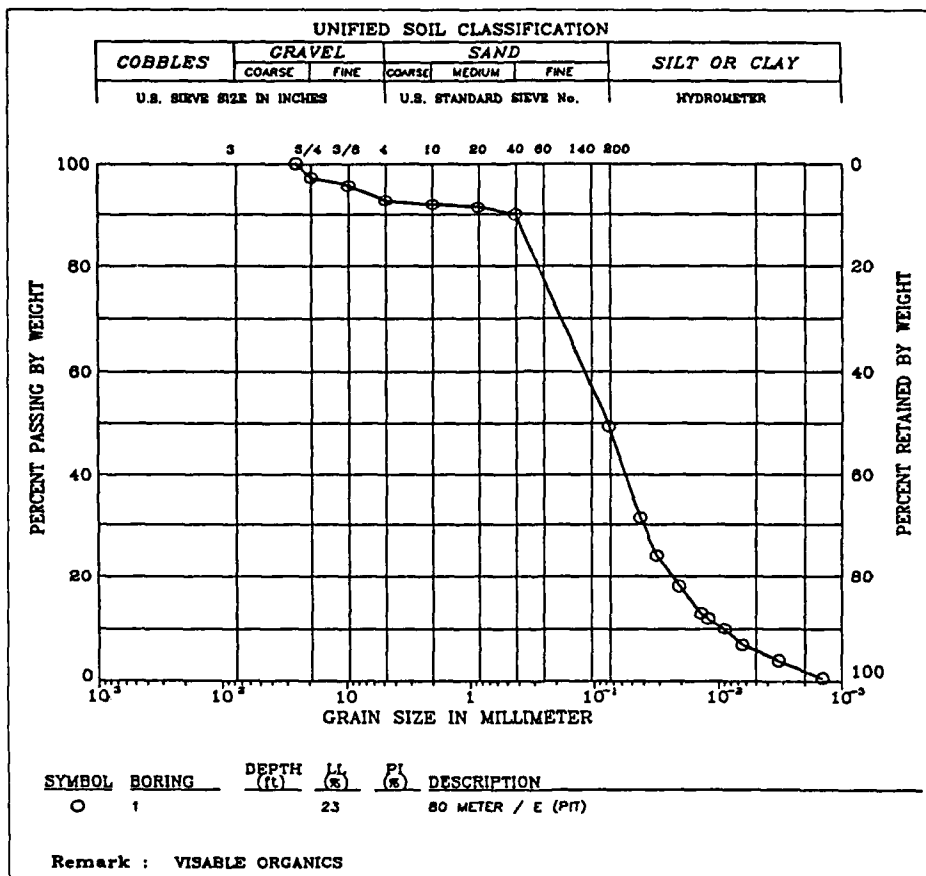


a. Sample 1.

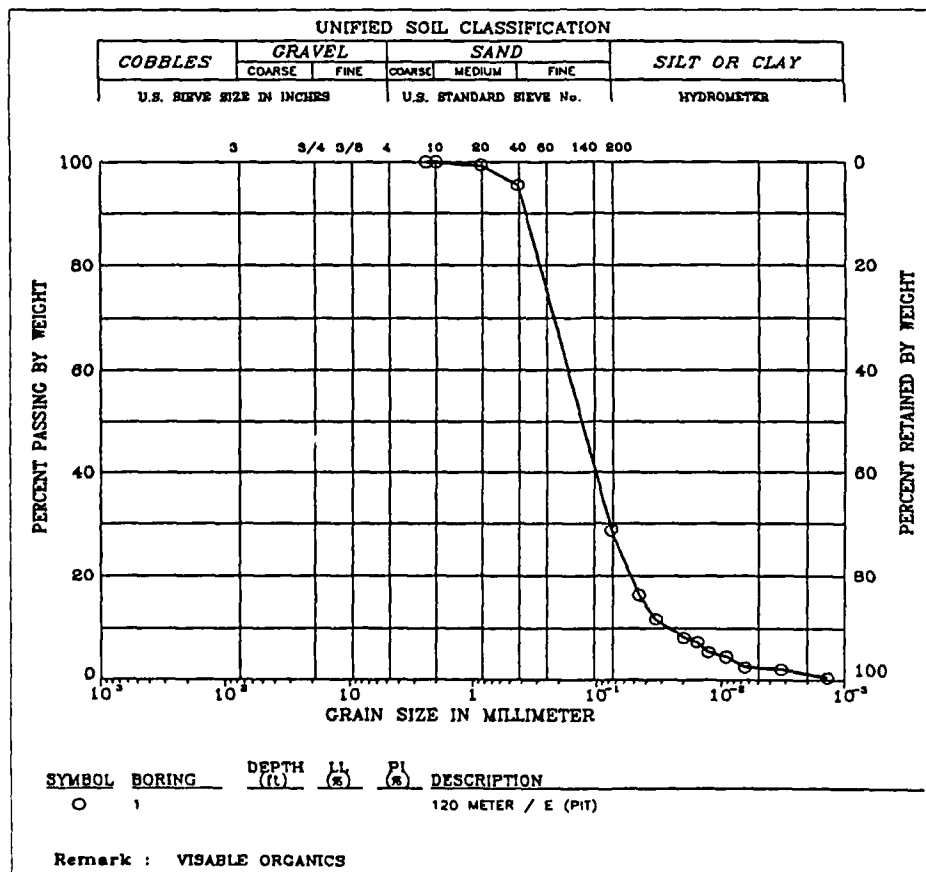


b. Sample 2.

Figure 23. Grain size distribution of the soil samples. See Figure 22 and Table 4 for sample locations and depths.

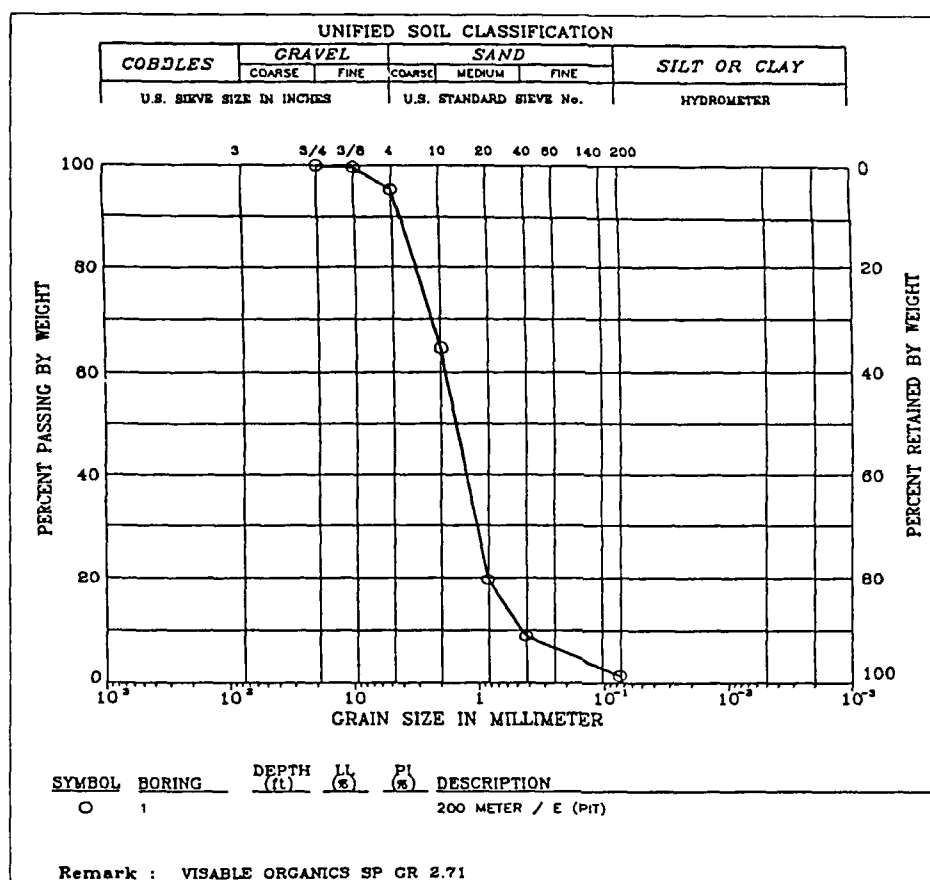


c. Sample 3.



d. Sample 4.

Figure 23 (cont'd).



e. Sample 5.

Figure 23(cont'd). Grain size distribution of the soil samples. See Figure 22 and Table 4 for sample locations and depths.

**Table 5. Snow layer profile of 26 January 1986, 1530 hours.**

Layer	Thickness (mm)	Density (kg m <sup>-3</sup> )	Temperature (°C)	Hardness index	Crystal size (mm)	Symbol*	Crystal type
1	40	192	-10	2.5	0.1	2b bk	Wind broken
2	30		-5	450	0.1-0.3	9d wc	Wind crust
3	40	198	-6	25	0.5	4a fa	Solid hexagonal and columnar
4	120	288	-2	250	1-2	4a fa	
5	20	900†	-3	3500	—	8c bi	Basal ice layer

\* Symbols according to the *International Classification for Seasonal Snow on the Ground* (Colbeck et al. 1990).

† Estimated.

for faceted crystals to develop\*), and as the crystals grow, bonds between the grains disappear and the snow strength decreases. There was a strong temperature gradient in the snow (see Table 5), so this

metamorphosis was continuing. The basal ice layer (0.02 m thick) formed from the refreezing of meltwater that drained to the bottom during previous warm periods.

The snow depths at each sensor and source location were measured using a meter stick and are listed in Table 6.

\* Personal communication with S. Colbeck, CRREL, 1990.

### Meteorological data

During the winter experiments, a portable met station was operated at the test site. This station recorded the temperature, relative humidity, and wind speed and direction at heights of 2 and 6 m. The data were recorded every minute by a Kaye Digi III data logger on a cassette tape. The tapes were returned to the laboratory and transferred to the Prime computer. The data are reproduced in Appendix C. These data were supplemented by data from weather stations at Burlington airport (44°28'N, 73°09'W, elevation 101 m) and Mount Mansfield summit (44°32'N, 72°49'W, elevation 1204 m), which are located approximately 17 and 8 km from the test site.

The data show that the winds remained nearly calm throughout the day (16 January), with clear skies and air temperatures between -8 and -3.5°C. The air temperature was lower near the cold snow cover, and increased with height, producing an inversion (positive temperature gradient). Normally, such an inversion would be expected to cause an increase in the sound level received by a source compared to measurements made in a homogeneous atmosphere because upward traveling sound rays will tend to be bent back toward the ground, but the attenuation caused by the snow cover completely masked this effect, as will be shown subsequently.

The coldest days of the winter in this area were 14 and 15 January 1986, with clear skies and calm winds. A thaw began on the 17<sup>th</sup>, followed by rain on the 19<sup>th</sup> and 20<sup>th</sup>. The 0.15-m-thick snow cover completely disappeared at the Burlington station, and presumably at the test location also. A bit of luck was involved in obtaining snow cover data that year, as such thaws usually don't occur until late February!

In the summer, the met station was not available for use, so the data from Burlington were relied on exclusively. The propagation experiments took place on 18-19 August 1986, when the high and low temperatures at Burlington were 27 and 19 and 24 and 15°C respectively. Both days were partly cloudy, hot and humid. The variable winds were estimated to range between speeds of 2 to 3 m s<sup>-1</sup>, blowing across the acoustic propagation path from the north, and causing a neutral (zero gradient) temperature profile. The measured speed of sound in the air was 346 m s<sup>-1</sup>.

### Elevations

The topography of the site was measured in May 1986, and included the elevation of every source and receiver location used during the propagation experiments. This survey was conducted using a Zeiss 30X level, and revealed that a maximum elevation change

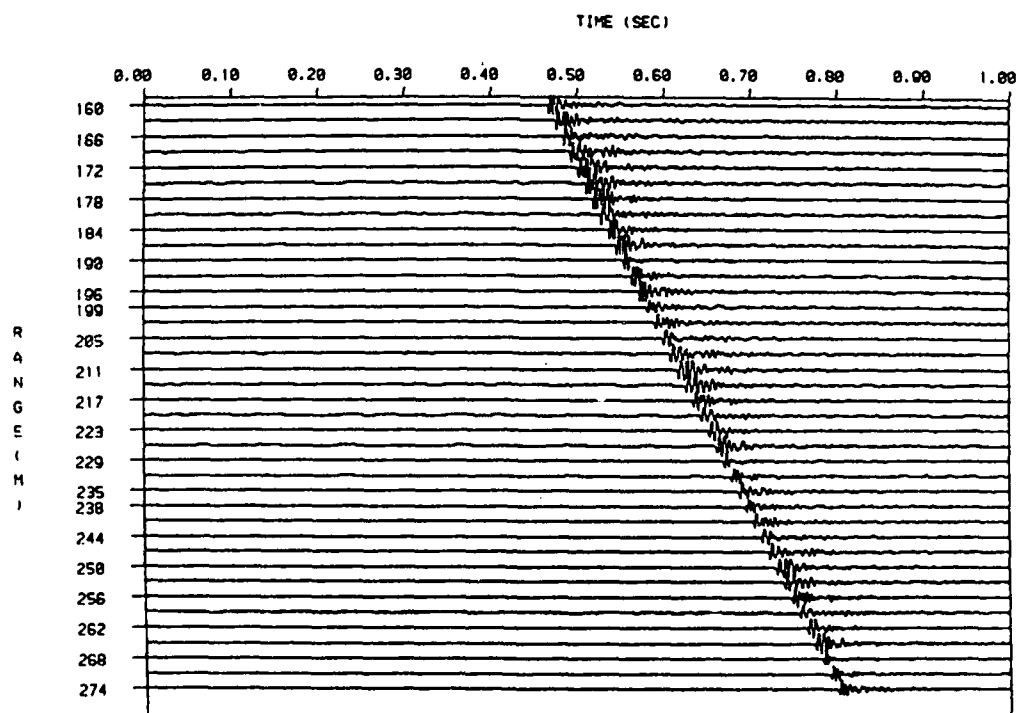
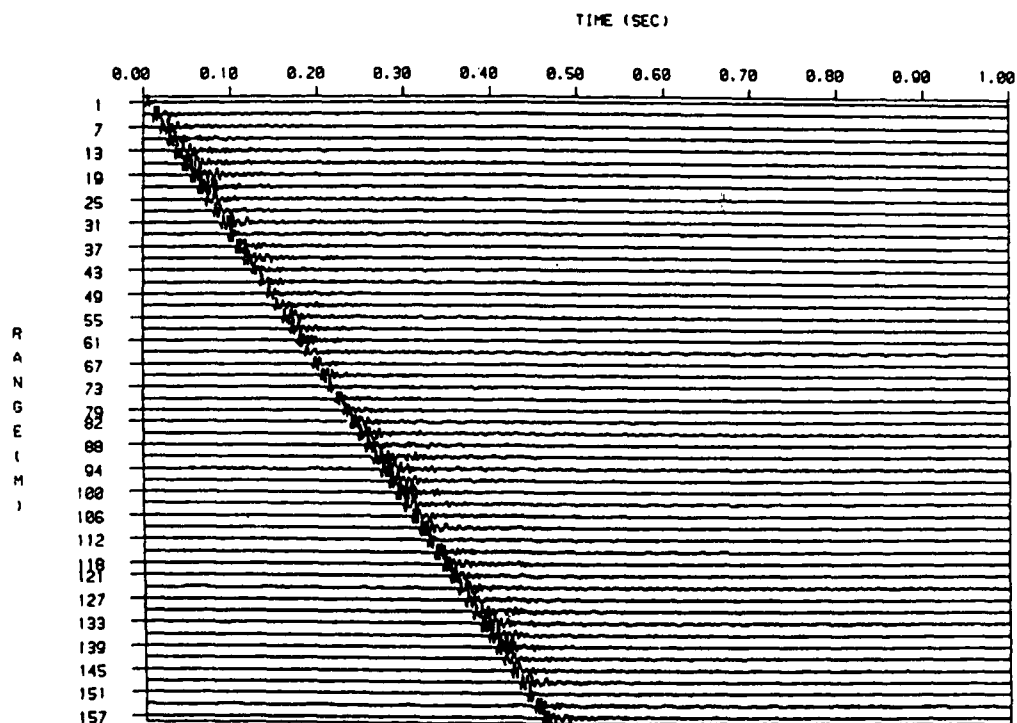
Table 6. Snow depths and ground surface elevations.

Location	Snow depth (m)	Elevation (m)
118 W	0.41	-1.31
79 W	0.20	-0.40
55 W	—	0.06
40 W	0.32	-0.18
1 W	0.23	—
0	0.25	0.00
1 E	—	0.00
2 E	—	0.00
3 E	0.23	0.03
4 E	—	0.03
5 E	—	0.00
6 E	0.25	0.00
7 E	—	0.00
8 E	—	0.03
9 E	0.25	0.03
10 E	—	0.06
11 E	—	0.09
12 E	0.29	0.06
13 E	—	0.09
14 E	—	0.12
15 E	0.26	0.21
18 E	0.21	0.37
21 E	—	0.43
24 E	0.21	0.43
27 E	0.19	0.43
30 E	0.21	0.49
34 E	0.15	—
33 E	—	0.64
36 E	—	0.76
39 E	—	0.95
40 E	0.16	0.98
47 E	—	1.19
79 E	0.18	1.71
118 E	0.04	2.38
156 E	0.03-0.09	2.68
160 E	—	2.96
163 E	—	2.53
196 E	0.23	2.26
235 E	0.25	2.71
274 E	0.26	2.96

of 4.27 m over the 392-m line of sources and receivers (Table 6). The site generally sloped upwards from west to east, with some irregularities. All of the receiver locations were within 0.95 m in elevation.

### OBSERVED DATA

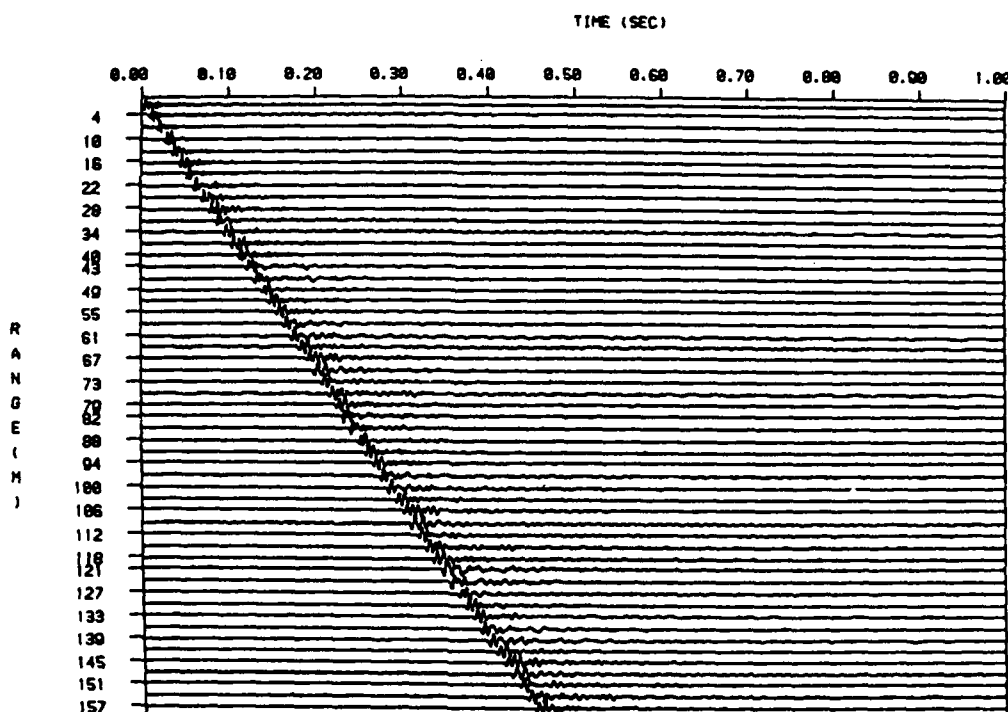
This section is an overview and gives examples of the experimentally observed waveforms. Visual interpretations of the data and major findings are given here, while detailed analyses and comparisons with theory are presented later.



*a. Source was located east of the sensors.*

Figure 24. Vertical component geophone recordings of .45 caliber blank pistol shots in the summer.





*b. Source was located west of the sensors.*

Figure 24 (cont'd).

#### Data set

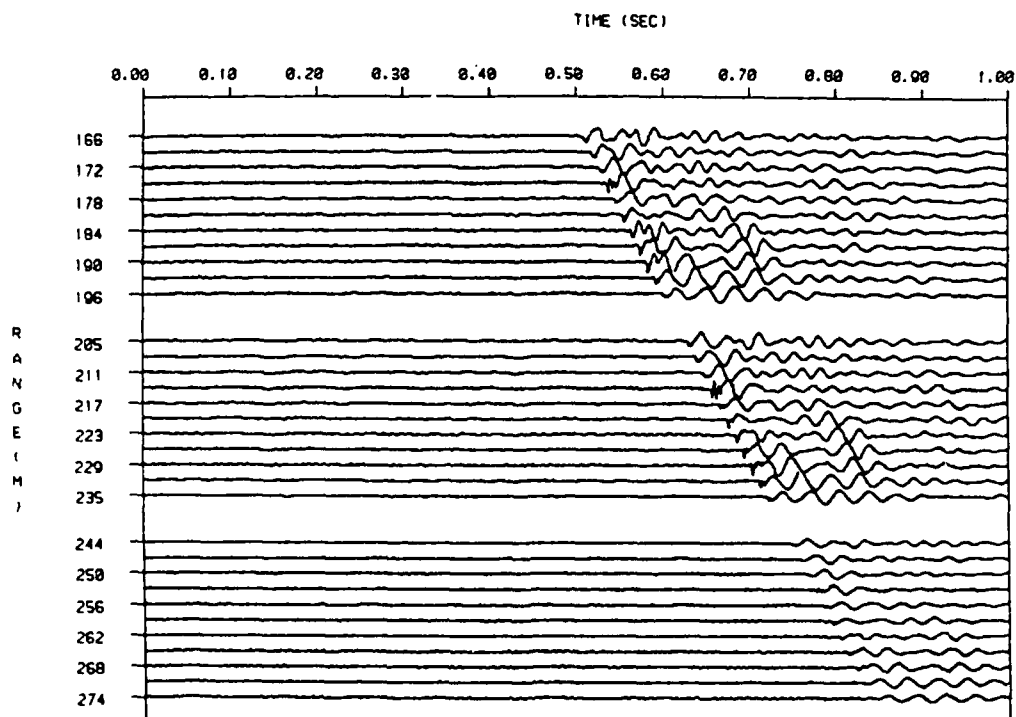
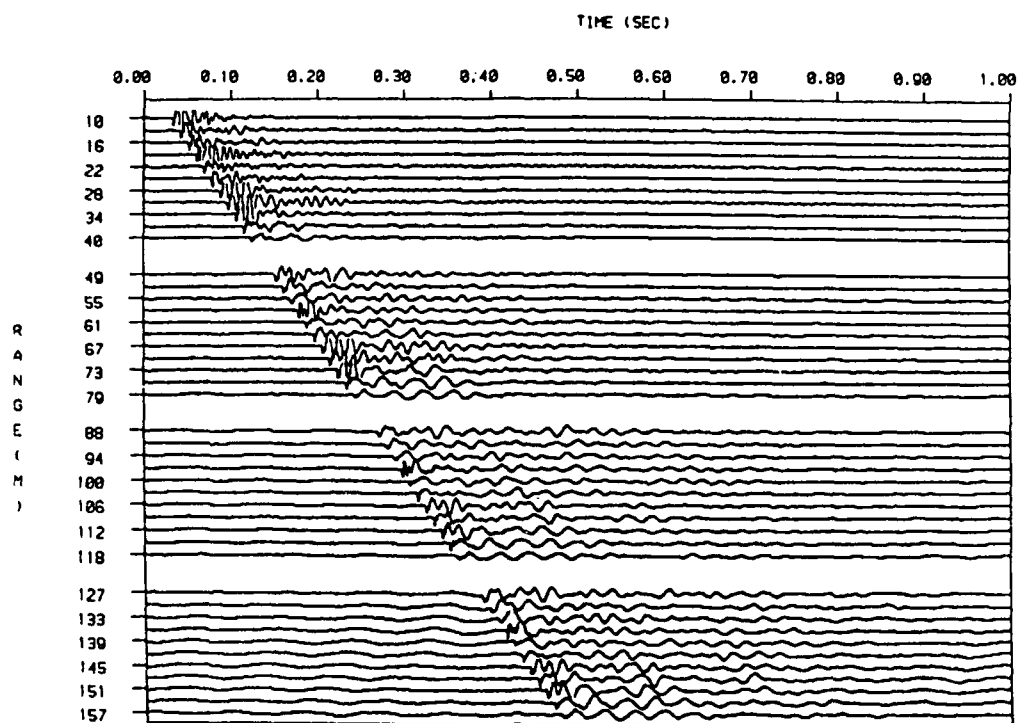
All of the data obtained in the summer and winter are shown in Figures 24 through 27. Figure 24 shows the .45 caliber blank pistol shots recorded by surface geophones in the summer, with the source to the east and the west of the sensors. The winter recordings are shown in Figure 25. The summer data show a strong, high-frequency air wave arrival, which rapidly damps out (within 0.05 seconds). This high-frequency air wave is much diminished in the winter recordings, and a low-frequency surface wave becomes the largest part of the signal after 40 m of propagation. The surface wave lasts about 0.2 seconds. The acoustic wave speeds determined from the air wave travel times are  $346 \text{ m s}^{-1}$  in the summer and  $329 \text{ m s}^{-1}$  in the winter. The different speeds are caused by the different air temperatures during the two experiments.

Recordings of vertical hammer blows in the summer are displayed in Figure 26. The wave field is more complicated than for the acoustic source, and a number of different wave types can be identified. The first arrival on all of the traces, especially visible from 80 m and further, is the refracted *P* wave. This arrival is of relatively high frequency and has a travel time of

less than 0.1 second at 274 m, so its average speed is about  $3 \text{ km s}^{-1}$ . Details of the *P*-wave velocities were presented in the *Site Characterization* section. Following the *P* wave are shallow refractions, reflections and *PL*-mode arrivals. The next arrival, traveling at about  $340 \text{ m s}^{-1}$ , is the high-frequency air wave. The following low-frequency wave train is a Rayleigh wave, a normally dispersed (low frequencies followed by high frequencies) oscillation lasting 1 second at 150 m. Since the air wave arrives before the Rayleigh wave, the speed of sound in air must be greater than the *S*-wave speed at shallow depths in the soil. The winter data shown in Figure 27 are nearly identical to the summer data, except that the air wave is not observed. A detailed discussion of these data is presented below.

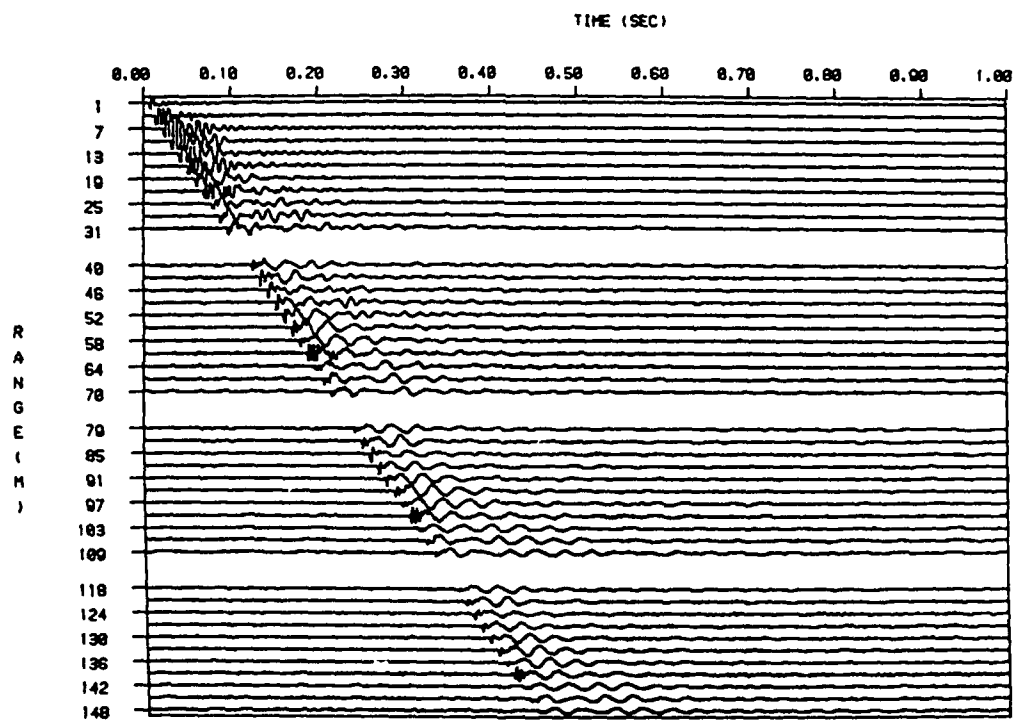
#### Air wave coupling

Figure 28 shows a typical example of the observed signal output from a microphone, 0.5 m high, in summer and winter. The air wave from the pistol shot causes an increase in pressure, followed by a rarefaction and then another compression before dying away. This pulse is a combination of the direct wave through the air and the wave reflected from the sur-



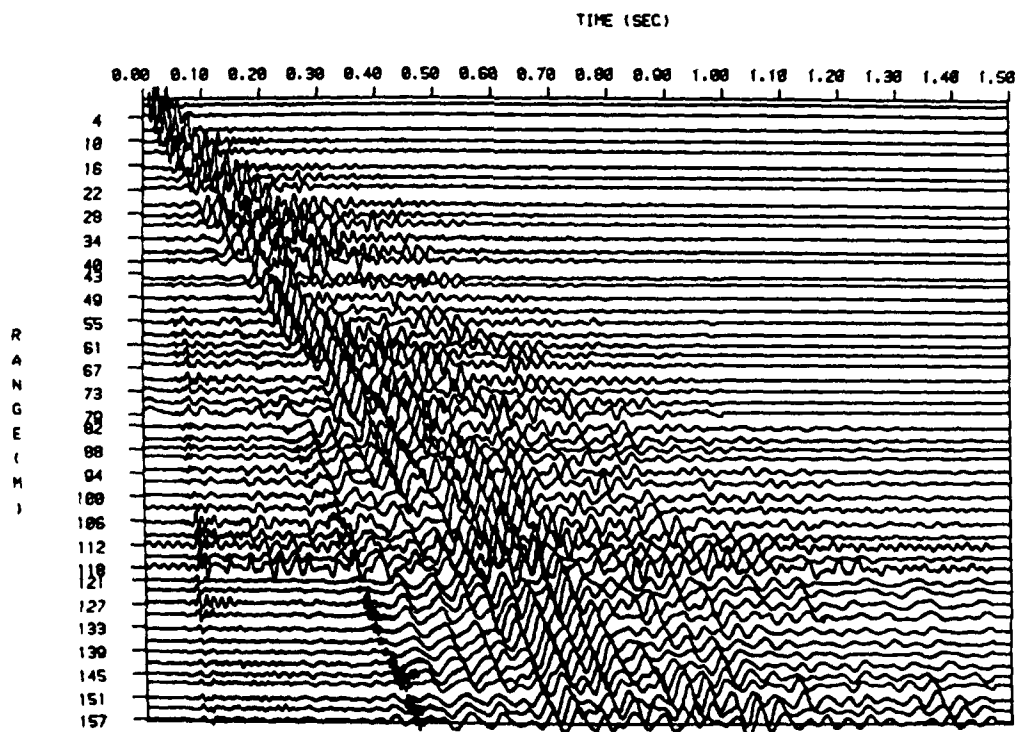
a. Source was located east of the sensors.

Figure 25. Vertical component geophone recordings of .45 caliber blank pistol shots in the winter.



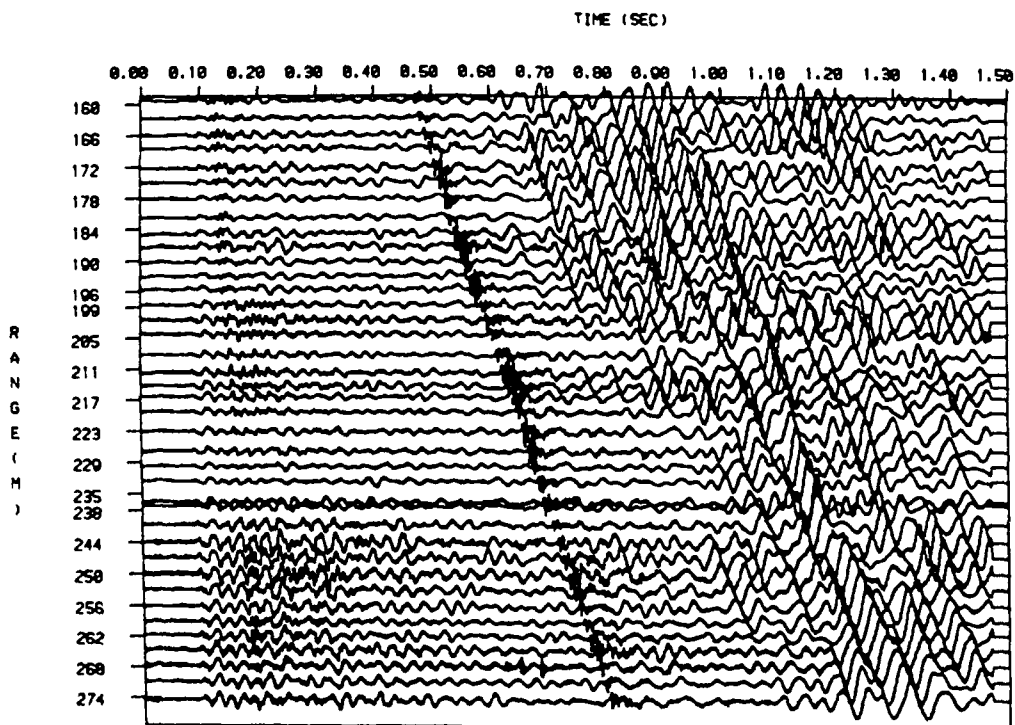
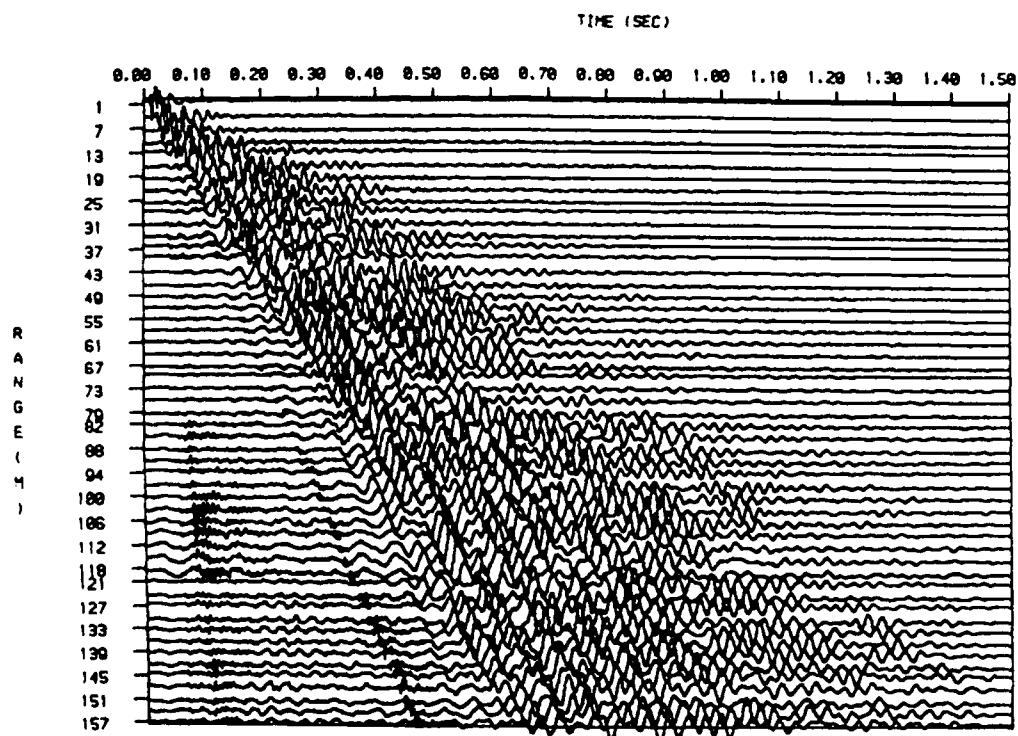
*b. Source was located west of the sensors.*

Figure 25 (cont'd).



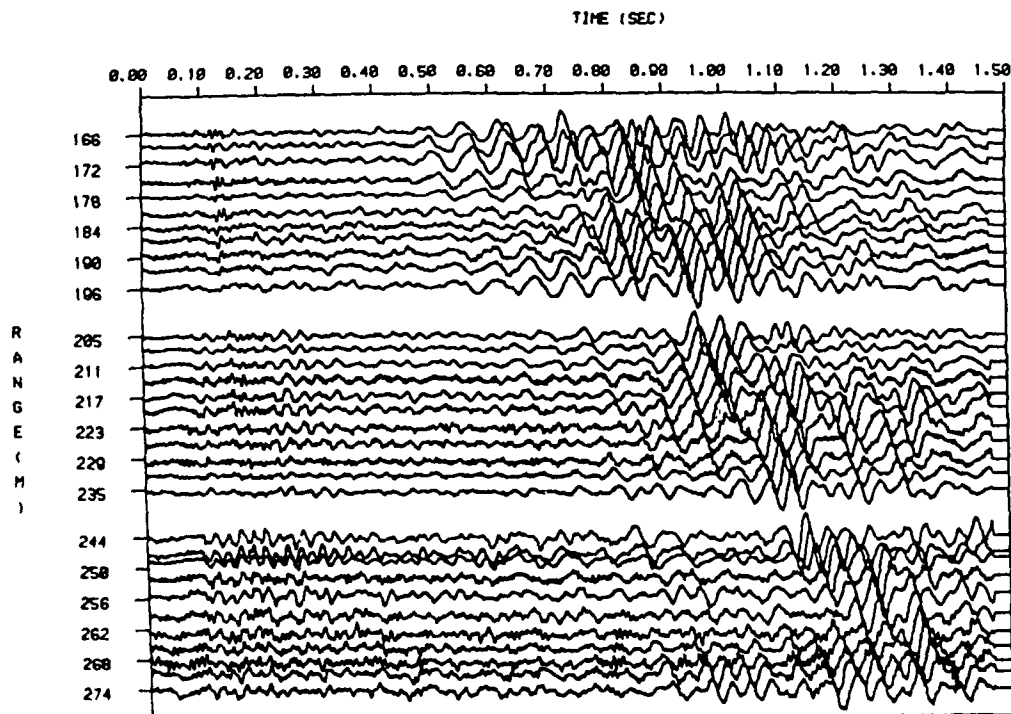
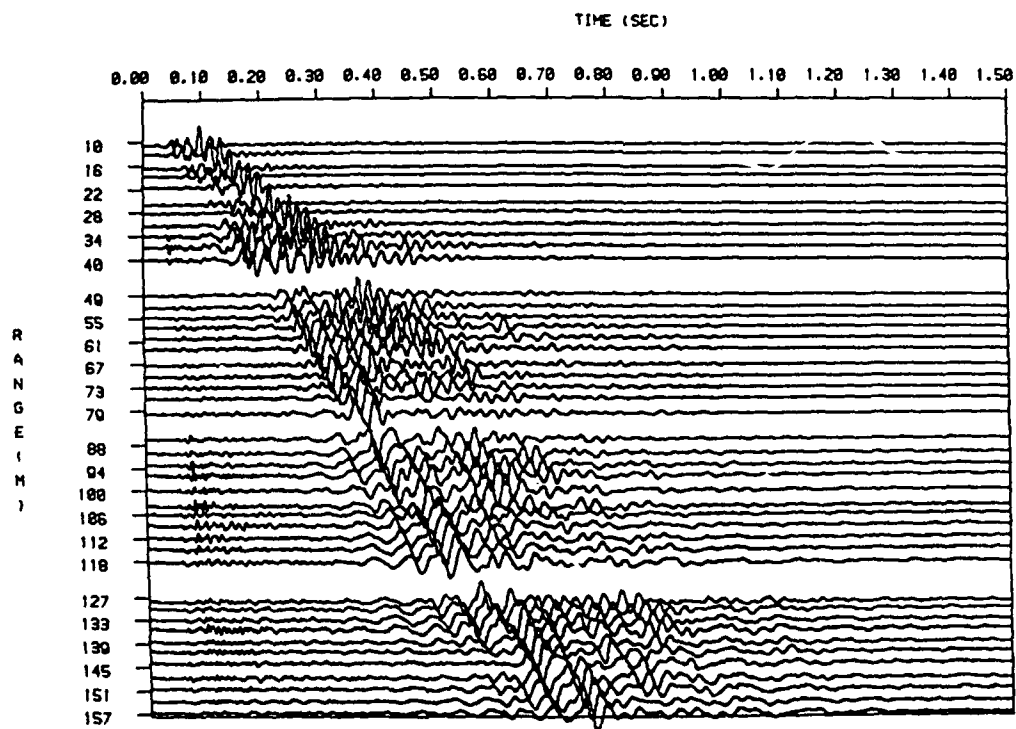
*a. Source was located west of the sensors.*

Figure 26. Vertical component geophone recordings of vertical sledge hammer blows in the summer.



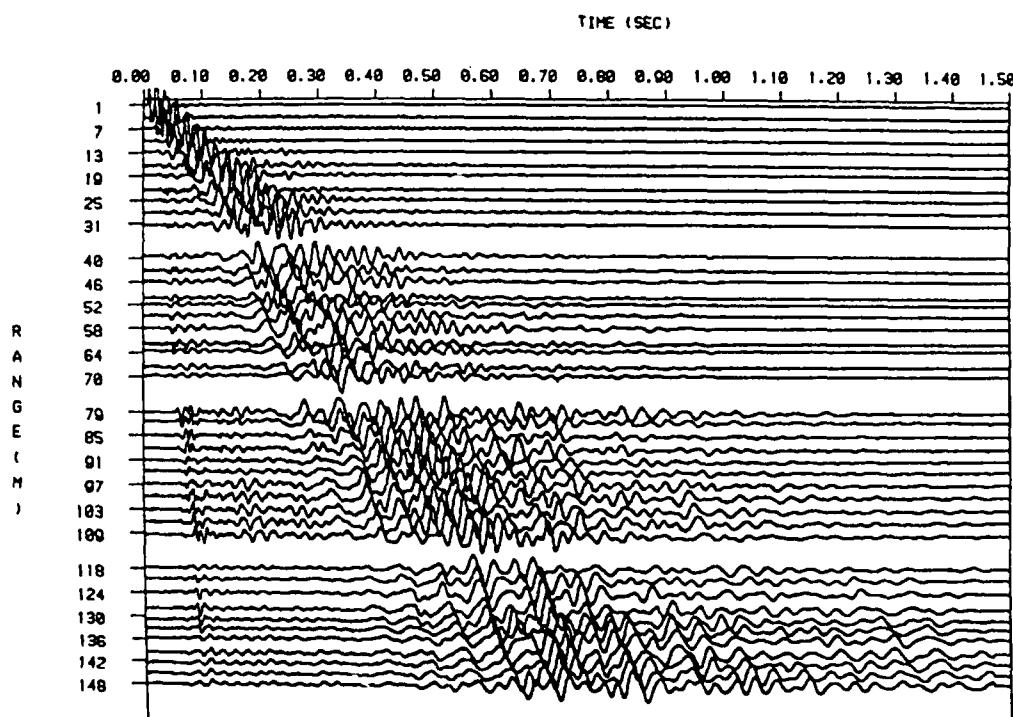
*b. Source was located east of the sensors.*

*Figure 26 (cont'd). Vertical component geophone recordings of vertical sledge hammer blows in the summer.*



a. Source was located east of the sensors.

Figure 27. Vertical component geophone recordings of vertical sledge hammer blows in the winter.



*b. Source was located west of the sensors.*

Figure 27 (cont'd). Vertical component geophone recordings of vertical sledge hammer blows in the winter.

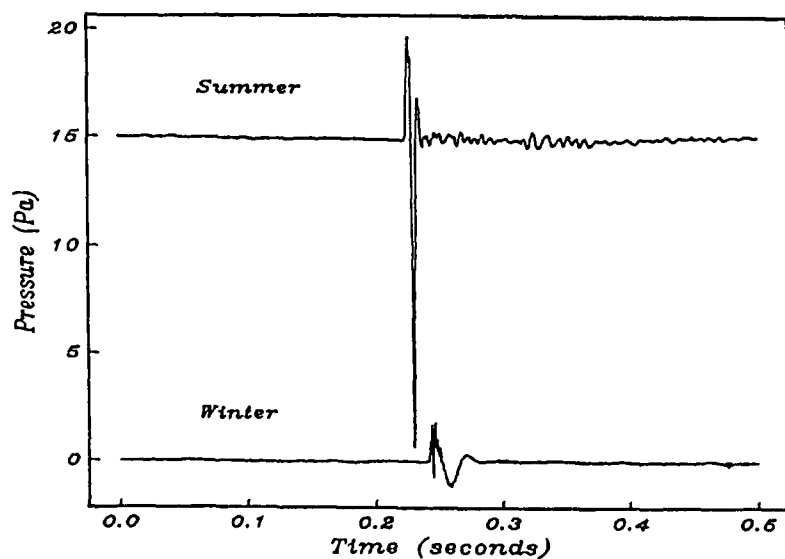


Figure 28. Comparison of recordings from a microphone 0.5 m above the surface in summer (top) and in winter (below). The source was a single firing of a .45 pistol using a blank round. The source and receiver locations are identical for both traces.

face of the ground. The peak pressures were 4.6 and -14 Pa in the summer and only 1.8 and -0.7 Pa in the winter, a 6:1 ratio. In the winter, the pulse from the air wave coincides with a low-frequency wave not present in the summer. The low-frequency pulse peak of -1.2 Pa was about the same size as the air wave.

The pulse is delayed in the winter relative to the summer arrival time because of the temperature-induced change of the speed of sound in air.

Figure 29 shows summer and winter comparisons for two vertical component geophones at the same location as the microphones in the previous figure.

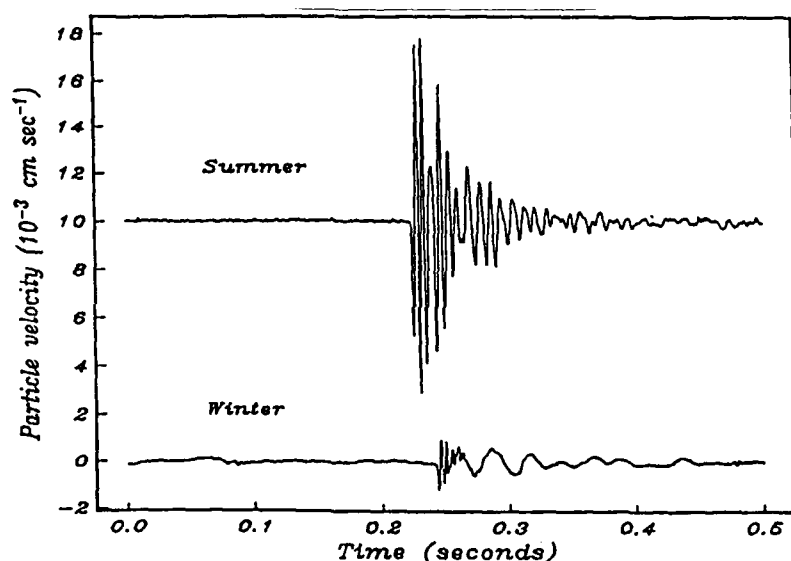


Figure 29. Comparison of recordings from vertical component geophones at the surface in summer (top) and winter (bottom), using the same source and receiver locations as in Figure 28. In the summer, the geophone was on the ground surface, while in the winter the geophone was on the top of the snow cover.

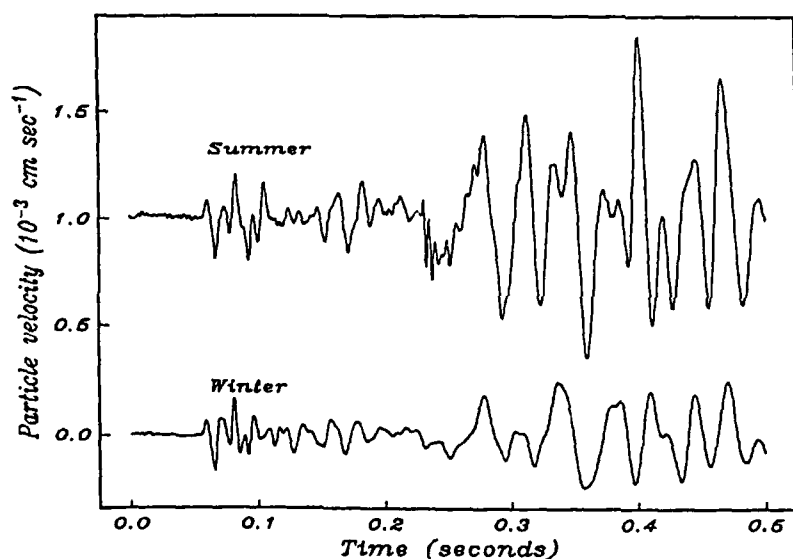


Figure 30. Comparison of recordings for the same vertical component geophones as in Figure 29, using 10 vertical sledge hammer blows on a metal plate on the ground at the previous source location. The initial waveforms are nearly identical. Note the high-frequency arrival at about 0.22 seconds on the summer recording; this is the sound of the hammer striking the metal plate. It does not appear on the winter recording.

The summer geophone was placed at the soil surface, while the winter geophone was placed at the snow surface. The initial motion is downward and is followed by rapid, high-frequency oscillations that persist for a longer time in the summer than in the winter. Again, there is a low-frequency wave train present in the winter data that is not observed in the summer. The ratio of the summer and winter amplitudes is 8:1. The ratio of induced particle velocity to incident pressure was  $7.7 \times 10^{-6} \text{ m s}^{-1} \text{ Pa}^{-1}$  in the summer and  $6.8 \times 10^{-6} \text{ m s}^{-1} \text{ Pa}^{-1}$  in the winter.

The differences in signal amplitude between summer and winter recordings persist at all of the propagation ranges, and have three possible causes, to be examined below: 1) changes in the sensor or record-

ing system sensitivity at different temperatures, 2) changes in the source pulse produced by the pistol or 3) changes in the propagation caused by the different atmospheric sound speed profiles and the presence of the snow cover.

Figure 30 shows the output of the same geophones when sledge hammer blows on a metal plate served as the source. The source locations are the same as for Figures 28 and 29. Although this source is not as repeatable as the pistol shots, the figure shows a very close match between the two recordings. The refracted *P*-wave arrivals between 0.05 and 0.1 seconds are nearly identical in both amplitude and waveform, an exceedingly good match. The surface waves arriving from 0.3 seconds onward are also in general agree-

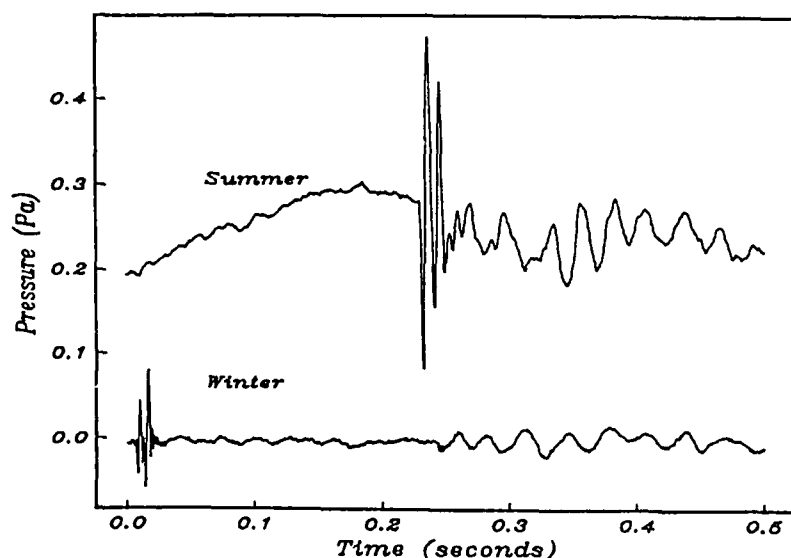


Figure 31. Comparison of recordings for the same microphones as in Figure 28, using 10 vertical sledge hammer blows on a metal plate on the ground at the previous source location. The air wave is just visible on the winter recording. The initial arrival on the winter recording is from instrument noise caused by the time break signal.

ment, with the amplitudes within a factor of two, quite good considering the uncontrolled source. The high-frequency arrival at 0.22 seconds in the summer trace is the air wave produced by the sound of the hammer striking the plate. It is invisible in the winter, and this difference was also noticeable during the tests—the hammer blow was easily heard in the summer as a sharp, high-frequency clang, but was very muffled or inaudible in the winter.

Figure 31 shows the microphone recordings for the same hammer blows. These recordings are much noisier than the geophone recordings, and a cross-talk pulse appears in the winter caused by the startup of the recording system. Despite the higher noise levels, the sound of the hammer blow is visible in both traces. The summer recording shows a high-frequency arrival, as expected. On the winter recording, the arrival is much smaller and slightly later than in the summer, but the surface wave induced by this air wave is clearly visible. Since Figure 30 shows that the hammer blows were of nearly equal strength, the differences in signal level shown in Figure 31 cannot be caused by changes in sensor sensitivity.

Although no direct measurements of the pistol shot amplitudes were made right at the source (since the amplitudes were too high to record without clipping), the observations of the hammer blow sounds also discount this possibility as the reason for the signal differences observed in Figures 28 and 29. Thus, the amplitude differences between the summer and winter data are attributable to changes in the propagation and are not caused by source or instrument effects.

To show that the winter surface geophone signal is not just a filtered version of the summer signal, a zero phase low pass filter was applied to the signals (Fig. 32). The low-frequency surface wave does not appear in the summer geophone signal when the high frequencies are removed. This figure shows that the surface wave is not just masked by other arrivals in the summer, it is not present in the summer and appears only when a snow cover is introduced.

An attempt was made to measure the travel time differences at different depths, but the time interval was too small to provide an accurate velocity. It appeared that the down-going wave was traveling at about the acoustic speed ( $330 \text{ m s}^{-1}$ ), consistent with an interpretation that it travels within the pores of the material, and in agreement with the recent work applying porous media theory to soils (Attenborough et al. 1986, Richards et al. 1985, Sabatier et al. 1986c). The surface wave is induced in the solid or frame of the soil and snow, and it attenuates much less rapidly with depth. Although these waves are expected to show an exponential decrease with depth, this decay was not observed because the measurements were so shallow compared to the wavelengths involved.

#### Coupling to body waves

In addition to the motion induced by the passage of the air wave from the pistol shots, earlier arrivals were also recorded (Fig. 33). Since these waves arrive at almost the same time as the compressional waves recorded using hammer blows, and have measured phase velocities of  $1660 \text{ m s}^{-1}$ , they must travel primarily through the ground, and penetrate at least to



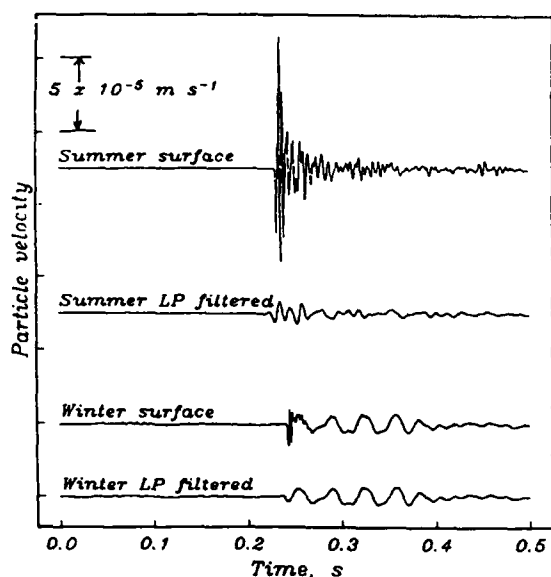


Figure 32. Effect of low-pass filtering on recordings of .45 caliber pistol shots in the summer and winter. Same source and receiver locations as in Figures 28 and 29. The top trace is a vertical component geophone in the summer without filtering; below it is the same signal after low-pass filtering. The third trace is an unfiltered vertical component geophone at the surface of the snow, and the bottom trace is the same as the third with a low-pass filter applied. Removing the high frequencies from the summer recording does not reveal the presence of a low-frequency surface wave like the one apparent in the winter recording.

the water table. They were strongest 40 to 80 m from the source, but were detected out as far as 230 m. This is far beyond the distance that footsteps could be detected, so these early arrivals cannot have been caused by the movement of the shooter. These arrivals are produced by energy that couples into the ground directly beneath the source, and then travels through the subsurface as a seismic compressional (*P*) wave.

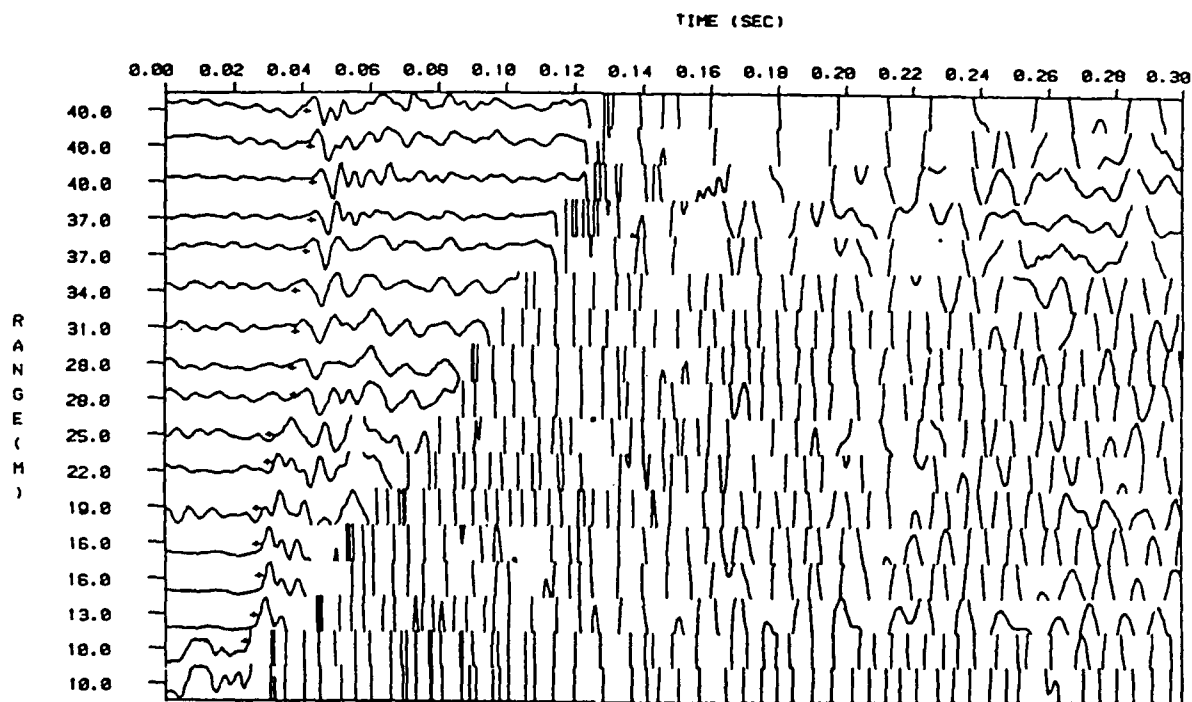
The evidence used to identify the early arrivals as body waves from the saturated soil and not the layer above the water table was the following: First, the group velocity is slightly less than that of the *P* waves from hammer blows, and the phase velocity is  $1660 \text{ m s}^{-1}$ . The early arrival time means that the waves must get into the ground soon after the shot is fired, and eliminates the possibility of a mostly airborne ray path. In addition, the relatively high velocity and early arrival time eliminate the possibility of a near-surface path for these waves, i.e., the waves must penetrate at least to the saturated soil level where the velocity is  $1700 \text{ m s}^{-1}$ . The two-way travel time to the

depth (15–25 m) of a comparable shear wave velocity would introduce too long of a time lag, so the waves cannot have traveled even part of the path as shear waves.

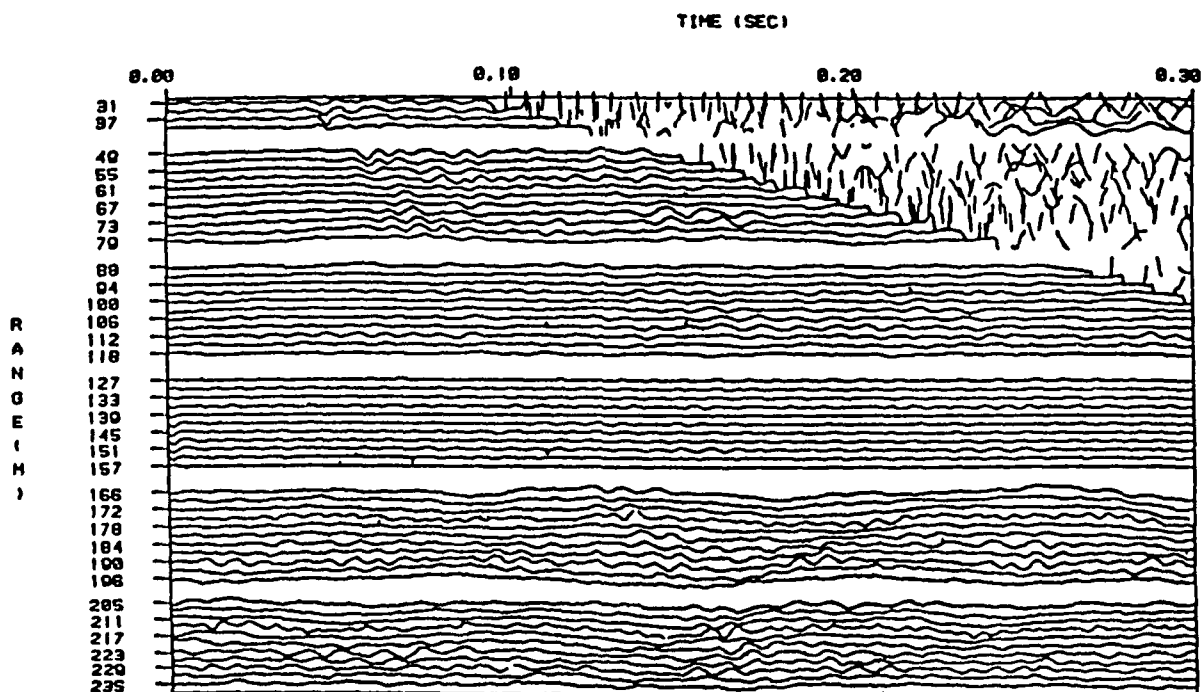
Second, the waveforms of the early arrivals were impulsive rather than being a dispersed wave train. An impulsive waveform is expected for a body wave arrival, but not for a leaky mode or a surface wave. Also, if the arrivals were Rayleigh waves affected by the bedrock shear wave velocity, their period would have to be much longer. Finally, synthetic seismogram calculations for an explosion source in the air and receivers at the surface predict arrivals with the same travel times, waveforms and amplitude (relative to the air wave). By calculating synthetic seismograms for receivers at various depths in the ground, the wavefront of the arrival can be determined, and the wavefront is consistent with the interpretation of a body wave.

These body waves are about a factor of 100 smaller in amplitude than the air waves in the summer. In the winter, the presence of the snow layer actually enhances these waves and they are only about a factor of 10 smaller than the air waves. The enhancement is caused by impedance matching that increases the transmission coefficient when snow is present. The bare ground reflects acoustic waves well; the snow does not and in effect "traps" more of the incident energy.

In the winter, a dependence of the amplitude of these body wave arrivals on the source location was noticed. For a source located 157 m away from the array (ranges 127–157 m in Figure 33b), the arrivals were not present, but they were again observed when the source point was moved 196 m away (ranges 166–196 m). The shot amplitudes are nearly the same, so the difference cannot be attributed to a change in source strength, and one normally expects the amplitude of the waves to decrease with increasing range. The main difference between the two shots was the conditions at the source region. The closer shot point was located in a gravel road that crossed the site, and although the road was not plowed and no vehicles had traveled on it, the snow was very shallow there and the entire area was wind blown with a hard, icy crust present. The shot further out was in a more normal location with 23 cm of softer snow cover. A similar amplitude variation was observed as the source location crossed the road in the summer as well. These amplitude observations also support the interpretation that the arrivals are produced by energy that couples into the ground directly beneath the source, and then travels through the subsurface as a seismic compressional (*P*) wave.



a. The direct waves arriving before the large (clipped) air wave is clearly visible as the first arrival. Plus marks on the plot were used to determine the arrival time of the waves.



b. The plot shows the direct waves arriving before the air wave. These waves have a phase velocity of  $1660 \text{ m s}^{-1}$ , similar to P waves traveling through the water table, so they must penetrate at least 5 m into the soil (Fig. 21). Note the disappearance of the body wave at ranges between 127 and 156 m. Each trace has been multiplied by its range to remove geometrical spreading. The distance between two hash marks on the range axis corresponds to a particle velocity (in  $\text{cm s}^{-1}$ ) of  $0.02/(\text{range in meters})$ .

Figure 33. Vertical component seismograms obtained from .45 caliber blank pistol shots in the winter, with a 0.25-m-thick snow cover present at the site.

## Summary

Visual inspection of the measured data has shown three major differences in acoustic pulses propagating near the ground under summer and winter conditions. First, the peak amplitude levels are much lower in the winter. Second, the winter waveforms are low-pass filtered compared to the summer waveforms. Third, a low-frequency surface wave appears in the winter data when a snow cover is present.

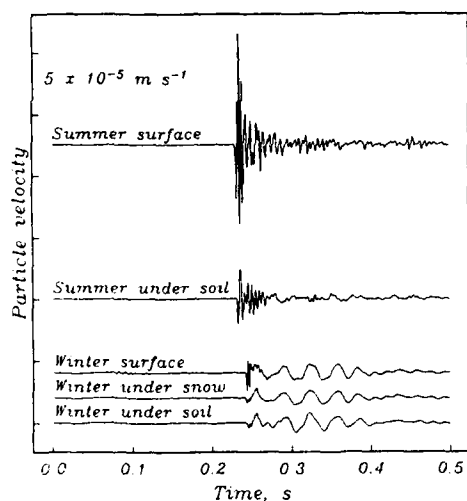
The data also show that an acoustic source will cause two arrivals at surface geophones. The largest arrival is caused by the passage of the air wave, which induces motion in the soil as it passes the sensor. An earlier arrival was also recorded and is interpreted as a body wave that traveled primarily through the subsurface, penetrating at least 4 m deep after coupling into the ground directly beneath the source. The body wave amplitudes increased slightly when a 0.25-m-thick snow cover was introduced because of improved impedance matching. The snow cover introduced a low-frequency air-coupled surface wave that was the largest arrival in the winter.

## DATA ANALYSIS

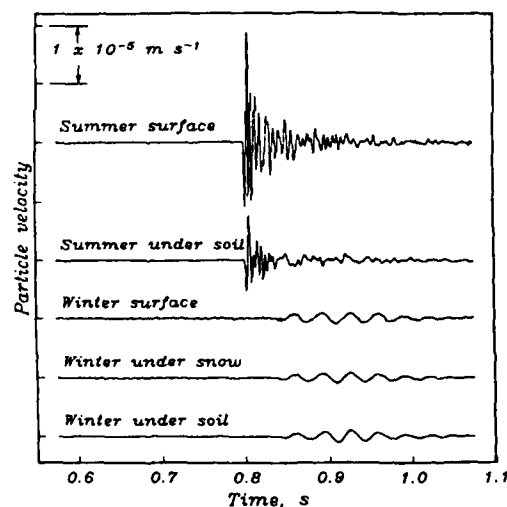
### Observations

#### Site characterization

Figure 34 shows typical examples of the observed signal output from vertical component geophones in the summer and winter, and displays how the signals change as they penetrate a short distance beneath the surface. The source is a .45 caliber blank pistol shot 1 m above the ground surface. The large amplitude arrival near 0.2 seconds in Figure 34a and 0.8 seconds in Figure 34b is the seismic pulse induced by the passage of the acoustic wave from the shot. It is this seismic arrival, which travels primarily through the atmosphere and couples locally into the ground, that I call the air wave in this report. In the summer, the initial soil particle motion is downward and is followed by rapid, high-frequency oscillations. In the winter the air wave is greatly reduced in amplitude and is followed by a low-frequency wave train that is not observed in the summer. The air wave is de-



a. The source was a .45 blank pistol shot from a location 1 m above the snow and 79 m to the east of the geophones, which were located at the horizontal axis origin shown in Figures 4 and 21. The source and receiver locations are identical for all traces. In the summer, the surface geophone was on the ground surface, while in the winter the surface geophone was on the top of the 0.25-m-thick snow cover. The buried geophone was 0.33 m deep in the summer and 0.25 m below the ground surface in the winter.



b. For 10 firings from a position located 274 m to the east of the geophones. The receivers are identical to those in Figure 34a.

Figure 34. True amplitude comparison of vertical component geophone recordings in summer and winter.

layed in the winter relative to the summer arrival time because of the temperature-induced change of the speed of sound in air. The ratio of the summer and winter pulse amplitudes is about 8:1. These differences between summer and winter amplitudes persist at all the propagation ranges and are caused by the different atmospheric sound speed profiles and the presence of the snow cover.

The ratio of induced particle velocity to incident pressure was determined from peak values of the air wave recorded by collocated vertical component surface geophones and surface microphones. In the summer, 64 separate shots or stacked shots gave a mean ratio of  $6.9 \pm 0.4 \times 10^{-6} \text{ m s}^{-1} \text{ Pa}^{-1}$  with 95% confidence interval bounds. In the winter, 54 individual measurements yielded a mean ratio of  $5.9 \pm 0.6 \times 10^{-6} \text{ m s}^{-1} \text{ Pa}^{-1}$ . Since all the measurements were at grazing angles of incidence, no range dependence of the ratio was observed. These ratios are similar to values obtained previously for other soil types. Using continuous sources, researchers have reported peak values (at a single frequency) of  $5 \times 10^{-6}$  to  $10 \times 10^{-6} \text{ m s}^{-1} \text{ Pa}^{-1}$  for silt loam (Bass et al. 1980),  $8 \times 10^{-6}$  for loess (Sabatier et al. 1986a), and  $13 \times 10^{-6}$  for dredged sand (Sabatier et al. 1986a). Using an impulsive source, van Hoof and Doorman (1983) reported a value of  $2 \times 10^{-6} \text{ m s}^{-1} \text{ Pa}^{-1}$  for sandy soil.

The dimensionless energy density ratio ER of the seismic to the acoustic waves can be estimated using

$$ER = \rho_s v^2 / (p^2 / \rho_a c^2) = \rho_s \rho_a c^2 v^2 / p^2 \quad (1)$$

where  $\rho$  = density ( $\text{kg m}^{-3}$ )  
 $c$  = speed of sound in air ( $\text{m s}^{-1}$ )  
 $v$  = particle velocity in the solid ( $\text{m s}^{-1}$ )  
 $p$  = pressure in air (Pa)

and the subscripts  $a$  and  $s$  refer to air and solid (soil or snow), respectively. Assuming  $1.2 \text{ kg m}^{-3}$  for the density of air and substituting the measured values of  $\rho_s$ ,  $c$  and  $v/p$  (the average seismic to acoustic ratio) into eq 1 gives energy ratios of 1.2 and 0.09% in the summer and winter. Since  $v/p$  is nearly constant for the two seasons, the difference in energy transmitted arises mainly from the order of magnitude difference between the soil and snow densities.

By comparing the signals from the surface and buried geophones, their decay as they penetrate beneath the surface can be determined. For example, the signals displayed in both Figures 34a and b show that in the summer the large amplitude air wave is reduced by a factor of 2 as it penetrates from the surface to 0.33 m depth. In the winter, the air wave again is strongly attenuated, dropping by a factor of

Table 7. Attenuation measurements.

No. of points	$\alpha$ (m)	95% confidence interval	Season	Material
33	3.25	1.11	Summer	Soil
20	1.46	1.64	Winter	Soil
100	1.86	0.27	Winter	Snow

3 in passing from the surface through 0.25 m of snow, and by a factor of 4 in passing through the snow and 0.25 m of soil. Because the air wave is at grazing incidence in these examples, the attenuation does not depend on the propagation range. The decay in amplitude is caused by mechanical losses in the soil and snow, i.e., the conversion of elastic energy to heat. The attenuation coefficient  $\alpha$ , defined by

$$A(z) = A(0) e^{-\alpha z} \quad (2)$$

where  $z$  = depth (m)

$A(z)$  = amplitude ( $\text{m s}^{-1}$ ) of geophone at depth  $z$

$A(0)$  = amplitude at the surface

was determined from all of the measured amplitudes for propagation ranges of 40 m or greater (Table 7). For the both the soil and the snow,  $\alpha$  has a value of

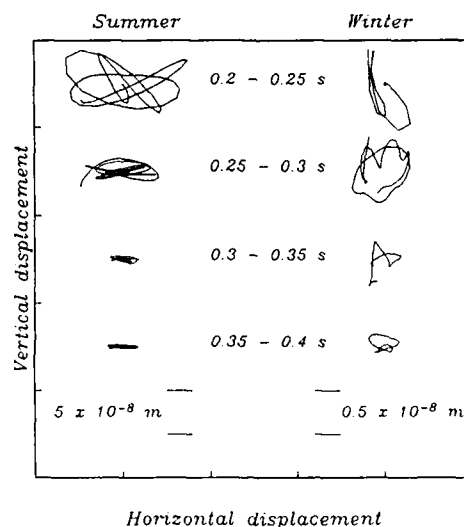


Figure 35. Particle motion diagrams from summer and winter surface geophones at horizontal location zero (Fig. 4 and 21). The pistol was held 1 m above the surface at horizontal location 79 m east. The summer motion is in the left column; the winter in the right. From top to bottom, each segment shows a successive time interval 0.05 seconds long, starting 0.2 seconds after the pistol shot.

around  $2 \text{ m}^{-1}$ . The actual path length  $h$  through the snow or soil should be used in place of the vertical depth  $z$  in eq 2, but this path length depends on the subsurface velocity (which is hard to measure accurately) via the equation

$$h = z [1 - (c_s/c)^2]^{-1/2} \quad (3)$$

where  $c_s$  and  $c$  are the wave velocities in the subsurface material and in air. For the soil, the measured velocity of  $200 \text{ m s}^{-1}$  indicates that  $h = 1.26 z$ , i.e., the two values of  $\alpha$  for soil in Table 7 are about 25% too high. For snow, the estimated velocity of  $100 \text{ m s}^{-1}$  or less leads to an overestimate of less than 5%. The corresponding (corrected) values are 2.6 and  $1.8 \text{ m}^{-1}$  for soil and snow. Though the values themselves are not very accurate because of the scatter in the measurements and the imprecisely known path length, it can be concluded that the attenuation in both materials is quite severe.

Integrating the output from collocated vertical and horizontal geophones provides a picture of the particle motion caused by the air wave. Figure 35 shows the motion when the acoustic source was 79 m from the sensors (the same source and receiver geometry as Fig. 34a). In the summer, the initial soil particle motion starting 0.2 seconds after the shot is down and away from the source as expected, but it almost immediately becomes retrograde\* elliptical with both components about equal in size. Within 0.05 seconds, the horizontal component becomes much larger than the vertical component, and remains so until the motion ends. After two retrograde loops, the motion switches to prograde (at 0.25 seconds), then back again. It remains mostly retrograde and gradually flattens out to purely horizontal motion by 0.4 seconds. The maximum peak-to-peak displacements occur early in the motion, and reach  $6 \times 10^{-8} \text{ m}$  vertically and  $13 \times 10^{-8} \text{ m}$  horizontally. The final horizontal motion 0.4 seconds after the shot remains at about  $2 \times 10^{-8} \text{ m}$ .

In the winter, the motion also starts down and away from the source. The motion is at first prograde and nearly all in the vertical plane. During the next 0.05 seconds, the motion continues to be generally prograde, but both components are about equal in size. About 0.325 seconds after the shot, the motion switches from prograde to retrograde, with the horizontal component being the larger one. This retro-

grade motion continues for two revolutions before the motion dies away. The maximum peak-to-peak displacement is  $1 \times 10^{-8} \text{ m}$  vertically and  $0.6 \times 10^{-8} \text{ m}$  horizontally.

Classically, elliptical particle motion is associated with surface waves in seismology, and this type of motion is especially clear on the winter recordings; it is the low-frequency wave following the air wave in Figure 34. The initial vertical motion is caused by the force applied to the surface from the passage of the air wave. The prograde and retrograde motions arise from surface waves coupled to the air wave, traveling in the snow layer and in the shallow soil. Although some elliptical motion is present in the summer, most of it is rectilinear in the horizontal plane. (Rectilinear motion is usually, but not always, associated with body waves in seismology, so it cannot be used to characterize the wave type.)

Figure 36 shows how the air wave pulse amplitudes decayed as range increased. Least-squares fitting of the data for all of the surface vertical component geophones and for propagation ranges greater than 1 m to the equation

$$A(r) = A_1 r^{-\beta} \quad (4)$$

where  $r$  = distance from the source (m)

$A(r)$  = amplitude ( $\text{m s}^{-1}$ ) of a vertical component geophone on the surface at range  $r$

$A_1$  = constant (the amplitude at  $r = 1 \text{ m}$ )

$\beta$  = distance attenuation exponent

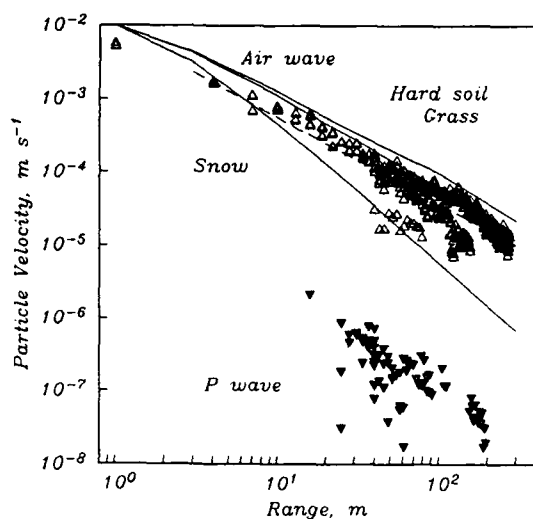
showed that the decay rate in the winter ( $\sim r^{-1.9}$ ) was much higher than in the summer ( $\sim r^{-1.2}$ ). A similar analysis was carried out for the microphones, but the results are not as accurate because there were fewer microphones in the array and because some of the recorded microphone waveforms were clipped, especially in the summer, and could not be used. Additional details of the fit of the data to eq 4 are given in Table 8.

There are two primary mechanisms affecting the measured decay rate: the bending of acoustic rays by

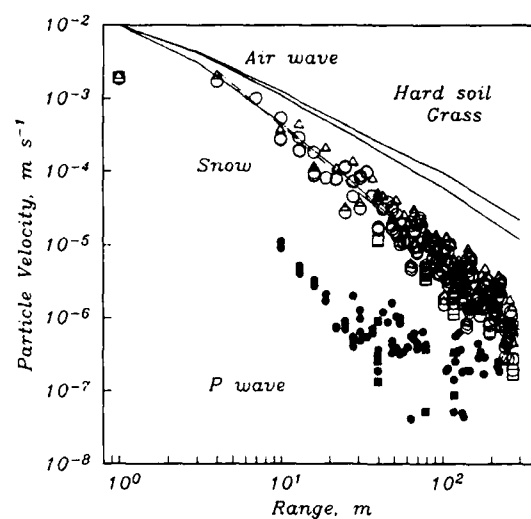
Table 8. Range decay for air waves.

No. of points	$\beta$	95% confidence interval	Season
458	1.17	0.09	Summer geophones
352	1.89	0.15	Winter geophones
66	1.31	0.59	Summer microphones
142	1.52	0.45	Winter microphones

\* Retrograde motion is opposite in direction to the motion of a point on the surface of a disk that is rolling along the ground from the source to the receiver.



a. Summer. Initial motion was up for the P waves (solid symbols) and down for the air waves (open symbols). Triangles denote amplitudes measured by receivers on the surface.



b. Winter. Triangles, circles, and squares denote receivers at the snow surface, under the snow, and buried in the ground, respectively. Solid symbols are the P-wave arrivals, open symbols the air wave.

Figure 36. Plot of first arrival amplitude vs distance from the source for vertical component geophones. A dashed line shows the least squares fit to the air wave amplitude data used to determine the decay rate given in Table 8. The solid lines are amplitudes predicted for a relatively hard soil (top), grassland (middle) and snow (bottom) using Attenborough's (1985) model.

the inhomogeneous atmospheric sound speed profile and the absorption of energy by the finite impedance ground surface. For a neutral atmosphere, the sound ray paths are straight lines spreading outward evenly from the source, and the amplitude decay rate is mainly like  $r^{-1}$ . For the summer measurements, the  $3\text{ m s}^{-1}$  wind kept the atmosphere at a nearly constant temperature by mixing, and since the wind was blowing perpendicular to the propagation direction, its effect was to slightly bend the ray direction (by  $0.8^\circ$ ) and to decrease the sound velocity (by  $0.04\text{ m s}^{-1}$ ), with very little effect on the amplitude decay. The split in the air waves beyond 100 m (Fig. 36a) corresponds to source locations to the west (lower amplitudes) and to the east (higher amplitudes) of the receiver array; these recordings were made on different days when atmospheric conditions may have been slightly different. In the winter, the positive temperature gradient (inversion) tended to bend upward-propagating rays back down towards the ground, decreasing the amplitude decay rate and enhancing the amplitude at a given range. This gradient was about  $2\text{ to }4^\circ\text{C m}^{-1}$  from the surface to 2-m height, and about  $1^\circ\text{C m}^{-1}$  from 2 to 6 m.

The second mechanism affecting the amplitude decay rate is absorption of the airborne acoustic wave

by the ground. If the ground were completely rigid, all of the rays impinging on it would be reflected back into the air without loss, and the total amplitude produced at a given range by a spherically symmetric source would be doubled by the reflection from the boundary. There has been extensive study of the effect of a ground surface with finite impedance on acoustic waves (Embleton and Daigle 1987, Embleton et al. 1976, Nicolas et al. 1985). Such ground conditions will increase the decay rate by absorption and transmission. Since the acoustic wave from the source propagates mainly through the atmosphere and couples locally into the ground, the decay rate of the airborne waves caused by ground absorption was calculated (see Albert and Orcutt [1990] for further details on the method used to calculate ground absorption) for comparison with the amplitude decay measured by the geophones. Using a four-parameter model developed by Attenborough (1985) and the Weyl-Van der Pol formulation, I determined the excess attenuation produced by the boundary at selected ranges as a function of frequency. I then integrated over the frequency bandwidth of our recording instruments to determine the effect of ground impedance on pulse amplitudes in a manner similar to that used by Don and Cramond (1987). Pulse amplitude

decay rates for three types of ground were calculated and are plotted in Figure 36: a relatively hard soil (with effective flow resistivity  $\sigma_e = 1820 \text{ kN s m}^{-4}$ ), a softer soil representative of grassland ( $\sigma_e = 366 \text{ kN s m}^{-4}$ ), and snow ( $\sigma_e = 10 \text{ kN s m}^{-4}$ ). The input parameters for these grounds used in the calculations were taken from Attenborough (1985) and from Attenborough and Buser (1988).<sup>\*</sup> The calculated acoustic attenuation for propagation above grassland shows the same decay rate as that observed by the surface geophones in the summer, and the calculated acoustic attenuation above snow-covered ground agrees with the decay observed in the winter (Fig. 36). From these comparisons I conclude that the attenuation rates measured for the air wave by the geophones in summer and winter are accounted for by differences in the ground absorption of the airborne acoustic wave. The enhancement from ray bending in the winter was not observed in the data because the absorbing effect of the ground surface, which decreased the amplitude as the range increased, was much stronger than the refraction effect.

In addition to the motion induced by the passage of the air wave from the pistol shots, earlier arrivals were also recorded by the vertical component geophones. Since these waves arrive at almost the same time as the compressional waves recorded using hammer blows, and have measured phase velocities of  $1660 \text{ m s}^{-1}$ , they must travel primarily through the ground, and penetrate at least as deep as the water table. They were strongest 40 to 80 m from the source, but were detected out as far as 230 m. This is far beyond the distance that footsteps could be detected, so these early arrivals cannot have been caused by the movement of the shooter. The decay of these waves as a function of range is also shown in Figure 36. The above observations and synthetic seismogram modeling work indicate that these arrivals are produced by energy that couples into the ground directly beneath the source, and then travels through the subsurface as a seismic compressional (*P*) wave.

These body waves are about a factor of 100 smaller in amplitude than the air waves in the summer. In

the winter, the presence of the snow layer actually enhances these waves and they are only about a factor of 10 smaller than the air waves. The enhancement is caused by impedance matching that increases the transmission coefficient when snow is present. Such matching can be demonstrated by the following simple example in which we treat the ground as a purely elastic material. The plane wave amplitude transmission coefficient at normal incidence is

$$T = (2\rho_1c_1)/(\rho_1c_1 + \rho_2c_2)$$

where  $\rho$  and  $c$  are the density and acoustic velocity, respectively, and the subscripts refer to the upper or lower medium. With values of 0.407, 12.5 and  $369 \text{ kg m}^{-2} \text{ s}^{-1}$  for the impedances  $\rho c$  of the air, snow and soil, the transmission coefficient from air to soil is 0.002; for air to snow to soil it is 0.004, a factor of 2 higher. Including the porosity and other details of the ground's structure would enhance the transmission coefficient of the higher porosity snow and strengthen my conclusion. The bare ground reflects acoustic waves well; the snow does not and in effect "traps" more of the incident energy.

#### Summary

Observations have shown that an acoustic source will cause two arrivals at surface geophones or geophones buried at shallow depths. The largest arrival is caused by the passage of the air wave that induces a surface wave in the soil with elliptical particle motion. A 0.25-m-thick snow cover caused increased amplitude decay of the air wave, and a relative enhancement of the low-frequency air-coupled surface wave. The direction of particle motion also switched from retrograde to prograde. Under these experimental conditions, the effect of ground absorption dominates the pulse amplitudes and overrides any refractive effects of the atmosphere. Theoretical calculations of the amplitude decay of the airborne acoustic wave using Attenborough's model (Attenborough 1985) are in good agreement with observations. An earlier arrival was also recorded for a body wave that traveled primarily through the subsurface, penetrating at least 4 m after coupling into the ground directly beneath the source. The body wave amplitudes increased slightly when a snow cover was introduced because of improved impedance matching.

#### Comparison of theoretical and experimental acoustic waveforms

In this section, I outline the theory used to describe the effect of an absorbent boundary on acoustic waves, and models that are used to estimate the

<sup>\*</sup> The input parameters required for the four-parameter model are the flow resistivity  $\sigma_e$ , porosity  $\Omega$ , pore shape factor ratio  $s_f$  and grain shape factor  $n'$  (see Attenborough [1985] for the definition of the latter two parameters). For all of the calculations, I set  $n' = 0.5$ . For the hard soil, the other input parameters were  $\sigma_e = 1820 \text{ kN s m}^{-4}$ ,  $\Omega = 0.38$  and  $s_f = 0.73$ . For grass, I used  $\sigma_e = 366$ ,  $\Omega = 0.27$  and  $s_f = 0.73$ . For snow, I used  $\sigma_e = 10$ ,  $\Omega = 0.60$  and  $s_f = 0.50$ . This layer was 0.25 m thick, and was over a soil layer with the parameters  $\sigma_e = 300$ ,  $\Omega = 0.40$  and  $s_f = 0.75$ .

absorbing characteristics of the ground. Additionally discussed is the method used to predict the pulse waveforms expected after propagation along an absorbing boundary. I present some examples of calculated waveforms and make comparisons with data obtained for propagation over grassland and over snow. Also, the predicted and observed amplitude decays as a function of range for these two ground surfaces are compared.

### Theory

**Effect of an absorbing boundary.** The well-known expression (e.g., Chessell 1977, Embleton et al. 1983, Don and Cramond 1987, Attenborough et al. 1980) for the pressure  $p$  received at a height  $h_r$  above an impedance boundary from a continuously emitting point source at a height  $h_s$  and a distance  $r_1$  away (Fig. 37) is given by

$$\frac{p}{p_0} = \frac{1}{k_1 r_1} e^{ik_1 r_1} + \frac{1}{k_1 r_2} Q e^{ik_1 r_2} \quad (5)$$

where  $p_0$  is a reference pressure level near the source,  $k_1$  is the wavenumber in the air, and  $r_1$  and  $r_2$  are the direct and reflected waves' path lengths. The first term in eq 5 gives the pressure from the direct wave; the second gives the contribution from the boundary. The dimensionless image source strength  $Q$  is defined to include the reflection from the boundary and the ground wave term

$$Q = R_p + (1 - R_p) F(w) \quad (6)$$

where the plane wave reflection coefficient  $R_p$  is

$$R_p = \frac{(Z_2 \sin \phi - Z_1 s^{1/2})}{(Z_2 \sin \phi + Z_1 s^{1/2})} \quad (7)$$

with  $Z_1$  and  $Z_2$  representing the specific acoustic impedances of the two media,  $\phi$  the angle of incidence defined in Figure 37, and

$$s = 1 - (k_1/k_2)^2 \cos^2 \phi. \quad (8)$$

A steepest descent approach (Attenborough et al. 1980) can be used to evaluate  $F$  and gives

$$F(w) = 1 + i(\pi)^{1/2} w e^{-w^2} \operatorname{erfc}(-iw) \quad (9)$$

where  $i = \sqrt{-1}$  and the dimensionless numerical distance  $w$  is defined by

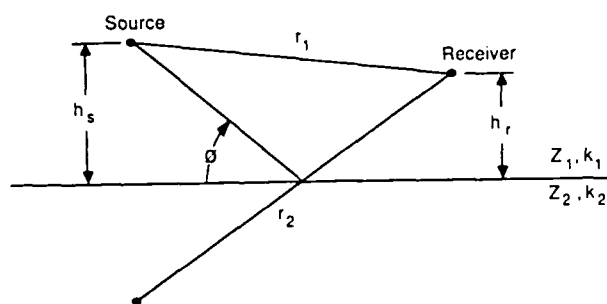


Figure 37. Geometry of the calculations and observations. The two acoustic media have impedances and propagation constants of  $Z_1, k_1$  and  $Z_2, k_2$  respectively. The source and receiver are both in medium 1, at heights of  $h_s$  and  $h_r$ , and the direct and reflected wave path lengths are  $r_1$  and  $r_2$ . The angle of incidence is  $\phi$ .

$$w^2 = 2ik_1 r_2 (1 - R_p)^{-2} (Z_1/Z_2)^2. \quad (10)$$

The steepest descent derivation involves a high-frequency approximation, which requires that

$$kr \gg 1 \quad (11)$$

or, equivalently

$$f \gg c/(2\pi r) \quad (12)$$

where  $f$  is the frequency in hertz and  $c$  the acoustic wave speed. This limiting frequency value is 5 Hz for a 10-m propagation range in air and 1 Hz for 40 m, the shortest propagation range for the measurements reported on here.

The equations were derived using a local reaction condition, which assumes that the surface acoustic impedance of the boundary is independent of the incident angle (or equivalently that the transmitted waves are refracted vertically into the lower medium). The assumptions that the waves arrive at grazing incidence and that  $|Z_2| > |Z_1|$  were also used in the derivation.

In all calculations, I have assumed a homogeneous atmosphere (i.e., no refraction of acoustic rays) without turbulence. I have omitted atmospheric absorption from the calculations, since Don and Cramond's (1987) and my own calculations have shown that it is negligible at these ranges (less than 300 m) and frequencies (less than 500 Hz). The next subsection discusses the models used to determine the ground impedance  $Z_2$  needed for the calculation of pulse waveforms via eq 7 and 10.



*Models of ground impedance.* Past predictions of acoustic pulse waveforms (Don and Cramond 1987, Raspet et al. 1983, 1985) have exclusively employed Delaney and Bazley's (1970) single-parameter model of ground impedance. This model consists of the empirically determined relationships

$$Z'_2/\rho c = 1 + 0.05 (f/\sigma)^{-0.75} \quad (13)$$

$$Z''_2/\rho c = 0.077 (f/\sigma)^{-0.73} \quad (14)$$

where  $Z'_2$  and  $Z''_2$  are the real and imaginary parts of the ground impedance  $Z_2$ ,  $\rho$  is the density of the air, and  $\sigma$  is the flow resistivity of the porous ground. (The numerical constants in eq 13 and 14, and in eq 16 and 17 below, actually have units that cancel those of the  $(f/\sigma)$  terms, making the equations dimensionless.) Attenborough (1983) pointed out that Delaney and Bazley (1970) derived their model using materials for which the porosity was nearly 1, and gave a theoretical argument showing that the measured flow resistivity should be multiplied by the porosity before substitution into eq 13 and 14. It is this value, termed the *effective* flow resistivity, that is denoted by the symbol  $\sigma$  in this report.  $\sigma$  has units of  $\text{N s m}^{-4}$  or  $\text{mks rays m}^{-1}$ . This report gives numerical values in  $\text{kN s m}^{-4}$  ( $= 10^3 \text{ N s m}^{-4}$ ), which makes the values the same as those expressed in cgs units in some earlier papers.

The ground sometimes behaves as a layered porous medium, rather than the infinitely thick layer assumed in eq 13 and 14. If we let  $h$  be the layer thickness and  $k_2$  be the wavenumber in the layer, then the resulting impedance of the medium is (Brekhuskikh 1980)

$$Z = \frac{Z_2 (Z_3 - i Z_2 \tan k_2 h)}{(Z_2 - i Z_3 \tan k_2 h)} \quad (15)$$

where  $Z_2$  and  $Z_3$  are the impedances of the upper and lower materials, respectively, found using eq 13 and 14. Delaney and Bazley (1970) also determined formulae for the wavenumber  $k_2 = k' + ik''$  such that

$$k'/k_1 = 1 + 0.098 (f/\sigma)^{-0.70} \quad (16)$$

$$k''/k_1 = 0.19 (f/\sigma)^{-0.59} \quad (17)$$

The second model of ground impedance that I use in my calculations was developed by Attenborough (1985). This model treats the porous medium as a rigid frame with randomly varying pore sizes. The model requires four parameters to describe

the material: effective flow resistivity  $\sigma$ , porosity  $\Omega$ , grain shape factor  $n'$  and pore shape factor ratio  $s_f$ . Propagation in the porous medium is then described by Attenborough's (1985) eq 8 and 9

$$k_2^2 = q^2 \left[ 1 - \frac{2}{\lambda_i^{1/2}} T(\lambda_i^{1/2}) \right]^{-1} \times \left[ 1 + \frac{2(\gamma - 1)}{\lambda_i^{1/2} N_{Pr}^{1/2}} T(\lambda_i^{1/2} N_{Pr}^{1/2}) \right] \left( \frac{\omega}{c} \right)^2 \quad (18)$$

$$Z_2 = \frac{q^2}{k_2 \Omega} \left[ 1 - \frac{2}{\lambda_i^{1/2}} T(\lambda_i^{1/2}) \right]^{-1} \quad (19)$$

where  $q^2 = \text{tortuosity} = \Omega^{-n'}$  (dimensionless)

$\gamma = \text{ratio of specific heats}$

$\omega = 2\pi f$

$T(x) = \text{ratio of cylindrical Bessel functions} = J_1(x)/J_0(x)$

$\lambda = (1/s_f) [8\rho q^2 \omega / \Omega \sigma]^{1/2}$

$N_{Pr} = \text{Prandtl number.}$

The impedance of a layered medium is determined by eq 15, 18 and 19. In all of the computations, we have set  $n' = 0.5$ , and we have taken  $N_{Pr} = 0.712$  and  $\gamma = 1.4$  for air. Most of the other values were taken from measurements reported by Attenborough (1985) for soils and by Attenborough and Buser (1988) for snow.\*

With the definition  $\sigma_e = s_f^2 \sigma / \Omega$ , Attenborough (1985) also obtained a low-frequency approximation of the four-parameter model that requires only two parameters

$$Z_2 = (4\pi\gamma\rho)^{-0.5} (\sigma_e/f)^{0.5} (1 + i) \quad (20)$$

$$k_2 = Z_2 \gamma \Omega. \quad (21)$$

#### Calculation of pulse waveforms

In the following equations, lower case letters are used to denote sampled quantities in the time domain, and capital letters the corresponding frequency domain values;  $m$  and  $n$  are used as subscripts for the particular index value in the time and frequency domain.

\* Note that Attenborough and Buser (1988) have a different definition of the pore shape factor ratio, using  $s_p = 2s_f$ . The tabulated values for snow in Attenborough and Buser (1988) were thus multiplied by 2 for these computations.

The sampled source pulse is given by the sequence  $\{s_m\}$ ,  $m = 0, 1, \dots, N-1$  with an interval of  $\Delta t$  seconds between samples. The source pulse components in the frequency domain are found by taking the discrete Fourier transform

$$S_n = \sum_{m=0}^{N-1} s_m e^{i2\pi m n / N} \quad (22)$$

$$n = 0, 1, \dots, N-1.$$

The elements of the complex sequence  $\{S_n\}$  occur at frequency values  $f_n = n/(N \Delta t)$ ; i.e., the frequency spacing is  $\Delta f = 1/(N \Delta t)$  and the highest is  $f_N = 1/(2 \Delta t)$ . The image response  $Q_n$  is computed at all of the desired frequencies using either the single-parameter (Delaney and Bazley 1970) model or the four-parameter (Attenborough 1985) model, or its low-frequency approximation. The resultant  $X_n$  of the direct and reflected pulse is then

$$X_n = S_n \left[ (4\pi r_1)^{-1} \exp(i2\pi f_n r_1 / c) + (4\pi r_2)^{-1} \exp(i2\pi f_n r_2 / c) Q_n \right] \quad (23)$$

For a receiver at the surface,  $r_2 = r_1 (= r)$ , so eq 23 becomes

$$X_n = (4\pi r)^{-1} S_n (1 + Q_n) \exp(i2\pi f_n r / c). \quad (24)$$

In the above equation, the exponential term is merely a phase delay that determines the arrival time of the pulse. This term was replaced by  $\exp(i2\pi f_n t_0)$  in the computations, where  $t_0$  is a fixed time shift. This replacement is equivalent to the use of a reduction velocity to align the pulses for all ranges at the time  $t_0$ , and avoids the need to compute additional terms as the range increases.

Next, a window is applied to limit the calculations to the recording system's bandwidth of 500 Hz. The window coefficients used reproduce the effect of the recording system's anti-aliasing filter and are given by

$$W_n = \sin^4 \left[ (n-1) \pi / N \right] \quad (25)$$

$$n = 0, 1, \dots, N-1.$$

The resultant pulse in the frequency domain then becomes

$$X_n = \frac{W_n S_n}{4\pi r} (1 + Q_n) \exp(i2\pi f_n t_0). \quad (26)$$

The time domain pulse  $x_m$  was then computed from eq 26 using the inverse discrete Fourier transform

$$x_m = \frac{1}{N} \sum_{n=0}^{N-1} X_n e^{-i2\pi m n / N} \quad (27)$$

$$m = 0, 1, \dots, N-1.$$

In all of the computations, the recording system's sampling interval of  $\Delta t = 0.5$  ms was used. The Fast Fourier Transform (FFT) algorithm was used to compute eq 22 and 27, with the number of points  $N$  set to 2048, so  $\Delta f = 0.997$  Hz and  $f_N = 1$  kHz. Since  $Q_n$  turns out to vary smoothly, a wider frequency spacing could probably have been used, and direct integration without the use of the FFT algorithm may be more efficient. For all of the calculations, the source height was set to 1 m and the receiver was on the surface.

#### Results and discussion

*Theoretical examples.* I first calculate two examples, chosen to illustrate the extremes in the importance of the ground impedance on propagating acoustic pulses. The first is presented in Figures 38 and 39. The single-parameter impedance model (Delaney and Bazley 1970) was used, with  $\sigma$  set to 32,000 kN s m<sup>-4</sup>, a value representative of an old asphalt surface (Embleton et al. 1983) and of the highest value the effective flow resistivity could be expected to reach for outdoor propagation. Figure 38 shows the excess attenuation and the magnitude and phase of the image source ( $Q$  in eq 6) calculated at propagation distances of 10, 100 and 1000 m. The high effective flow resistivity value used specifies an acoustically hard surface, and the response is generally flat up to 1 kHz, implying that very little waveform change will occur. Figure 39 shows the calculated waveforms, using the source waveform shown, for ranges up to 3 km. The source waveform used in this and in all of the following calculations is an estimated one, because my measurements from microphones close to the source were clipped. I estimated the peak amplitude of the experimental pulse as 2 kPa at 1 m.

Two sets of waveforms are shown in Figure 39, one set with and one set without air absorption (American National Standard Institute 1978). The pulse waveforms are virtually identical at all propagation distances when air absorption is ignored. When absorption is included, the peak amplitudes

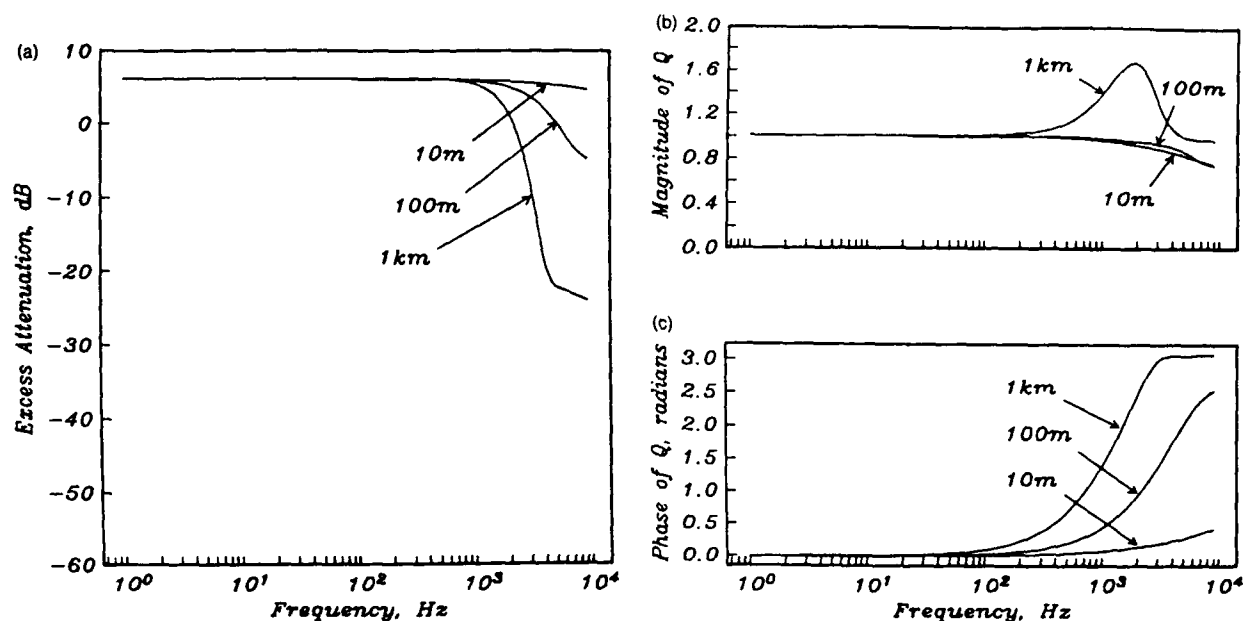


Figure 38. Excess attenuation (a), image source magnitude (b) and image source phase (c) as a function of frequency calculated using the Delaney and Bazley (1970) model with  $\sigma = 32,000 \text{ kN s m}^{-4}$ . Propagation distances are 10, 100 and 1000 m, source height is 1 m, and receiver is at the surface.

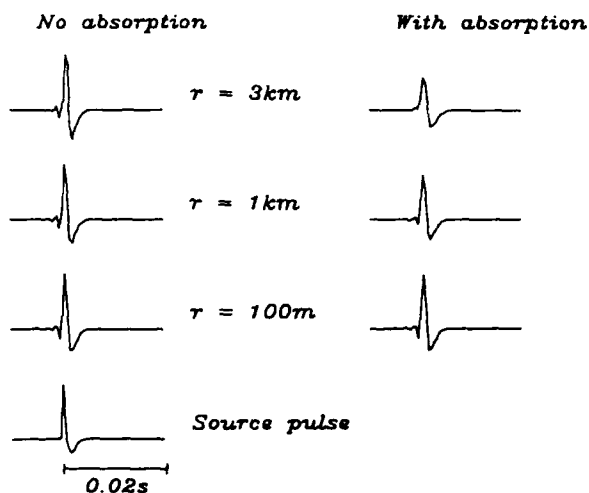


Figure 39. Waveforms calculated using the Delaney and Bazley (1970) model with  $\sigma = 32,000 \text{ kN s m}^{-4}$  for ranges of 0.1, 1 and 3 km. Source height 1 m, receiver at the surface. The source pulse used is shown at the bottom of the figure, and the spectrum is band limited to 500 Hz. The waveforms on the left were calculated ignoring the effects of atmospheric absorption; those on the right include absorption. The waveforms on the left are normalized; the peak amplitudes are 2000, 33, 3 and 1 Pa, respectively, from bottom to top. The waveforms on the right are plotted at the same scale as those on the left, and they have peak amplitudes of 32, 2.5 and 0.6 Pa.

are lower and the waveforms are slightly broader. The amplitude reduction is only a few percent at 100 m and about 20% at 1 km.

The next calculation used  $\sigma = 10 \text{ kN s m}^{-4}$ , a value representing a very absorptive surface like snow (Nicolas et al. 1985), near the lower bound of effective flow resistivity. The excess attenuation and image source curves shown in Figure 40 now exhibit a more complicated structure in the frequency band of interest. At low frequencies, the boundary is fully reflecting, and the sound level is double that of the

free space value, with a corresponding excess attenuation value of 6 dB. The attenuation begins to increase at higher frequencies, reaching 0 dB at 100, 45 and 20 Hz for propagation distances of 10, 100 and 1000 m. This decay arises from the phase change that occurs on reflection from the boundary.

The effects of the low effective flow resistivity surface on propagating acoustic pulse shapes are shown in Figure 41. The pulse amplitudes are much lower than in the previous example, and low frequencies dominate and elongate the waveform for ranges be-

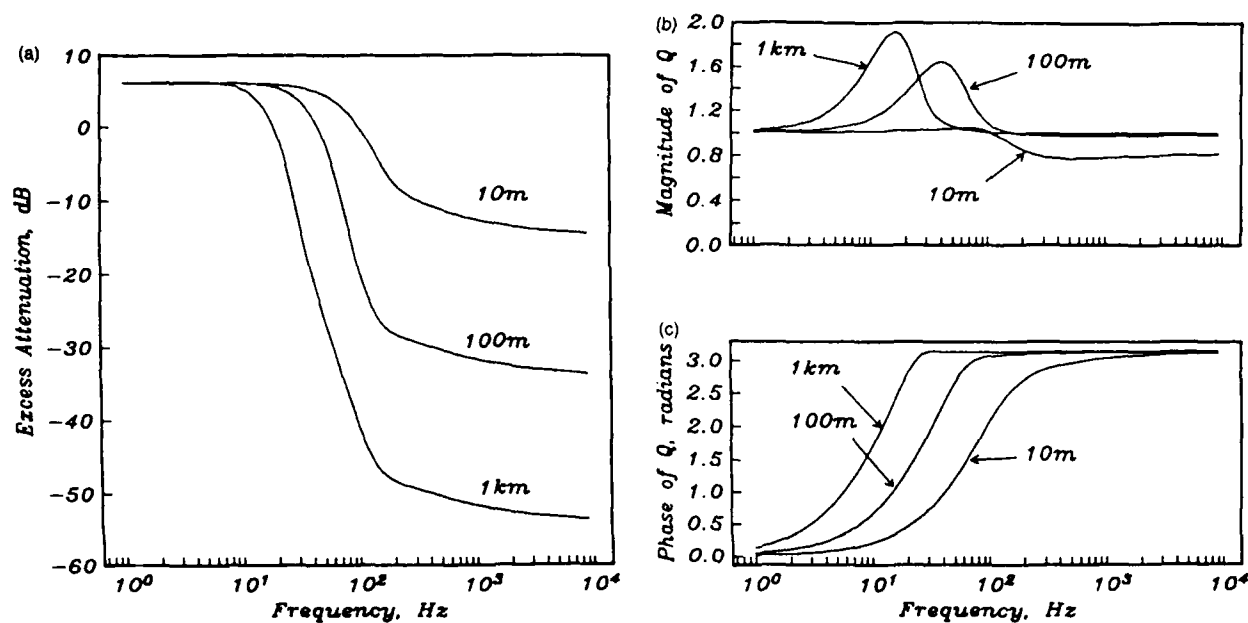


Figure 40. Excess attenuation (a), image source magnitude (b) and image source phase (c) as a function of frequency calculated using the Delaney and Bazley (1970) model with  $\sigma = 10 \text{ kN s m}^{-4}$ . Same source and receiver geometry as in Figure 39.

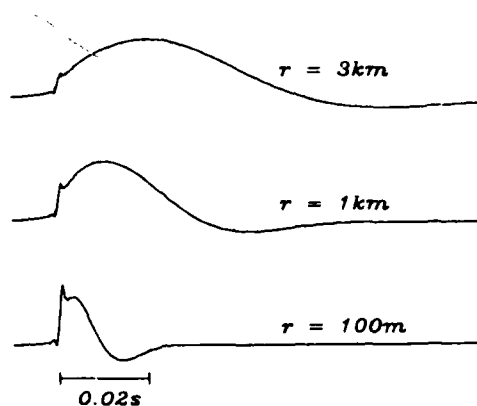


Figure 41. Waveforms calculated using the Delaney and Bazley (1970) model with  $\sigma = 10 \text{ kN s m}^{-4}$  for ranges of 0.1, 1 and 3 km. The source pulse used is shown in Figure 39. The waveforms shown as solid lines ignore the effect of atmospheric absorption. Waveforms that were calculated including the absorption effects were identical to those calculated in the absence of air absorption at this scale. The peak amplitudes are 1.5 Pa at 100 m, 0.03 Pa at 1 km and 0.005 Pa at 3 km.

yond a few tens of meters. This enhancement of the lower frequencies is the result of integrating over the image source magnitude shown in Figure 40b, with the dominant frequencies of the waveforms at 100 and 1000 m corresponding to the peak image source

magnitudes at 40 and 15 Hz. Two sets of waveforms were calculated, with and without the effect of air absorption. In this case, the waveforms were nearly identical, even at a range of 3 km, because the low frequencies that dominate these pulses are not greatly affected by air absorption.

These examples show that hard boundaries, i.e., those with a high effective flow resistivity, act as good reflectors and have little effect on pulse waveforms, while soft, absorbent boundaries with low effective flow resistivities can produce radically different waveforms by absorbing the higher frequencies. Additional calculations (omitted here) revealed that the three other parameters involved in Attenborough's model have an influence on the waveforms smaller than that of the effective flow resistivity. This explains the success of the Delaney and Bazley model in past work; it concentrates on the most important parameter, the effective flow resistivity. In the next subsection, I show that calculated waveforms using either of the models can successfully match the waveforms observed in outdoor sound propagation experiments.

*Observations and waveform comparisons.* Figure 42 shows typical summer surface microphone recordings (solid line) for the series of pistol shots at ranges from 40 to 274 m. These shots were recorded during a 75-minute period by moving the source farther away from the receivers in an eastward direction. I ran a number of sample calculations using the single-

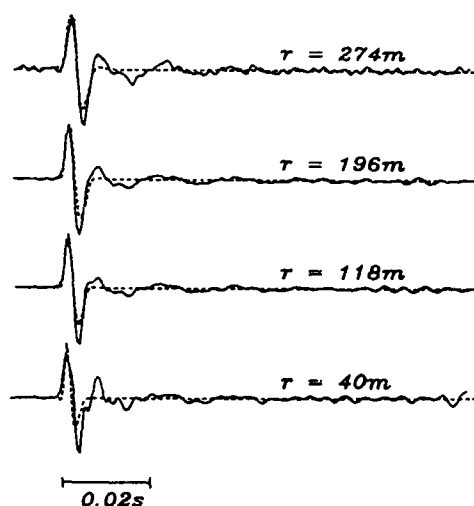


Figure 42. Comparison of normalized waveforms for pulse propagation over grassland for ranges from 40 to 274 m. The solid lines are the waveforms recorded by surface microphones, and the observed peak amplitudes were 12, 9.1, 4.6 and 2.0 Pa, respectively, from bottom to top. The dashed lines are waveforms calculated using the Delaney and Bazley (1970) model with  $\sigma = 200 \text{ kN s m}^{-4}$ . For the calculated waveforms, the source pulse shown in Figure 39 was used, and the spectrum is limited to 500 Hz.

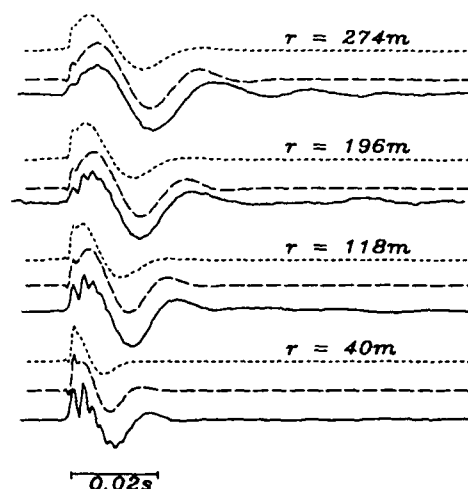


Figure 43. Comparison of normalized waveforms for pulse propagation over snow for ranges from 40 to 274 m. The solid lines are the waveforms recorded by surface microphones, and the observed peak amplitudes were 5.1, 0.91, 0.60 and 0.17 Pa, respectively, from bottom to top. The long-dashed lines above the solid lines are waveforms calculated using Attenborough's (1985) model for a layered ground. The first layer was 0.15 m thick and had parameter values of  $\sigma = 20 \text{ kN s m}^{-4}$ ,  $\Omega = 0.7$ ,  $s_f = 0.8$  and  $n' = 0.5$ . The underlying material had values of  $\sigma = 366 \text{ kN s m}^{-4}$ ,  $\Omega = 0.269$ ,  $s_f = 0.725$  and  $n' = 0.5$ . The short-dashed lines are waveforms calculated using the Delaney and Bazley (1970) model for two layers with  $\sigma = 20$  and  $366 \text{ kN s m}^{-4}$  and a layer thickness of 0.15 m. For the calculated waveforms, the source pulse shown in Figure 39 was used, and the spectrum is limited to 500 Hz.

parameter model in a trial and error forward modeling process, and found that a value of  $\sigma = 200 \pm 50 \text{ kN s m}^{-4}$  gave good agreement with the observed pulse waveforms. The calculated waveforms are shown as dashed lines in Figure 42.

Typical waveforms observed in the winter by microphones at the snow surface are shown as solid lines in Figure 43. These recordings were made at the same locations as the summer measurements and were obtained over a 130-minute period. The waveforms are markedly different from those observed in the summer, but show some of the same properties of the waveforms calculated with  $\sigma = 10 \text{ kN s m}^{-4}$  that were displayed in Figure 41: the high-frequency portion of the pulse is severely attenuated, and the lower frequencies become increasingly dominant as the propagation range increases. The complicated

high-frequency pulse shapes near the beginning of the waveforms in Figure 43 are ascribable to reflections from within the snowpack.

Modeling of these waveforms was unsuccessful without the addition of a hard layer beneath the snow. In fact, the best match with an unlayered ground was achieved by the waveforms shown in Figure 41. Nicolas et al. (1985) found that they required a layered ground to fit their measurements of excess attenuation over snow at much shorter ranges and at higher frequencies. I also achieved much better results when the ground was modeled as a layer over a half space.

The short-dashed line in Figure 43 shows the best waveform match achieved using the single-parameter model with a hard subsurface layer. The upper and lower effective flow resistivities were 20 and 366 kN

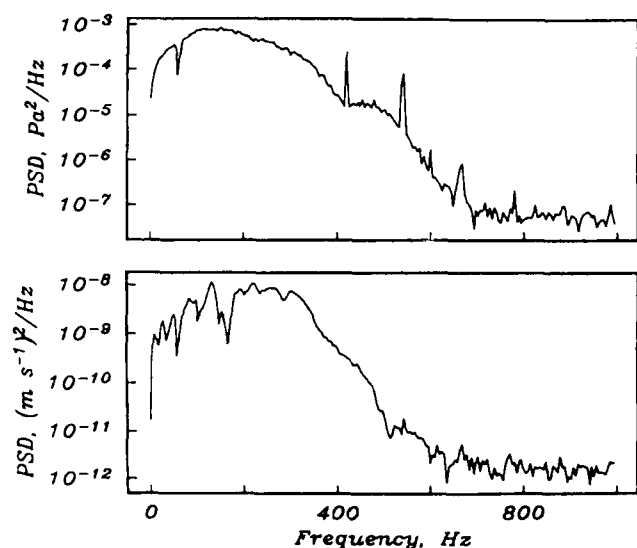


Figure 44. Power spectral density (PSD) as a function of frequency for a surface microphone (top) and a surface vertical component geophone (bottom) in the summer. The source was a blank pistol shot 1 m above the ground and 196 m away from the sensors.

$\text{s m}^{-4}$ , respectively, and the layer thickness was 0.15 m. The surface effective flow resistivity was determined by matching the decay of the high-frequency pulses and the layer thickness by matching the elongation of the waveform. Estimated errors are  $10 \text{ kN s m}^{-4}$  for the effective flow resistivity and 0.05 m for the layer thickness. Slightly better results were achieved using the four-parameter model with the same effective flow resistivities (the long-dashed lines in Figure 43). The assumed porosities and pore shape factor ratios were  $\Omega = 0.7$  and  $s_f = 0.8$  for the snow, and  $\Omega = 0.269$  and  $s_f = 0.725$  for the hard, underlying soil (Attenborough 1985, Attenborough and Buser 1988). The overall elongated shape of the waveform and its relative amplitude in comparison to the higher frequency pulses match the observed data slightly better than the results using the single-parameter model. For both models, the snow layer thickness of 0.15 m was less than the thickness of 0.25 m directly beneath the microphone, but close to the average thickness of 0.19 m along the propagation path. Calculated waveforms using the low-frequency approximation (eq 20 and 21) were identical to the waveforms for the four-parameter model and have been omitted from the plot.

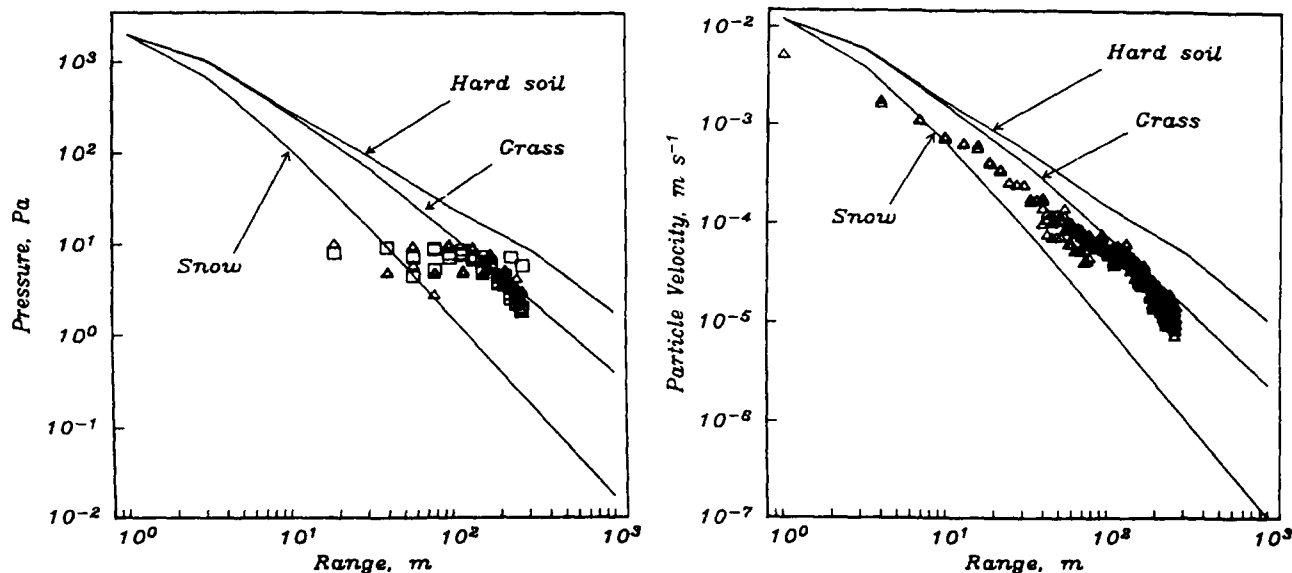
The data presented here have shown that propagation over an absorptive ground like snow can greatly modify pulse waveforms by attenuating the higher frequencies. My calculations show that any of

the three models can be used to determine waveforms that agree satisfactorily with the observed changes.

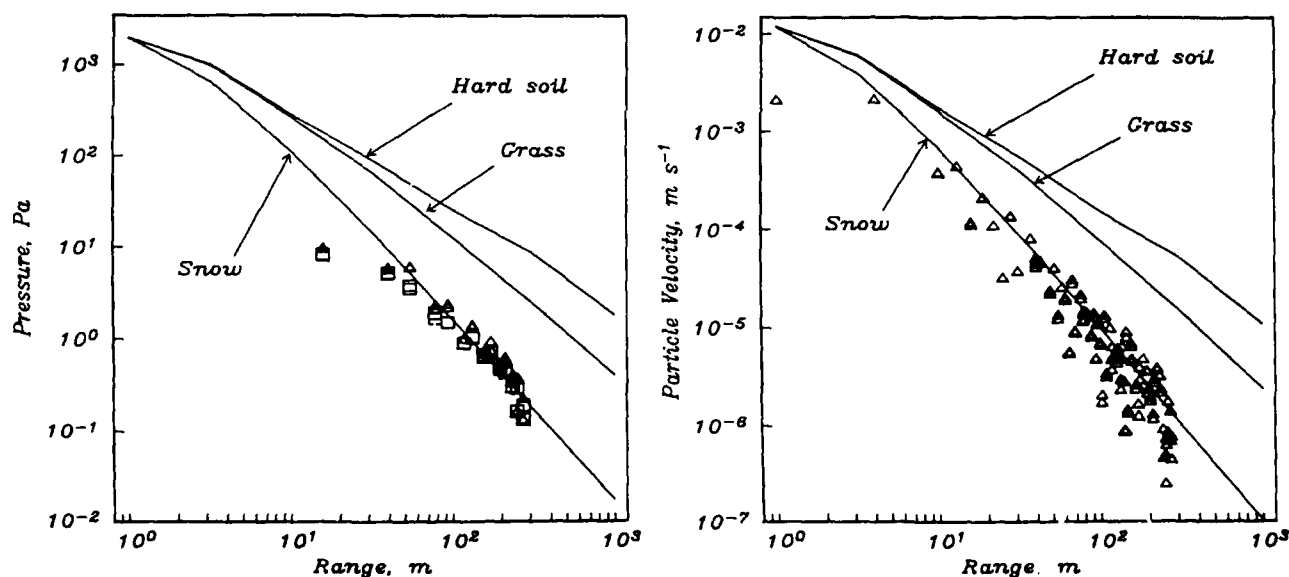
*Amplitude decay rate comparisons.* Along with waveform comparisons, the observed pulse amplitude decay as a function of propagation distance can also be compared with the calculated values. The most direct way of comparing the decay rates is to use the microphone observations; however, as mentioned before, many of the amplitudes on the microphone recordings, especially at the shorter propagation ranges and in the summer, exceeded the dynamic range of the microphones and were thus unreliable. The geophones do not have the same problems and the larger number used provides a better estimate of the amplitude decay. The geophones respond to the direct air pulse that propagates in the atmosphere and is locally coupled into the ground. I used my estimated source amplitude of 2 kPa at 1 m and the measured (Albert and Orcutt 1989) acoustic-to-seismic coupling ratio of  $6 \times 10^{-6} \text{ m s}^{-1} \text{ Pa}^{-1}$  (the ratios were nearly the same for grassland and snow) to convert the calculated pressure amplitudes to particle velocity for comparison with the geophone measurements.

Figure 44 shows that the frequency response curves for a microphone and a geophone at the ground surface are very similar. These curves were obtained using a pistol shot 196 m away where the microphone responds without clipping; the recording was made in the summer. The microphone and geophone curves have about the same bandwidth. The dip caused by a 60-Hz notch filter used during the recording is visible in the microphone curve, as well as two noise peaks at about 420 and 540 Hz. The notch filter dip is also visible in the geophone response curve, and the low-frequency portion of the curve (below 200 Hz) is much less smooth than for the microphone. Some of the roughness in the geophone spectrum is probably caused by the subsurface layering (Sabatier et al. 1986a). The pulse amplitudes are controlled by the integral over these response curves and will not be greatly affected by these differences.

Comparisons of observed and calculated pulse amplitudes as a function of propagation distance are presented in Figure 45, where the symbols are observed measurements and the lines are calculated decay rates. The lines labeled hard soil and grass were calculated using the single-parameter model (Delaney and Bazley 1970), with effective flow resistivity values of 1820 and  $200 \text{ kN s m}^{-4}$  respectively (Attenborough 1985, Chessell 1977, Embleton et al. 1983).



a. Over grassland. Triangles denote amplitudes measured using receivers on the surface; squares are amplitudes measured using microphones 0.5 m high.



b. Over snow. Triangles denote amplitudes measured using receivers at the snow surface; squares are amplitudes from microphones 0.5 m above the snow.

Figure 45. Plot of first arrival amplitude vs distance from the source for pulse propagation. (Right) Peak amplitudes from microphones; (left) peak amplitudes from vertical component geophones. The lines are amplitudes calculated using the Delaney and Bazley (1970) model with effective flow resistivities of 1820 (hard soil) and 200  $\text{kN s m}$  (grass). The line for snow was calculated using Attenborough's (1985) model and the parameters listed in the caption for Figure 43. The flat trend in the microphone amplitudes at the shorter ranges is the result of exceeding the dynamic range of the microphones (see text).

The line labeled snow was calculated using the four-parameter model (Attenborough 1985) that used the parameter values given in the caption to Figure 43. At this lower effective flow resistivity, care was taken to use the amplitude of the high-frequency pulse, not the low-frequency portion of the waveforms, as this is how the observed data are plotted.

Figure 45a shows the observed amplitudes in the summer, when 92 measurements were made with microphones, and 320 with vertical component geophones. The plot shows that the microphone data are clipped until the propagation range exceeds 100 m; then the amplitudes match those calculated for grass quite well. The geophone observations are slightly lower than those calculated for grass, but decay at about the same rate. Considering all of the assumptions used to make these comparisons, the agreement is acceptable.

Figure 45b compares the observed amplitudes in the winter with the calculated amplitudes. Only a few of the 56 microphone amplitudes, those for ranges less than 40 m, may be clipped. The observations agree with the absolute amplitudes and with the decay rate calculated for snow. For the geophones, the agreement between the 126 observations and the calculated values is also very good.

#### Summary

Calculations have been used to investigate the effects of ground absorption on waveforms and amplitude decay for acoustic pulses. Hard grounds with high effective flow resistivities ( $\sim 32,000 \text{ kN s m}^{-4}$ ) are good reflectors and absorb very little energy; consequently, in the absence of air absorption there is little change in the predicted waveforms for ranges up to 3 km. As the effective flow resistivity decreases ( $\sim 200 \text{ kN s m}^{-4}$ ), absorption by the ground increases, and the pulse amplitudes decay faster as a function of range. At still lower effective flow resistivities ( $10\text{--}20 \text{ kN s m}^{-4}$ ), increased absorption and a change in the image source magnitude cause marked changes in waveforms, with the low frequencies dominating. A layered ground must then be used to correctly model the waveforms. Satisfactory agreement can be obtained between observed and calculated acoustic pulse waveforms and peak amplitude decay rates for two quite different ground surfaces, grassland and snow. The Delaney and Bazley (1970) model and Attenborough's (1985) model, and its low-frequency approximation, all give good agreement with observations.

The measurements, along with the calculated waveforms and amplitude decay rates, illustrate the silencing effect that a strongly absorbing snow layer

has. The sound of the pistol shots was noticeably muffled to our ears during the winter experiments, and such quieting of sound levels is commonly observed when a snow layer is present. Since we have confirmed that both models can correctly account for these effects, they can be used with confidence in predicting acoustic pulse propagation over different ground conditions.

## MODELING OF ACOUSTICALLY INDUCED GROUND MOTION

A computer model of the process of coupling of acoustic waves into the Earth was developed that allows synthetic seismograms to be calculated for a set of assumed geological parameters, using a technique known as wavenumber integration. The resultant synthetic seismograms include the body waves and the surface waves that are observed experimentally. Representative synthetic seismograms show that the physical properties of the upper few meters of the Earth control the waveform's appearance. The method of calculating synthetic seismograms is discussed in the next subsection, followed by example calculations and comparisons with experimental data.

#### Computation of induced ground motion

The wavenumber integration method (Apsel 1979, Kennett 1983) has been adapted to allow the ground motion produced by sources in the atmosphere to be calculated numerically from the (assumed known) velocities and densities of the air and soil layers. Such a calculation is a solution to the *forward* problem. The *inverse* problem is the computation of the physical parameters, i.e., the seismic velocities and densities as a function of depth, directly from the observed seismograms, a procedure that is tractable only in a few very simple cases. In this section, synthetic seismograms are computed for a model of the Earth composed of plane, horizontal and viscoelastic layers (Fig. 46), but with an atmospheric half space at the top of the model replacing the free surface boundary condition normally used in seismic computations. Sources and receivers can be placed at any depth or range within the model layers.

The advantages of the wavenumber integration method are that 1) it produces complete seismograms, including all body waves, surface waves, interface waves, multiple reflections, refractions and interconversions; 2) it includes the effect of material attenuation (i.e., viscoelastic layers rather than the perfectly elastic layers required in many other methods); and



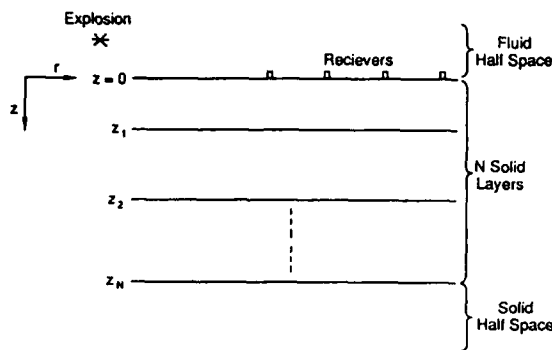


Figure 46. Model of the Earth used for the synthetic seismogram calculations. A halfspace of air containing an explosion source is underlain by 0 to N horizontal viscoelastic solid layers and a viscoelastic solid half space. Displacements are calculated for receivers on the air/solid interface.

3) it is numerically stable at all frequencies and wavenumbers. The main disadvantages of the method are that 1) it is limited to plane, horizontal layers rather than the more complicated geometry often encountered in the real Earth, and 2) it is an expensive code to run because of the completeness and complexity of the calculations.

The procedure for obtaining synthetic seismograms starts with the linear wave equation, expressed in the cylindrical coordinate system  $(r, \phi, z)$ . By applying a temporal and two spatial transforms, this partial differential equation is converted into a set of coupled ordinary differential equations of the form (Kennett 1983)

$$d_z \underline{B}(k, \ell, z, \omega) = \underline{A}(k, z) \times \underline{B}(k, \ell, z, \omega) + \underline{C}(k, \ell, z, \omega) \quad (28)$$

Here,  $\underline{B}$  is the stress-displacement vector,  $\underline{A}$  a matrix of material properties, and  $\underline{C}$  a vector containing source terms. The transformed variables are the wavenumber  $k$ , angular order  $\ell$  and frequency  $\omega$ . The displacement is represented as a sum of orthogonal vector cylindrical harmonics (see Kennett 1983, p. 35). The solutions to these coupled ordinary differential equations are determined in the transformed domain by applying the relevant boundary and radiation conditions.

Let  $u_i^k$  represent the  $i^{\text{th}}$  component of displacement in the  $k^{\text{th}}$  layer, and represent the components of the stress tensor by  $\sigma_{ij}^k$ , the  $j^{\text{th}}$  component of the traction acting across a plane normal to the  $i^{\text{th}}$  direction in the  $k^{\text{th}}$  layer. Then, to derive the boundary conditions, it is assumed that no slip is allowed be-

tween solid media and that cavitation does not occur in fluid media. With these assumptions, the boundary conditions are:

1. Displacement components are continuous across solid/solid interfaces:

$$u_i^k = u_i^{k+1}, \quad i = r, \theta, z.$$

2. The normal displacement component is continuous across the fluid/solid interface:

$$u_z^1 = u_z^2.$$

3. Stress components are continuous across solid/solid interfaces:  $\sigma_{zi}^k = \sigma_{zi}^{k+1}$ .

4. The normal component of stress is continuous and the tangential components are zero across the fluid/solid interface:

$$-p^1 = \sigma_{zz}^2, \quad 0 = \sigma_{zr}^2, \quad 0 = \sigma_{z\theta}^2.$$

In addition, a radiation condition is imposed to ensure that there are no up-going waves below any sources in the lower half space. These boundary conditions are standard for elastic materials, but they ignore any pores in the solids, an assumption that is not justified when snow is present and leads to poor performance of the model in this case, as will be shown below.

At the surface, the usual boundary condition in seismology is that of a free surface, i.e., that the stress is zero there. To allow for sources in the atmosphere, the free surface has been replaced with a fluid/solid interface with the above boundary conditions and a radiation condition that there are no down-going waves above any sources in the air. Although this is a simple change conceptually, the modifications needed to the code were quite lengthy and tedious.

To solve for the ground motion produced by a source, generalized reflection and transmission coefficients are determined by recursive application of the boundary conditions for all of the interfaces in the model. These coefficients are used to determine the plane wave response of the model for all frequencies and wavenumbers of interest. Application of the inverse transforms then recovers the time-domain displacement,  $u$

$$u(r, \phi, z, t) = \frac{1}{2\pi} \int_{-\infty}^{\infty} d\omega e^{-i\omega t} \int_{-\infty}^{\infty} dk \sum_{\ell} (C_1^{\ell} R_k^{\ell} + C_2^{\ell} S_k^{\ell} + C_3^{\ell} T_k^{\ell}) \quad (29)$$

where  $R$ ,  $S$  and  $T$  are the vector cylindrical harmonics (dependent only on  $r$  and  $\phi$ ), and  $C_1$ ,  $C_2$  and  $C_3$  are the coefficients of these harmonics determined by the recursive process (dependent only upon  $\ell$  and  $z$ ). For simple sources such as explosions or point forces, the sum over angular order  $\ell$  is usually reduced to one or two terms. The integral over  $k$  is done first (thus the name, wavenumber integration) using a numerical method developed by Apsel (1979), and the integral over  $\omega$  is then carried out using the Fast Fourier Transform (FFT) algorithm. The computer program itself consists of about 6000 lines of Fortran code.

### Synthetic seismograms for simple Earth models

By use of the above method, synthetic seismograms have been calculated for a series of assumed input parameters, or models, of the Earth's structure. The physical properties of the model layers are given in Tables 9 through 11.

For each layer in the model, the thickness, density,  $P$ - and  $S$ -wave velocities, and attenuation were specified. The attenuation for both the  $P$  and  $S$  waves was given in terms of the dimensionless quality factor  $Q$  that is commonly used in seismology.  $Q$  can be defined (for  $Q \gg 1$ ) by the equation  $Q = (\pi f / \alpha V)$ , where  $f$  is the frequency,  $V$  is the wave velocity, and  $\alpha$  is the spatial attenuation coefficient given (for plane waves) by  $A(x) = A_0 e^{-\alpha x}$  (Aki and Richards 1980, Johnson and Toksoz 1981). From these definitions, a constant value of  $Q$  implies that  $\alpha$  is a linear function of frequency. As the attenuation increases,  $\alpha$  increases but  $Q$  decreases.

For each input model, the vertical and horizontal displacements at the ground surface resulting from

an explosion 1 m above the air/ground interface were calculated at 10 ranges between 20 and 200 m. After the wavenumber integration, a cosine squared taper was applied to the high frequencies to avoid aliasing effects before transforming back to the time domain. The frequency spacing  $\Delta f$  was determined by convergence tests. Then, the number of frequencies  $N$  was selected so that the time duration  $T = 1/(N \Delta f)$  of the seismograms was long enough to include all of the wave arrivals at the longest propagation range and avoid "wrap-around" problems.

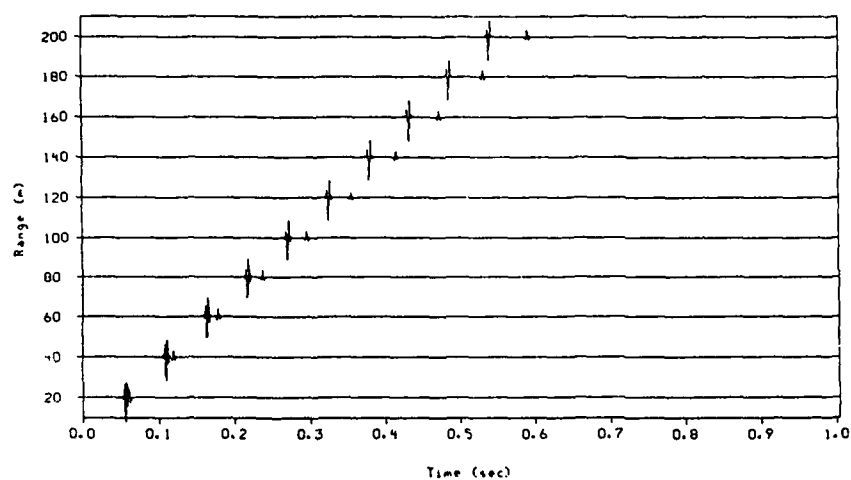
### Half space models

The simplest calculations are for models consisting of two half spaces, with air above and an elastic solid below. Three arrivals are expected at a receiver on the surface: a direct wave (traveling through the air; this arrival is referred to as the air wave), a compressional ( $P$ ) wave, and a shear ( $S$ ) wave; these last two waves travel mostly in the solid after transmission from the air directly below the source. A Rayleigh wave is also expected, but is nearly indistinguishable from the  $S$  wave in the examples presented below.

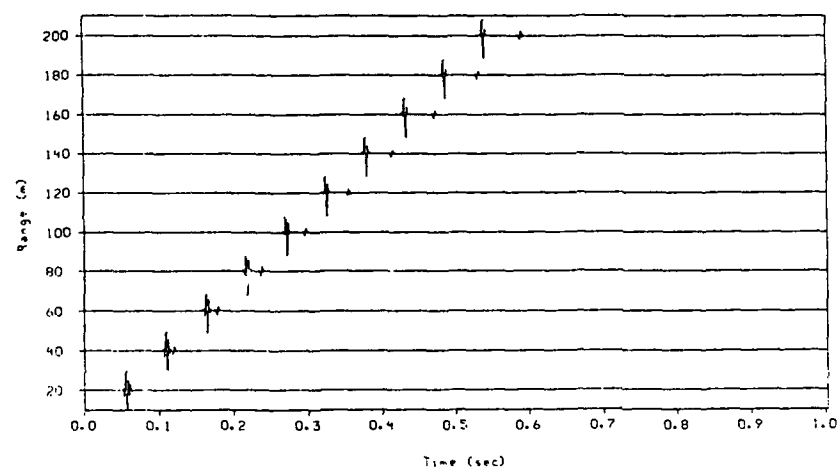
The first model synthetics to be presented are for a "hard" surface, where both the  $P$ - and  $S$ -wave velocities in the solid are higher than the speed of sound in air; this case is denoted by  $V_p > V_s > c$  (half space model 1 in Table 9). This situation corresponds to materials like frozen soil, caliche or concrete. The synthetic seismograms, calculated for 512 frequencies with  $\Delta f = 1$  Hz and a cosine squared taper from 256 to 512 Hz, are shown in Figure 47. Two waves are visible in these normalized plots: the first and largest arrival at each location is the shear-Rayleigh wave and it is followed by the air wave, which is 25% as

Table 9. Physical properties of the half space models.

Layer	$V_p$ ( $m s^{-1}$ )	$V_s$ ( $m s^{-1}$ )	$\rho$ ( $Mg m^{-3}$ )	Thickness (m)	$Q_p$	$Q_s$
<i>Half space model 1</i>						
1	340	0	0.001225	$\infty$	$1 \times 10^4$	
2	800	400	1.8	$\infty$	750	300
<i>Half space model 2</i>						
1	340	0	0.001225	$\infty$	$1 \times 10^4$	
2	400	160	1.8	$\infty$	750	300
<i>Half space model 3</i>						
1	340	0	0.001225	$\infty$	$1 \times 10^4$	
2	200	60	1.8	$\infty$	750	300



a. Vertical component.

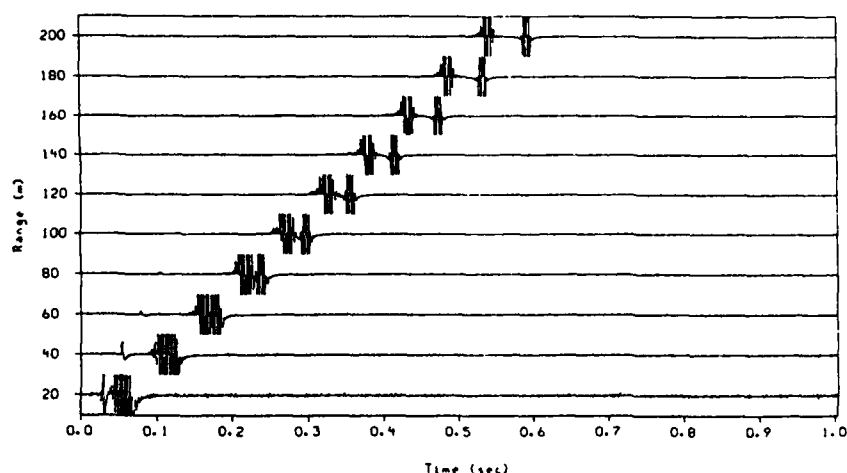


b. Horizontal component.

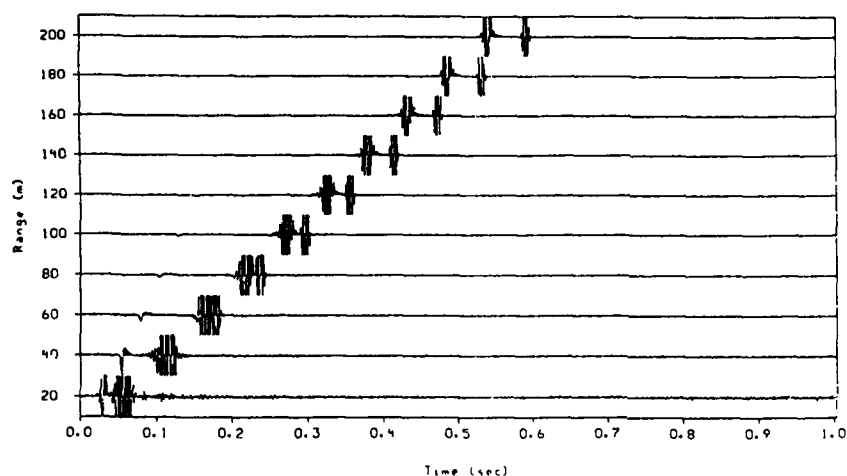
Figure 47. Synthetic seismograms for air over a solid half space with  $V_p > V_s > c$ . Displacements at the air/ground interface are shown between 20 and 200 m from an explosion source 1 m high in the air. Each individual trace is normalized to have the same maximum displacement as all of the others. Table 9 gives the material parameters of this model, half space model 1. The largest amplitude arrival is a shear-Rayleigh wave, and it is followed by the air wave.

Table 10. Physical properties of the single layered models.

Layer	$V_p$ ( $m s^{-1}$ )	$V_s$ ( $m s^{-1}$ )	$\rho$ ( $Mg m^{-3}$ )	Thickness (m)	$Q_p$	$Q_s$
Single layered model 1						
1	340	0	0.001225	$\infty$	$1 \times 10^4$	
2	400	160	1.8	1.0	75	30
3	1700	360	1.8	$\infty$	750	300
Single layered model 2						
1	340	0	0.001225	$\infty$	$1 \times 10^4$	
2	200	60	1.8	1.0	75	30
3	1700	360	1.8	$\infty$	750	300



a. Vertical component.



b. Horizontal component.

Figure 48. Same seismograms as in Figure 47, plotted at a constant (and large) gain. The shear-Rayleigh wave and the air wave are both clipped, and an earlier arriving P wave is visible on some of the traces close to the source.

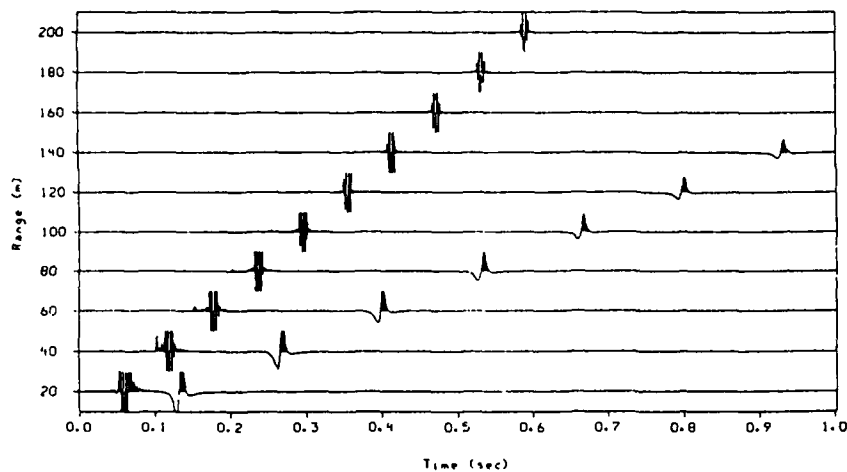
large. Only with a tremendous increase in the gain of the plot (Fig. 48) does the P wave become visible as the earliest arrival, and it still dies out before reaching the receiver at 200 m.

The next calculation is for the case  $V_p > c > V_s$  (half space model 2 in Table 9), a situation that occurs for some "hard" soils (Fig. 49). Because of the lower S-wave velocity, the time window had to be increased, so for these calculations  $N = 1024$ . The air wave is now the largest arrival (Fig. 49), followed by the smaller S wave, and preceded by the very small P wave. In Figure 50, seismograms for the "soft" soil case  $c > V_p > V_s$  (half space model 2 in Table 9) are plotted. These calculations required 2048 frequency points, and the S wave appears only on the first few traces because of the time scale used on the plot. Again the air wave is the largest arrival, followed by the S

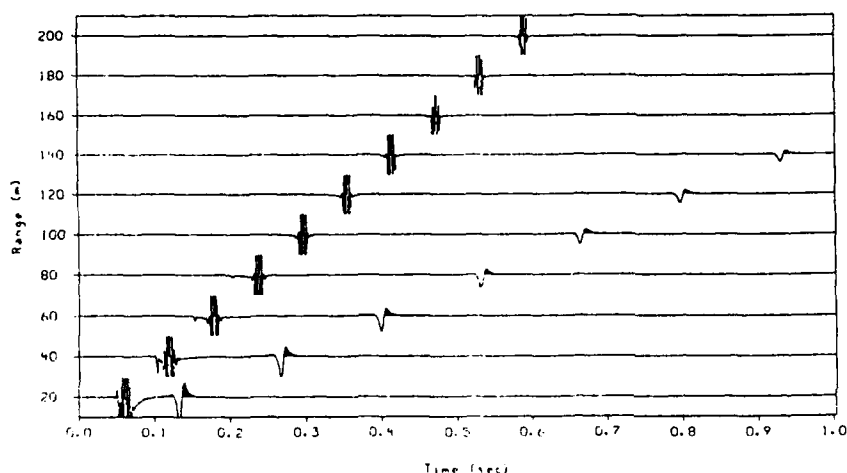
wave. A P wave does arrive shortly after the air wave, but is too small to be visible on these plots.

#### Effect of viscoelastic attenuation in the ground

The above calculations were done with nominal material attenuation ( $Q_p = 750$ ,  $Q_s = 300$ , typical values for crustal rocks) so that all of the wave arrivals could be seen. The calculations were repeated with other attenuation values, and the effect of increasing the attenuation for the case  $V_p > V_s > c$  (velocity parameters the same as half space model 1 of Table 9) can be seen in Figure 51. As the attenuation increases (i.e.,  $Q$  decreases from  $Q_p = 750$ ,  $Q_s = 300$  to  $Q_p = 75$ ,  $Q_s = 30$ ), the air wave becomes the largest arrival (about seven times larger than the S wave at 100 m distance); the S-wave amplitude decreases markedly (by about a factor of 35 at 100 m), and the P-wave



a. Vertical component.



b. Horizontal component.

Figure 49. Displacements for halfspace model 2, consisting of air over a solid halfspace with  $V_p > c > V_s$  (Table 9). Same gain as for Figure 48. A small P wave is barely visible on some close traces as the first arrival. The large air wave is next, followed by the slower shear-Rayleigh wave.

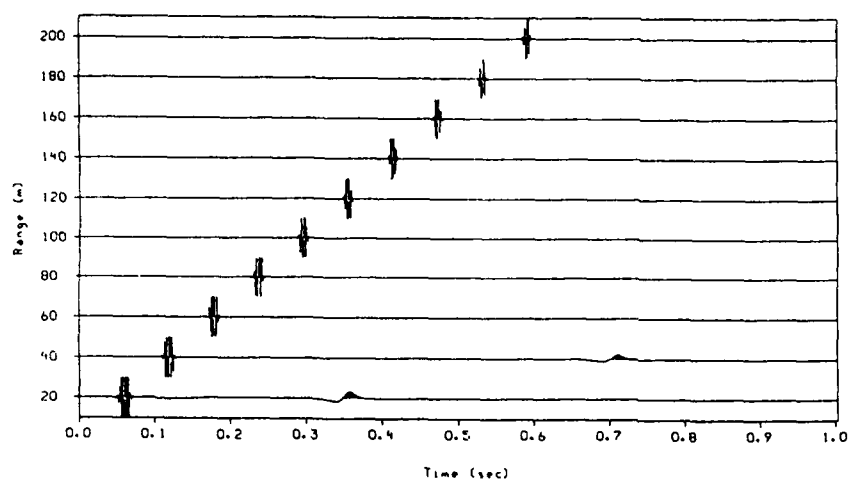
amplitude decreases by about a factor of 2. With a further increase in attenuation by decreasing  $Q_p$  to 7.5 and  $Q_s$  to 3 (an extremely lossy material), the P wave shows an additional factor of 2 decrease and the S wave disappears. It is important to note that the air wave amplitude decreases only slightly as the attenuation parameters of the elastic solid increase. The same attenuation effects occur for the other models.

#### Single layered models

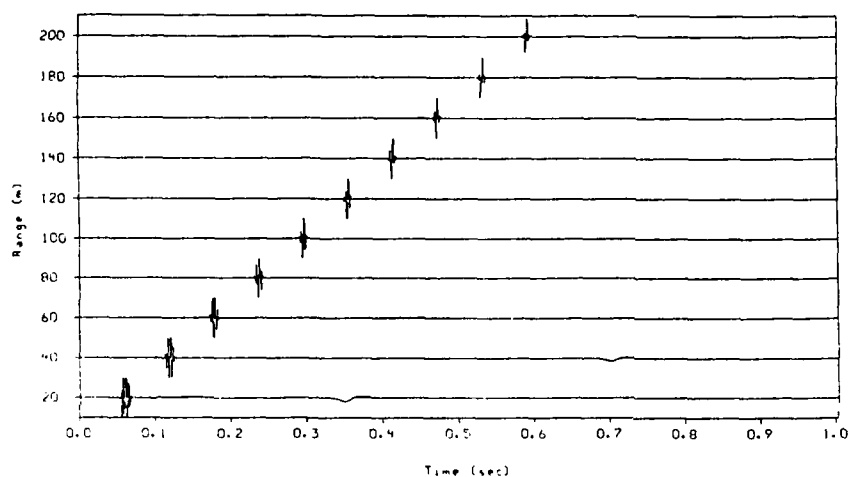
Although there are a few locations where half space models may be appropriate, most grounds consist of layered soils. Introducing even a single layer in the model increases the complexity of the ground response since the additional boundary allows upward traveling waves to exist: reflections, multiples and

dispersed surface waves now appear as a result of the additional interface. To investigate the effect of this layer, calculations were done for a series of models with a half space of air above a finite-thickness soil layer, which is underlain by a soil half space. The input parameters for these models are listed in Table 10.

For all of the single layered models, the substrate material has P- and S-wave velocities of 1700 and 360 m s<sup>-1</sup>, respectively, with  $Q_p = 75$  and  $Q_s = 30$ . These velocities are typical of the water table, where the soil becomes saturated. (Note that the usual calculation of Poisson's ratio from these velocities would be erroneous, since the saturated soil is a porous material, and the P-wave velocity is greatly increased by the presence of water in the soil's pores.) Again, the calculations were done for a bandwidth of 512



a. Vertical component.



b. Horizontal component.

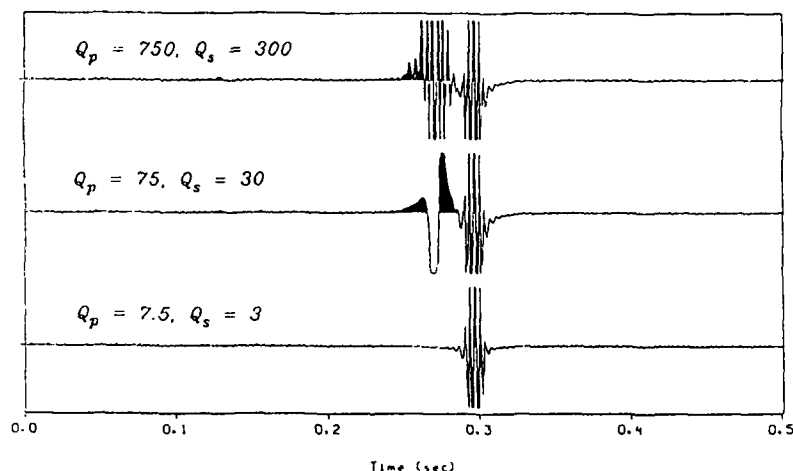
Figure 50. Displacements calculated for half space model 3, consisting of air over a solid half space with  $c > V_p > V_s$ . See Table 9 for material parameters. Same gain as for Figure 48. The large, clipped first arrival is the air wave. A slow shear-Rayleigh wave is visible on the first two traces; it arrives too late to be seen farther from the source. A small P wave is visible arriving after the air wave only on the trace at 20 m range.

Hz, with a cosine-squared low pass filter applied from 256 to 512 Hz. For these models, 2048 frequencies at a spacing of  $\Delta f = 0.25$  Hz were required.

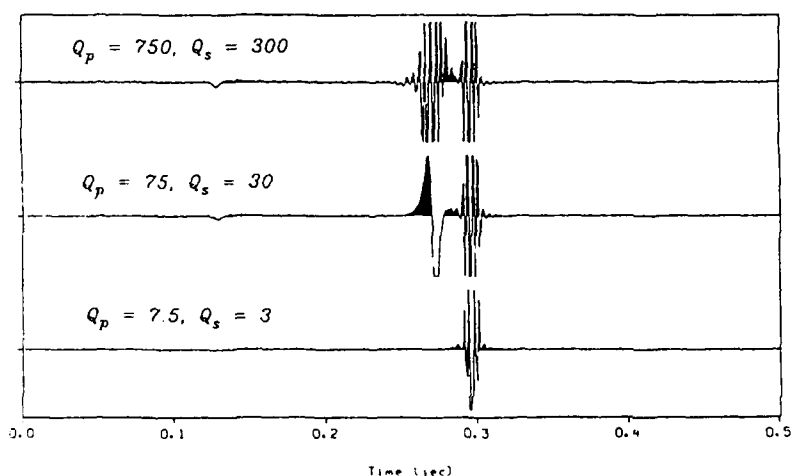
Figure 52 shows the effect of adding a single, low-velocity layer on the computed ground motion at a propagation distance of 100 m. The top traces are a repeat of the half space model 2 seismogram for the "fast soil" velocities (400 and 160 m s<sup>-1</sup> for the P and S waves); these traces are followed by seismograms for a 1-m-thick layer with the "fast soil" and the "slow soil" (200 and 60 m s<sup>-1</sup>) velocities underlain by the water table. The input parameters for these calculations are listed as single layered models 1 and 2, respectively, in Table 10. From Figure 52, the air wave is the largest arrival for all of the traces, as expected. For the models with a layer, the air wave arrival

shows more structure than for the half space model. The first portion of the air wave is identical in shape with the half space model; this is the direct wave (the blast noise). Immediately following are reflections and multiple reflections from within the single layer. From the time interval between the multiples, these arrivals are identified as shear waves traveling within the fast soil layer and compressional waves in the slow soil layer.

The response for the "fast soil" layer also includes a low-frequency wave train following the multiple reflections. These arrivals have the general appearance and 90° phase difference between the horizontal and vertical components that characterizes them as air-coupled Rayleigh waves with retrograde elliptical particle motion. This dispersed wave train does



a. Vertical component.



b. Horizontal component.

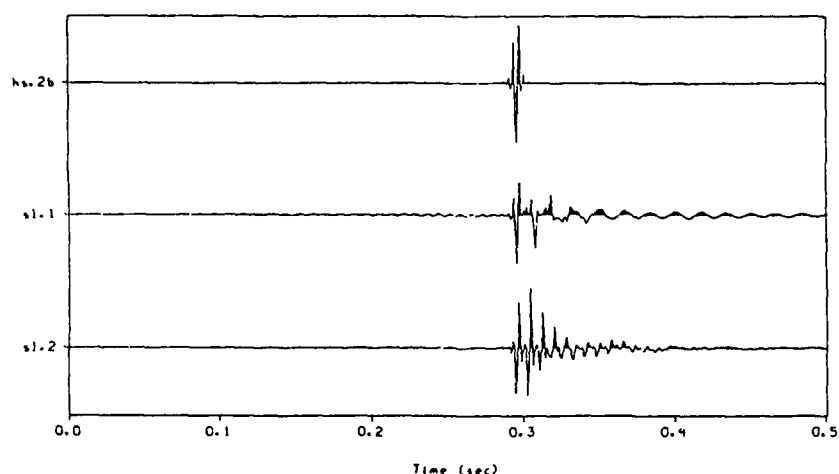
Figure 51. Comparison of the effect of increasing attenuation in the solid. Displacements at a range of 100 m. Except for the attenuation, the parameters for the three models are the same as for half space model 1 in Table 9 ( $V_p > V_s > c$ ). Attenuation parameters are  $Q_p = 750$ ,  $Q_s = 300$  (top trace), 75 and 30 (center trace) and 7.5 and 3 (bottom trace). All of the traces are plotted at the same gain level.

not appear on the "slow soil" layered model, because the layer is effectively a half space at the computed wavelengths, and Rayleigh waves are not dispersive on a half space. For example, the wavelengths of the shear wave at 100 Hz are 4 m for the "fast" soil model and 0.6 m for the "slow" soil model, so there are 0.25 and 1.7 vertical wavelengths in the 1-m-thick layer used in these calculations.

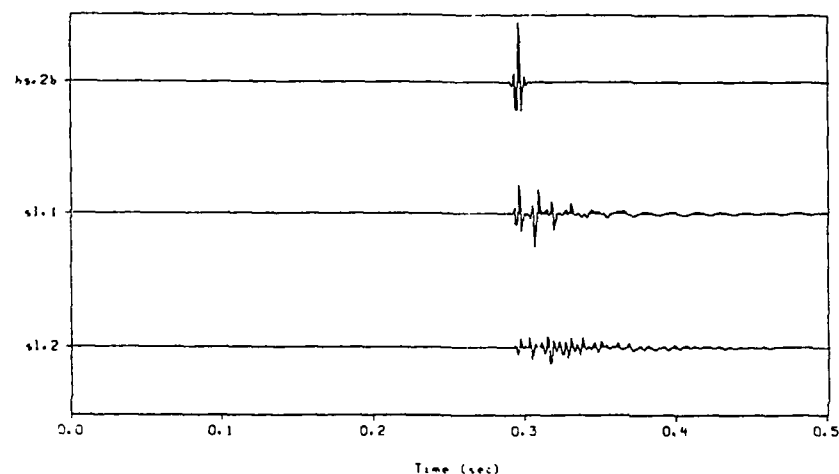
Figures 52c and d, at high gain, show that the first arrivals for both layered models occur before 0.1 second, implying a group velocity greater than 1 km  $s^{-1}$ , and thus these early arrivals must have traveled at least some of the way as  $P$  waves in the subsurface water table. A long series of multiple reflected and refracted waves are visible behind the first arrival. This wave train is identified as a leaky mode or  $PL$  wave.

To summarize, these comparisons show that the introduction of a single layer into the Earth model causes a marked change in the waveforms of all of the arrivals that can be explained by the existence of multiple reflections and refractions within the layer. A very early  $P$  wave refracted from the substrate appears, followed by a lengthy leaky mode. In some cases, depending on the layer thickness and velocities, a low-frequency air-coupled Rayleigh wave also appears.

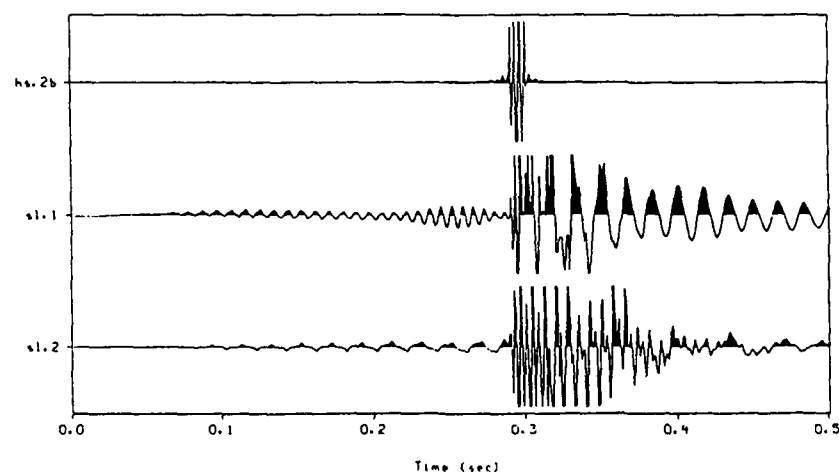
The effect of viscoelastic attenuation in the soil layer is shown by the seismograms in Figure 53. For these traces, the response of a 1-m-thick "slow soil" layer with  $P$ - and  $S$ -wave velocities of 200 and 60 m  $s^{-1}$  was calculated as  $Q_p$  dropped from 75 to 30 to 7.5 and  $Q_s$  dropped from 30 to 10 to 3. As the attenuation increases, the duration of the multiples follow-



a. Vertical displacement at the surface, plotted at a constant gain.



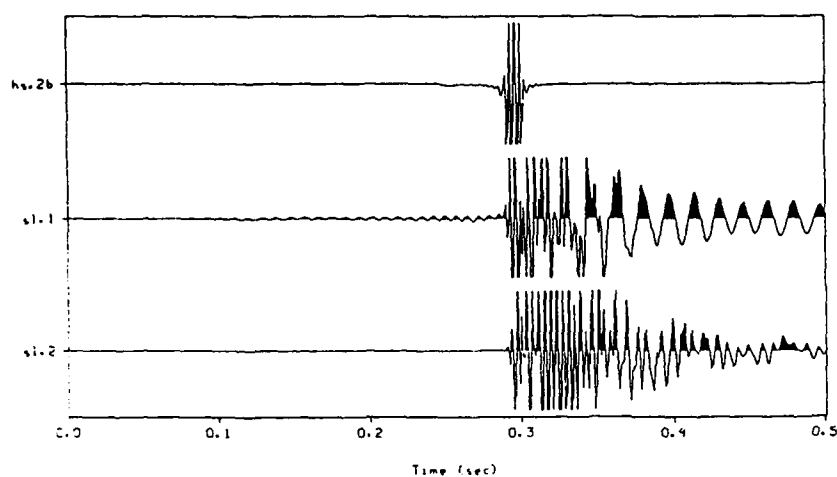
b. Horizontal displacement at the surface.



c. Vertical displacement at the surface, with the gain increased to reveal the early arrivals.

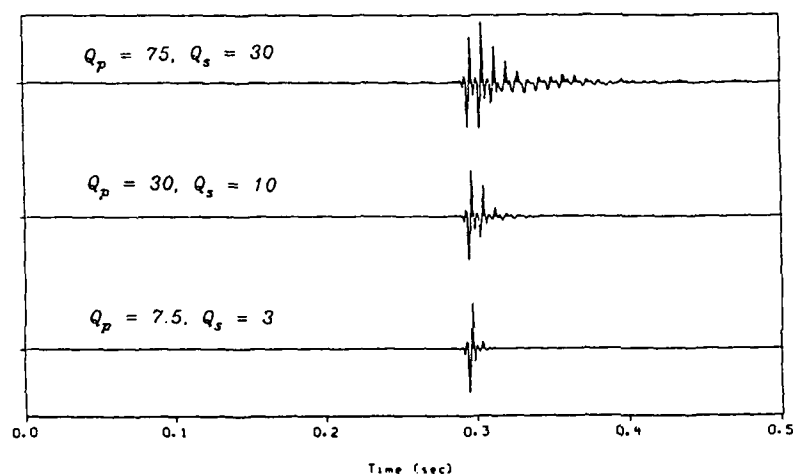
Figure 52. Calculated response of models with a single soil layer over a half space to an explosion in the air, 1 m above the ground surface. The top traces are for a half space with  $V_p > c > V_s$  (same parameters as for half space model 2 in Table 9 except that  $Q_p = 75$ ,  $Q_s = 30$ ); the center traces are for single layered model 1 of Table 10, consisting of a 1-m-thick layer identical to the top trace underlain with a half space having properties similar to a water table; and the bottom traces are for a 1-m-thick layer with  $c > V_p > V_s$  over a water table (single layered model 2 of Table 10).



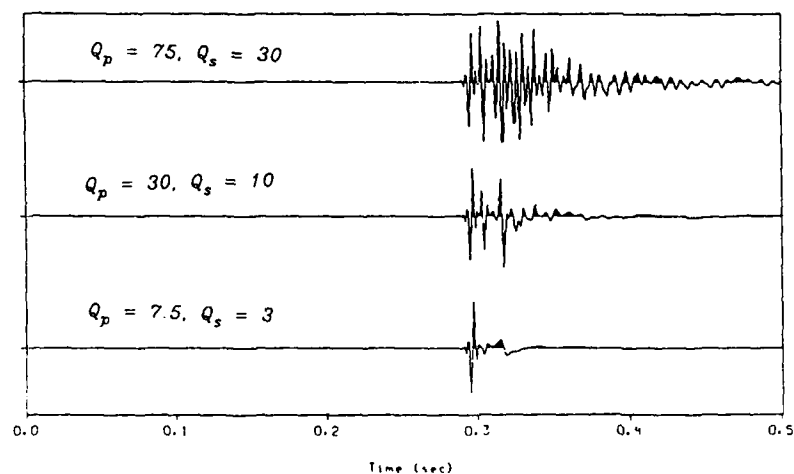


*d. Horizontal displacement at the surface, with the gain increased to reveal the early arrivals.*

*Figure 52 (cont'd).*

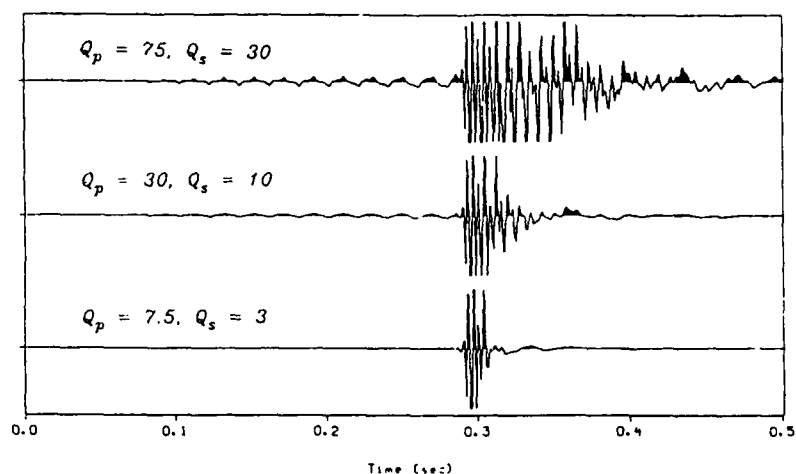


*a. Vertical displacement at the surface plotted at a constant gain.*

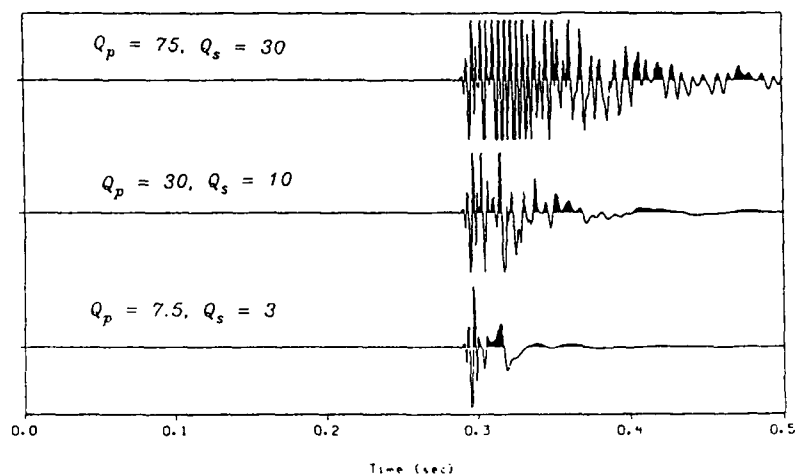


*b. Horizontal displacement at the surface.*

*Figure 53. Calculated effect of ground attenuation for a single layer over a half space, with  $c > V_p > V_s$  and a layer thickness of 1 m. Top traces are for solid layer and half space  $Q_p = 75$ ,  $Q_s = 30$  (single layered model 2 in Table 10); center traces are for  $Q_p = 30$ ,  $Q_s = 10$ , and bottom traces for  $Q_p = 7.5$ ,  $Q_s = 3$ .*

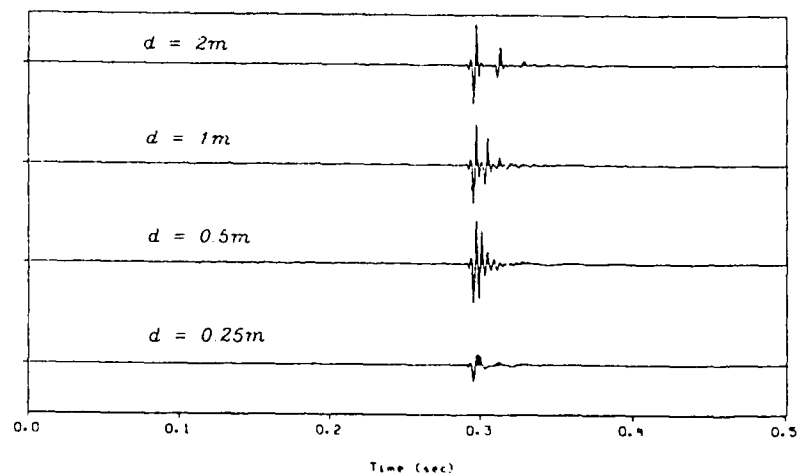


c. Vertical displacements plotted with the gain increased.



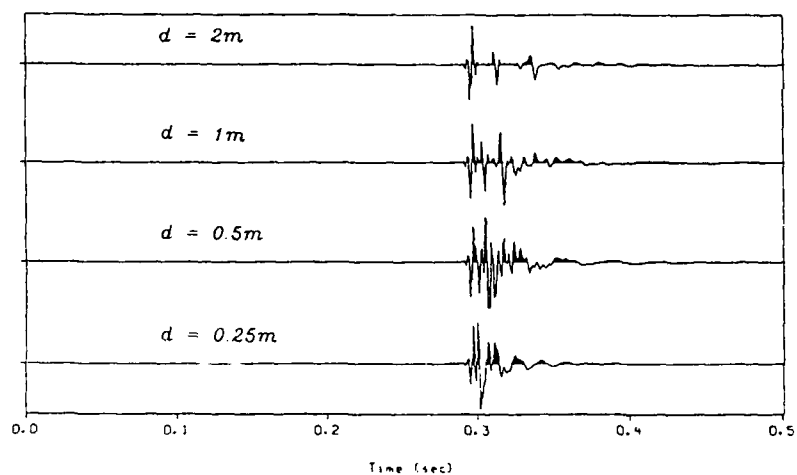
d. Horizontal displacements plotted with the gain increased.

Figure 53 (cont'd). Calculated effect of ground attenuation for a single layer over a half space, with  $c > V_p > V_s$  and a layer thickness of 1 m. Top traces are for solid layer and half space  $Q_p = 75$ ,  $Q_s = 30$  (single layered model 2 in Table 10); center traces are for  $Q_p = 30$ ,  $Q_s = 10$ , and bottom traces for  $Q_p = 7.5$ ,  $Q_s = 3$ .

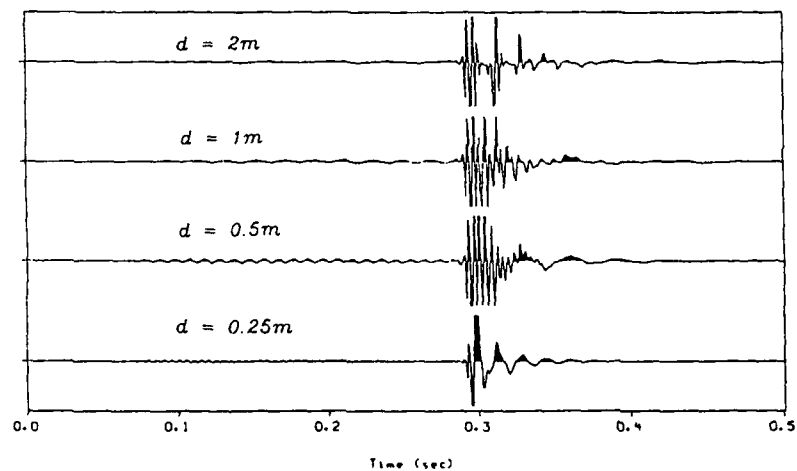


a. Vertical displacement at the surface plotted at a constant gain.

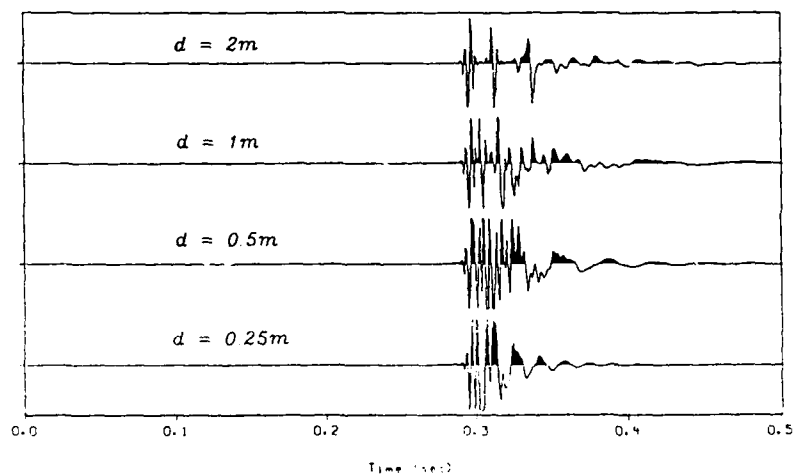
Figure 54. Calculated effect of layer thickness on ground motion. Models with parameters identical to single layered model 2 (Table 10) with  $c > V_p > V_s$  were used, except that  $Q_p = 30$ ,  $Q_s = 10$ , and the layer thickness was varied. The layer thickness from the top to the bottom traces was 2, 1, 0.5 and 0.25 m respectively.



*b. Horizontal displacement at the surface.*



*c. Vertical displacements plotted with the gain increased.*



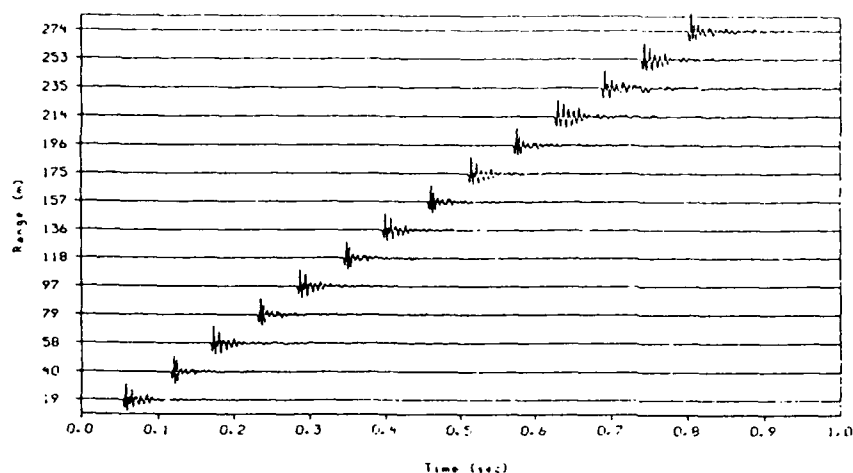
*d. Horizontal displacements plotted with the gain increased.*

Figure 54 (cont'd).

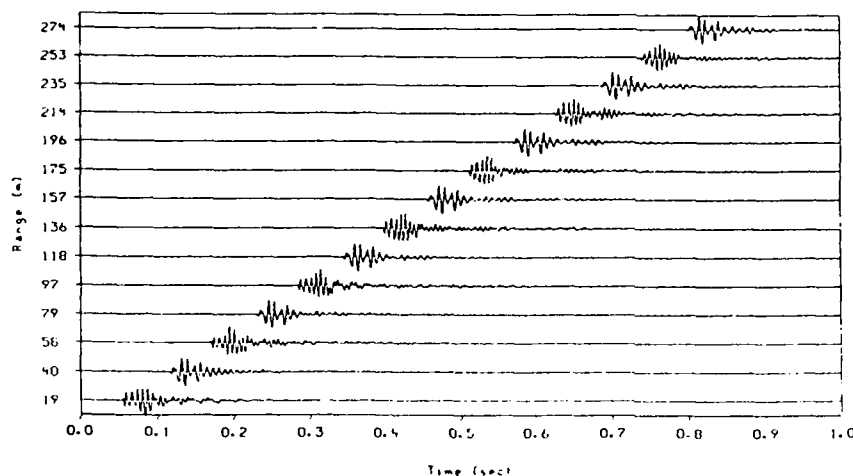
ing the air wave decreases. The leaky mode arrivals are also similarly affected.

Figure 54 shows the effect of layer thickness, for a layer with  $Q_p = 30$ ,  $Q_s = 10$  and the same velocities as for the previous figure (single layered model 2 in Table 10). Decreasing the layer thickness decreases

the time interval between the multiple reflections after the air wave and after the first arrival in the leaky mode, causing the apparent frequency of these wave trains to increase. A dispersed air-coupled Rayleigh wave train is just starting to form as the layer thickness decreases to 0.5 m and is visible at 0.25 m; ap-



a. Vertical component.



b. Horizontal component.

Figure 55. Observed waveforms of surface particle velocity in the summer. Waveforms recorded by surface geophones from a .45 caliber blank pistol shot 1 m high in the air. The sensors used to record the traces at 40, 79, 118, ... m were at horizontal location 0 m in Figure 4; traces at 19, 58, 97, ... m were at location 21 m. The source location was moved to different locations to the east of the array to produce these traces.

parently, the layer has become thin enough to be distinguished from a half space so dispersion is introduced.

The examples of this subsection provide some insight into the response of the Earth to an acoustic impulse. In the next subsection, experimental measurements are presented and compared with calculated ground motions.

#### Comparison with experimental measurements

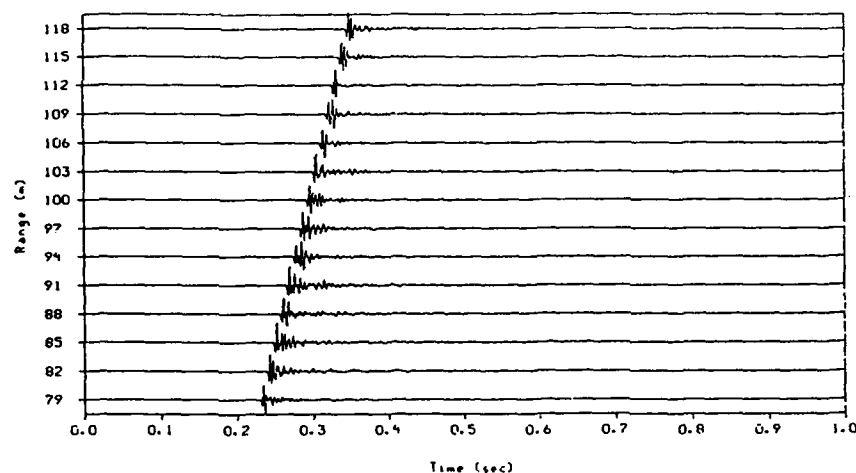
The field measurements conducted to investigate acoustic-to-seismic coupling showed that the strongest coupling into the ground occurred as the air wave passed, although weaker compressional body waves were also induced in the ground immediately under the source, and arrived first at the sensors. Body wave

ground motion amplitudes were observed to be one or two orders of magnitude lower than amplitudes induced by the later-arriving air wave (Fig 36).

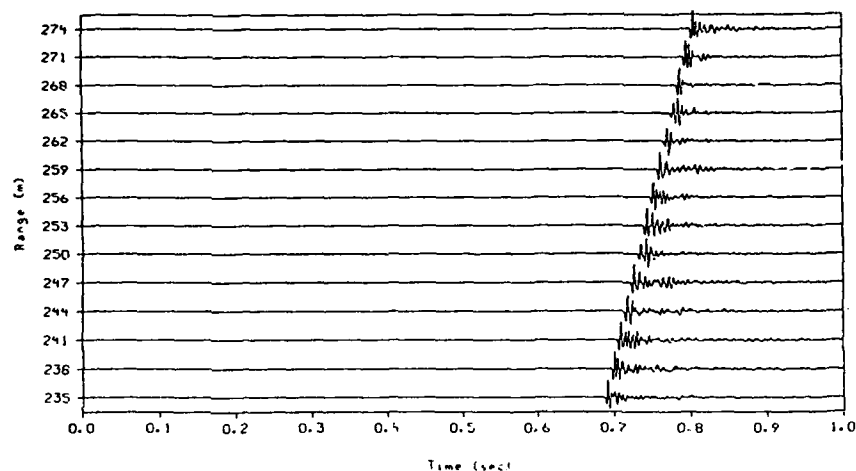
The wave arrival types, travel times and relative amplitudes observed in these experiments already agree qualitatively with the computed ground response for the single-layered models, and indicate that the computational procedure has the potential to explain these observations.

#### Summer measurements

Figure 55 shows the vertical and horizontal particle velocity recordings (measured by surface geophones) obtained in the summer on grassland. Alternate traces on the recordings are from the same sensor locations; the source was moved between shots to collect data for the propagation ranges shown. The



a. Waveforms for a pistol shot located 118 m to the east of the farthest geophone (at horizontal location 0 m).



b. Waveforms for a pistol shot located 274 m to the east of the farthest geophone.

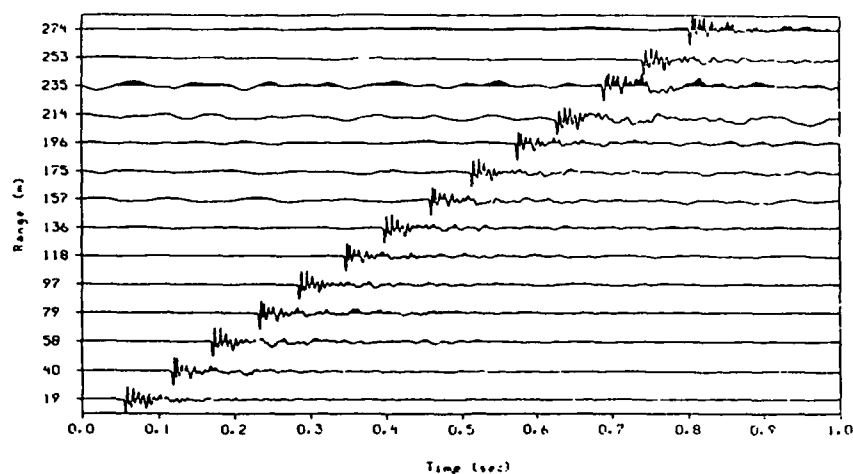
Figure 56. Observed waveforms of surface vertical particle velocity for the entire sensor array in the summer. The geophones were spaced 3 m apart and were located as shown in Figure 4.

vertical component waveforms are fairly similar, but the two sensor locations for the horizontal component recordings show quite different waveforms. These differences are most likely caused by local soil variations at the two sensor locations and differences in the emplacement of the geophones in the ground.

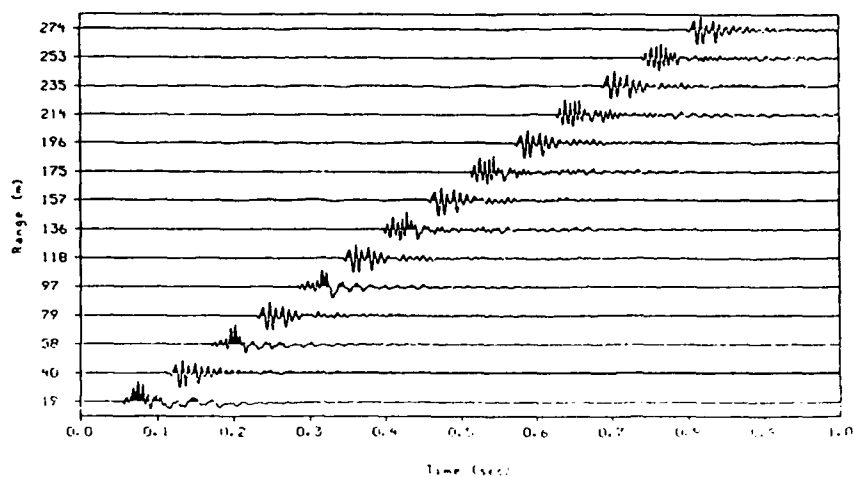
The near-surface soil variations can be assessed by examining Figure 56a. In this figure, all of the vertical component surface geophones used in the array are plotted for a typical shot; the pistol was located 118 m east of the farthest geophone. (The traces at 118 and 97 m for this figure and for Figure 55a are identical). Figure 56 shows that the traces are all similar in terms of the frequency content, but the details of the waveforms vary considerably in complexity and duration. Figure 56b shows the ground motion across the same array, with the source position moved

to a location 274 m from the farthest geophone. Comparing Figures 56a and b shows that the waveforms at each sensor location remain largely unchanged, even though the source has been moved a large distance. I conclude from this comparison that the ground motion waveform depends only slightly upon the overall propagation, but is instead affected primarily by local conditions. This figure shows that it is not realistic to expect to obtain more than a qualitative match with the observed waveforms, in contrast to the close match that was obtained for the acoustic data in the previous section.

Since the computations are for displacements, the particle velocity data of Figure 55 were integrated to convert them to displacements also and the results are shown in Figure 57. The integration process introduced a phase shift in the waveforms and de-



a. Vertical component waveforms.



b. Horizontal component waveforms.

Figure 57. Observed waveforms of surface displacement in the summer, obtained by integrating the data in Figure 55.

Table 11. Input parameters used to calculate traces for comparison with the summer observations (Fig. 58 and 59).

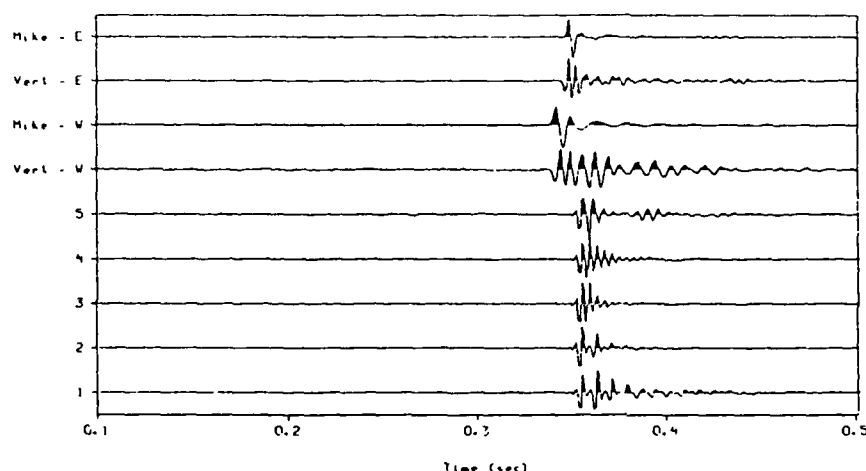
Layer	$V_p$ ( $m\ s^{-1}$ )	$V_s$ ( $m\ s^{-1}$ )	$\rho$ ( $Mg\ m^{-3}$ )	Thickness (m)	$Q_p$	$Q_s$
<b>Trace 1 (same as single layered model 2)</b>						
1	340	0	0.001225	$\infty$	$1 \times 10^4$	
2	200	60	1.8	1.0	75	30
3	1700	360	1.8	$\infty$	750	300
<b>Trace 2 (same as trace 1 except:)</b>						
2	200	60	1.8	1.0	30	10
<b>Trace 3 (same as trace 2 except:)</b>						
2	200	60	1.8	0.5	30	10
<b>Trace 4 (layered model 1)</b>						
1	340	0	0.001225	$\infty$	$1 \times 10^4$	
2	200	60	1.8	0.5	60	20
3	400	160	1.8	1.0	60	20
4	800	360	1.8	3.0	60	20
5	1725	360	1.8	20.0	60	20
6	4630	2900	2.4	$\infty$	700	300

creased the signal-to-noise ratio. The dominant frequency of the oscillations within the waveforms was also lowered slightly. Since integrating the experimental data introduced too much noise, the synthetics were differentiated instead to obtain calculated particle velocity waveforms. This differentiation was done by multiplying the calculated response by the factor  $i\omega$  in the frequency domain before transforming to the time domain. This procedure was used on all of the comparisons below.

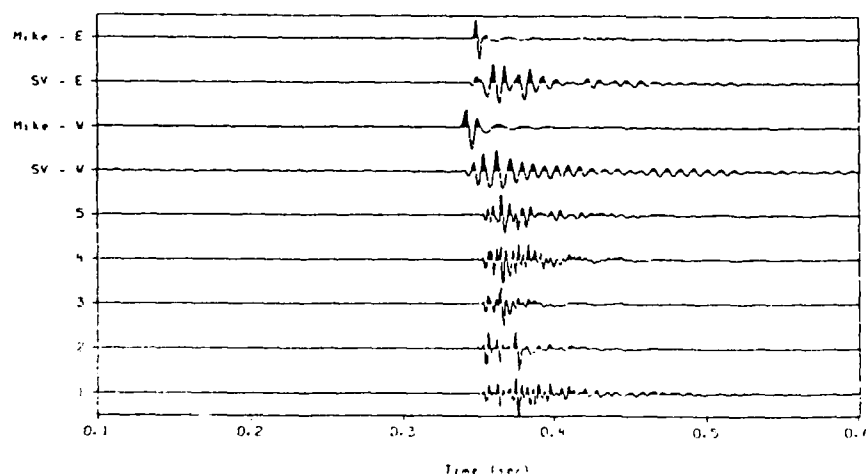
The forward modeling process in which I was attempting to match the observed summer waveforms and the computed waveforms is illustrated in Figure 58a. The top four traces are measured data, and below these are five calculated traces. The top two traces are surface microphone and vertical component geophone outputs, respectively, recorded for a pistol shot 118 m to the west of the sensors, and the sensors at

horizontal location 0 m in Figure 21. The next two traces are for the same microphone and geophone, with the pistol shot 118 m away to the east. The different microphone waveforms and arrival times are indicative of the effects of topography along the propagation paths (see Fig. 21) and different atmospheric sound speed profiles, since the pistol shots were recorded on two different days.

Under the four measured data traces in Figure 58 are particle velocity traces calculated for series of assumed Earth models, whose parameters were based on the seismic refraction experiments conducted at the site and discussed in the *Site Characterization* section. These traces were calculated for an explosion source 1 m high and 120 m away. The input parameters used to calculate all of the traces in Figure 58 are listed in Table 11. The lowest trace (trace 1) in Figure 58 was calculated for the single layered model

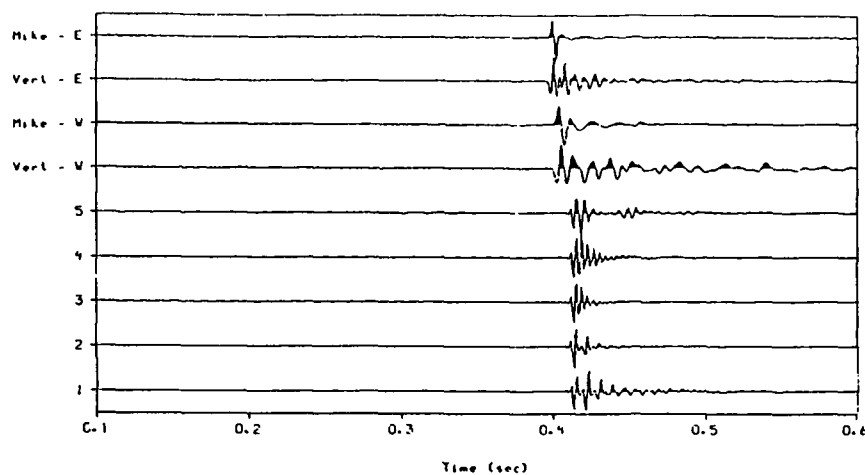


a. Vertical component waveforms.

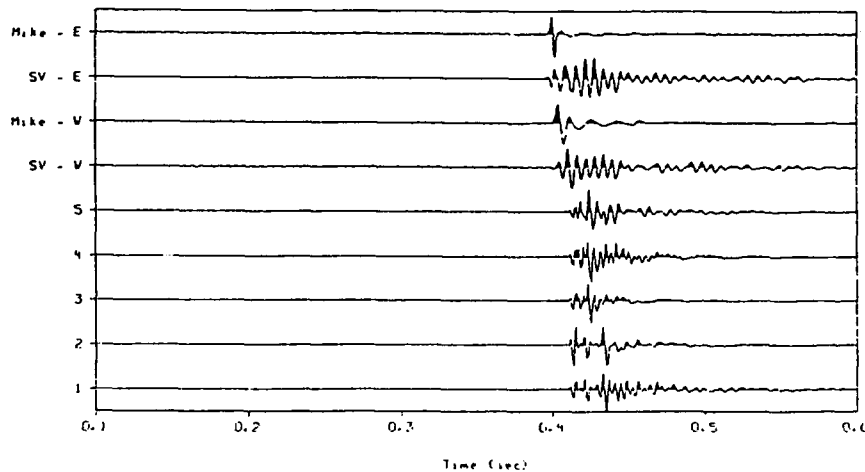


b. Horizontal component waveforms.

**Figure 58.** Comparison of observed and calculated waveforms for summer conditions. The propagation ranges were 118 m for the observed waveforms, 120 m for the calculated ones. In both plots, the top four traces are the experimentally measured sound pressures and particle velocities for sensors at horizontal location 0 m in Figure 21. For the first two traces, the pistol was fired from a spot 118 m to the west of the sensors; the source was 118 m to the east of the sensors for the next two traces. Below the four measured traces are the calculated particle velocity waveforms. Table 11 gives the input parameters used in these calculations.



a. Vertical component waveforms.



b. Horizontal component waveforms.

**Figure 59.** Comparison of observed and calculated waveforms for summer conditions. In both plots, the top four traces are the experimentally measured sound pressures and particle velocities, for sensors at horizontal location 21 m in Figure 4. For the first two traces, the pistol was fired from a spot 139 m to the west of the sensors; the source was 136 m to the east of the sensors for the next two traces. Below the four measured traces are the calculated particle velocity waveforms for an explosion 1 m high in the air and a propagation range of 140 m. Table 11 gives the input parameters used in these calculations.

2 of Table 10. Since this calculated waveform's duration was longer than the observed waveform, the second trace was calculated for the same model, but with the attenuation increased to  $Q_p = 30$ ,  $Q_s = 10$ . The duration of this waveform was closer to that of the observed trace, but the reflection from the bottom of the soil layer occurred too late, so the following trace (trace 3) used the same attenuation parameters with the soil layer thickness reduced from 1 to 0.5 m. The calculated vertical component waveform for this model is in good agreement with the waveform on the observed trace with the pistol shot to the east, but its horizontal component waveform's oscillations are too rapid and its duration too short. Finally, trace 4 was calculated for the same surface layer with  $Q_p = 60$ ,  $Q_s = 20$ , but with two additional layers beneath that were based on the refraction results.

This last calculated waveform shows general agreement with the observed data in shape and duration. Its oscillatory frequency is slightly too low on the vertical component and slightly too high on the horizontal. There is also a pulse appearing about 50 ms after the air wave that does not appear in the experimental data.

Figure 59 shows the same forward modeling process for a propagation range of 140 m. The data traces in this figure correspond to the other sensor location of Figure 55 (horizontal location 21 m in Fig. 21). The top two traces are for a propagation distance of 139 m from the west, and the next two traces are for a distance of 136 m from the east. Again, these traces were recorded on different days and show the effects of topography and meteorological conditions. The same models as for Figure 58 were used to cal-



culate the traces in Figure 59. Trace 4 again shows general agreement with the observed data, but is slightly too high in frequency in comparison with the measured horizontal component data. Considering the variations in the observed data, this is probably about as close a match as should be attempted.

Figure 60 shows the vertical component amplitude decay rates for the measured data and the calculated models of Table 11. The calculated waveforms have been normalized so that their peak amplitudes at a range of 20 m are equal, and only the slopes of these decay lines are meaningful. The figure shows that there is little difference in the decay rates calculated for the models, and that the rates agree with the observed data.

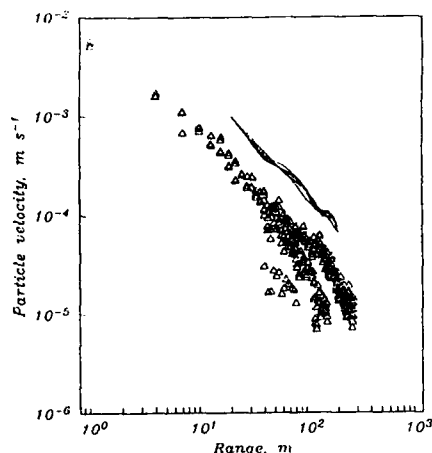
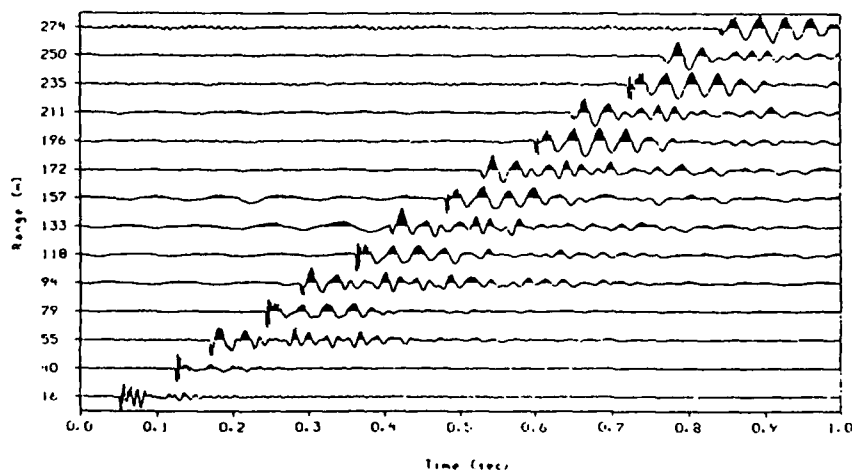


Figure 60. Peak amplitude decay as a function of range measured in the summer and calculated for the models in Table 11. Triangles denote amplitudes measured from vertical component surface geophones; lines are amplitudes predicted by the calculations. The predicted amplitudes have been normalized to the same (arbitrary) value at the 20-m range.

#### Winter measurements

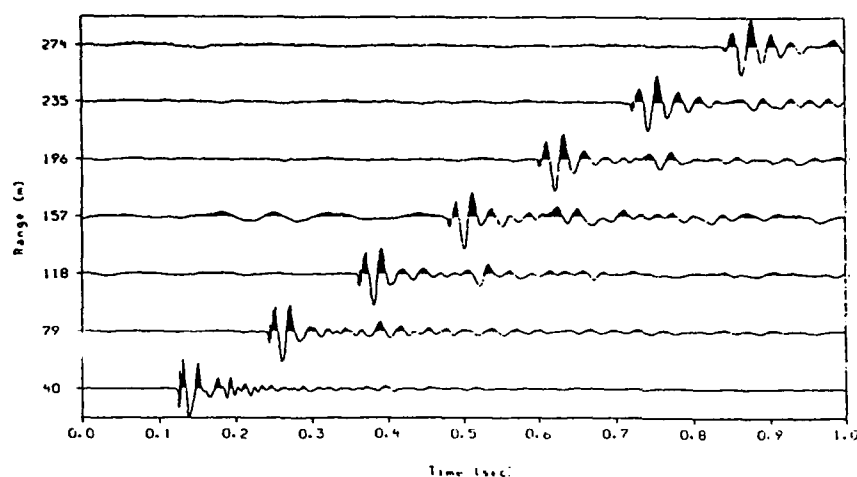
Figure 61 shows the vertical and horizontal components of particle velocity measured by geophones at the surface of the snow cover during the winter experiments. The waveforms are quite different from those recorded in the summer (Fig. 55), and there are considerable differences between the two sensor locations (horizontal location 0 and 24 m in Fig. 4) used to construct Figure 61a; local variations are once again suggested as causing these variations.

Since questions are occasionally raised about the accuracy of geophones emplaced in such a low-density, low-strength material as snow, Figure 62 compares collocated vertical component geophone pairs across the entire array for a typical pistol shot. At the five locations, the top trace in the figure is from a geophone mounted with a spike in the ground beneath the snow, while the lower trace is a geophone at the surface of the snow. The figure clearly demonstrates that, although the waveforms vary markedly across the short array, those at each location have nearly identical waveforms. The main difference between the two geophone signals at each location is that the high frequency oscillation at the beginning of the waveform is damped considerably in the



a. Vertical component waveforms.

Figure 61. Observed surface particle velocity waveforms in the winter recorded by surface geophones from a .45 caliber blank pistol shot 1 m high in the air. The sensors used to record the traces at 40, 79, 118, ... m were at horizontal location 0 m in Figure 4; traces at 16, 55, 94, ... m were at location 24 m. The source location was moved to different locations to the east of the array to produce these traces. There was no horizontal component geophone at the 24-m location.



b. Horizontal component waveforms.

Figure 61 (cont'd). Observed surface particle velocity waveforms in the winter recorded by surface geophones from a .45 caliber blank pistol shot 1 m high in the air. The sensors used to record the traces at 40, 79, 118, ... m were at horizontal location 0 m in Figure 4; traces at 16, 55, 94, ... m were at location 24 m. The source location was moved to different locations to the east of the array to produce these traces. There was no horizontal component geophone at the 24-m location.

ground surface geophones; this behavior is consistent with the interpretation of the high-frequency pulse as an air wave that is strongly attenuated as it travels downward through the pores of the snow cover to the ground geophone (see next section). The remarkable agreement between the waveforms indicates that the geophones at the snow surface are accurately measuring the motion induced in the snow by the pistol shot.

A forward modeling procedure similar to, but more extensive than, the procedure used in Figure 58 was employed in an attempt to match the waveforms recorded in the winter; Figure 63 shows some examples. In this figure, the top four traces are the observed waveforms, and the following traces are calculated particle velocity waveforms. The parameters used to calculate these waveforms are listed in Table 12.

The first trace in Figure 58 was calculated for a single snow layer 0.2 m thick, with P- and S-wave speeds of 100 and 40 m s<sup>-1</sup>, respectively, underlain by a hard soil with P- and S-wave speeds of 800 and 460 m s<sup>-1</sup>. The trace shows an early body wave arrival followed by an air wave, whose initial waveform is impulsive and followed by a dispersed, air-coupled wave train of low amplitude. (Because of the wave velocities used in the model, this wave train is

most likely an air-coupled PL wave rather than an air-coupled Rayleigh wave.) Although the calculated and observed wave arrival types are the same, the calculated waveforms are quite different from those on the measured traces. The impulsive arrival is too

Table 12. Input parameters used to calculate traces for comparison with the winter observations (Fig. 63).

Layer	$V_p$ (m s <sup>-1</sup> )	$V_s$ (m s <sup>-1</sup> )	$\rho$ (Mg m <sup>-3</sup> )	Thickness (m)	$Q_p$	$Q_s$
Trace 1 (same as single layered model 2)						
1	326	0	0.001225	$\infty$	$1 \times 10^4$	
2	100	40	0.25	0.2	7.5	3
3	800	460	1.9	$\infty$	750	300
Trace 2 (same as trace 1 except:)						
2	30	17	0.25	0.2	7.5	3
Trace 3 (same as Trace 2 except:)						
3	3800	2000	1.0	$\infty$	75	30
Trace 4 (same as trace 3 except:)						
3	200	60	1.8	0.4	60	20
4	340	160	1.8	$\infty$	60	20
Trace 5 (layered model 2)						
1	326	0	0.001225	$\infty$	$1 \times 10^4$	
2	30	17	0.25	0.2	7.5	3
3	200	60	1.8	0.4	60	20
4	400	160	1.8	1.5	60	20
5	800	360	1.8	2.1	60	20
6	1725	360	1.8	20.0	60	20
7	4630	2900	2.4	$\infty$	700	300

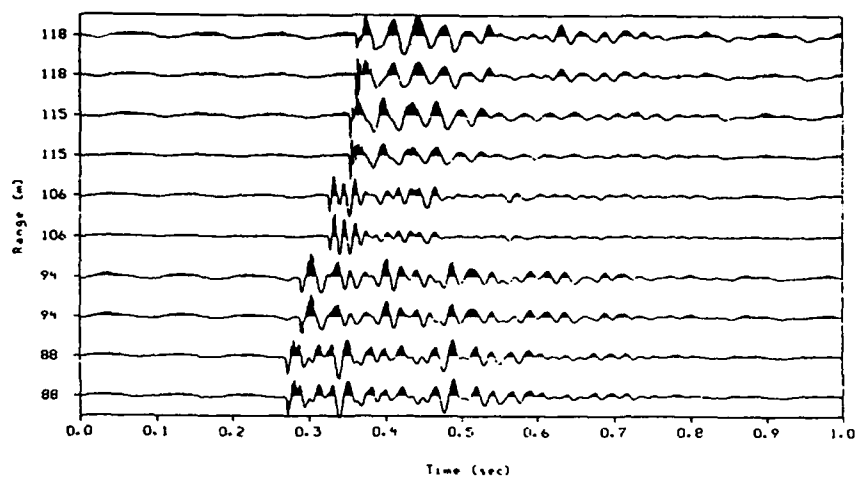
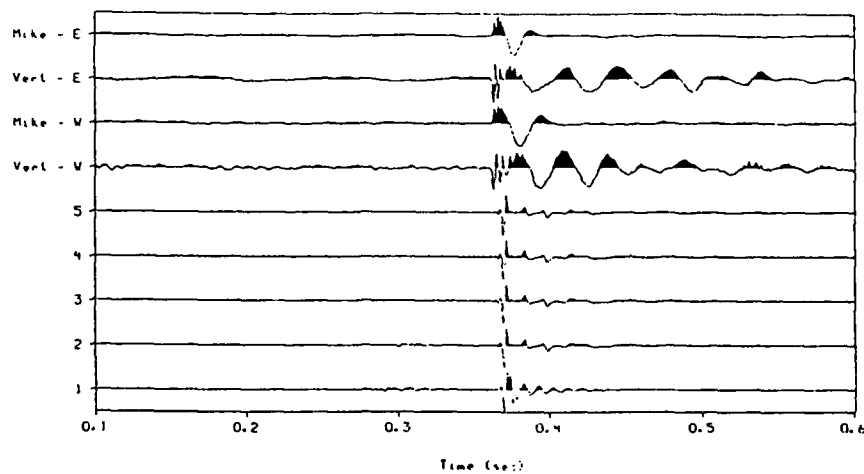
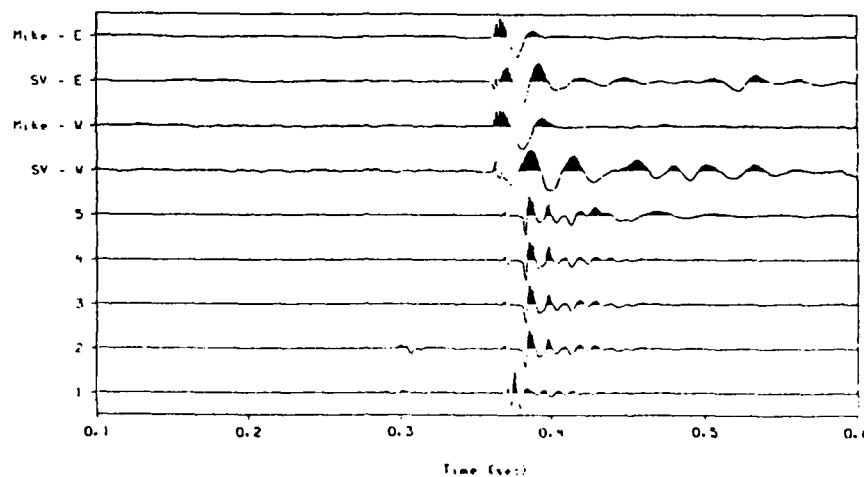


Figure 62. Observed snow surface and ground surface (beneath the snow) vertical particle velocity waveforms for the entire sensor array in the winter. At each location, the top trace is the ground surface geophone; under it is the snow surface geophone. The pistol was fired from a location 118 m to the east of the farthest geophones; the geophones were at horizontal locations 0, 3, 12, 24 and 30 m in Figure 21.

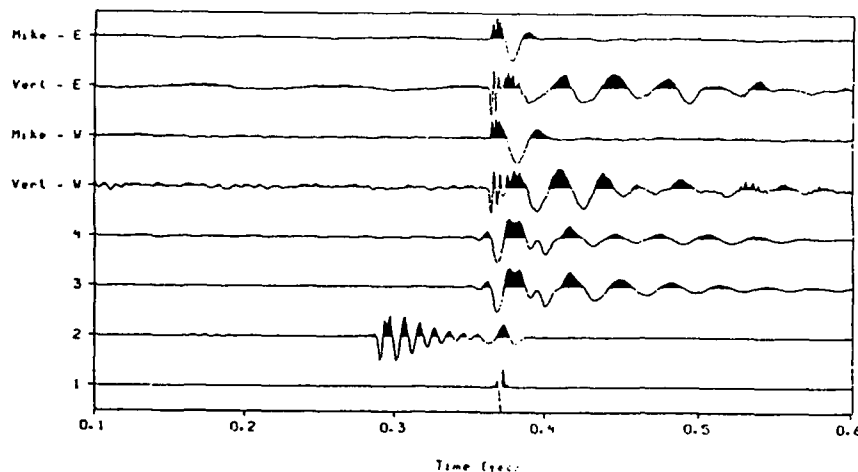


a. Vertical component waveforms.

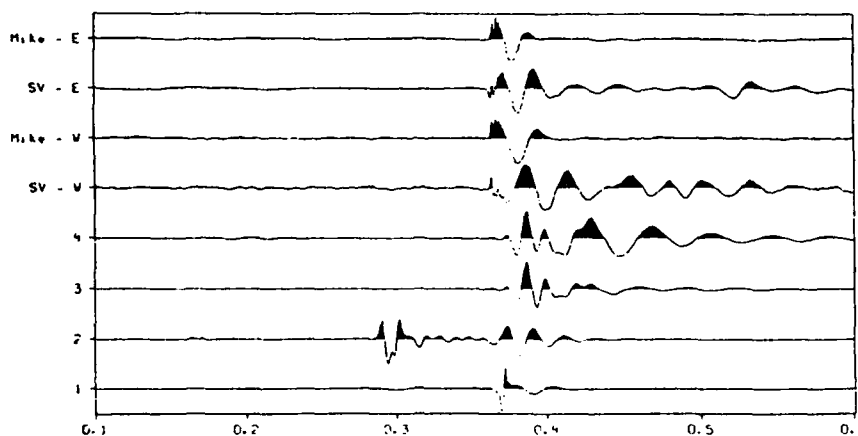


b. Horizontal component waveforms.

Figure 63. Comparison of observed and calculated waveforms for winter conditions. The propagation range was 118 m for the observed waveforms and 120 m for the calculated ones. In both plots, the top traces are the experimentally measured sound pressures and particle velocities for sensors at horizontal location 0 m in Figure 21. For the first two traces, the pistol was fired from a spot 118 m to the west of the sensors; the source was 118 m to the east of the sensors for the next two traces. Below the four measured traces are the calculated particle velocity waveforms. Table 12 gives the input parameters used in these calculations



a. Vertical component waveforms.



b. Horizontal component waveforms.

**Figure 64.** Comparison of observed winter condition waveforms with waveforms calculated using various nonlinear attenuation mechanisms. The propagation range was 118 m for the observed waveforms, 120 m for the calculated ones. The top four traces are the same experimentally measured sound pressures and particle velocities as in Figure 63. Below the four measured traces are the calculated particle velocity waveforms. Traces 1 and 2 were calculated with  $Q_p$  and  $Q_s$  proportional to  $f^{-2}$  in the snow and air respectively. Traces 3 and 4 are low pass filtered versions of traces 3 and 5 in Figure 63. Table 13 gives a detailed description of how these traces were calculated.

**Table 13.** Input parameters and nonlinear attenuation mechanisms used to calculate traces for comparison with the winter observations (Fig. 64).

**Trace 1**—Same material parameters as for trace 1 in Table 12, except that the attenuation in layer 2 is given by

$$Q_p = Q_{p0} (10/f)^2, \quad Q_s = Q_{s0} (10/f)^2$$

for frequencies  $f$  greater than 10 Hz.  $Q_{p0}$  and  $Q_{s0}$  are the starting values of 7.5 and 3 respectively.

**Trace 2**—Same as trace 1 except that the attenuation of layer 1 (the air layer) was varied.

**Trace 3**—Same as trace 3 of Table 12, except that the response was low-pass filtered with a cosine-squared taper between 50 and 100 Hz before transforming to the time domain.

**Trace 4**—Same as trace 5 of Table 12, except that the response was low-pass filtered with a cosine-squared taper between 50 and 100 Hz before transforming to the time domain.

large compared with the air-coupled wave train, and the dominant frequency of this wave train is too high. A number of adjustments were made to the input parameters, and the calculations were repeated to try to improve the match.

For the second calculated trace in Figure 63, the snow layer's  $P$ - and  $S$ -wave velocities were lowered to 30 and 17 m s<sup>-1</sup> respectively—very low velocities. This change allows the multiple reflections within the snow layer to be clearly distinguished on the vertical component trace. The horizontal component trace does show a lower-frequency air-coupled wave train, but its frequency is still far too high in comparison with the observed waveform. For the next two traces, the hard soil under the snow was replaced by an ice layer (trace 3) or by two unfrozen soil layers (trace 4). These waveforms are nearly identical with the second trace. Finally, trace 5 was computed for a model with six layers closely corresponding to the velocities determined by the seismic refraction experiments. The vertical and horizontal component traces remain identical with the previous traces.

By comparing the microphone waveforms in Figure 63 with those in Figure 58, it is apparent that the snow layer has had a large effect on the air wave itself, removing the high frequencies. This effect was successfully modeled in the previous section by treating the snow as a rigid, porous material. It is apparent that the *wavenumber integration method* should predict similar acoustic waveforms as a prerequisite for successfully modeling the winter ground motion data.

To attenuate the high frequencies, waveforms were calculated for a number of additional models, but the results were unsuccessful. Even very low  $Q$  values for the snow and soil failed to produce enough attenuation, so some nonlinear attenuation mechanisms were investigated. Figure 64 shows the results. First, allowing the attenuation to increase more than linearly with frequency was investigated. Trace 1 in Figure 64 shows the results for a model identical to trace 1 of Figure 63, except that both  $Q_p$  and  $Q_s$  varied as  $f^{-2}$  above 10 Hz. The initial impulsive portion of the air wave has broadened only slightly, with the main change being the loss of the later arrivals, so it does not resemble the measured waveforms. Trace 2 was calculated (in desperation) by allowing the  $Q$  in the air to vary as  $f^{-2}$ . This was done just to see if any viscoelastic mechanism could get the right frequencies. This trace does show the correct frequencies, but the character of the waveforms does not resemble the observed ones. In addition, the body wave amplitude is far too high relative to the air wave.

Next, traces 3 and 4 of Figure 63 were calculated

using the same models as traces 3 and 5 of the previous figure, except that a low-pass cosine-squared shaped filter limiting the frequency content to 100 Hz was applied to the calculated response before transforming to the time domain. These low-pass filtered traces are approaching the observed waveforms' appearance, since they exhibit the correct dominant frequencies and air-coupled wave train durations. No impulse appears at the beginning of the air wave arrival, however, since it has been eliminated by the low pass filter.

None of the calculations presented in Figure 63 are physically plausible. The problem in matching the observed winter data is that the viscoelastic model does not allow enough energy to be absorbed from the acoustic wave by the snow cover, because the effect of the pores in the snow has been ignored. The fluid/solid boundary conditions at the air/snow interface must be replaced with fluid/porous solid boundary conditions. In the next section, the correct boundary conditions will be investigated for plane waves, and it will be shown that transmission of energy into the pores is a major cause of the air wave attenuation.

### Summary

A method has been presented to calculate the ground motion induced by impulsive acoustic sources. Synthetic seismograms have been calculated for a series of models in an effort to match the experimentally observed waveforms. These calculations show that the near-surface properties control the waveform properties. Variations in the observed waveforms as the observation point changed precludes obtaining an exact match with a laterally homogeneous model, but the overall features have been suitably matched for measurements conducted on grassland. However, when snow is present, the modeling method fails because no reasonable viscoelastic model could be found to produce enough attenuation of the air wave to match the observed data. The method failed because it ignores the presence of the pores in the snow, which drastically change the boundary conditions at the surface and allow energy to be lost by transmission into the pores.

### REFLECTION AND TRANSMISSION OF PLANE WAVES ACROSS A FLUID/POROUS-SOLID INTERFACE

Although elastic or viscoelastic wave theory has proven to be very useful for many applications in seismology and acoustics, there are problems involv-

ing porous materials where such treatment is not appropriate, and consideration must be given to both the fluid and solid phases of the material. Biot (1956a, 1956b, 1962) developed a theory of wave propagation based upon a macroscopic averaging that allows calculations to be made for porous materials.

In Biot's theory, the porous material is treated as a solid frame filled with a viscous fluid. By examining the coupling between the two phases and by averaging over a volume containing many pores, Biot derived constitutive equations governing this material. (The volume average limits the theory to wavelengths that are much greater than the pore size, which is the case considered here.) These constitutive equations were used to examine small motions; solutions of the resulting wave equations correspond to two compressional waves and one shear wave propagating in the porous material. For all three of these waves the motion of the fluid and solid phases are coupled.

This section examines the transmission of sound from air into an air-saturated porous medium in an effort to determine why the modeling of snow as a viscoelastic material in the previous section failed to agree with the measured data. Biot's theory has been previously applied to problems in aeroacoustics and acoustic-to-seismic coupling by a number of researchers (Attenborough 1983, 1985, 1987, Attenborough and Richards 1989, Attenborough et al. 1986, Sabatier et al. 1986b). Biot's theory has also been applied to wave propagation in snow by Johnson (1982, 1985). Predictions for porous soils and for snow will also be made here.

Biot's theory is reviewed in this section. The equations of motion and plane wave solutions are derived, and the relationship between the fluid and solid motions are investigated, along with the reflection and transmission of plane waves across a fluid/porous solid interface. This section presents results for soil and snow, and a summary follows. Appendix D discusses various formulations used for viscosity losses.

## Summary of Biot's theory

### Equations of motion

Letting  $\mathbf{u}$  represent the displacement of the solid frame,  $\mathbf{U}$  the displacement of the fluid,  $\Omega$  the porosity and  $\mathbf{w} = \Omega(\mathbf{u} - \mathbf{U})$  the fluid displacement relative to the frame, Biot (1962) derived the constitutive equations

$$\sigma_{ij} = 2\mu e_{ij} + [(H - 2\mu)e - C\zeta]\delta_{ij} \quad (30)$$

where  $\sigma_{ij}$  = components of stress

- $e_{ij}$  = components of the strain tensor
- $\mu$  = complex shear modulus of the skeletal frame
- $H$  and  $C$  = complex moduli
- $e = \nabla \cdot \mathbf{u}$
- $\zeta = \nabla \cdot \mathbf{w}$
- $\mathbf{u}$  = volumetric strain of the solid
- $\mathbf{w}$  = increment of fluid content
- $\delta_{ij}$  = Kronecker delta.

Comparing this stress-strain relation with that for an isotropic elastic medium

$$\sigma_{ij} = 2\mu e_{ij} + \xi e \delta_{ij} \quad (31)$$

(where  $\xi$  is the Lamé parameter) shows that the forms are similar, with additional complex moduli introduced to describe the effect of the fluid-filled pores. Stoll and Bryan (1970) give expressions for calculating values of the new moduli  $H$  and  $C$  (and  $M$ , which appears below) from the bulk moduli of the solid and fluid components of the porous material and the frame bulk modulus ( $K_{fr}$ ). The values of the solid particle density  $\rho_s$  and solid bulk modulus  $K_s$  are required, along with the fluid density  $\rho_f$ , bulk modulus  $K_f$  and kinematic viscosity  $\nu$ . For the skeletal frame, the porosity  $\Omega$ , permeability  $k_s$ , tortuosity  $q^2$ , shear modulus  $G$  and Poisson's ratio  $n$  must also be given. The bulk frame modulus  $K_{fr}$  is then estimated using the relation

$$K_{fr} = G \left[ \frac{2}{3} + \frac{2n}{1-2n} \right].$$

Viscoelastic losses are incorporated into the theory by specifying a value for the loss decrement  $\delta$ , and by replacing, e.g., the shear modulus by a complex modulus  $\mu = G(1 + i\delta)$ .

Using the constitutive eq 30, Biot derived the coupled equations of motion

$$\mu \nabla^2 \mathbf{u} + (H - \mu) \nabla e - C \nabla \zeta = \rho \partial_t^2 \mathbf{u} - \rho_f \partial_t^2 \mathbf{w} \quad (32)$$

$$C \nabla e - M \nabla \zeta = \rho_f \partial_t^2 \mathbf{u} - m \partial_t^2 \mathbf{w} - \frac{\rho_f \nu}{k_s} F(\lambda) \partial_t \mathbf{w} \quad (33)$$

where  $M$  = complex modulus

$m$  = mass coefficient

$\rho$  = average density

$\lambda$  = dimensionless parameter

$F(\lambda)$  = frequency-dependent correction to the viscosity.

There are three pore geometries for which  $F(\lambda)$  has been derived: slit-like pores, cylindrical pores and pores of arbitrary shape. Since there is little difference in the correction factor for typical materials (see Appendix D), we use the slit-like pore correction factor for the calculations in this paper.

If all of the pore fluid moved in phase with the pressure gradient, the coefficient  $m$  in eq 33 would simply be  $\rho_f/\Omega$ . However, because of the shape and orientation of the pores, an additional force or drag is exerted on the fluid. This force is treated by an added mass coefficient  $C_\alpha$  or equivalently by the tortuosity of the pore structure  $q^2$ . The coefficient is

$$m = (1 + C_\alpha) \frac{\rho_f}{\Omega} = q^2 \frac{\rho_f}{\Omega}$$

where  $(1 + C_\alpha) = q^2$  ranges from 1 to 3 (Stoll 1974) for most materials. Attenborough (1983) has proposed the relationship

$$q^2 = \Omega^{-n'}$$

where for most soils the grain shape factor  $n'$  is 0.5. By use of this relationship, porosities of 0.362 and 0.783 (those for soil and snow used as examples in this report) lead to values of 1.66 and 1.13, respectively, for the tortuosity. Yamamoto (1983a) and Stoll and Kan (1981) both previously used a value of 1.25 for marine sands.

#### Propagation of plane waves

The solid and fluid displacements can be represented by scalar and vector potentials

$$\mathbf{u} = \nabla \phi_s + \nabla \times \psi_s \quad (34)$$

$$\mathbf{w} = \nabla \phi_f + \nabla \times \psi_f \quad (35)$$

with  $\psi = (0, \psi, 0)$ . We first examine curl-free motion by setting the  $\psi$  terms to zero, and then substitute these potentials into eq 32 and 33. This process leads to the coupled wave equations

$$H \nabla^2 \phi_s - C \nabla^2 \phi_f = \rho \partial_t^2 \phi_s - \rho_f \partial_t^2 \phi_f \quad (36)$$

$$\begin{aligned} C \nabla^2 \phi_s - M \nabla^2 \phi_f &= \rho_f \partial_t^2 \phi_s \\ &- m \partial_t^2 \phi_f - \frac{\eta F(\lambda)}{k_s} \partial_t \phi_f \end{aligned} \quad (37)$$

where  $\eta = \rho_f \nu$  is the dynamic viscosity of the fluid.

Next, by substituting in the plane wave potentials  $\phi_s = A_i \exp[i(\omega t - \mathbf{k} \cdot \mathbf{r})]$  and  $\phi_f = B_i \exp[i(\omega t - \mathbf{k} \cdot \mathbf{r})]$ , eq 36 and 37 reduce to

$$\begin{bmatrix} H|\mathbf{k}|^2 - \rho\omega^2 & \rho_f\omega^2 - C|\mathbf{k}|^2 \\ C|\mathbf{k}|^2 - \rho_f\omega^2 & m'\omega^2 - M|\mathbf{k}|^2 \end{bmatrix} \begin{bmatrix} \phi_s \\ \phi_f \end{bmatrix} = \begin{bmatrix} 0 \\ 0 \end{bmatrix} \quad (38)$$

where  $m' = m - i\eta F(\lambda)/(k_s\omega)$ . This system of equations has solutions when the determinant of the  $2 \times 2$  matrix is zero. Writing out this determinant leads to a quadratic expression in  $k^2 = |\mathbf{k}|^2$ , which has two solutions for the complex wavenumber  $\mathbf{k}$ . This result shows that there are two propagating compressional waves, with different propagation velocities, that are termed the fast and slow compressional waves and denoted by  $P_1$  and  $P_2$ . Yamamoto (1983a, eq 10) gives explicit expressions for these wave velocities. The expression for the wavenumbers is

$$\begin{aligned} k_{1,2}^2 &= \frac{\omega^2}{2(C^2 - HM)} \times \\ &\left\{ -(m'H + \rho M - 2\rho_f C) \pm \left[ (m'H - \rho M)^2 + \right. \right. \\ &\quad \left. \left. 4(\rho_f H - m' C)(\rho_f M - m' C) \right]^{1/2} \right\}. \end{aligned}$$

By explicitly writing the real and imaginary parts of the complex wavenumber  $k = k' + ik''$ , the exponential term  $e^{-ikr}$  becomes

$$e^{-ikr} = e^{-ik'r} e^{k''r}.$$

Substituting  $k = \omega/V$ , where  $V$  is the complex velocity, gives

$$e^{-ikr} = e^{-i\omega V'r/|V|^2} e^{\omega V''r/|V|^2}.$$

Spatial attenuation is usually represented by a coefficient  $\alpha$  (with units  $\text{m}^{-1}$ ) in a term of the form  $e^{-\alpha r}$  so we can identify

$$\alpha = -k'' = \omega V''/|V|^2$$

In this report, the calculated attenuations are given in terms of the quality factor

$$Q = \frac{V'}{2V''}$$

By setting the scalar potentials  $\phi$  to zero in eq 34 and 35 and substituting into eq 32 and 33, the shear wave equations are found to be

$$\mu \nabla^2 \psi_s = \rho \partial_t^2 \psi_s - \rho_f \partial_t^2 \psi_f \quad (39)$$

$$(\eta/k_s) F(\lambda) \partial_t \psi_f = \rho_f \partial_t^2 \psi_s - m \partial_t^2 \psi_f \quad (40)$$

and substituting plane wave potentials for  $\psi$  leads to

$$\begin{bmatrix} \omega^2 \rho - \mu k_3^2 & -\omega^2 \rho_f \\ \omega^2 \rho & -\omega^2 m' \end{bmatrix} \begin{bmatrix} \psi_s \\ \psi_f \end{bmatrix} = \begin{bmatrix} 0 \\ 0 \end{bmatrix} \quad (41)$$

Setting the determinant of the matrix to zero leads to a linear equation in  $k_3^2$ , with a single solution

$$k_3^2 = \frac{\omega^2 \rho}{\mu} \left[ 1 - \frac{\rho_f^2}{\rho m'} \right] \quad (42)$$

Displacements induced in the solid and fluid phases of the porous medium are coupled into one another, i.e., a disturbance propagating in the solid matrix induces a displacement in the pore fluid (even for shear waves), and, similarly, a disturbance in the pore fluid induces one in the solid matrix. The relation between the motion in the solid and fluid phases is related to the displacement potential ratios ( $B_i/A_i$ ) for the compressional and shear waves. These ratios can be derived by substituting the plane wave potentials into the wave equations (eq 36 and 39) and leads to the expressions

$$\frac{B_i}{A_i} = \frac{H|k_i|^2 - \rho\omega^2}{C|k_i|^2 - \rho_f\omega^2} \quad i = 1, 2 \quad (43)$$

for the two compressional waves and

$$\frac{B_3}{A_3} = \frac{\rho\omega^2 - \mu|k_3|^2}{\rho_f\omega^2} \quad (44)$$

for the shear waves. By use of eq 43 and 44, the fluid to solid displacement amplitude ratios can be calculated from the expression

$$\frac{U}{u} = 1 - \frac{B}{\Omega A} \quad (45)$$

#### Fluid/porous-solid interface

In this subsection, the interaction of a plane wave incident from a fluid onto a porous solid is investigated. Following Stoll and Kan (1981), we introduce wave potentials and write the boundary conditions in terms of them. In the fluid, we assume a down-going pressure wave at an angle of  $\theta$  from the vertical. The wavenumber in the fluid is  $k_f = \omega/c$ , and the vertical and horizontal wavenumbers are  $k_z = k_f \cos \theta$  and  $k_x = k_f \sin \theta$ . The incident and reflected wave potentials are

$$\phi_i = A_i \exp[i(\omega t - k_z \cos \theta \cdot z - k_x x)]$$

$$\phi_r = A_r \exp[i(\omega t + k_z \cos \theta \cdot z - k_x x)]$$

while in the porous material, the potentials are

$$\phi_s = A_1 \exp[i(\omega t - k_{1z} z - k_x x)]$$

$$+ A_2 \exp[i(\omega t - k_{2z} z - k_x x)]$$

$$\phi_f = B_1 \exp[i(\omega t - k_{1z} z - k_x x)]$$

$$+ B_2 \exp[i(\omega t - k_{2z} z - k_x x)]$$

$$\psi_s = A_3 \exp[i(\omega t - k_{3z} z - k_x x)]$$

$$\psi_f = B_3 \exp[i(\omega t - k_{3z} z - k_x x)]$$

Here, the subscripts 1, 2 and 3 stand for the  $P_1$ ,  $P_2$  and  $S$  waves with solid motion potential amplitudes  $A_i$ , fluid motion potential amplitudes  $B_i$  and vertical wavenumbers  $k_{iz}$ .

The boundary conditions for the fluid/solid interface are the continuity of normal fluid displacement, normal traction, fluid pressure and tangential traction. These boundary conditions are written in matrix form as

$$A_i \begin{bmatrix} k_f \cos \theta \\ -\rho_f \omega^2 \\ -\rho_f \omega^2 \\ 0 \end{bmatrix} =$$



$$\begin{bmatrix}
k_f \cos \theta & k_{1z} \left(1 - \frac{B_1}{A_1}\right) & k_{2z} \left(1 - \frac{B_2}{A_2}\right) & k_x \left(1 - \frac{B_3}{A_3}\right) \\
\rho_f \omega^2 \left(\frac{B_1}{A_1} C - H\right) (k_x^2 + k_{1z}^2) + 2\mu k_x^2 & \left(\frac{B_2}{A_2} C - H\right) (k_x^2 + k_{2z}^2) + 2\mu k_x^2 & -2\mu k_x k_{3z} \\
\rho_f \omega^2 \left(\frac{B_1}{A_1} M - C\right) (k_x^2 + k_{2z}^2) & \left(\frac{B_2}{A_2} M - C\right) (k_x^2 + k_{2z}^2) & 0 \\
0 & 2k_x k_{1z} & 2k_x k_{2z} & k_x^2 - k_{3z}^2
\end{bmatrix}
\times
\begin{bmatrix}
A_r \\
A_1 \\
A_2 \\
A_3
\end{bmatrix}$$

and are solved numerically using LINPACK subroutines (Dongarra et al. 1979).

#### Application to air-filled materials: soil and snow

In this subsection the acoustic properties of porous soils and of snow predicted by Biot's theory will be examined, and the effects that the elastic frame moduli, frame attenuation, tortuosity and permeability have on these predicted properties will be investigated. These materials are of interest in determining the ground absorption effect on acoustic propagation and for other applications in aeroacoustics.

##### Determining the Biot parameters

For most experiments in aeroacoustics, the only available measurements of the ground properties are the density, grain size distribution, compressional wave velocity and sometimes the shear wave velocity. The wave speeds and density can be used to provide the following porous material properties:

$$\text{shear modulus: } \mu = \rho V_3^2$$

$$\text{porosity: } \Omega = \frac{\rho - \rho_s}{\rho_f - \rho_s}$$

$$\text{Poisson's ratio: } n = \frac{[(V_1/V_3)^2 - 2]}{2[(V_1/V_3)^2 - 1]}$$

The bulk modulus  $K_s$  can be estimated using an approximation (Yamamoto 1983a) to Gassmann's (1951) equation, which is (White 1983)

$$K_s = K_{fr} + \frac{\left(1 - \frac{K_{fr}}{K_r}\right)^2}{\frac{\Omega}{K_f} + \frac{(1 - \Omega)}{K_r} - \frac{K_{fr}}{K_r^2}}$$

where  $K_r$  is the bulk modulus of the solid material and  $K_{fr}$  the modulus of the skeletal frame. The rigidity of the solid particles (ice) is usually much greater than that of the frame,  $K_{fr}/K_r \approx 0$ , so

$$K_s = K_{fr} + \frac{K_r K_f}{\Omega K_r + (1 - \Omega) K_f}$$

For snow,  $K_{air} \ll K_{ice}$  (i.e.,  $K_f \ll K_r$ ) so

$$K_s = K_{fr} + K_f/\Omega$$

(Note that the above equation is not valid as  $\Omega$  approaches zero, for then the equation becomes  $K_s \approx K_r$ .) The frame modulus is estimated from the wave speeds in the snow, so the bulk modulus is obtained from

$$K_s = \rho V_1^2 + K_f/\Omega - (4/3) \rho V_3^2$$

which is the same as

$$K_s = \frac{K_f}{\Omega} + \mu \left[ \frac{2}{3} + \frac{2n}{1 - 2n} \right]$$

After these parameters are determined, one still needs to estimate the permeability  $k_s$ , the frame loss decre-

ment  $\delta$  and the tortuosity  $q^2$  before Biot's theory can be applied.

An estimate of the permeability  $k_s$  can be obtained in a number of ways, including previous measurements on similar materials appearing in the literature, published empirical relations between grain size and permeability, and from acoustic data taken in the field. Direct measurements of the permeability in situ are most accurate, but are rarely used because of the difficulty of making these measurements. Future work may improve this situation (Chacho and Johnson 1987).

#### Soil

*Parameters for soil.* Three different soils will be examined first, each distinguished by its  $P_1$ - and  $S$ -wave speeds relative to the speed of sound in air (taken to be  $329 \text{ m s}^{-1}$ ). The first two soils were from the Vermont site (Albert and Orcutt 1989). The measured  $P_1$ - and  $S$ -wave velocities were  $200$  and  $60 \text{ m s}^{-1}$  for soil 1 and  $400$  and  $160 \text{ m s}^{-1}$  for soil 2. Soil 3, with speeds of  $800$  and  $400 \text{ m s}^{-1}$ , is also examined. (This last soil would be an extremely hard one, and the reader should note that these velocities are not realistic except, perhaps, for frozen ground, caliche, or artificially compacted ground. This example is included to allow investigation of a very high velocity surface material.) Thus, the soils represent materials having both frame wave velocities below the acoustic velocity [ $c > v_1 > v_3$ ], only the  $S$ -wave velocity below the acoustic velocity [ $v_1 > c > v_3$ ] and both velocities above the acoustic velocity [ $v_1 > v_3 > c$ ]. Classical elasticity theory would predict 0, 1 and 2 critical angles for acoustic waves reflecting from soils of these velocity structures.

As mentioned above, determining the permeability of a soil or snow in situ is difficult. Unfortunately, this parameter is the most important one needed to make predictions of the acoustic properties of the materials, and it also varies markedly for naturally occurring materials. For example, Turcotte and Schubert (1982) give a range of values varying by a factor of 100 for sand and gravel. Hunt (1984) lists permeability values for a number of different types of soils; most vary by a factor of 100, and some vary by as much as a factor of  $10^5$ . The permeability was estimated from the relation

$$k_s = \eta / \sigma$$

where  $\eta = 1.8 \times 10^{-5} \text{ kg m}^{-1} \text{ s}^{-1}$  is the dynamic viscosity for air and  $\sigma$  is the flow resistivity at zero frequency. The effective flow resistivity is estimated from acoustic experiments (Albert and Orcutt 1989) to be about  $200 \text{ kN s m}^{-4}$ , implying that  $k_s = 1 \times 10^{-10} \text{ m}^2$ . This value also falls within the range of  $0.5$  to  $20 \times 10^{-10} \text{ m}^2$  for glacial outwash deposits, and is typical of a medium-grained sand (Hunt 1984).

The loss factor for the soils is assumed to be  $\delta = 0.02$ , and the tortuosity  $q^2$  is set to 1.25. The measured parameters for these soils are given in Table 14, along with the calculated parameters used to model the soils as porous materials.

As discussed in Appendix D, there is little difference between the predictions made using the three available viscosity correction terms, so  $F(\lambda_s)$ , the correction for slit-like pores, has been used in all of the calculations.

*Effect of frame velocities.* Predicted acoustic properties of these soils are shown in Figure 65. Figures

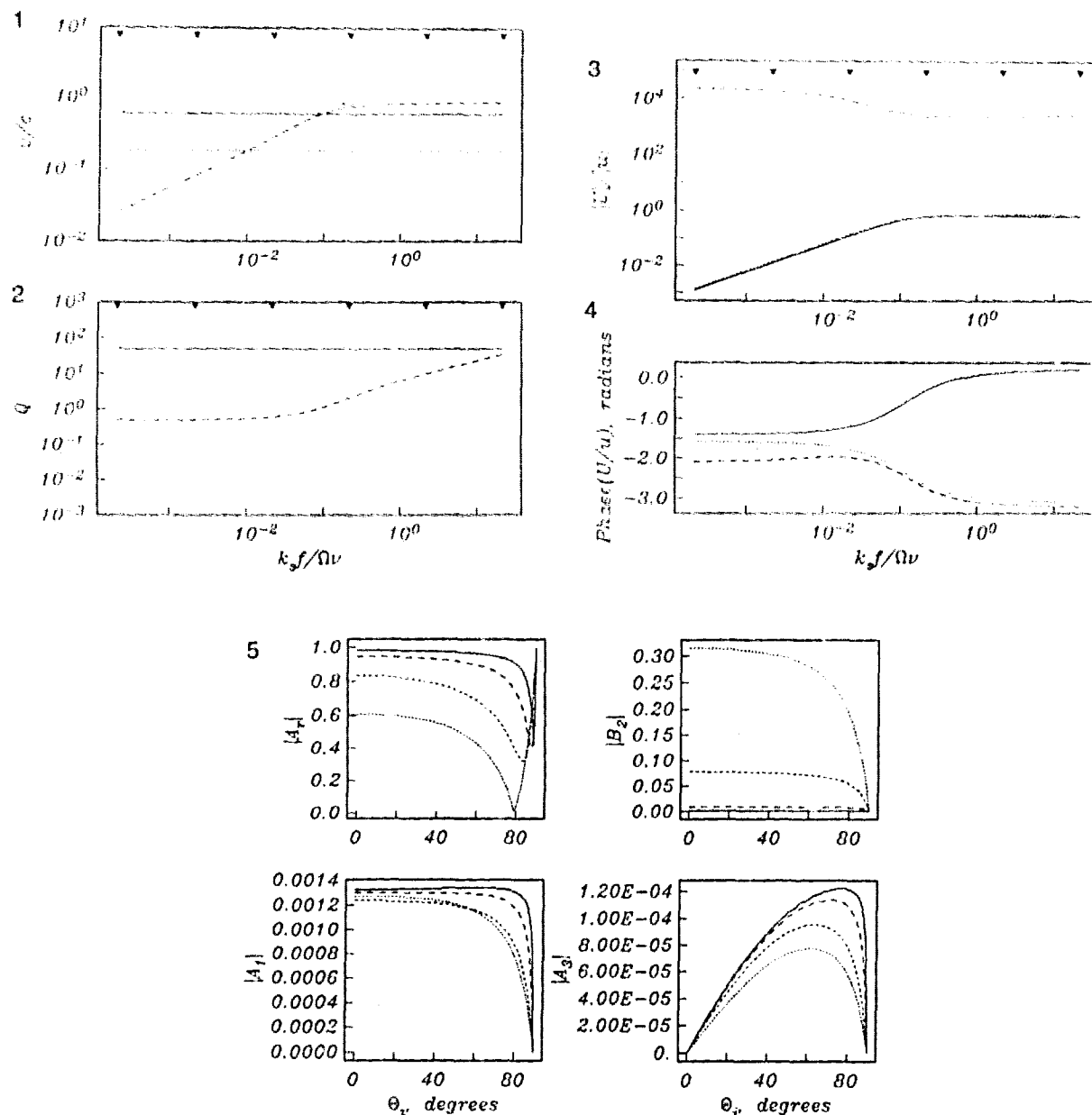
Table 14. Estimated and derived parameters.

#### a. For porous media.

	$V_P$ ( $\text{m s}^{-1}$ )	$V_S$ ( $\text{m s}^{-1}$ )	$\rho$ ( $\text{kg m}^{-3}$ )	$n$	$\Omega$	$K_{fr}$ ( $\text{Pa}$ )	$\mu$ ( $\text{Pa}$ )	$k_s$ $\text{m}^2$	$\delta$	$q^2$
soil 1	200	60	1800	0.45	0.321	$6.34 \times 10^7$	$6.48 \times 10^6$	$1 \times 10^{-10}$	0.02	1.25
soil 2	400	160	1800	0.40	0.321	$2.27 \times 10^8$	$4.61 \times 10^7$	$1 \times 10^{-10}$	0.02	1.25
soil 3	800	400	1800	0.33	0.321	$7.68 \times 10^8$	$2.88 \times 10^8$	$1 \times 10^{-10}$	0.02	1.25
snow 1	300	180	200	0.20	0.783	$1.78 \times 10^7$	$6.74 \times 10^6$	$10 \times 10^{-10}$	0.02	1.25
snow 2	160	90	85	0.20	0.910	$1.78 \times 10^6$	$7.19 \times 10^5$	$100 \times 10^{-10}$	0.02	1.25
snow 3	500	229	210	0.37	0.772	$3.78 \times 10^7$	$1.10 \times 10^7$	$2.7 \times 10^{-10}$	0.02	1.25
snow 4	100	40	200	0.40	0.783	$1.46 \times 10^6$	$3.20 \times 10^5$	$10 \times 10^{-10}$	0.02	1.25

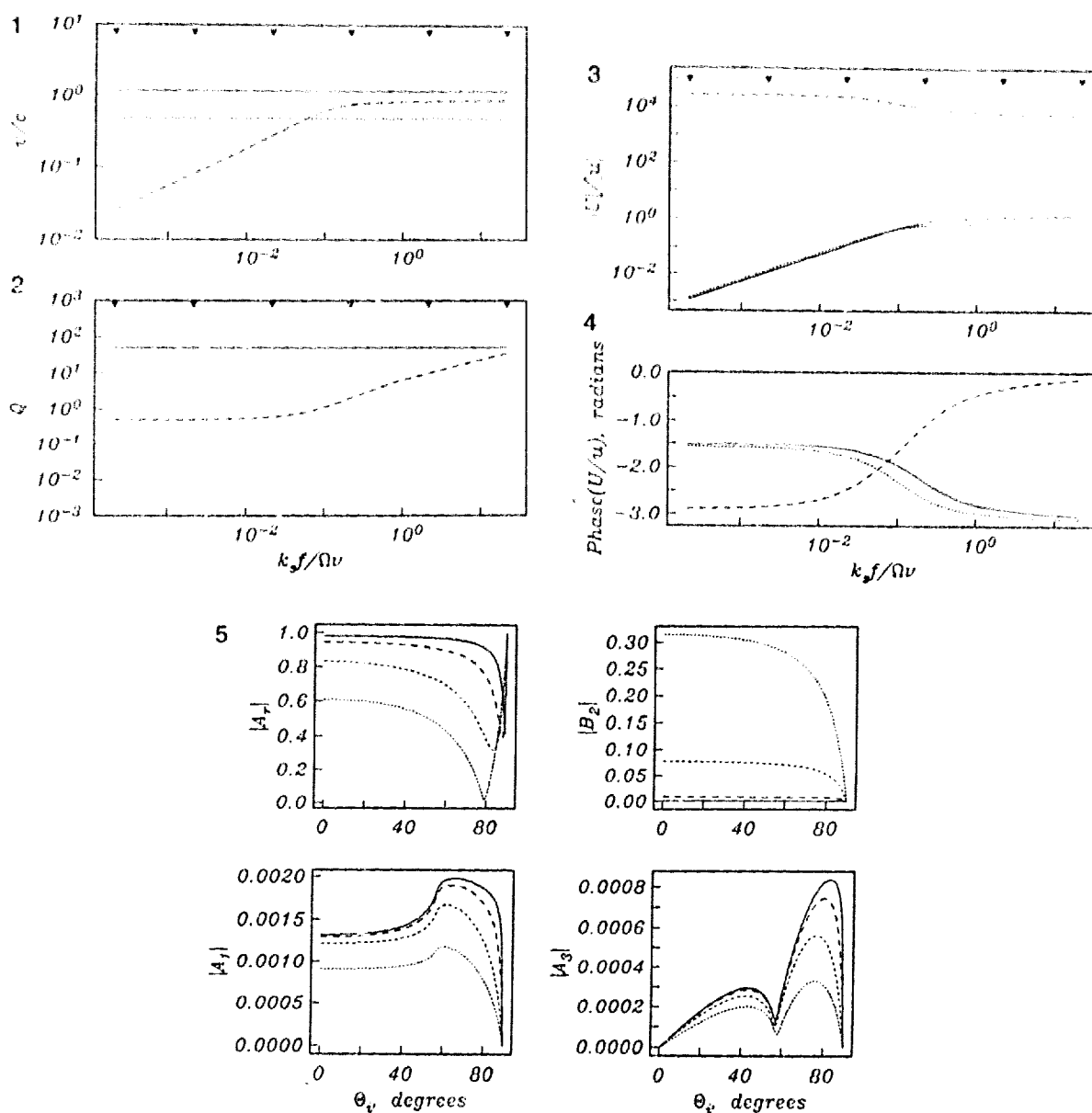
#### b. For air.

$\rho_f$ ( $\text{kg m}^{-3}$ )	$K_f$ ( $\text{Pa}$ )	$v$ ( $\text{m}^2 \text{ s}^{-1}$ )
1.2	$1.3 \times 10^5$	$1.45 \times 10^{-5}$



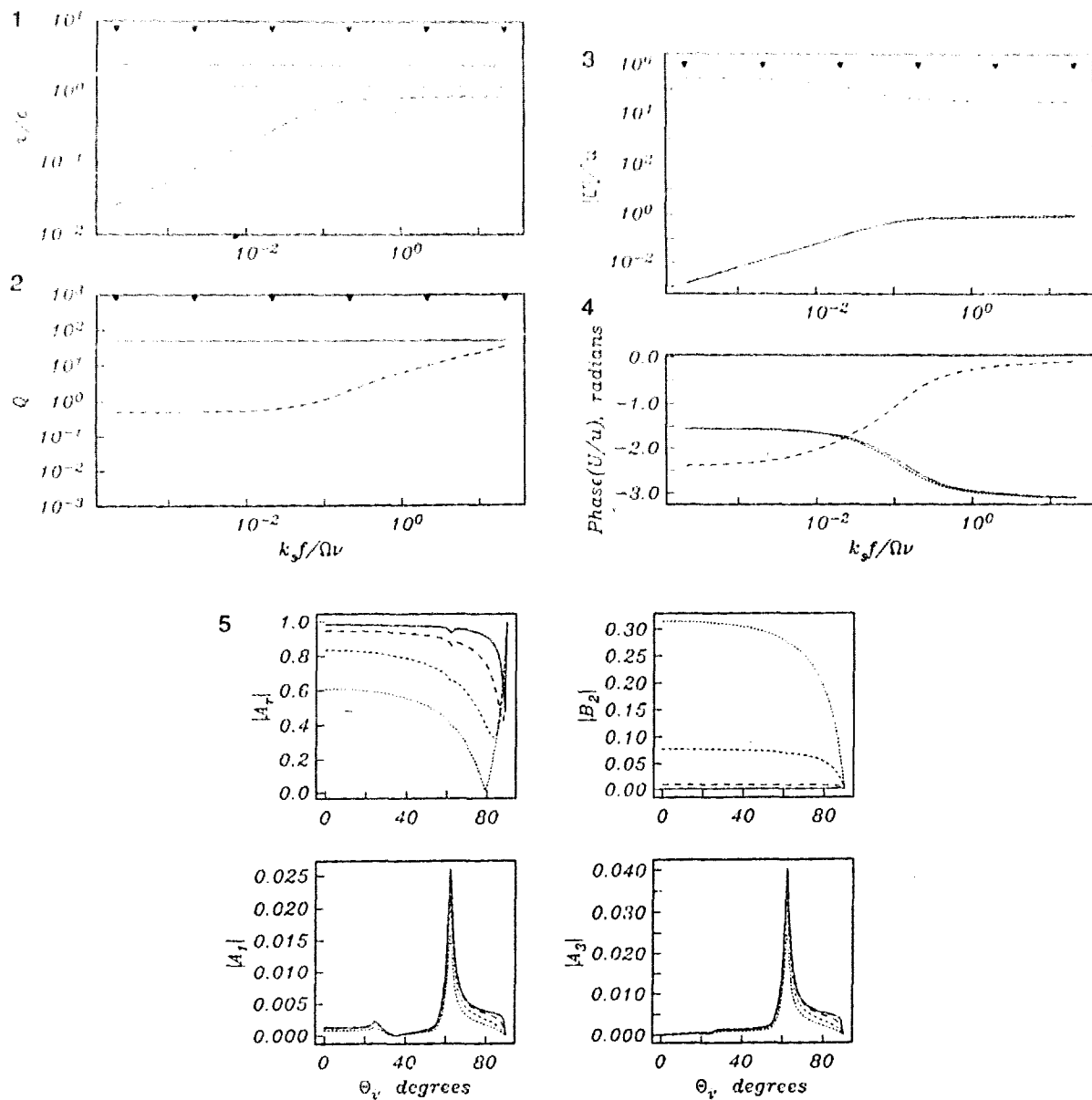
a. Soil 1.

Figure 65. Acoustic properties predicted by the Biot theory for soils 1, 2 and 3 (see Table 14 for the parameters used to make these predictions). (1) Velocities normalized by the fluid velocity  $c = 329 \text{ m s}^{-1}$ , (2) dimensionless attenuation parameter  $Q$ , (3) magnitude, and (4) phase of the fluid/solid displacement ratios for the three types of waves as a function of the poro-viscous frequency number  $N_f = k_s f / \Omega \nu$ . Small triangles mark the frequencies 10,  $10^2$ ,  $10^3$ ,  $10^4$ ,  $10^5$  and  $10^6$  Hz. Solid lines are plotted for the  $P_1$  (fast compressional) wave, dashed lines for the  $P_2$  (slow compressional) wave, and dotted lines for the S (shear) wave. A positive phase corresponds to fluid motion lagging behind the solid motion. (5) Plane wave reflected and transmitted displacement potential amplitude coefficients for a wave (of amplitude  $|A_i| = 1$ ) incident on an air/air-filled soil interface as a function of incident angle. The angle of incidence is measured from the vertical (i.e.,  $0^\circ$  corresponds to normal incidence).  $|A_r|$  is the amplitude of the displacement potential of the reflected wave in the fluid;  $|A_1|$  is the amplitude of the solid displacement potential of the transmitted  $P_1$  wave;  $|B_2|$  is the amplitude of the fluid displacement potential of the transmitted  $P_2$  wave;  $|A_3|$  is the amplitude of the solid displacement potential of the transmitted S wave. The solid line is for a frequency of 10 Hz; progressively shorter dashed lines correspond to frequencies of  $10^2$ ,  $10^3$  and  $10^4$  Hz.



b. Soil 2.

Figure 65 (cont'd). Acoustic properties predicted by the Biot theory for soils 1, 2 and 3 (see Table 14 for the parameters used to make these predictions). (1) Velocities normalized by the fluid velocity  $c = 329 \text{ m s}^{-1}$ , (2) dimensionless attenuation parameter  $Q$ , (3) magnitude, and (4) phase of the fluid/solid displacement ratios for the three types of waves as a function of the poro-viscous frequency number  $N_f = k_s f / \Omega v$ . Small triangles mark the frequencies  $10, 10^2, 10^3, 10^4, 10^5$  and  $10^6$  Hz. Solid lines are plotted for the P<sub>1</sub> (fast compressional) wave, dashed lines for the P<sub>2</sub> (slow compressional) wave, and dotted lines for the S (shear) wave. A positive phase corresponds to fluid motion lagging behind the solid motion. (5) Plane wave reflected and transmitted displacement potential amplitude coefficients for a wave (of amplitude  $|A_i| = 1$ ) incident on an air/air-filled soil interface as a function of incident angle. The angle of incidence is measured from the vertical (i.e.,  $0^\circ$  corresponds to normal incidence).  $|A_r|$  is the amplitude of the displacement potential of the reflected wave in the fluid;  $|A_1|$  is the amplitude of the solid displacement potential of the transmitted P<sub>1</sub> wave;  $|B_2|$  is the amplitude of the fluid displacement potential of the transmitted P<sub>2</sub> wave;  $|A_3|$  is the amplitude of the solid displacement potential of the transmitted S wave. The solid line is for a frequency of 10 Hz; progressively shorter dashed lines correspond to frequencies of  $10^2, 10^3$  and  $10^4$  Hz.



c. Soil 3.

Figure 65 (cont'd).

65a1, 65b1 and 65c1 show the predicted velocities of the three wave types ( $P_1$ ,  $P_2$  and  $S$ ) as a function of the poro-viscous frequency number  $N_f = k_s f / \Omega \nu$ . Both the  $P_1$ - and  $S$ -wave speeds are essentially constant as a function of  $N_f$  (or frequency). The  $P_2$ -wave velocity increases as the frequency increases until  $N_f \approx 0.1$  ( $f \approx 4500$  Hz), after which it remains constant. As the frame velocities increase, the constant  $P_1$ - and  $S$ -wave velocities move upward on the plot, but the  $P_2$  line is constant for all of the plots. This means that the  $P_2$  waves (at high frequencies) travel faster than the  $P_1$

and  $S$  waves for soil 1, are slower than the  $P_1$  waves but faster than the  $S$  waves for soil 2, and are slower than both waves for soil 3.

The wave attenuations are shown in Figures 65a2, 65b2 and 65c2. For the  $P_1$  and  $S$  waves,  $Q$  is constant with respect to frequency, so the attenuation constant  $\alpha$  in the term  $e^{-\alpha r}$  increases as  $f$  increases. For the  $P_2$  wave, the attenuation is very large at low frequencies, decreases to a value of  $Q = 1$  at about  $N_f = 0.1$ , and continues to decrease as the frequency increases. Values of  $Q$  less than 1 imply that the wave is not a

true propagating wave because the attenuation is so large; energy diffuses at these frequencies. The value  $N_f = 0.1$  is where the viscous drag and the inertial losses are approximately equivalent, and where the  $P_2$  wave becomes a propagating rather than a diffusive wave. As Yamamoto (1983b) points out, the general behavior of the material remains the same if the permeability  $k_s$  changes. Although changing  $k_s$  causes a shift in frequency, the velocities and attenuations remain constant at constant  $N_f$ . The attenuation  $Q$  is the same for all three soil examples. With  $\delta = 0.02$ ,  $Q$  is about 50 for the  $P_1$  and  $S$  waves.

Figures 65a3, 65b3 and 65c3 show the magnitude of the ratio of the fluid and solid motions, determined from eq 43-45, for the three wave types in the air-filled soil, again plotted as a function of  $N_f$ . For  $P_1$  and  $S$  waves, the fluid/solid displacement ratios ( $U/u$ ) are very small at low frequencies but increase as the frequency increases and become constant near  $N_f = 0.1$ , with a maximum of about 0.06. For the  $P_2$  waves, the fluid/solid coupling ratio is greater than  $10^3$ , while it is far less for the other two waves. The coupling ratio for the  $P_2$  waves decreases for frequencies above  $N_f = 0.1$  by about an order of magnitude for all of the soils. As the frame velocities increase (soil 1  $\rightarrow$  soil 3), this ratio increases from about  $10^4$  to  $10^5$ . Thus, this wave is essentially decoupled from the solid and propagates mainly through the pores.

The phases of the coupling coefficients for the second and third soils are similar, while the first soil shows a different pattern (Fig. 65a4, 65b4 and 65c4). For soil 1, the solid frame displacement of the  $P_1$  wave lags behind the fluid displacement by about  $\pi/2$  at low frequencies, but the phase difference decreases and the motions become in phase as the frequency increases. The  $P_2$ - and  $S$ -wave fluid components also lag behind the solid component by about  $\pi/2$  and  $\pi/3$  at low frequencies, but increase to  $\pi$  (completely out of phase) as the frequency increases. For soil 2 and soil 3, the  $P_2$ -wave solid component is out of phase at low frequencies, but becomes in phase with the fluid component as the frequency increases. The  $P_1$ - and  $S$ -wave solid displacements are  $\pi/2$  behind the fluid component at low frequencies, and become out of phase as the frequency increases.

Figures 65a5, 65b5 and 65c5 show the magnitude of the displacement potential reflection and transmission coefficients for plane waves from normal ( $0^\circ$ ) to grazing ( $90^\circ$ ) incidence for an air/air-saturated-soil boundary. The coefficients for frequencies of 10,  $10^2$ ,  $10^3$  and  $10^4$  Hz are shown. All of the coefficients exhibit some frequency dependence. The  $P_2$  transmission coefficient increases with frequency, and the

reflected,  $P_1$  and  $S$  transmission coefficients decrease with frequency. The  $P_2$  transmission coefficient is the largest, indicating that most of the transmitted energy (kinetic energy  $\sim \rho_s [\partial_t u]^2 + m [\partial_t u \partial_t w + \rho [\partial_t w]^2$ ) will be converted into  $P_2$  waves, not  $P_1$  waves or  $S$  waves.

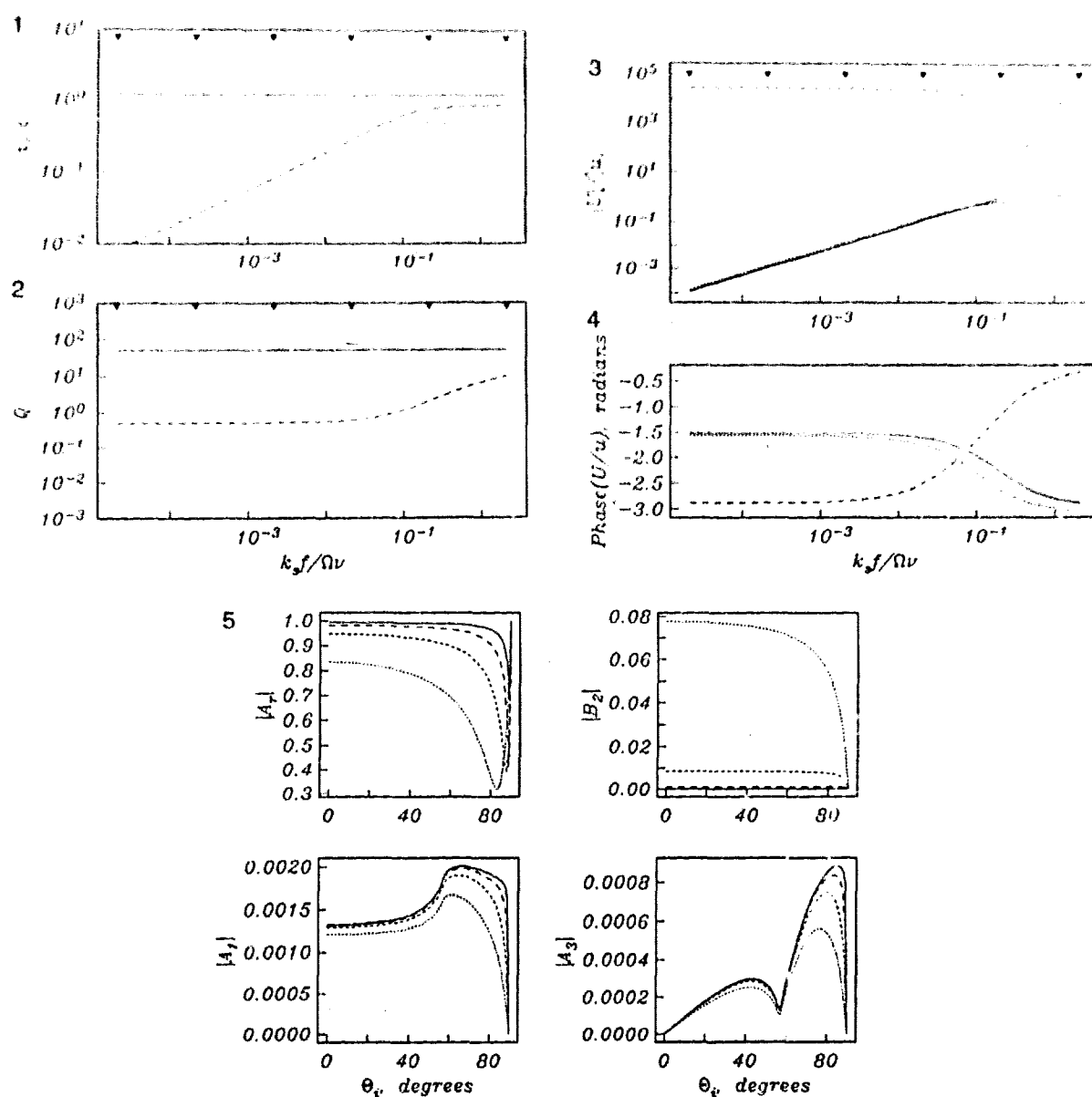
The reflection coefficient  $|A_r|$  and the transmission coefficient to  $P_2$  waves  $|B_2|$  are similar for all three soils in both curve shape (i.e., dependence on angle of incidence) and amplitude. At normal incidence, the reflection coefficient drops from around 1.0 to 0.6 as the frequency increases from 10 to  $10^4$  Hz, while the transmission coefficient increases from near 0 to around 0.35.

The transmission coefficients for  $P_1$  waves and  $S$  waves are typically 2-3 orders of magnitude smaller than the reflection and  $P_2$  transmission coefficients, and they vary in both shape and amplitude level for the three soils. For soil 1, the transmission coefficients are smooth and of low amplitude. As the frame velocities increase, peaks in the coefficients are introduced at certain angles. Soil 2 displays a broad peak in the  $P_1$  transmission coefficient and a double humped shape in the  $S$ -wave transmission coefficient. For soil 3, both coefficients are sharply peaked. The  $P_1$  coefficient has a small peak at around  $25^\circ$  and a large, sharp peak near  $65^\circ$ . The  $S$ -wave coefficient has a small dip and a large peak at the same angles. The expected "critical" angles for this soil are  $24$  and  $55^\circ$ , and these curves are similar to those expected for an elastic solid. The large peak occurs near the horizontal slowness for elastic Rayleigh waves, corresponding to an angle of  $\theta_R = \sin^{-1}[c/[(0.92)V_3]] = 63^\circ$ .

This example shows that, for air-filled materials, it is the  $P_2$  (slow compressional) wave that is most important, and a rigid porous model, ignoring the  $P_1$  and  $S$  waves, has found wide application in this situation (e.g., Attenborough 1985, Sabatier et al. 1986b, Albert and Orcutt 1990).

*Effect of permeability.* To investigate the effect of the permeability, additional calculations were done with  $k_s$  set to 0.1 and  $10 \times 10^{-10} \text{ m}^2$  for comparison with the previous results (where  $k_s = 1 \times 10^{-10} \text{ m}^2$ ). As expected from the earlier discussion, the velocities, attenuations and coupling coefficients are unchanged except for a shift in frequency. All of the reflection and transmission coefficients decrease slightly as the permeability increases, except for the  $B_2$  transmission coefficient, which increases slightly. Figures 65b and 66 show the effects for soil 2.

*Effect of tortuosity.* To investigate the effect of the tortuosity of the soil on its acoustic properties, the calculations were repeated for the three soils with



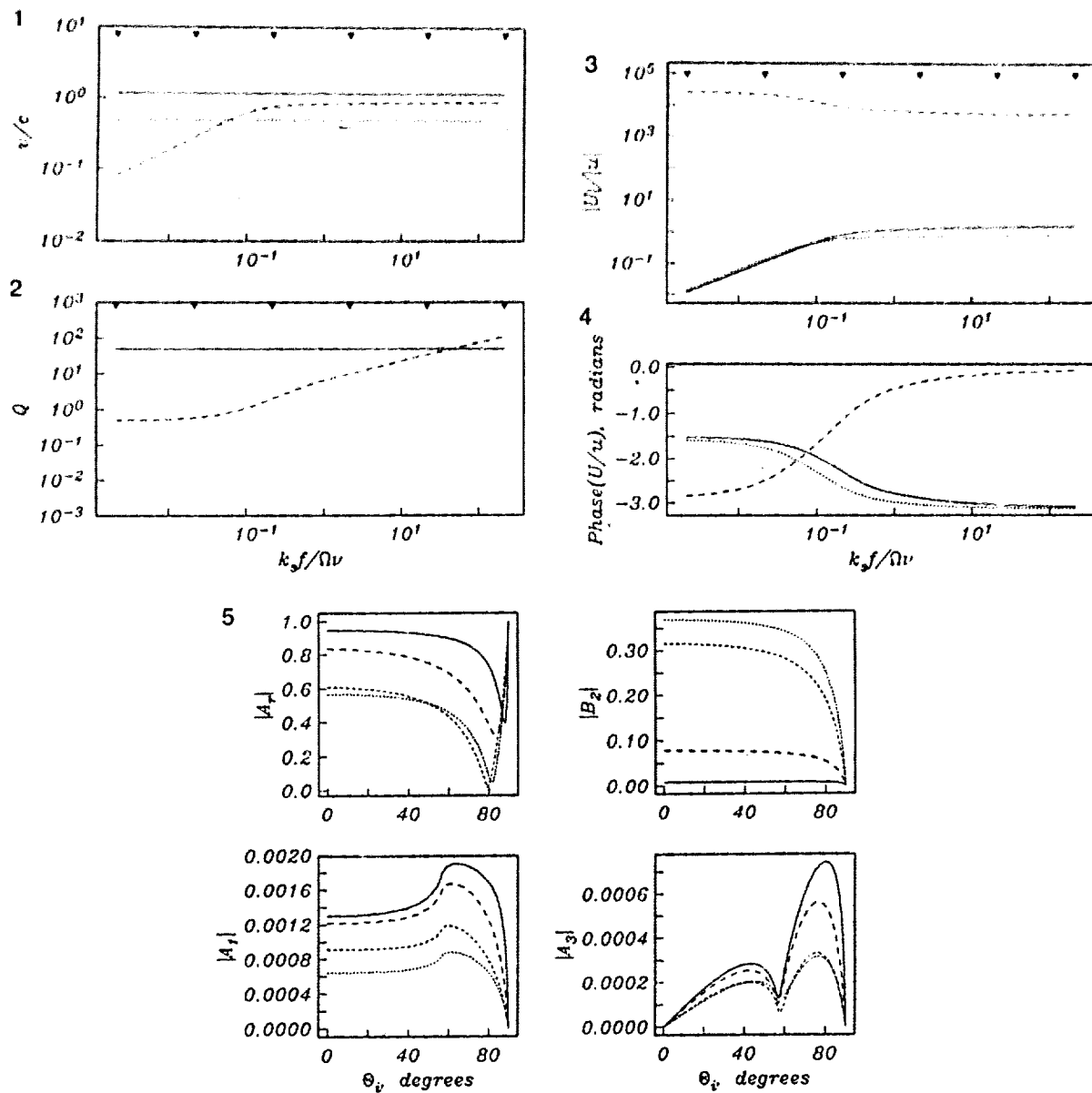
a. With the permeability set to  $k_s = 0.1 \times 10^{-10} \text{ m}^2$ .

Figure 66. Predicted acoustic properties for soil 2. (1) Velocities, (2) attenuation, (3) magnitude, and (4) phase of the fluid/solid displacement ratios for the three types of waves as a function of the poro-viscous frequency number  $N_f$ . (5) Plane wave reflected and transmitted displacement potential amplitude coefficients as a function of incident angle.

the tortuosity  $q^2$  doubled from a value of 1.25 to 2.5. Increasing the tortuosity decreases the final value of  $V_2$  at higher frequencies from 290 to 195  $\text{m s}^{-1}$ . Since increasing the tortuosity makes the pathway through the pores more convoluted, more time is required for the  $P_2$  waves to travel through the material, resulting in a lower wave speed. The frequency where the  $V_2$  curve levels out shifts to a slightly higher frequency for all of the models. There are only slight changes in

the fluid/solid coupling ratios for the three wave types. This ratio drops from  $10^3$  to  $10^2$  at high frequencies for soil 1, but is relatively unchanged for the other two soils. The phase changes are also slight.

The plane wave coefficients are also nearly unaffected by the increase in tortuosity. Only at high frequencies (above 1 kHz) are there discernable effects: the reflection coefficient increases and the  $P_2$ -wave transmission coefficient decreases as the tortuosity



b. With the permeability set to  $k_s = 10 \times 10^{-10} \text{ m}^2$ .

Figure 66 (cont'd). Predicted acoustic properties for soil 2. (1) Velocities, (2) attenuation, (3) magnitude, and (4) phase of the fluid/solid displacement ratios for the three types of waves as a function of the poro-viscous frequency number  $N_f$ . (5) Plane wave reflected and transmitted displacement potential amplitude coefficients as a function of incident angle.

increases. Typical changes (Fig. 67) for normal incidence at 10 kHz are  $0.61 \rightarrow 0.65$  for the reflection coefficient and  $0.33 \rightarrow 0.19$  for the  $P_2$ -wave transmission coefficient.

**Effect of frame loss decrement.** The calculations were repeated for the three soils using  $\delta$  values of 0.1 and 0.2 for comparison with the original value of 0.02. For all of the soils, the velocities are unchanged, as is the attenuation  $Q$  of the  $P_2$  wave. As  $\delta$  increases, the

value of  $Q$  for the  $P_1$  and  $S$  waves drops from 50 to 10 to 5. The ratio of fluid to solid motion for the  $P_2$  waves drops slightly and its phase at low frequencies shifts slightly; the couplings for the other waves are unaffected.

The main effect is on the plane wave transmission coefficients. The reflection coefficient and the  $P_2$ -wave transmission coefficient are unchanged, but the  $P_1$ - and  $S$ -wave transmission coefficients decrease slightly



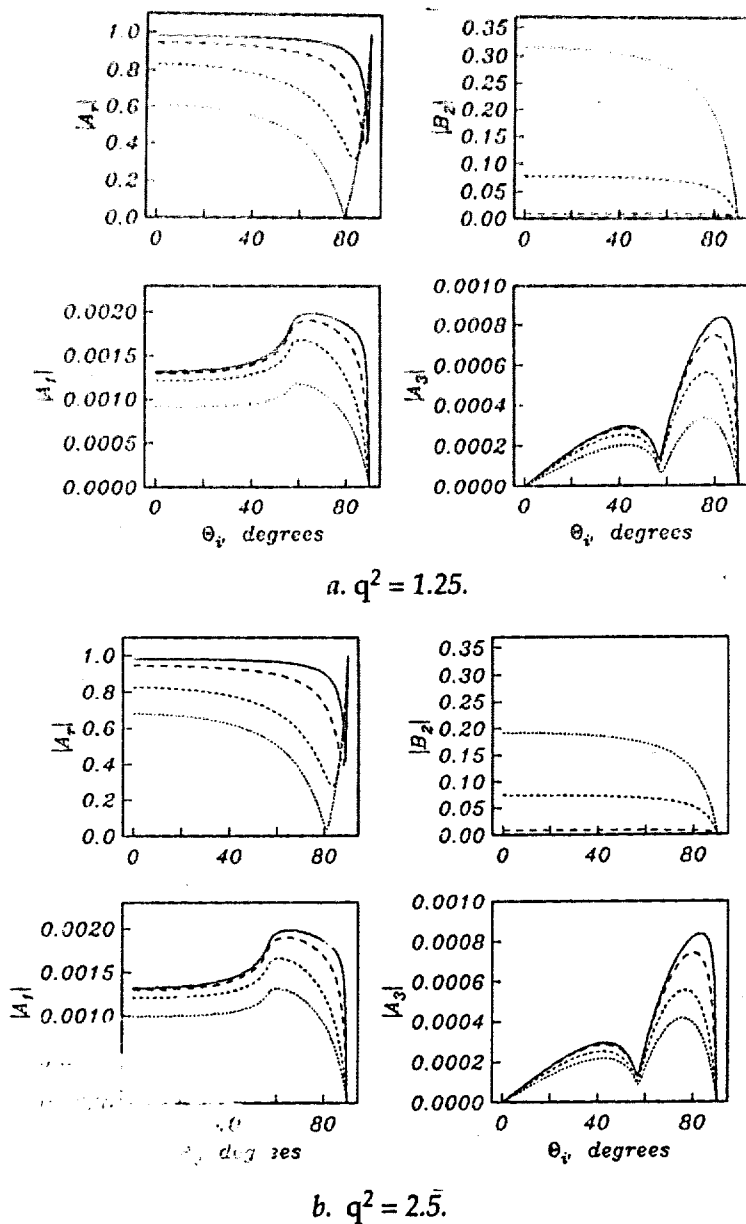


Figure 67. Effect of tortuosity  $q^2$  on the plane wave reflection and transmission coefficients for soil 2.

and any peaks or troughs broaden as the loss decrement increases. Figure 68 shows the changes in these coefficients for soil 2 and soil 3.

**Summary of results for soil.** As the above examples show, the permeability and the frame velocities are the parameters with the largest effect on the acoustic properties of the material. However, in most situations, the velocities are usually fairly well known while the permeability is not. Thus, the largest uncertainty in the parameter estimates and in the resulting acoustic predictions results from the uncertainty in the permeability. The value of the permeability controls the critical frequency, above which

the  $P_2$  wave becomes a propagating wave. Its other main effect is that the higher the permeability, the higher the transmission coefficients, especially for  $P_2$  waves at high frequencies.

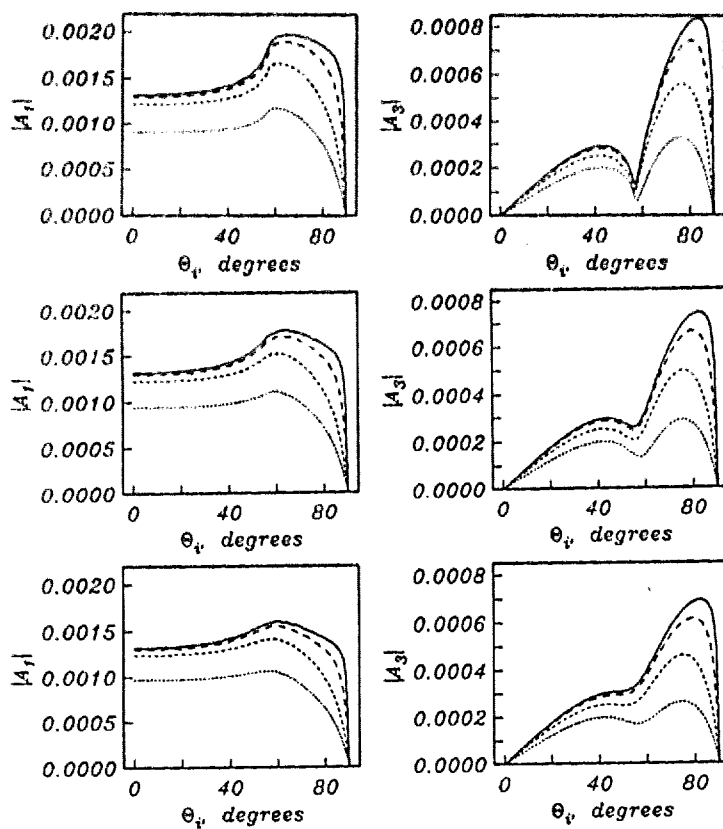
Whether the  $P_2$  wave is slower or faster than the other two waves is controlled by the frame velocities or moduli. These relationships may determine which waves arrive first at a detector under certain experimental geometries. As the frame velocities increase above the acoustic velocity, the plane wave transmission coefficients for  $P_1$  and  $S$  waves develop peaks that increase the transmission for specific angles of incidence. The reflection and  $P_2$  transmission coefficients remain the largest and are not affected significantly by the frame velocities.

#### Snow

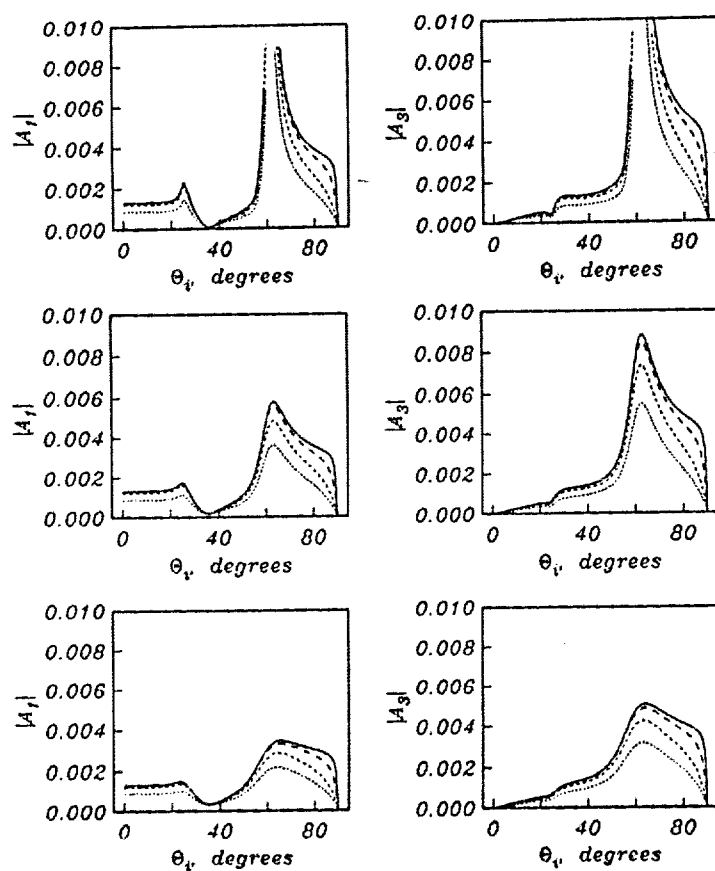
**Parameters for snow.** Attempting to model seasonal snow is fraught with uncertainty, primarily from two sources: First, the snow itself varies tremendously in its physical structure and mechanical properties. Second, measurements of seasonal snow's basic properties are infrequent, and experimentally determined values have large variations, especially the most important parameter, permeability. Therefore, a detailed description of the parameters used will be presented. The reader is warned that the modeling results presented in this section should be taken only as a guide.

Compressional and shear wave velocities can be used to estimate the bulk moduli  $K_s$  and  $\mu$  needed for the Biot model, and these measurements are easily done and give accurate values for most materials. However, wave velocity measurements on seasonal snow covers are difficult to obtain with commonly used

seismic refraction techniques because the snow cover is so thin. I am unaware of any velocity measurements on seasonal snow covers appearing in the literature, with the exception of the work of Yamada et al. (1974). This paper reported values of 500 and 230 m s<sup>-1</sup> for  $P$ - and  $S$ -wave velocities, respectively (i.e.,  $V_1 > c > V_3$ ), for snow with a density of 210 kg m<sup>-3</sup>. These values were obtained by measuring the travel time of ultrasonic pulses on samples removed from the snow cover. Because of the method used, the values reported are for rather competent snow that can withstand such handling. For many snow covers, the snow would simply crumble if attempts were made to re-



a. Soil 2. (Top)  $\delta = 0.02$ , (center)  $\delta = 0.1$  and (bottom)  $\delta = 0.2$ .



b. Soil 3. (Top)  $\delta = 0.02$ , (center)  $\delta = 0.1$  and (bottom)  $\delta = 0.2$ .

Figure 68. Effect of loss decrement  $\delta$  on the  $P_1$ - and S-plane wave transmission coefficients.

move samples, so the values reported are considered to be representative of snow that has been on the ground for some time and has increased its strength (compared to newly fallen snow) by sintering.

Since newly fallen snow is a much weaker material than most soils, it seems reasonable to assume that it can have velocities even lower than those used above for soil 1. Also, my comparisons of travel time differences between geophones at the top and at the bottom of a snow cover indicated that  $c > V_1$ , although the experimental errors were too large to give accurate values. Accurate, in-situ measurements of snow's wave velocities are sorely needed.

Obtaining an accurate estimate of the permeability of a snow cover is also quite difficult. Measured values of this parameter vary considerably, again because of natural variations as well as experimental difficulties. Values reported for "new," low density snow range between  $10$  and  $90 \times 10^{-10} \text{ m}^2$  (Buser 1986, Chacho and Johnson 1987, Ishida 1965, Shimizu 1970, Sommerfeld and Racchio 1989). Chacho and Johnson (1987) also report values of up to  $600 \times 10^{-10} \text{ m}^2$  for large-grained, metamorphosed snow (i.e., depth hoar).

In addition to direct measurements of snow's permeability, there are two other approaches that can be used to estimate these values. First, acoustic experiments can be used to determine the effective flow resistivity of a snow cover, and thus the permeability. Nicolas et al. (1985) reported measured effective flow resistivity values of  $5$  to  $50 \text{ kN s m}^{-4}$ , which correspond to permeabilities of around  $36$  to  $4 \times 10^{-10} \text{ m}^2$ . The acoustic waveform modeling presented earlier in this report resulted in a value of  $20 \text{ kN s m}^{-4}$ , which converts to  $9 \times 10^{-10} \text{ m}^2$ . Additional measurements reported by Albert (1990) can be used to obtain permeability values ranging from  $5$  to  $20 \times 10^{-10} \text{ m}^2$  for seven different seasonal snow covers. (All of these permeability values treat the effective flow resistivity as the zero frequency value, since the corrections needed are small.)

Second, Shimuzu (1970) has presented a widely used empirical formula relating the snow grain diameter  $d$  to the permeability

$$k_s = 0.077 d^2 \exp \{-7.8 \rho_{\text{snow}} / \rho_{\text{water}}\}.$$

For snow of density  $200 \text{ kg m}^{-3}$ , this equation predicts permeability values of  $41$ ,  $160$  and  $650 \times 10^{-10} \text{ m}^2$  for typically observed grain sizes of  $0.5$ ,  $1$  and  $2 \text{ mm}$ . However, Sommerfeld (1987) has cautioned that this empirical relationship may lead to large errors, and the equation seems to predict values that are too

high compared with the measurements described above.

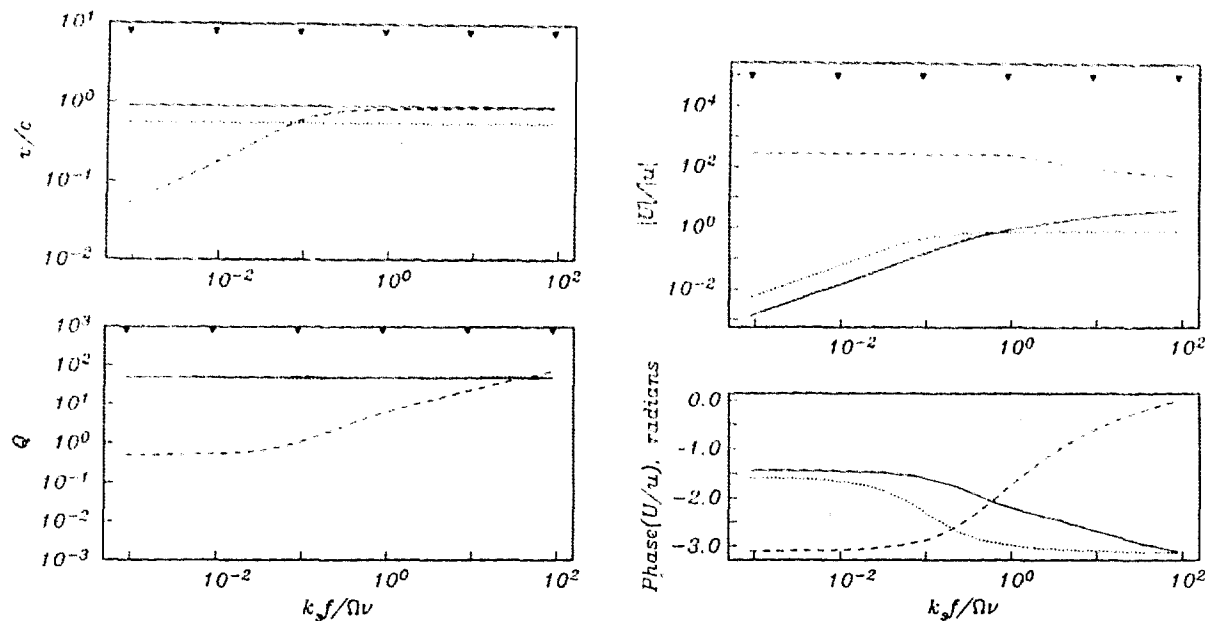
In view of the above discussion, a compressional wave velocity  $V_1$  of  $300 \text{ m s}^{-1}$ , a density of  $200 \text{ kg m}^{-3}$  and a Poisson's ratio of  $0.2$  have been assumed for a typical New England snow cover. These values imply a shear wave velocity  $V_3$  of  $180 \text{ m s}^{-1}$  and the other parameters listed in Table 14. A permeability value of  $10 \times 10^{-10} \text{ m}^2$  (in agreement with the measured values) was used.

Johnson (1982) has previously applied Biot's theory to predict the acoustic velocities and attenuations of waves propagating in snow. This study differs from Johnson's in that frame attenuations are included in these calculations, the frame velocity structure is different (Johnson used  $V_1 > c > V_3$  and  $V_1 > V_3 > c$ ), and these calculations include the coupling coefficients and reflection and transmission coefficients. Johnson (1985) studied transmission from air into snow, but in terms of a wave impedance formulation, which, although accurate for audible sound transmission, does not explicitly address transmission into  $P_1$  and  $S$  waves.

The results of the calculations for snow are shown in Figure 69. The  $P_1$ - and  $S$ -wave velocities are constant with respect to frequency, and the  $P_2$ -wave velocity increases with frequency, leveling off at a constant value at high frequencies. For this snow, the critical  $N_f$  occurs at about  $1.1 \text{ kHz}$ , and the high-frequency  $P_2$ -wave velocity value is just slightly less than the  $P_1$ -wave velocity ( $292$  vs  $300 \text{ m s}^{-1}$ ). The attenuation  $Q$  of the  $P_1$  and  $S$  waves is constant, while that for the  $P_2$  wave increases with frequency. The  $P_2$  coupling ratio is always at least an order of magnitude higher than the ratio for the other two waves, and the reflection and transmission coefficients are smoothly varying without critical angles.

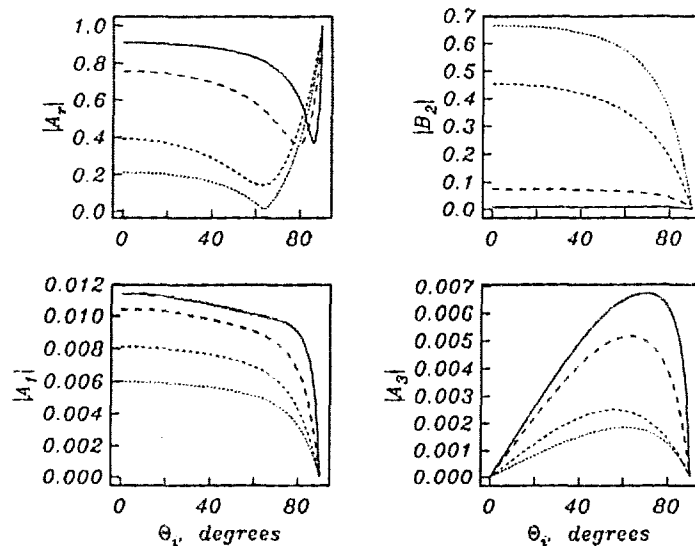
Comparison with Figure 65a shows that the velocities and attenuations are very similar to that for soil 1, as expected, since for both materials  $c > V_1 > V_3$ . The reflection and transmission coefficients are also similar. The shapes of the reflection and  $P_2$ -wave transmission coefficients are nearly identical, with the transmission coefficient for snow being larger at higher frequencies. The  $P_1$ - and  $S$ -wave transmission coefficients are of the same order of magnitude.

*Effect of permeability.* To investigate the effect of permeability on the predicted wave propagation properties of snow, the calculations were repeated for the same snow example, with the permeability varied over the very wide range from  $10^3$  to  $10^{-1} \times 10^{-10} \text{ m}^2$ , while the rest of the input parameters remained unchanged. The results are shown in Figures 70 to 73.



a. Velocities (top) and attenuation.

b. Magnitude (top) and phase.



c. Plane wave reflected and transmitted displacement potential amplitude coefficients for a wave incident on an air/air-filled snow interface as a function of incident angle.

Figure 69. Acoustic properties predicted by the Biot theory for snow 1 (see Table 14 for the parameters used to make these predictions). Velocities, attenuation, magnitude and phase of the fluid/solid displacement ratios for the three types of waves as a function of the poro-viscous frequency number  $N_f$ . Solid lines are plotted for the  $P_1$  (fast compressional) wave, dashed lines for the  $P_2$  (slow compressional) wave, and dotted lines for the  $S$  (shear) wave. The solid line is for a frequency of 10 Hz; progressively shorter dashed lines correspond to frequencies of 10<sup>2</sup>, 10<sup>3</sup> and 10<sup>4</sup> Hz.

As expected, decreasing the permeability is equivalent to increasing  $N_f$  and linearly shifts the velocity and coupling coefficient curves to higher frequencies. Figure 70 shows the  $P_2$ -wave velocity for three different permeabilities; the other wave velocities remain constant and are omitted from the plot. The

figure shows that the  $P_2$ -wave velocity at low frequencies is higher for snow of higher permeability, since the  $P_2$  wave can propagate, rather than diffuse, through the more open pore structure. At higher frequencies, the velocities become constant and identical.

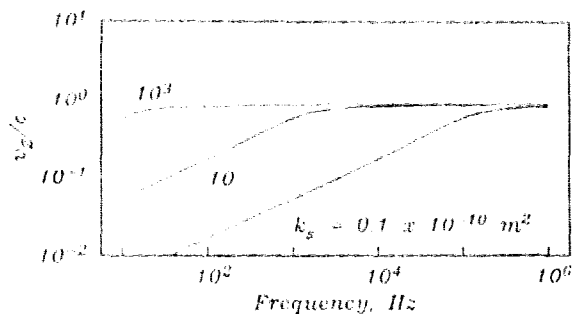


Figure 70.  $P_2$ -wave velocity as a function of frequency for snow with permeability values of 0.1, 10 and  $10^3 \times 10^{-10} \text{ m}^2$ . The other input parameters are the same as those for snow 1 in Table 14.

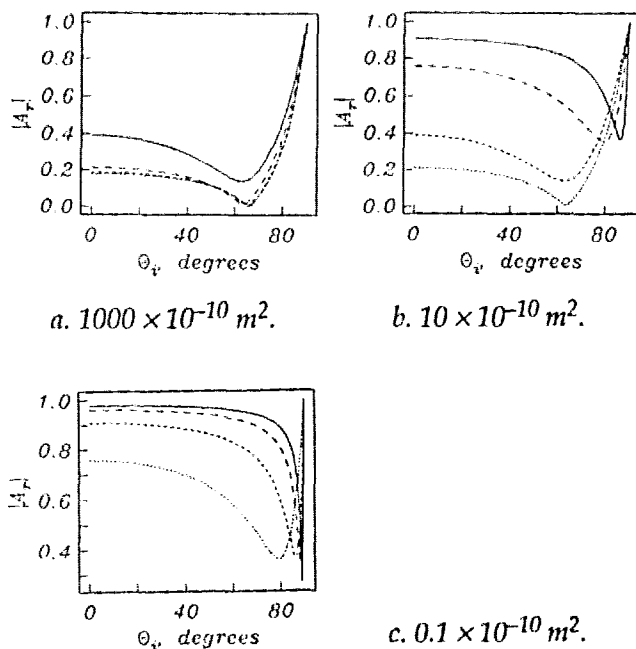


Figure 71. Plane wave potential amplitude reflection coefficient  $|A_r|$  for a wave incident on an air/snow interface as a function of incident angle. The snow permeabilities are  $1000 \times 10^{-10}$ ,  $10 \times 10^{-10}$  and  $0.1 \times 10^{-10} \text{ m}^2$ , with the other parameters for snow 1 listed in Table 14. Solid lines are for a frequency of 10 Hz; progressively shorter dashed lines correspond to frequencies of  $10^2$ ,  $10^3$  and  $10^4$  Hz.

The effect of the permeability on the reflection and transmission coefficients is shown in the following figures. Figure 71 shows that as the permeability decreases, the reflection coefficient  $|A_r|$  increases and approaches 1 for all angles of incidence and all frequencies. Also, the  $P_2$ -wave transmission coefficient decreases dramatically (Fig. 72). Both of these results show that the snow becomes acoustically harder as the permeability decreases; that is, more incident energy is reflected back into the air and less is transmit-

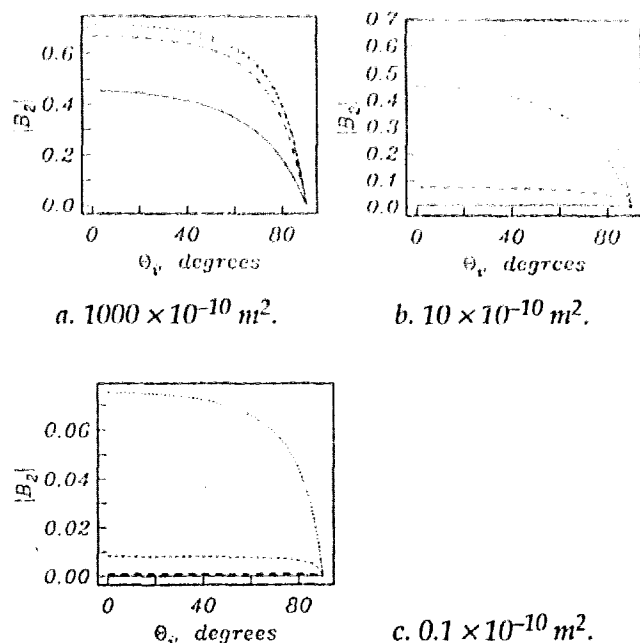


Figure 72. Plane wave potential amplitude transmission coefficient  $|B_2|$  (slow compressional waves) for a wave incident on an air/snow interface as a function of incident angle. The snow permeabilities are  $1000 \times 10^{-10}$ ,  $10 \times 10^{-10}$  and  $0.1 \times 10^{-10} \text{ m}^2$ , with the other parameters for snow 1 listed in Table 14. Solid lines are for a frequency of 10 Hz; progressively shorter dashed lines correspond to frequencies of  $10^2$ ,  $10^3$  and  $10^4$  Hz.

ted into the snow. The much smaller  $P_1$ - and S-wave transmission coefficients lose their frequency dependence by approaching the low-frequency (10 Hz) curves, with peak values near 0.012 and 0.008 respectively (Fig. 73).

**Different types of snow.** Two additional calculations were carried out, using parameters representing a very low density snow (snow 2) and the harder snow (snow 3) measured by Yamada et al. (1974) and used in Johnson's (1982) calculations. The properties of these materials are listed in Table 14, and the calculated results are given in Figure 74. These examples are intended to show how normally encountered variations in seasonal snow properties affect wave propagation.

Comparing the three types of snow in order of increasing frame stiffness (Fig. 74a, 69 and 74b) reveals a number of patterns. First, the  $P_1$ - and S-wave velocities increase as the snow frame becomes stiffer, while the high-frequency asymptotic value of the  $P_2$  wave remains constant and  $\approx c$ . Thus, the  $P_1$  and S velocities may be faster or slower than the  $P_2$  velocity, depending on the snow characteristics. Second, the displacement ratio  $|U|/|u|$  for  $P_2$  waves in-

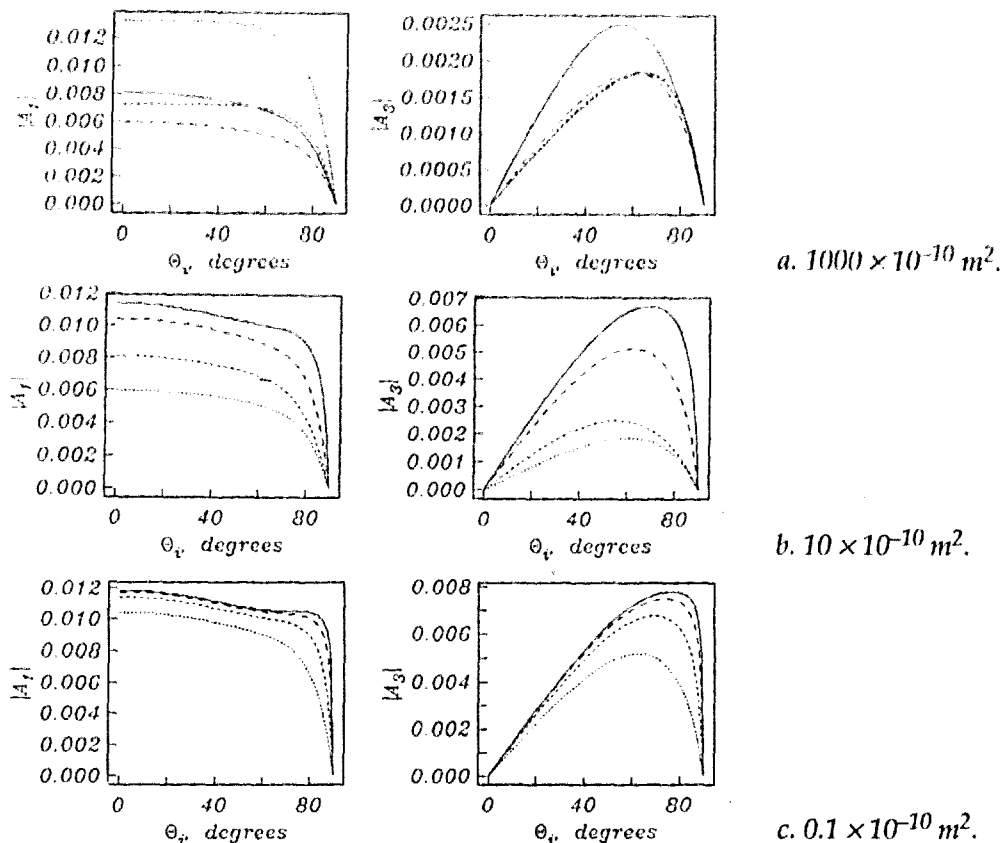


Figure 73. Plane wave potential amplitude transmission coefficients  $|A_1|$  (fast compressional waves) and  $|A_3|$  (shear waves) for a wave incident on an air/snow interface as a function of incident angle. The snow permeabilities are  $1000 \times 10^{-10}$ ,  $10 \times 10^{-10}$  and  $0.1 \times 10^{-10} \text{ m}^2$ , with the other parameters for snow 1 listed in Table 14. Solid lines are for a frequency of 10 Hz; progressively shorter dashed lines correspond to frequencies of 10<sup>2</sup>, 10<sup>3</sup> and 10<sup>4</sup> Hz.

creases from  $\sim 50$  to  $10^4$  as the frame stiffness increases. Finally, as the frame stiffness increases, the reflection coefficient  $|A_r|$  increases while the transmission coefficient  $|B_2|$  decreases, with lower frequencies (i.e., those for which  $N_f < 0.1$ ) showing the greatest change. At higher frequencies, the reflection coefficient remains essentially unchanged. The  $P_1$ -wave transmission coefficient  $|A_1|$  generally decreases (except for possible critical angle peaks), and the S-wave transmission coefficient  $|A_3|$  increases, as the frame stiffness increases.

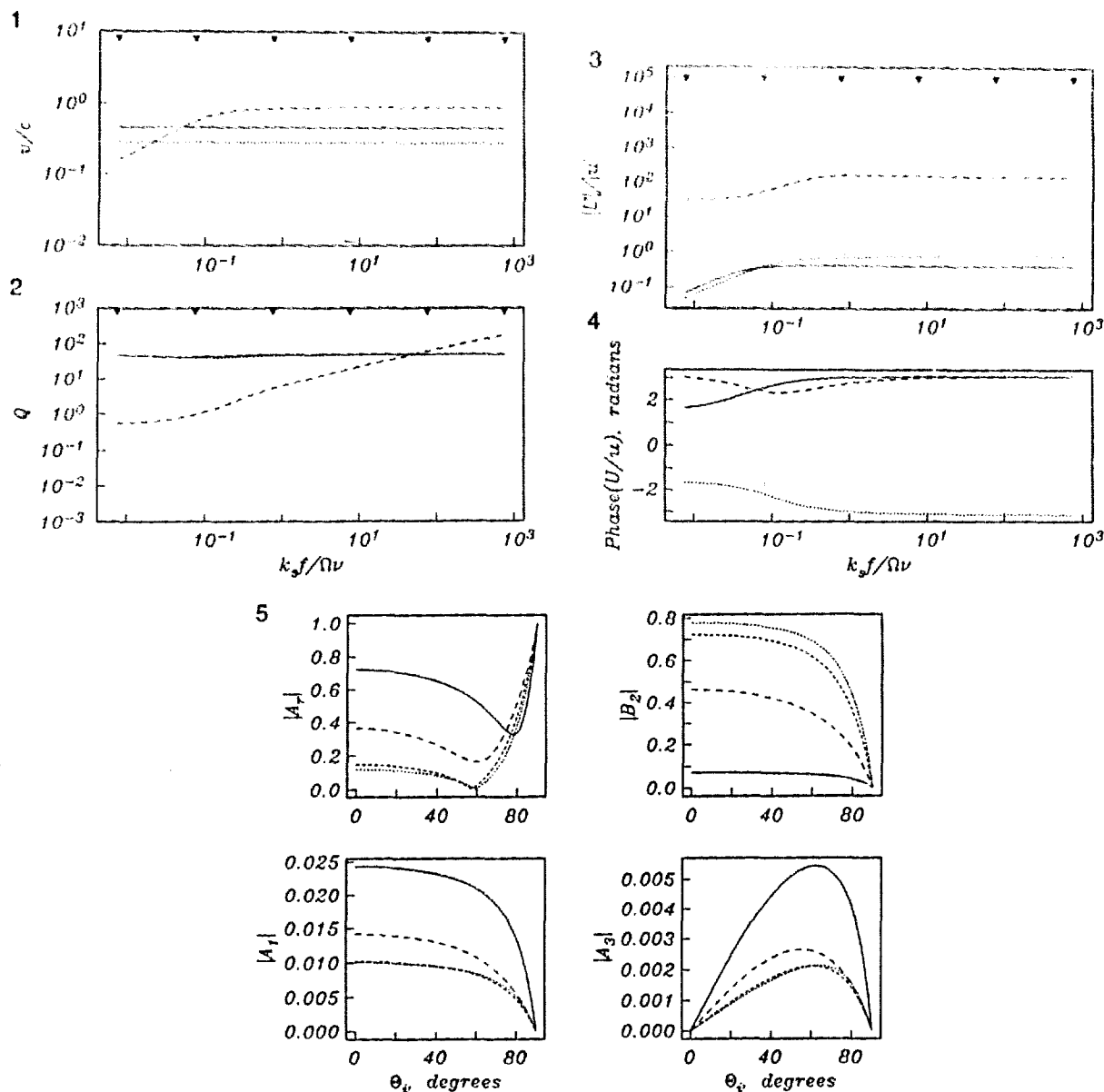
#### Summary of soil and snow modeling

Generally, the predicted acoustic properties of snow are quite similar to those predicted for surface soils. The main difference between the two materials is that the soil has lower permeability, a stiffer solid frame (i.e., higher  $P_1$ - and S-wave velocities), and less frame attenuation. Thus, except for the possible influence of critical angles, the transmission of plane waves from air into the porous material is predicted to be higher for snow than soil for all three wave

types. The largest transmission coefficient  $|B_2|$  is typically twice as large for snow than for soil at a given frequency, and this increase is caused by snow's larger permeability. The  $P_1$ - and S-wave transmission coefficients,  $|A_1|$  and  $|A_3|$ , are larger for snow because of its lower frame stiffness. These results agree with the observation that sound propagating in the atmosphere will be more strongly attenuated when snow is present on the ground because of increased transmission through, and less reflection from, the air/ground boundary.

As an illustration, Figure 75 shows the power spectral densities calculated for blank pistol shots experimentally recorded by a surface microphone 196 m away, with and without a snow cover present. The summer power spectral density shows a relatively flat shape out to about 400 Hz, while the winter power spectral density decays rapidly above 100 Hz. These differences are caused primarily by the relative absorption of sound by the ground as the wave propagates from the source to the receiver.

Figure 76 compares the calculated reflection and



a. Snow 2.

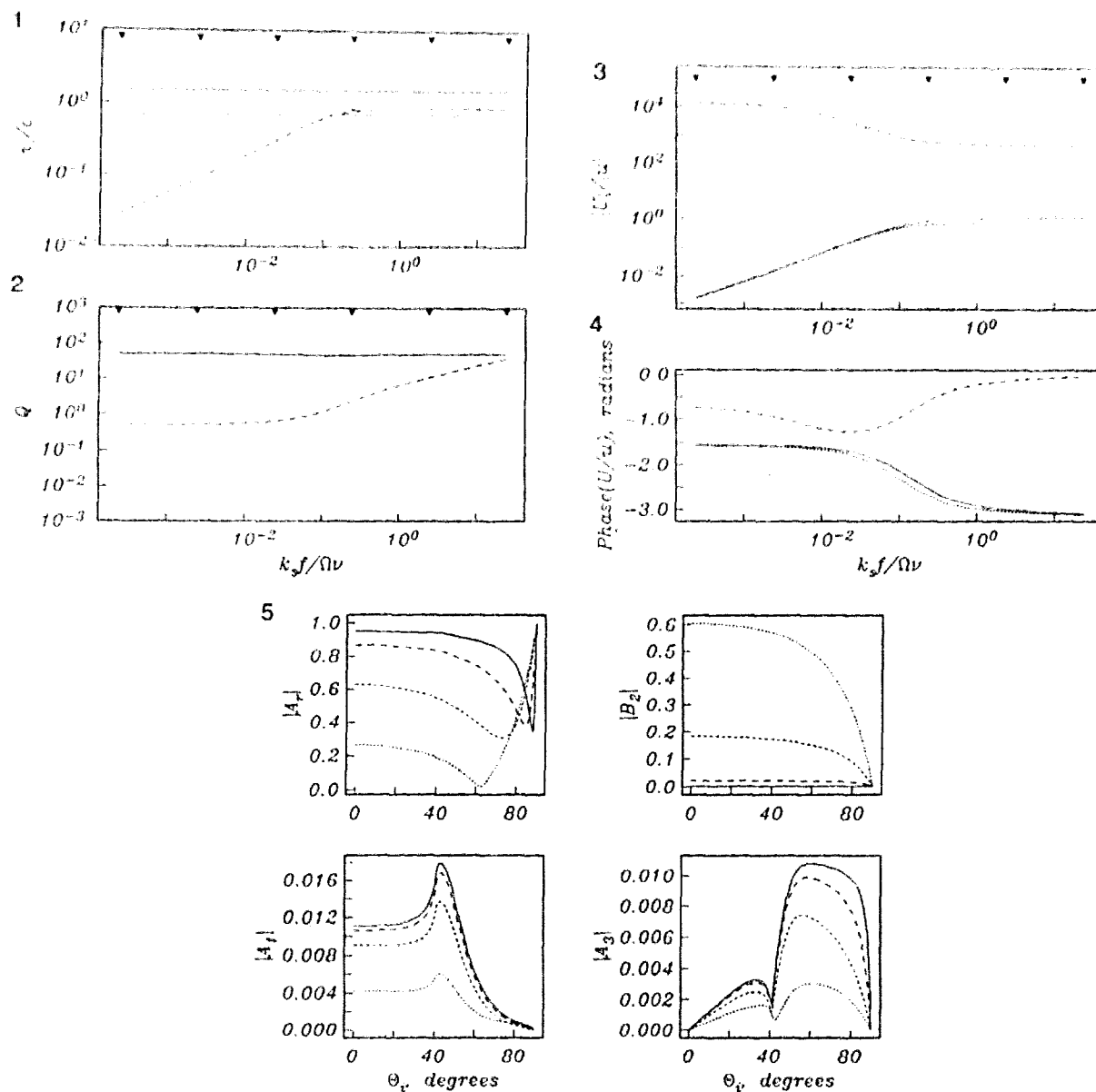
Figure 74. Acoustic properties predicted by the Biot theory (see Table 14 for the parameters used to make these predictions). (1) Velocities, (2) attenuation, (3) magnitude, and (4) phase of the fluid/solid displacement ratios for the three types of waves as a function of the poro-viscous frequency number  $N_f$ . Solid lines are plotted for the  $P_1$  (fast compressional) wave, dashed lines for the  $P_2$  (slow compressional) wave, and dotted lines for the S (shear) wave. (5) Plane wave reflected and transmitted displacement potential amplitude coefficients for a wave incident on an air/air-filled snow interface as a function of incident angle. The solid line is for a frequency of 10 Hz; progressively shorter dashed lines correspond to frequencies of  $10^2$ ,  $10^3$  and  $10^4$  Hz.

transmission coefficients for soil 1 and snow 4 of Table 14; these models are based on the properties at the experimental site determined by the seismic refraction measurements of the *Site Characterization* section and the modeling of the previous section. At 100 Hz, the reflection coefficient is seen to be higher for soil than for snow, while the transmission coefficients are all higher for snow than for soil. Thus, these calcu-

lations predict the preferential attenuation of high frequencies by snow in winter seen in the measured data of Figure 75.

### Summary

Calculations using Biot's theory have been made to investigate the properties of air-filled porous materials. These calculations show that such materials



b. Snow 3.

Figure 74 (cont'd). Acoustic properties predicted by the Biot theory (see Table 14 for the parameters used to make these predictions). (1) Velocities, (2) attenuation, (3) magnitude, and (4) phase of the fluid/solid displacement ratios for the three types of waves as a function of the poro-viscous frequency number  $N_f$ . Solid lines are plotted for the  $P_1$  (fast compressional) wave, dashed lines for the  $P_2$  (slow compressional) wave, and dotted lines for the S (shear) wave. (5) Plane wave reflected and transmitted displacement potential amplitude coefficients for a wave incident on an air/air-filled snow interface as a function of incident angle. The solid line is for a frequency of 10 Hz; progressively shorter dashed lines correspond to frequencies of  $10^2$ ,  $10^3$  and  $10^4$  Hz.

have  $P_1$ - and S-wave velocities that are essentially independent of frequency, with a  $P_2$  velocity that increases at low frequencies and levels off at a constant value at high frequencies. The fast and shear wave attenuations are constant, while the slow compressional wave attenuation decreases with frequency for these materials. The slow compressional wave's

fluid/solid coupling coefficient is greater than 100 for air-filled materials, implying that the wave motion is decoupled from the solid.

Calculations of plane wave transmission into this type of porous material shows that transmission to  $P_2$  waves is the most important.

Calculations for soil and snow show that the frame



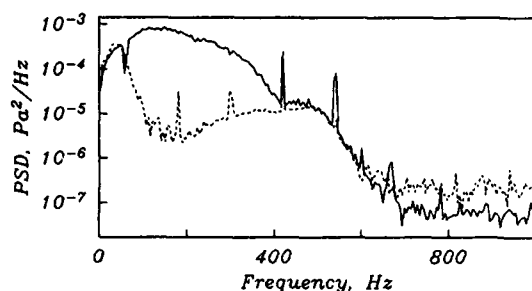


Figure 75. Power spectral densities for surface microphones in the summer (solid line) and winter (dashed line). The source was a blank .45 caliber pistol shot, 1 m high in the air and 196 m east of the microphone location. The sharp peaks in both spectra are at multiples of 60 Hz and are considered to be noise. A 60-Hz notch filter was used in the summer recording and is visible in the plot.

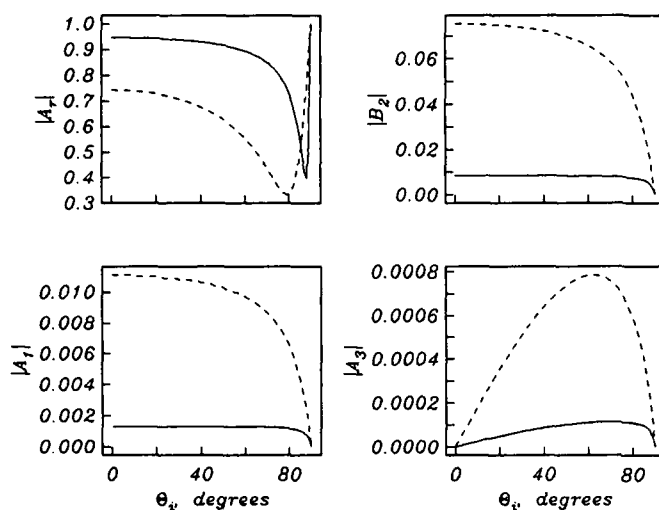


Figure 76. Plane wave reflected and transmitted displacement potential amplitude coefficients for a wave incident on an air/air-filled porous solid interface as a function of incident angle. The solid line is for soil 1, the dashed line for snow 4 (see Table 14). The calculations were done at a frequency of 100 Hz.

stiffness and the permeability are the most important parameters controlling the acoustic properties of these materials. The calculations also show that the greater permeability for snow leads to higher transmission coefficients, especially for  $P_2$  waves, and is responsible for the increased attenuation of airborne sound when a snow cover is present.

The calculations presented here have lead to greater insight into the controlling parameters and the physics of wave propagation in porous materials. Additional experimental work is planned to confirm the calculations. Sonic velocity and attenuation measurements as a function of frequency are planned in conjunction with in-situ permeability measurements; these measurements will be used to validate these calculations.

## CONCLUSIONS

This report describes the results of detailed measurements on the attenuation of sound propagating over grassland and snow. The experiments were conducted under conditions as controlled as possible for field work in a realistic environment, and were

supplemented with extensive site characterization measurements. The careful design of these experiments allowed the identification and accurate determination of velocities and amplitude decay rates for both the early arriving, low-amplitude body waves as well as the larger-amplitude air waves. Marked changes in the waveforms and decay rates were observed when a snow cover was present. The body wave amplitudes actually increased, because their coupling into the ground near the source was enhanced by the impedance matching effect of the snow. The air wave arrival was strongly attenuated by the snow cover, and a low-frequency, air-coupled, dispersive wave train appeared in both the microphone and geophone waveforms.

A model treating the ground as a rigid porous material was shown to be fully successful in matching the observed microphone waveforms and amplitude decay rates. This model provides a useful tool for the prediction of expected sound levels from impulsive sources in practical situations. A numerical procedure for calculating the induced ground motion from sources in the air was less successful; it correctly predicted the observed amplitude decay rates and the waveforms under summer conditions,

but failed when snow was present. This failure was shown to be a limitation of the model of the ground that was used; the viscoelastic treatment ignores the effect of the pores in the snow, a cause of substantial attenuation of the air wave.

Preliminary calculations using Biot's theory of wave propagation in porous materials show that this model correctly predicts the differential absorption of high frequencies caused by the presence of a snow cover; the increased attenuation is caused mainly by the higher permeability of snow compared to soil.

Many questions remain unanswered, and additional work is needed, both experimentally and theoretically, to understand fully the effect of snow on acoustic wave propagation.

One obvious gap is the need for additional measurements over a variety of snow covers to determine the range and effect of different snow properties on acoustic waves. Some of this work has already been done and reported in Albert (1990). Those measurements support the claimed importance of the snow permeability on the measured attenuation, as two snow covers with markedly different mechanical strengths (one a newly fallen, light powder, the other a highly sintered layer that could be walked upon without leaving footprints) gave similar attenuation rates.

Detailed measurements of the properties of seasonal snow covers, especially the *P*- and *S*-wave velocities and the permeability, are also sorely needed, both for general interest and in conjunction with acoustic experiments. Test equipment is currently under development to allow the wave speeds to be measured using high-frequency pulses; the main experimental problem to be solved is how to couple the transducers to the snow. A permeability meter based on the design of Chacho and Johnson (1987) is also under construction.

The most important theoretical work to be done is to extend the numerical method of calculating acoustically induced ground motion to include porous materials. The needed plane wave reflection and transmission coefficients were derived in the previous section. The next step is to incorporate these coefficients into the wavenumber integration code in place of the viscoelastic coefficients currently used. The same recursion scheme can then be adapted to determine the generalized reflection and transmission response of the layered model, determine the harmonic coefficients  $C_i^m$  of eq 47, and integrate. In principle, the present Fortran code can be modified; however, such changes will be quite tedious and ex-

tensive because the current  $4 \times 4$  sub-matrices used throughout for the viscoelastic *P*-*SV* system become  $6 \times 6$  sub-matrices in the porous *P*<sub>1</sub>-*P*<sub>2</sub>-*S* case, and all of the manual array indexing will need to be rewritten. It may be less time consuming to simply rewrite this part of the code, and then call the integration subroutines to calculate the response. One of the strengths of the present wavenumber integration code is its stability at all frequencies and wavenumbers. This stability results in part from a special reparameterization at large wavenumbers (Apsel 1979); a new derivation of these equations will also be needed for the porous case.

## LITERATURE CITED

- Aki, K. and P.G. Richards (1980). *Quantitative Seismology*. San Francisco: W.H. Freeman and Company.
- Albert, D.G. (1986) FORTRAN subroutines for zero-phase digital frequency filters. USA Cold Regions Research and Engineering Laboratory, Special Report 86-4.
- Albert, D.G. (1987a) Recent research on acoustic to seismic coupling. In *Proceedings of the DOD Symposium and Workshop on Arctic Environmental Sciences*, 27-30 January, Laurel, Maryland. Hampton, Virginia: Science and Technology Corp., p. 223-225.
- Albert, D.G. (1987b) The effect of snow on vehicle-generated seismic signatures. *Journal of the Acoustical Society of America*, 81: 881-887.
- Albert, D.G. (1990) Preliminary analysis of measured sound propagation over various seasonal snow covers. *Proceedings of the Fourth International Conference on Long Range Sound Propagation*, 16-17 May, Hampton, Virginia. Washington D.C.: National Aeronautics and Space Administration, Conference Publication 3101, p. 51-57.
- Albert, D.G. and J. Orcutt (1989) Observations of low frequency acoustic-to-seismic coupling in the summer and winter. *Journal of the Acoustical Society of America*, 86: 352-359.
- Albert, D.G. and J.A. Orcutt (1990) Acoustic pulse propagation above grassland and snow: Comparison of theoretical and experimental waveforms. *Journal of the Acoustical Society of America*, 87: 93-100.
- ANSI S1.26 (1978) *American National Standard Method for the Calculation of the Absorption of Sound by the Atmosphere*. New York: American National Standard Institute.
- Apsel, R.J. (1979) Dynamic Green's functions for layered media and applications to boundary-value

- problems. Ph.D. Dissertation, University of California at San Diego, La Jolla, California (unpublished).
- Attenborough, K.** (1985) Acoustical impedance models for outdoor ground surfaces. *Journal of Sound and Vibration*, **99**: 521-544.
- Attenborough, K.** (1987) On the acoustic slow wave in air-filled granular media. *Journal of the Acoustical Society of America*, **81**: 93-102.
- Attenborough, K. and O. Buser** (1988) On the application of rigid-porous models to impedance data for snow. *Journal of Sound and Vibration*, **124**: 315-327.
- Attenborough, K. and T.L. Richards** (1989) Solid particle motion induced by a point source above a poroelastic half-space. *Journal of the Acoustical Society of America*, **86**: 1085-1092.
- Attenborough, K., J.M. Sabatier, H.E. Bass and L.N. Bolen** (1986) The acoustic transfer function at the surface of a layered poroelastic soil. *Journal of the Acoustical Society of America*, **79**: 1353-1358.
- Attenborough, K., S.I. Hayek and J.M. Lawther** (1980) Propagation of sound above a porous half-space. *Journal of the Acoustical Society of America*, **68**: 1493-1501.
- Attenborough, K.E.** (1983) Acoustical characteristics of rigid fibrous absorbents and granular materials. *Journal of the Acoustical Society of America*, **73**: 785-799.
- Barry, K.M., D.A. Cavers and C.W. Kneale** (1975) Recommended standards for digital tape formats. *Geophysics*, **40**: 344-352.
- Bass, H.E., L.N. Bolen, D. Cress, J. Lundien and M. Flohr** (1980) Coupling of airborne sound into the earth: frequency dependence. *Journal of the Acoustical Society of America*, **67**: 1502-1506.
- Biot, M.A.** (1956a) Theory of propagation of elastic waves in a fluid-saturated porous solid. I. Low-frequency range. *Journal of the Acoustical Society of America*, **28**: 168-178.
- Biot, M.A.** (1956b) Theory of propagation of elastic waves in a fluid-saturated porous solid. II. Higher frequency range. *Journal of the Acoustical Society of America*, **28**: 179-191.
- Biot, M.A.** (1962) Mechanics of deformation and acoustic propagation in porous media. *Journal of Applied Physics*, **33**: 1482-1498.
- Brekhovskikh, L.M.** (1980) *Waves in Layered Media*, Second Edition. New York: Academic Press, p. 17.
- Buser, O.** (1986) A rigid frame model of porous media for the acoustic impedance of snow. *Journal of Sound and Vibration*, **111**: 71-92.
- Chacho, E.F. and J.B. Johnson** (1987) Air permeability of snow. *EOS (Transactions of the American Geophysical Union)*, **68**: 1271 (abstract).
- Chessell, C.I.** (1977) Propagation of noise along a finite impedance boundary. *Journal of the Acoustical Society of America*, **62**: 825-834.
- Colbeck, S.C., E. Akitaya, R. Armstrong, H. Gubler, J. Lafeuille, K. Lied, D. McClung and E. Morris** (1990) *The International Classification for Seasonal Snow on the Ground*. The International Commission on Snow and Ice of the International Association of Scientific Hydrology (available from the World Data Center, University of Colorado, Boulder).
- Delaney, M.E. and E.N. Bazley** (1970) Acoustical properties of fibrous absorbent materials. *Applied Acoustics*, **3**: 105-116.
- Doll, C.G., W.M. Cady, J.B. Thompson, Jr. and M.P. Billings** (1961). *Centennial geologic map of Vermont*. Montpelier, Vermont: Vermont Geological Survey 1970.
- Don, C.G., and A.J. Cramond** (1987) Impulse propagation in a neutral atmosphere. *Journal of the Acoustical Society of America*, **81**: 1341-1349.
- Dongarra, J.J., J.R. Bunch, C.B. Molar and G.W. Stewart** (1979) *LINPACK User's Guide*. Philadelphia: SIAM.
- Embleton, T.F.W. and G.A. Daigle** (1987) Near-ground sound fields and surfaces of finite impedance. *Journal of the Acoustical Society of America*, **82**: S76.
- Embleton, T.F.W., J.E. Piercy and G.A. Daigle** (1983) Effective flow resistivity of ground surfaces determined by acoustical measurements. *Journal of the Acoustical Society of America*, **74**: 1239-1244.
- Embleton, T.F.W., J.E. Piercy and N. Olson** (1976) Outdoor sound propagation over ground of finite impedance. *Journal of the Acoustical Society of America*, **59**: 267-277.
- Gassmann, F.** (1951) Elastic waves through a packing of spheres. *Geophysics*, **16**: 673-685.
- Gubler, H.** (1977) Artificial release of avalanches by explosives. *Journal of Glaciology*, **19**: 419-429.
- Gudesen, A.** (1985) Air to ground coupling on a sandy soil in northwest Germany. In *Proceedings of the Second Symposium on Long Range Sound Propagation and Seismic/Acoustic Coupling, February 13-16, New Orleans, Louisiana* (H.E. Bass and K. Attenborough, Ed.). Oxford, Mississippi: University of Mississippi, 1985, p. 405-423.
- Harris, F.J.** (1978) On the use of windows for harmonic analysis with the discrete Fourier transform. *Proceedings of the Institute of Electrical and Electronic Engineers*, **66**: 51-83.
- Hatherly, P.J.** (1982) A computer method for determining seismic first-arrival times. *Geophysics*, **47**: 1431-1436.

- Hess, H.M., K. Attenborough and N.W. Heep (1990) Ground characterization by short-range propagation measurements. *Journal of the Acoustical Society of America*, 87: 1975-1986.
- Hoover, G.M. and J.T. O'Brien (1980) The influence of the planted geophone on seismic land data. *Geophysics*, 45: 1239-1253.
- Hunt, R.E. (1984) *Geotechnical Engineering Investigation Manual*. New York: McGraw-Hill, p. 154.
- Ishida, T. (1965) Acoustic properties of snow. *Contributions from the Institute of Low Temperature Science*, Ser. A, 20, 23-68.
- Johnson, D.H. and M.N. Toksoz (1981). *Seismic Wave Attenuation*. Tulsa: Society of Exploration Geophysicists, p. 1-5.
- Johnson, J.B. (1985) Audibility within and outside deposited snow. *Journal of Glaciology*, 31: 136-142.
- Johnson, J.B. (1982) On the application of Biot's theory to acoustic wave propagation in snow. *Cold Regions Science and Technology*, 6: 49-60.
- Kennett, B.L.N. (1983) *Seismic Wave Propagation in Stratified Media*. Cambridge, England: Cambridge University Press.
- Knapp, R.W. (1986) Observations of the air-coupled wave as a function of depth. *Geophysics*, 51: 1853-1857.
- Krohn, C.E. (1984) Geophone ground coupling. *Geophysics*, 49: 722-731.
- Mooney, H.M. (1973) *Handbook of Engineering Geophysics*. Minneapolis, Minnesota: Bison Instruments, Inc.
- Nicolas, J., J.-L. Berry and G.A. Daigle (1985) Propagation of sound above a finite layer of snow. *Journal of the Acoustical Society of America*, 77: 67-73.
- Northwood, E.J., R.C. Weisinger and J.J. Bradley (1967) Recommended standards for digital tape formats. *Geophysics*, 32: 1073-1084.
- Peck, L. (1987) Acoustic-to-seismic coupling through a snow layer. In *Proceedings of SNOW Symposium IV*, August, 1986, Hanover, New Hampshire (A.W. Hogan and R. Redfield, Ed.). USA Cold Regions Research and Engineering Laboratory, Special Report 87-12.
- Raspet, R., H.E. Bass and J. Ezell (1983) Effect of finite ground impedance on the propagation of acoustic pulses. *Journal of the Acoustical Society of America*, 74: 267-274.
- Raspet, R., J. Ezell and H.E. Bass (1985) Additional comments on and erratum for "Effect of finite ground impedance on the propagation of acoustic pulses" (*Journal of the Acoustical Society of America*, 74: 267-274 [1983]), *Journal of the Acoustical Society of America*, 77: 1955-1958.
- Richards, T.L., K. Attenborough, N.W. Heep and A.P. Watson (1985) Penetration of sound from a point source into a rigid porous medium. *Journal of the Acoustical Society of America*, 78: 956-963.
- Sabatier, J.M., H.E. Bass and G.R. Elliott (1986c) On the location of frequencies of maximum acoustic-to-seismic coupling. *Journal of the Acoustical Society of America*, 80: 1200-1202.
- Sabatier, J.M., H.E. Bass L.N. Bolen and K. Attenborough (1986a) Acoustically induced seismic waves. *Journal of the Acoustical Society of America*, 80: 646-649.
- Sabatier, J.M., H.E. Bass, L.N. Bolen, K. Attenborough and V.V.S.S. Sastry (1986b) The interaction of airborne sound with the porous ground: The theoretical formulation. *Journal of the Acoustical Society of America*, 79: 1345-1352.
- Sheriff, R.E. and L.P. Geldart (1982) *Exploration Seismology*. New York: Cambridge University Press.
- Shimuzu, H. (1970) Air permeability of deposited snow. *Contributions from the Institute of Low Temperature Science*, Series A, Hokkaido University, Sapporo, Japan, 1-32.
- Sommerfeld, R.A. (1987) The permeability of snow. *EOS (Transactions of the American Geophysical Union)* 68: 1271 (Abstract).
- Sommerfeld, R.A. and J. Rocchio (1989) The Darcy permeability of fine-grained compact snow. *Proceedings of the 46th Annual Eastern Snow Conference*, 8-9 June 1989, Quebec City, Quebec, p. 121-128.
- Stewart, D.P. and P. McClintock (1970). *Surficial geologic map of Vermont*. Montpelier, Vermont: Vermont Geological Survey.
- Stoll, R.D. (1974) Acoustic waves in saturated sediments. In *Physics of Sound in Marine Sediments* (L. Hampton, Ed.). New York: Plenum Press, p. 19-39.
- Stoll, R.D. and T.-K. Kan (1981) Reflection of acoustic waves at a water-sediment interface. *Journal of the Acoustical Society of America*, 77: 149-156.
- Stoll, R.D. and G.M. Bryan (1970) Wave attenuation in saturated sediments. *Journal of the Acoustical Society of America*, 47: 1440-1447.
- Turcotte, D.L. and G. Schubert (1982) *Geodynamics*. New York: John Wiley and Sons.
- van Hoof, H. (1985). Acoustic/seismic measurements in the Netherlands. *Proceedings of the Second Symposium on Long Range Sound Propagation and Seismic/Acoustic Coupling*, February 13-16, 1985, New Orleans, Louisiana, p. 453-463.
- van Hoof, H.A.J.M., and K.W.F.M. Doorman (1983). Coupling of airborne sound in a sandy soil. Oegstgeest: Netherlands Organization for Applied

Scientific Research, Laboratory for Electronic Developments for the Armed Forces, 1983) TNO/LEOK Report No. TR 1983-09.

**White, J.E.** (1983) *Underground Sound*. New York: Elsevier, p. 60.

**Yamada, T., T. Hasemi, K. Izumi and A. Sato** (1974) On the dependencies of the velocities of P- and S-waves and thermal conductivity of snow upon the

texture of snow. *Low Temperature Science, Ser A*(32): 71-80, (in Japanese with English summary).

**Yamamoto, T.** (1983a) Propagator matrix for continuously layered porous seabeds. *Bulletin of the Seismological Society of America*, 73: 1599-1620.

**Yamamoto, T.** (1983b) Acoustic propagation in the ocean with a poro-elastic bottom. *Journal of the Acoustical Society of America*, 73: 1587-1596.

## APPENDIX A: CONVERSION OF DATA FROM SEG Y IBM FLOATING POINT FORMAT

The Fortran fragment below shows how the conversion from the 4 byte SEG Y IBM floating point format to a Fortran real variable was accomplished. The conversion relies on two non-standard functions:

- (1) RS(x,num): shifts the contents of x num bits to the right.
- (2) AND(x,y): binary "and" operator. The individual bits are set to 1 if either of the arguments have a 1 in that bit location, and 0 if neither have a 1 at that bit location, e.g. the call AND(1010,0011) returns the value 1011.

The notation :num indicates that num is a hex number.

```

      INTEGER*4 IMANT,SIXTEEN
      INTEGER*2 IM(2),NUMP
      REAL*4 PDAT(6000)
      EQUIVALENCE(IMANT,IM(1))
      DATA SIXTEEN/16/
C      XCORR = 5.96E-8
      XCORR = 2.**(-24.)
C
      NUMP = 0
      DO 10 I = 121,ICNT,2
                                     /* index for the data points
                                     /* skip over the trace header,
                                     /* then step through the data

      NUMP = NUMP+1
      ISIGN = RS(IDAT(I),15)
                                     /* decode the sign
      IF(ISIGN.EQ.1) ISIGN = -1
      IF(ISIGN.EQ.0) ISIGN = 1
      IXPN = AND(RS(IDAT(I),8),:177)
                                     /* decode the exponent
      IM(1) = DAT(I)
                                     /* decode the mantissa
      IM(2) = IDAT(I+1)
      IM(1) = AND(IM(1),:377)
      XMANT = IMANT
      XMANT = XMANT*XCORR
C                                     /* convert to a real number
      PDAT(NUMP) = ISIGN*SIXTEEN**(IXPN-64)*XMANT
10    CONTINUE

```

## APPENDIX B: SEISMIC REFRACTION DATA

This appendix gives the travel time data obtained using the seismic refraction method. Figure 14 shows the locations of the sensor arrays, and Table 3 gives the results of inverting these data using the intercept time method.

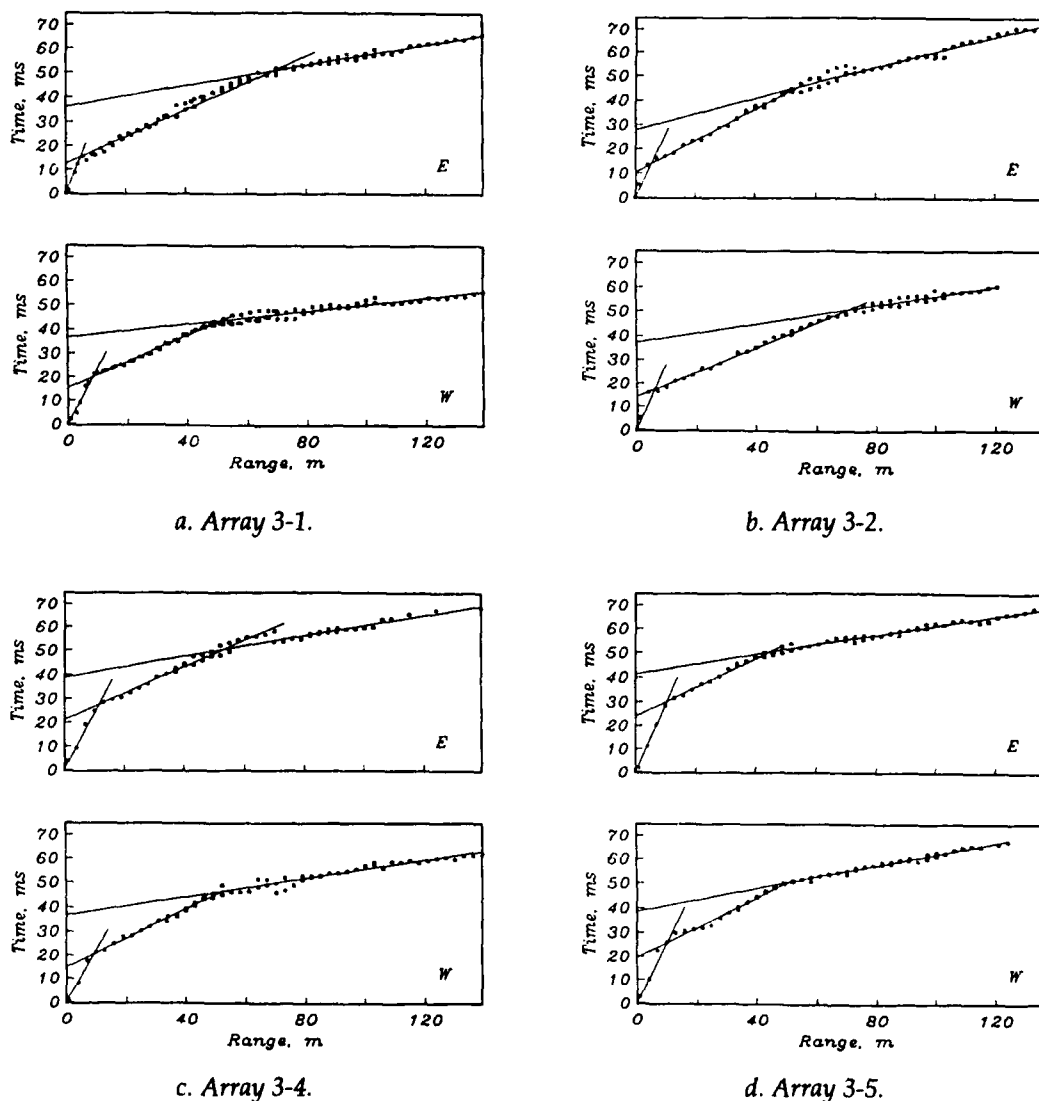
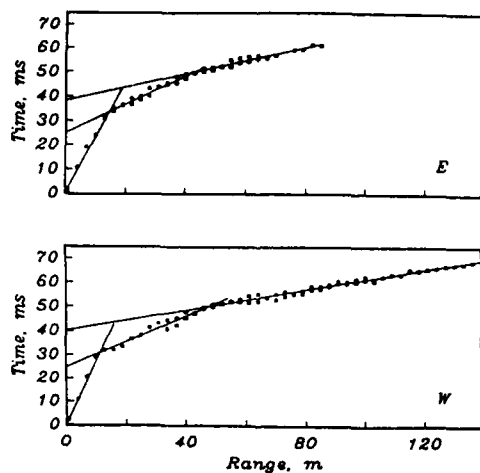
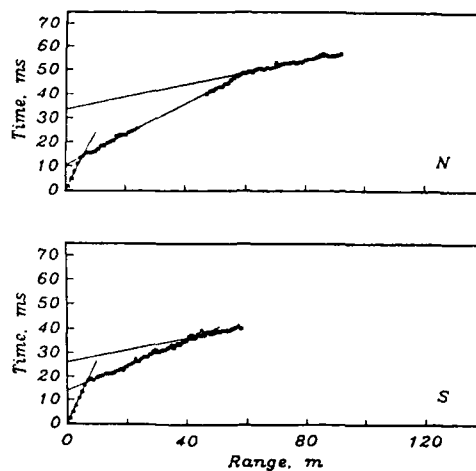


Figure B1. Distance vs travel time plots for P-wave refraction arrays. Squares are the first arrival times picked from the seismograms. The three line segments are least-squares fits to the travel times. Travel times for the source to the east (top) and west (bottom) of the array are shown.



e. Array 3-6.



f. Array 3-3.

Figure B1 (con't). Distance vs. travel time plots for P-wave refraction arrays. Squares are the first arrival times picked from the seismograms. The three line segments are least-squares fits to the travel times. Travel times for the source to the east (top) and west (bottom) of the array are shown.

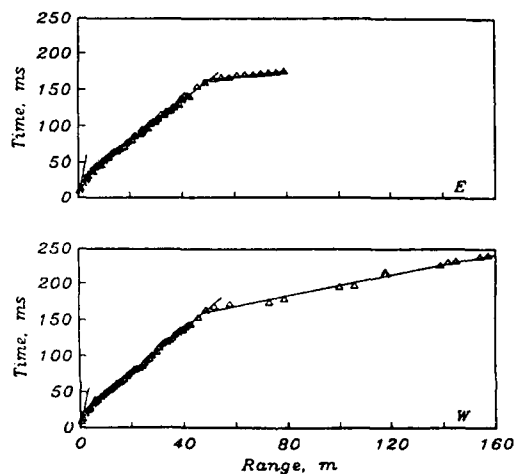


Figure B2. Distance vs. travel time plots for SH-wave refraction array 2. Triangles are the first arrival times picked from the seismograms. The three line segments are least-squares fits to the travel times. Travel times for the source to the east (top) and west (bottom) of the array are shown.



**APPENDIX C: METEOROLOGICAL DATA RECORDED AT  
THE CAMP ETHAN ALLEN TEST SITE, 6 JANUARY 1986**

Time (hr:min)	2 m high					6 m high				
	Temp (°C)	Humidity (%)	U(N)	V(E) (m/s)	W(V)	Temp (°C)	Humidity (%)	U(N)	V(E) (m/s)	W(V)
08:29	-16.6	81.5	0.0	0.0	0.0					
08:35	-16.4									
0x:xx	-14.9	77.5	0.1	0.0	0.0					
10:33	-9.7									
10:45	-9.0	44.3	0.0	0.0	0.0					
10:53	-8.5	43.2	0.1	0.0	0.0					
10:58	-8.6									
11:03	-8.8	42.8								
11:13	-8.6									
11:16	-8.5	41.5								
11:20	-8.1	41.3	-0.8	0.3	1.2					
11:23	-7.6	38.8	-0.5	0.1	0.8	-4.6	34.4	-0.4	0.0	0.0
11:29	-7.0	37.1	-0.7	0.2	1.1	-4.0	32.8	1.0	0.0	0.1
11:34	-6.6	37.8	-0.2	0.0						
13:37	-1.5	30.5	0.0	-0.7	0.0	1.7	24.8	0.0	-0.1	0.0
13:38	-2.0	31.9	0.0	0.0	0.3	1.6	25.3	0.0	0.0	0.0
13:39	-2.2	32.6	0.1	0.0	0.1	1.7	25.5	-0.2	0.0	0.0
13:40	-2.4	31.9	0.6	0.0	0.0	1.7	25.1	-0.3	0.0	0.0
13:41	-2.5	33.1	-0.3	0.0	1.0	1.6	25.2	-0.7	0.0	0.0
13:43	-3.2	36.2	-0.8	0.0	0.6	0.9	27.0	-0.8	0.0	0.0
13:44	-3.6	36.8	-0.5	0.0	0.1	0.6	27.6	-0.4	0.0	0.0
13:45	-3.7	36.5	-0.3	0.0	0.2	0.5	27.6	-0.3	0.0	0.0
13:47	-3.7	36.8	0.0	0.1	0.1	0.2	27.9	-0.8	0.0	0.0
13:48	-3.8	37.6	-0.4	0.0	0.9	0.2	28.2	-0.8	0.0	0.0
13:49	-4.0	-0.3	0.0	0.2		0.2	28.6	-0.7	0.0	0.0
13:51	-4.0	37.9	-0.2	0.0	0.2	0.2	29.2	-0.4	0.0	0.0
13:53	-3.7	37.1	0.0	0.0	0.0	0.2	28.7	-0.1	0.0	0.0
13:57	-3.2	36.7	-0.1	0.0	0.6	0.4	27.4	-0.6	0.0	0.1
13:58	-3.3	36.8	-0.3	0.0	0.0	0.4	27.7	-0.2	0.0	0.0
13:59	-3.4	36.3	-0.3	0.0	0.0	0.4	27.5	-0.4	0.0	0.0
14:00	-3.5	36.5	-0.3	0.0	0.0	0.4	27.4	-0.3	0.0	0.0
14:01	-3.4	36.4	-0.6	0.0	0.0	0.4	27.3	-0.4	0.2	0.0
14:06	-2.9	35.1	0.0	0.2	0.0	0.9	26.6	0.0	0.2	0.0
14:08	-2.9	35.2	0.0	0.5	0.6	1.2	25.6	0.1	0.4	-0.1
14:09	-3.0	35.6	0.0	0.7	0.7	1.4	25.4	0.0	0.6	0.0
14:12	-3.3	36.3	0.2	0.0	0.0	1.7	24.9	0.0	0.2	0.0
14:13	-3.3	36.3	0.0	0.2	0.0	1.8	24.4	0.0	0.0	0.0
14:19	-2.9	35.3	0.0	0.0	0.0	3.0	22.3	0.0	0.0	0.0
14:20	-2.8	35.1	0.0	0.0	0.0	3.1	22.0	0.0	0.0	0.0
14:21	-2.7	35.0	0.0	0.2	0.0	3.3	21.9	0.0	0.0	0.0
14:22	-2.7	35.4	0.0	0.2	0.0	3.4	21.8	0.0	0.0	0.0
14:25	-2.4	36.0	0.0	0.0	0.0	3.3	22.1	0.0	0.2	0.0
14:26	-2.4	36.2	1.2	0.0	0.0	3.2	22.4	0.0	0.2	0.0
14:27	-2.3	35.8	0.2	0.0	0.0	3.1	22.6	0.0	0.2	0.0
14:28	-2.3	35.7	0.7	0.0	0.0	3.0	22.9	0.0	0.4	0.0
14:29	-2.2	35.2	-0.2	0.0	0.1	2.9	23.1	-0.1	0.3	0.0
14:30	-2.2	35.5	-0.2	0.0	0.0	2.7	23.4	-0.2	0.4	0.0
14:31	-2.2	35.1	-0.3	0.0	0.0	2.5	23.8	-0.2	0.2	0.0
14:32	-2.2	34.6	-0.1	0.0	0.0	2.4	24.2	-0.4	0.0	0.0
14:34	-2.1	34.5	0.0	0.0	0.0	2.2	24.9	0.0	0.0	0.0
14:35	-1.9	34.9	0.0	0.0	0.0	2.3	24.5	0.0	0.0	0.0
14:36	-1.8	35.0	0.0	0.0	0.0	2.4	24.1	0.0	0.0	0.0
14:38	-1.6	33.3	-0.2	0.0	0.0	2.4	23.7	-0.3	0.0	0.0
14:39	-1.6	33.3	0.0	0.0	0.0	2.3	24.0	-0.3	0.0	0.0
14:40	-1.6	34.0	0.0	0.0	0.0	2.2	24.4	-0.5	0.0	0.0
14:41	-1.9	34.1	-0.4	0.0	0.0	2.0	24.8	-0.2	-0.1	0.0

14:42	-2.2	35.5	-0.4	-0.3	0.1	1.8	25.4	0.0	-0.4	0.0
14:43	-2.4	35.8	0.0	-0.2	0.1	1.6	25.9	0.0	-0.3	0.0
14:44	-2.6	36.1	0.0	-0.3	0.0	1.5	26.0	0.0	-0.3	0.0
14:45	-2.7	36.4	-0.1	-0.2	0.1	1.4	26.3	0.0	-0.3	0.0
14:46	-2.8	36.4	-0.2	-0.2	0.1	1.4	26.5	0.0	-0.2	0.0
14:48	-2.9	36.3	-0.2	0.0	0.0	1.5	26.3	0.0	0.0	0.0
14:50	-2.9	36.6	-0.3	-0.1	0.0	1.4	26.1	0.0	-0.1	0.0
14:51	-3.0	36.6	-0.1	0.0	0.1	1.5	26.3	0.0	-0.1	0.0
14:52	-3.0	36.9	0.0	-0.3	0.0	1.4	26.2	0.0	-0.2	0.0
14:54	-3.1	37.3	0.0	-0.3	0.0	1.2	26.7	0.0	-0.3	0.0
14:55	-3.2	36.9	0.1	0.0	0.0	1.2	26.8	0.0	-0.3	0.0
14:56	-3.1	36.3	-0.2	-0.3	0.0	1.1	26.3	-0.1	-0.7	0.0
14:57	-3.2	36.3	-0.1	-0.5	0.0	1.0	26.2	-0.1	-0.5	0.0
14:59	-3.4	37.6	0.0	-0.6	0.0	0.6		-0.1	-0.7	0.0
15:00	-3.5	37.2	-0.2	-0.5	0.0	0.5	27.4	-0.1	-0.6	0.0
15:01	-3.6	37.2	0.1	-0.2	0.2	0.4	27.6	0.0	-0.5	0.0
15:02	-3.6	37.1	-0.2	-0.5	0.0	0.4	27.6	0.0	-0.5	0.0
15:03	-3.6	37.3	-0.1	-0.4	0.0	0.3	27.6	0.0	-0.5	0.0
15:04	-3.7	37.5	-0.1	-0.2	0.0	0.3	27.7	0.0	-0.3	0.0
15:05	-3.6	37.7	0.0	-0.1	0.0	0.3	27.7	0.0	-0.5	0.0
15:06	-3.6	37.1	0.1	-0.4	0.0	0.3	27.9	0.0	-0.1	0.0
15:08	-3.6	37.4	0.0	-0.6	0.0	0.2	28.3	0.0	-0.3	0.0
15:09	-3.6	37.6	0.3	-0.3	0.2	0.2	28.6	0.0	-0.4	-0.1
15:10	-3.6	37.3	0.0	-0.7	0.0	0.2	28.7	0.0	-0.3	0.0
15:11	-3.7	37.1	0.0	-0.5	0.0	0.2	28.7	0.0	-0.3	0.0
15:12	-3.7	37.0	0.0	-0.4	0.4	0.2	28.8	0.0	-0.4	-0.1
15:14	-3.7	37.3	0.1	-0.6	0.0	0.2	29.0	0.0	-0.2	0.0
15:15	-3.8	37.6	0.3	-0.5	0.0	0.2	29.1	0.0	-0.4	0.0
15:17	-3.8	37.4	0.0	-0.1	0.0	0.2	29.2	0.0	-0.1	0.0
15:18	-3.7	37.2	0.3	0.0	0.0	0.2	28.7	0.0	0.0	0.0
15:19	-3.7	37.1	0.3	-0.1	0.0	0.2	28.4	0.0	0.0	0.0
15:23	-3.6	37.0	0.0	-0.4	0.0	0.2	28.2	0.0	0.0	0.0
15:24	-3.7	37.1	0.0	-0.5	0.0	0.2	28.3	0.0	0.0	0.0
15:25	-3.7	37.2	0.0	-0.5	0.0	0.2	28.5	0.0	0.0	0.0
15:26	-3.7	37.1	0.0	-0.4	0.0	0.2	28.6	0.0	0.0	0.0
15:27	-3.7	37.0	0.0	-0.4	0.0	0.2	28.8	0.0	0.0	0.0
15:28	-3.8	37.1	0.0	-0.3	0.0	0.2	28.8	0.0	0.0	0.0
15:29	-3.8	37.2	0.0	-0.5	0.0	0.1	28.9	0.0	0.0	0.0
15:30	-3.8	38.4	-0.3	-0.3	0.1	0.0	29.3	-0.1	-0.7	0.0
15:31	-3.9	39.0	-0.3	-0.5	0.0	-0.1	29.8	-0.1	-0.7	0.0
15:32	-4.0	39.1	-0.1	-0.4	0.1	-0.4	30.5	-0.1	-0.5	0.0
15:33	-4.1	39.7	-0.1	-0.5	0.0	-0.6	30.8	-0.1	-0.5	0.0
15:34	-4.2	40.4	-0.1	-0.3	0.0	-0.9	31.5	-0.1	-0.6	0.0
15:35	-4.2	41.9	-0.4	0.0	0.0	-1.1	32.2	-0.1	-0.6	0.0
15:36	-4.3	42.6	-0.4	0.0	0.0	-1.2	32.6	0.0	-0.4	0.0
15:37	-4.3	42.7	-0.3	0.0	0.0	-1.3	32.5	0.0	-0.1	0.0
15:38	-4.2	42.5	-0.2	0.0	0.0	-1.3	32.4	0.0	0.0	0.0
15:39	-4.2	44.0	-0.1	0.0	0.0	-1.4	32.6	0.0	0.0	0.0
15:40	-4.4	44.8	-0.2	0.0	0.0	-1.4	33.5	0.0	0.0	0.0
15:41	-4.6	45.6	0.0	0.0	0.0	-1.4	33.9	0.0	-0.3	0.0
15:42	-4.8	46.1	0.0	0.0	0.0	-1.4	33.8	0.0	0.0	0.0
15:45	-5.1	47.1	-0.6	0.0	0.0	-1.8	35.9	0.0	-0.4	0.0
15:46	-5.1	47.3	-0.5	0.0	0.0	-1.9	36.9	0.0	-0.2	0.0
15:49	-5.8	50.5	0.0	0.0	0.0	-2.2	39.4	0.0	-0.2	0.0
15:52	-6.2	51.7	-0.3	0.0	0.0	-2.6	40.7	-0.2	0.0	0.0
15:53	-6.2	52.1	-0.5	0.0	0.0	-2.8	41.1	-0.2	0.0	0.0
15:54	-6.2	52.0	-0.3	0.0	0.0	-2.9	41.5	-0.1	0.0	0.0
15:55	-6.2	52.2	-0.3	0.0	0.0	-3.1	41.4	-0.4	0.0	0.0
15:56	-6.3	52.4	0.0	0.0	0.0	-3.3	41.8	-0.1	-0.1	0.0
15:57	-6.4	52.7	0.0	0.0	0.0	-3.5	42.7	0.0	-0.2	0.0
15:58	-6.5	53.4	-0.3	0.0	0.2	-3.7	43.7	-0.1	-0.2	0.0
16:02	-7.4	57.4	-0.2	0.0	0.0	-4.2	45.6	-0.5	0.0	0.0
16:03	-7.6	59.1	-0.7	0.0	0.0	-4.4	46.6	-0.5	0.0	0.0
16:04	-7.8	60.6	-0.4	0.0	0.0	-4.7	47.5	-0.4	-0.2	0.0

16:05	-7.9	60.4	-0.4	0.0	0.0	-4.9	48.9	-0.5	-0.2	0.0
16:06	-8.0	60.2	-0.4	0.0	0.3	-5.1	49.6	-0.1	-0.4	0.0
16:09	-8.3	61.7	-0.4	0.0	0.0	-5.9	52.3	-0.3	0.0	0.0
16:10	-8.3	61.9	-0.5	0.0	0.0	-6.2	53.1	-0.4	0.0	0.0
16:11	-8.3	61.7	-0.3	0.0	0.0	-6.5	54.1	-0.7	0.0	0.0
16:12	-8.3	61.7	0.0	0.0	0.1	-6.8	55.3	-0.7	0.0	0.0
16:13	-8.3	61.4	-0.2	0.0	0.0	-7.0	55.7	-0.8	0.0	0.0
16:14	-8.3	61.0	-0.4	0.0	0.0	-7.2	56.4	-0.6	0.0	0.0
16:15	-8.3	60.7	-0.2	0.0	0.0	-7.3	57.1	-0.1	-0.1	0.0
16:16	-8.4	61.0	-0.1	0.0	0.0	-7.5	57.6	-0.1	-0.3	0.0
16:17	-8.4	60.9	0.0	0.0	0.0	-7.6	58.6	-0.1	-0.3	0.0
16:18	-8.5	61.4	0.3	0.0	0.0	-7.8	59.5	-0.1	-0.4	0.0
16:19	-8.7	61.8	0.0	0.0	0.0	-7.9	60.4	-0.1	-0.4	0.0
16:20	-8.8	62.3	0.0	0.0	0.0	-8.0	60.8	0.0	-0.4	0.0
16:21	-9.0	63.1	0.1	-0.1	0.0	-8.1	61.4	0.0	-0.4	0.0
16:22	-9.1	65.0	0.3	0.0	0.0	-8.2	62.3	0.0	-0.4	0.0
16:23	-9.2	65.5	-0.1	0.0	0.0	-8.4	63.0	0.0	-0.3	0.0
16:24	-9.3	66.3	-0.4	0.0	0.0	-8.5	63.3	-0.1	-0.3	0.0
16:25	-9.4	67.8	-0.3	0.0	0.0	-8.6	63.9	-0.5	-0.1	0.0

#### APPENDIX D: VISCOSITY CORRECTION TERM $F(\lambda)$ .

Since the viscous losses increase at high frequencies, Biot (1956b) derived a correction term  $F(\lambda)$  for two pore geometries. For slit-like, parallel sided pores, Biot found

$$F(\lambda_s) = \frac{\frac{1}{3} \lambda_s i^{1/2} \tanh(\lambda_s i^{1/2})}{1 - \tanh(\lambda_s i^{1/2}) / (\lambda_s i^{1/2})} \quad (D1)$$

where  $\lambda_s = b (\omega/\nu)^{1/2}$  and  $b$  is the half-width of the slit. For cylindrical pores,

$$F(\lambda_c) = \frac{\frac{1}{4} \lambda_c i^{1/2} T(\lambda_c i^{1/2})}{1 - 2T(\lambda_c i^{1/2}) / (\lambda_c i^{1/2})} \quad (D2)$$

where  $\lambda_c = a (\omega/\nu)^{1/2}$ ,  $a$  is the pore radius and  $T(x) = J_1(x)/J_0(x)$  is a ratio of Bessel functions. More recently, Attenborough (1983, 1987) has derived the correction factor needed for a distribution of pores of arbitrary shapes. The pore structure is characterized by a pore shape factor ratio  $s_f$ , a grain shape factor  $n'$ , an effective flow resistivity  $\sigma$  and the porosity  $\Omega$ . The correction factor is

$$F(\lambda_a) = \frac{\frac{s_f^2}{4} \lambda_a i^{1/2} T(\lambda_a i^{1/2})}{1 - 2T(\lambda_a i^{1/2}) / (\lambda_a i^{1/2})} \quad (D3)$$

where

$$\lambda_a = \frac{1}{s_f} \left( \frac{8\rho_f \omega \theta^2}{\sigma \Omega} \right)^{1/2}$$

and the tortuosity  $q^2 = \Omega^{-n'}$  has been introduced. Biot (1956b) showed that when

$$\lambda_c = \frac{4}{3} \lambda_s$$

the correction factors given by eq D1 and D2 are nearly identical. The form of  $F(\lambda_a)$  differs from  $F(\lambda_s)$  only by a multiplicative factor of  $s_f^2$  although the expressions for  $\lambda$  are different. When  $s_f = 1.0$ , the value for cylindrical pore shapes, the two expressions give identical results. The dimensionless parameters  $\lambda$  can be written in terms of macroscopic quantities

$$\lambda_s = \sqrt{6\pi} \left( \frac{k_s f}{\Omega \nu} \right)^{1/2}$$

$$\lambda_a = \frac{4\sqrt{\pi}}{s_f} q \left( \frac{k_s f}{\Omega \nu} \right)^{1/2}$$

# REPORT DOCUMENTATION PAGE

Form Approved  
OMB No. 0704-0188

Public reporting burden for this collection of information is estimated to average 1 hour per response, including the time for reviewing instructions, searching existing data sources, gathering and maintaining the data needed, and completing and reviewing the collection of information. Send comments regarding this burden estimate or any other aspect of this collection of information, including suggestion for reducing this burden, to Washington Headquarters Services, Directorate for Information Operations and Reports, 1215 Jefferson Davis Highway, Suite 1204, Arlington, VA 22202-4302, and to the Office of Management and Budget, Paperwork Reduction Project (0704-0188), Washington, DC 20503.

1. AGENCY USE ONLY (Leave blank)		2. REPORT DATE November 1993		3. REPORT TYPE AND DATES COVERED	
4. TITLE AND SUBTITLE  Attenuation of Outdoor Sound Propagation Levels by a Snow Cover				5. FUNDING NUMBERS  PE: 6.27.30A PR: 4A762730AT24 4A762730AT42	
6. AUTHORS  Donald G. Albert					
7. PERFORMING ORGANIZATION NAME(S) AND ADDRESS(ES)  U.S. Army Cold Regions Research and Engineering Laboratory 72 Lyme Road Hanover, New Hampshire 03755-1290				8. PERFORMING ORGANIZATION REPORT NUMBER  CRREL Report 93-20	
9. SPONSORING/MONITORING AGENCY NAME(S) AND ADDRESS(ES)  Office of the Chief of Engineers Washington, D.C. 20314-1000				10. SPONSORING/MONITORING AGENCY REPORT NUMBER	
11. SUPPLEMENTARY NOTES					
12a. DISTRIBUTION/AVAILABILITY STATEMENT  Approved for public release; distribution is unlimited.  Available from NTIS, Springfield, Virginia 22161				12b. DISTRIBUTION CODE	
13. ABSTRACT (Maximum 200 words)  The absorption of sound energy by the ground has been studied extensively because of its importance in understanding noise propagation through the atmosphere. This report investigates the attenuative effect of snow on sound propagation, and provides quantitative measurements and an accurate model for predicting these effects. Summer and winter experiments were conducted at a site in northern Vermont to investigate the effect of a snow cover on low energy sound propagation in the 5- to 500-Hz frequency band for propagation distances between 1 and 274 m. Pistol shots were used as the source of the acoustic waves, with geophones and microphones serving as the receivers. A comparison of the summer and winter recordings revealed a number of effects caused by the introduction of a 0.25-m-thick snow cover. The peak amplitude of the air wave was more strongly attenuated in the winter, with a decay rate proportional to $r^{-1.6}$ versus $r^{-1.2}$ in the summer, corresponding to an order of magnitude difference in the signal levels after 100 m of propagation. The waveforms were also markedly changed, with broadened pulses and greatly enhanced low frequencies appearing in the winter recordings. The pulse broadening and peak amplitude decay rates of the acoustic waveforms were successfully predicted theoretically using a layered, rigid, porous model of the snow, with an assumed surface effective flow resistivity of $20 \text{ kN s m}^{-4}$ . Calculations of ground motion induced by the atmospheric sound waves were made using a viscoelastic model of the ground and the wavenumber integration technique. Although soil ground motions were					
14. SUBJECT TERMS  Acoustic to seismic coupling Outdoor sound propagation  Porous medium acoustics Sound absorption Snow acoustics				15. NUMBER OF PAGES 114	
				16. PRICE CODE	
17. SECURITY CLASSIFICATION OF REPORT UNCLASSIFIED	18. SECURITY CLASSIFICATION OF THIS PAGE UNCLASSIFIED	19. SECURITY CLASSIFICATION OF ABSTRACT UNCLASSIFIED	20. LIMITATION OF ABSTRACT  UL		

13. ABSTRACT (*Cont'd.*)

successfully modeled, induced motions in the snow were not, and the model always underpredicted the observed decay rates. An investigation of plane wave transmission from a fluid into a porous solid using Biot's theory shows that the presence of pores in the solid is the most important factor in the acoustic energy loss, not attenuation by transmission to the solid frame, and an explicitly porous model will be necessary to compute correctly the motion induced in the snow.